

DESIGN REPORT TEVATRON 1 PROJECT

OCTOBER, 1982

SECOND PRINTING NOVEMBER 1982

**Fermi National Accelerator Laboratory
Batavia, Illinois**

**Operated by Universities Research Association Inc.,
under contract with the U.S. Department of Energy**

1. Introduction and Overview
2. Proton Acceleration and Extraction for Antiproton Production
3. Targeting and Transport
 - 3.1 Proton and Transport F18 to Target
 - 3.2 Antiproton Production
 - 3.3 Antiproton Target System Components
 - 3.4 Target Hall
 - 3.5 Antiproton Transport to Debuncher
4. Debuncher
 - 4.1 Purpose of the Debuncher
 - 4.2 Rotation and Debunching
 - 4.3 Debuncher Lattice
 - 4.4 Beam Transfer
 - 4.4.1 Injection
 - 4.4.2 Extraction
 - 4.5 Radio Frequency Systems
 - 4.5.1 Antiproton Debuncher RF
 - 4.5.2 Gap-Preserving RF
 - 4.6 Magnet and Power-Supply Systems
 - 4.7 Betatron Cooling
 - 4.7.1 Design Goal
 - 4.7.2 Design Considerations
 - 4.7.3 Hardware
 - 4.7.4 Computer Simulation
 - 4.7.5 Effect of the Gap on Betatron Cooling
5. Accumulator
 - 5.1 Accumulator-Functional Summary
 - 5.2 Momentum Cooling
 - 5.2.1 Introduction to Stochastic Stacking
 - 5.2.2 Summary of Design Considerations
 - 5.2.3 Building the Exponential Gain Profile
 - 5.2.4 Signal Suppression and Stability
 - 5.2.5 Core Cooling
 - 5.2.6 Numerical Calculations of Momentum Cooling
 - 5.3 Betatron Cooling
 - 5.3.1 Introduction
 - 5.3.2 Betatron Cooling in the Core
 - 5.3.3 Stack-Tail Betatron Cooling
 - 5.3.4 Operation of Betatron Cooling Systems
 - 5.4 Stochastic Cooling Hardware
 - 5.4.1 Pickup Electrodes
 - 5.4.2 Preamplifiers
 - 5.4.3 Notch Filters
 - 5.4.4 Travelling Wave Tubes (TWT's)
 - 5.4.5 Kicker Electrode Assemblies
 - 5.4.6 Other Considerations
 - 5.4.7 Accumulator Stochastic Cooling Layout
 - 5.5 Accumulator Lattice
 - 5.6 Radio Frequency Systems
 - 5.7 Accumulator Magnet and Power Supply Systems
 - 5.8 Vacuum System
 - 5.8.1 Vacuum Requirements

- 5.8.2 Vacuum System Layout Characteristics
- 6. Extraction of Antiprotons from the Accumulator and Transfer to the Main Ring.
 - 6.1 Extraction and Accumulator Beam Manipulation
 - 6.2 Main Ring RF Capture and Acceleration
 - 6.2.1 Introduction
 - 6.2.2 Injection and Rebunching
 - 6.2.3 Bunch Recombination at 150 GeV
- 7. The Main Ring in Tevatron I
 - 7.1 Functions of the Main Ring in Tevatron I
 - 7.2 Proton Acceleration and Rebunching Hardware
 - 7.3 Overpasses
- 8. The Energy Saver in Tevatron I
 - 8.1 Functions of the Energy Saver in Tevatron I
 - 8.2 Energy Saver Lattice
 - 8.2.1 Ring Location and Normal Lattice
 - 8.2.2 Normal and High-Beta Long Straight Sections
 - 8.2.3 Lattice Elements
 - 8.2.4 Low-Beta Long Straight Section
 - 8.3 Correction Systems and Operating Point
 - 8.3.1 Correction Magnets in Superconducting Accelerator
 - 8.3.2 Placement of Correction Elements
 - 8.3.3 Functions and Strengths
 - Steering Dipoles
 - Trim Quadrupoles
 - Sextupoles
 - Octupoles
 - Skew Quadrupoles
 - 8.3.4 Excitation
 - Current Tolerances
 - Circuits
 - 8.3.5 Power Supplies
 - Steering Dipole Supplies
 - High-Precision Supplies
 - 8.4 Main Ring Extraction and Energy Saver Injection and Abort
 - 8.5 Acceleration of Protons and Antiprotons
 - 8.5.1 Energy Saver RF Requirements for Colliding Beams
 - Cavity Spacing
 - 8.5.2 Failure Modes
 - 8.6 Energy Saver Diagnostics
 - 8.6.1 Energy Saver Position Detectors
 - 8.6.2 Beam-Loss Monitors
 - 8.6.3 Diagnostics for Collider Operation
- 9. Interaction Regions and Experimental Facilities
 - 9.1 Experimental Areas
 - 9.1.1 BO Experimental Area
 - 9.1.2 DO Experimental Area
 - 9.2 Low-Beta Design
 - 9.2.1 Lattice Design
 - 9.2.2 Transition to Low Beta
 - 9.3 Hardware Modifications
 - 9.3.1 Magnets

- 9.3.2 Power Supplies and Bus
- 9.3.3 Refrigeration
- 9.3.4 Vacuum
- 10. Performance and Luminosity
 - 10.1 Beam Geometry
 - 10.2 Beam Cross Section at the Collision Point
 - 10.3 Luminosity
 - 10.4 Beam-Beam Tune Shift
 - 10.5 Single-Beam and Luminosity Lifetime
 - 10.5.1 Effects of Residual Gas
 - 10.5.2 Intrabeam Scattering
 - 10.5.3 Beam-Beam Effects
- 11. Commissioning and Operation
 - 11.1 Commissioning
 - 11.2 Diagnostics
 - 11.2.1 Accumulator and Debuncher Diagnostics
 - 11.2.2 Targeting and Beam Transfer Diagnostics
 - 11.3 Controls
 - 11.4 Booster Test Beam Line

1. INTRODUCTION AND OVERVIEW

This report describes the design of the Tevatron I Project, which will enable Fermilab to produce proton-antiproton collisions in the Tevatron accelerator. Center-of-mass energies near 2 TeV, by far the highest available anywhere in the world for high-energy physics research until at least the decade of the 1990's, will provide enormous opportunities for exciting new physics.

After the energy, the most important parameter determining the utility of a colliding-beam facility is the luminosity, or interaction rate per unit cross section. The first goal of the Tevatron I project is to achieve a peak luminosity of $10^{30} \text{cm}^{-2} \text{sec}^{-1}$ for proton-antiproton collisions at the maximum energy in the Tevatron.

The luminosity depends on the intensity and phase space density of the interacting beams. The design luminosity of $10^{30} \text{cm}^{-2} \text{sec}^{-1}$ can be achieved with as few as 1.8×10^{11} protons and 1.8×10^{11} antiprotons of appropriate phase space density. The number and phase-space density of antiprotons produced by bombarding a dense target with one pulse of protons from the Main Ring are too small by orders of magnitude to achieve the design luminosity. Thus it is necessary to collect many pulses of antiprotons in an accumulator ring and to increase their phase-space density, i. e. to cool them, by roughly six orders of magnitude. To minimize user frustration and maximize the average luminosity, the accumulation time should be as short as possible, at least short compared to the luminosity lifetime, which is expected to be larger than twenty hours. The second goal of the project is to accumulate and cool the required number of antiprotons in five hours or less, starting with no antiprotons in the Accumulator.

The design presented here to meet these goals is based on the method of stochastic cooling developed by van der Meer, Thorndahl, and coworkers.¹ This method generates a non-uniform phase-space density distribution of the accumulated antiprotons, with only the high-density core useful for colliding beams. Thus the source has been designed to accumulate a total of 4.3×10^{11} antiprotons in 4 hours, of which typically 1.8×10^{11} antiprotons from the high-density core will be injected into the Tevatron. Subsequent accumulation cycles starting with the antiprotons left from the previous cycle will require considerably shorter times to achieve the necessary core density.

The amount of cooling to be done depends on the phase-space density at production. The higher the initial density, the easier it is to achieve the final density. The yield of antiprotons per incident proton is proportional to the product of the spatial solid angle and the momentum spread accepted by the beam-transport system, and the initial phase-space density can therefore be increased only by decreasing the spot size and time spread of the antiprotons. The initial protons that produce the antiprotons determine these parameters and it is therefore useful to reduce the proton spot size and time spread.

The proton rms spot size will be reduced to 0.38 mm by the use of standard quadrupole lenses. Further reduction would provide little gain because the apparent spot size is ultimately dominated by the large antiproton beam divergence and the finite length of the target.² The first collection lens must match the large angular divergence of the antiproton beam at the target into the small angular admittance that is characteristic of a beam-transport system or a storage ring. This is achieved by using a lithium lens of the type developed by the Institute of Nuclear Physics at Novosibirsk.³

The time spread can be minimized by rf manipulation of the proton beam in the Main Ring just prior to extraction. The narrow time spread and large energy spread of the resulting antiproton bunches can be transformed into bunches with a much lower energy spread by rf phase rotation in a separate ring called the Debuncher. The rf phase-rotation system⁴ makes it possible to start with a large momentum spread from the target, thereby increasing the antiproton flux. The reduced energy spread also greatly simplifies the design of the magnets and cooling systems of the Accumulator ring.

The design thus uses two fixed energy rings, the Debuncher and the Accumulator, located south of the Booster as shown in Fig. 1-1. The Accumulator has the same circumference as the Booster; the Debuncher is slightly larger. Both rings operate at a kinetic energy of 8 GeV, the Booster energy. The sequence of operations leading to colliding beams involves seven steps:

1. Proton Acceleration for Antiproton Production. Every two seconds, one Booster batch containing 2×10^{12} protons in 82 rf bunches is accelerated in the Main Ring to 120 GeV and held at that energy while the rf manipulation described in the next step is carried out.

2. Preparation of Protons for Targeting. The 53-MHz rf voltage is lowered to cause each proton bunch to spread in time to 9 nsec. The rf voltage is suddenly increased to 4 MV per turn and each proton bunch rotates by 90° in phase space in 1.3 msec to a short bunch of less than a nanosecond in width, but with an energy spread of about 0.4%. This train of short bunches is extracted from the Main Ring at F17 as soon as the bunch rotation is completed.

3. Antiproton Production and Transport. The short proton bunches strike a tungsten target, producing a train of 82 equally short antiproton bunches. The peak energy deposition in the target is the same as that used successfully at CERN. 7×10^7 8.9 GeV/c antiprotons are collected by the lithium lens and transported to the Debuncher. The momentum spread of the beam is 3% and the transverse beam emittances are 20π mm-mrad in each plane.

4. Bunch Rotation in the Debuncher. The antiprotons are injected into 53-MHz rf buckets in the Debuncher. The rf voltage is large enough

that the antiproton bunches rotate just as the proton bunches rotated in the previous step. After a quarter of a synchrotron oscillation, the narrow time structure and large momentum spread have been transformed into a small momentum spread and a broad time structure. The rf voltage is then rapidly lowered to match the bucket to the rotated bunch, and finally adiabatically lowered to reduce the momentum spread to 0.2%.

5. Transverse Cooling in the Debuncher. After the rf manipulations, the horizontal and vertical transverse emittances are stochastically cooled in the Debuncher from 20π mm-mrad to 7π mm-mrad during the almost two seconds before the next antiprotons are to be injected.

6. Antiproton Accumulation and Cooling. The antiprotons are extracted from the Debuncher and injected into the Accumulator. Successive batches are accumulated by rf stacking each batch at the edge of the stack. Between injection cycles, the stack is stochastically cooled using a combination of longitudinal and transverse cooling systems similar to the types developed by CERN for the AA ring.⁵ A new batch of antiprotons with a density of about 7 antiprotons per eV is deposited at the stack tail every 2 sec. The fresh batch is moved by the coherent force of the stochastic-cooling system away from the injection channel and toward the center of the stack. The strength of the coherent force diminishes exponentially as the particles move away from the edge of the tail, causing the particle density to increase. Diffusion forces resulting from the Schottky noise of the antiproton stack and the thermal noise of the amplifiers cause the antiprotons to migrate from the high-density region toward the low-density region. As long as the coherent force is greater than the diffusion forces, the stack builds up in intensity until it reaches the core region where the coherent force is zero. Some antiprotons are lost during transfer and rf stacking and some diffuse away from the stack into the chamber walls. Allowing for losses, 6×10^7 antiprotons are stacked in each pulse. In 4 hours, the core will grow to a density of 1.0×10^5 antiprotons per eV. The total number of antiprotons in the core will be 4.3×10^{11} . During this time the transverse cooling systems will have reduced the horizontal and vertical emittances to 2π mm-mrad.

7. Filling the Tevatron. After accumulation is complete, antiproton bunches of the desired intensity are individually extracted from the core, transferred to the Main Ring, accelerated to 150 GeV and injected into the Tevatron. The same number of proton bunches of similar intensity are prepared in the Main Ring and injected into the Tevatron. Whether it is better to inject the protons or antiprotons first will be determined empirically. Both beams are then simultaneously accelerated to the desired energy.

Sufficient antiprotons for a luminosity of $10^{30} \text{ cm}^{-2} \text{ sec}^{-1}$ can be produced in 4 hours by this sequence, even with reasonable losses in production, cooling, and beam transfer. The project includes a Main Ring beam overpass

at B0 to allow antiproton accumulation to proceed in parallel with colliding beams in the Tevatron. The design luminosity can be achieved without exceeding a beam-beam tune shift of 0.0018 per crossing. As the Tevatron and the Antiproton Source become more reliable, longer collection times will become practical, resulting in higher luminosity.

Beam accumulation techniques are developing rapidly and it seems highly advisable to design an antiproton source that can accommodate future improvements. Accordingly, the third goal of this design is to incorporate flexibility for future improvements so that the Antiproton Source may ultimately achieve a luminosity of $10^{31} \text{cm}^{-2} \text{sec}^{-1}$. The potential for luminosity of the proposed source is exhibited in Table 1-I, which shows the relationship between the number of accumulated antiprotons and the luminosity.

The peak luminosity and accumulation rate are limited not by the antiproton production rate but by the cooling systems of the Accumulator Ring. Higher luminosities may be achieved through improvements in these cooling systems. The present design uses less than a half of the total number of particles collected in each accumulation cycle to reach its design luminosity of $10^{30} \text{cm}^{-2} \text{sec}^{-1}$. If future improvements can increase the final density by a factor of three, it will be possible to approach a luminosity of $10^{31} \text{cm}^{-2} \text{sec}^{-1}$. The design of the rings therefore includes provisions (aperture and straight-section space) for:

- (i) Momentum precooling in the Debuncher,
- (ii) Improved stochastic cooling in the Accumulator,
- (iii) Improved Main Ring extraction for antiproton production.
- (iv) Intermediate energy electron cooling in the Accumulator.

Other future improvements may include:

- (v) A superquadrupole to reduce beam size in the interaction region.

These features are not part of the initial design because it is difficult to foresee which improvements will be most feasible and cost-effective. The most beneficial choices will be clear only after some experience in operating the collider.

The design of each system are described in greater detail in the following sections.

Table 1-I. LUMINOSITY PROGRESSION

$N_{\bar{p}}$ (10^{11})	N_p (10^{11})	N_B	N_T (10^{11})	L ($10^{30} \text{cm}^{-2} \text{sec}^{-1}$)
0.8	0.8	1	0.8	0.65
0.6	0.6	3	1.8	1.0 (design goal)
0.8	0.8	3	2.4	2.0
1.0	1.0	3	3.0	3.0
1.0	1.0	6	6.0	6.0

$N_{\bar{p}}$ and N_p are the numbers of antiprotons and protons per bunch, N_B is the number of bunches, N_T is the total number of antiprotons, $\beta^* = 1 \text{ m}$ is the value of β at the center of the interaction region, and L is the luminosity.

References

1. S. van der Meer, Stochastic Damping of Betatron Oscillations in the ISR CERN/ISR-PO/72-31 (1972) (unpublished).
D. Mohl, G. Petrucci, L. Thorndahl, and S. van der Meer, Physics Reports 58, p. 73 (1980).
2. C. Hojvat and A. Van Ginneken, Fermilab \bar{p} Note 139, July 16, 1981 (unpublished).
3. B. F. Bayanov et al., Nucl. Inst. Methods 190, 9 (1981).
4. A. G. Ruggiero, Fermilab \bar{p} Note 102, January, 1981 (unpublished).
5. S. van der Meer, Stochastic Stacking in the Antiproton Accumulator CERN/PS/AA/78-22 (1978) (unpublished).

2. PROTON ACCELERATION AND EXTRACTION FOR ANTIPROTON PRODUCTION

The production of antiprotons is done by bombarding a target with protons which have been accelerated to 120 GeV in the Main Ring. This chapter describes the acceleration of protons in the Main Ring and their subsequent extraction at F17.

2.1 Proton Acceleration

The accumulation cycle begins by accelerating a single Booster batch of protons in the Main Ring to 120 GeV with the existing rf system. This Booster batch consists of a string of 82 bunches spaced by 5.6 m; its total length is 457 m. A single batch fills less than one-thirteenth of the Main Ring circumference. The Booster intensity record for a single batch is 3.4×10^{12} . For the purpose of this report, it is assumed that an intensity 2.0×10^{12} protons per Booster batch will be standard operating intensity for \bar{p} production. The minimum time needed to accelerate a single batch to 120 GeV in the Main Ring can be reduced to 1.87 seconds. A flat-top of 0.13 sec is added to provide time for the rf beam manipulation before extraction. The cycle time is 2 seconds. The major beam properties are given in Table 2-I.

A reasonable estimate for the normalized betatron emittance, based on measurements,¹ is 24π mm-mrad. This value includes 95% of the beam. If $\sigma_{H,V}$ denotes the rms beam size and $\beta_{H,V}$ the lattice amplitude function, the emittance can be expressed in terms of these quantities as

$$\epsilon_{H,V} = 6\pi \frac{\sigma_{H,V}^2}{\beta_{H,V}}.$$

The longitudinal phase-space area S of individual bunches in a booster batch has been measured to be 0.3 eV-sec or less.² If the particle distribution is biGaussian in these variables, this value includes 95% of the beam. There is reason to believe this number could be reduced to 0.2 eV-sec in the future when improvements are made to the Main Ring and the Booster rf systems.

For energies well above the transition energy, a bunch area S half as large as the bucket area, and a bunch shape matched to the rf bucket, the rms bunch length σ_e and rms momentum spread σ_p/p are

$$\sigma_e = (142\text{cm}) \frac{S}{\sqrt{E}} \quad \sigma_p/p = (0.0112) \frac{S}{\sqrt{E^3/V}}.$$

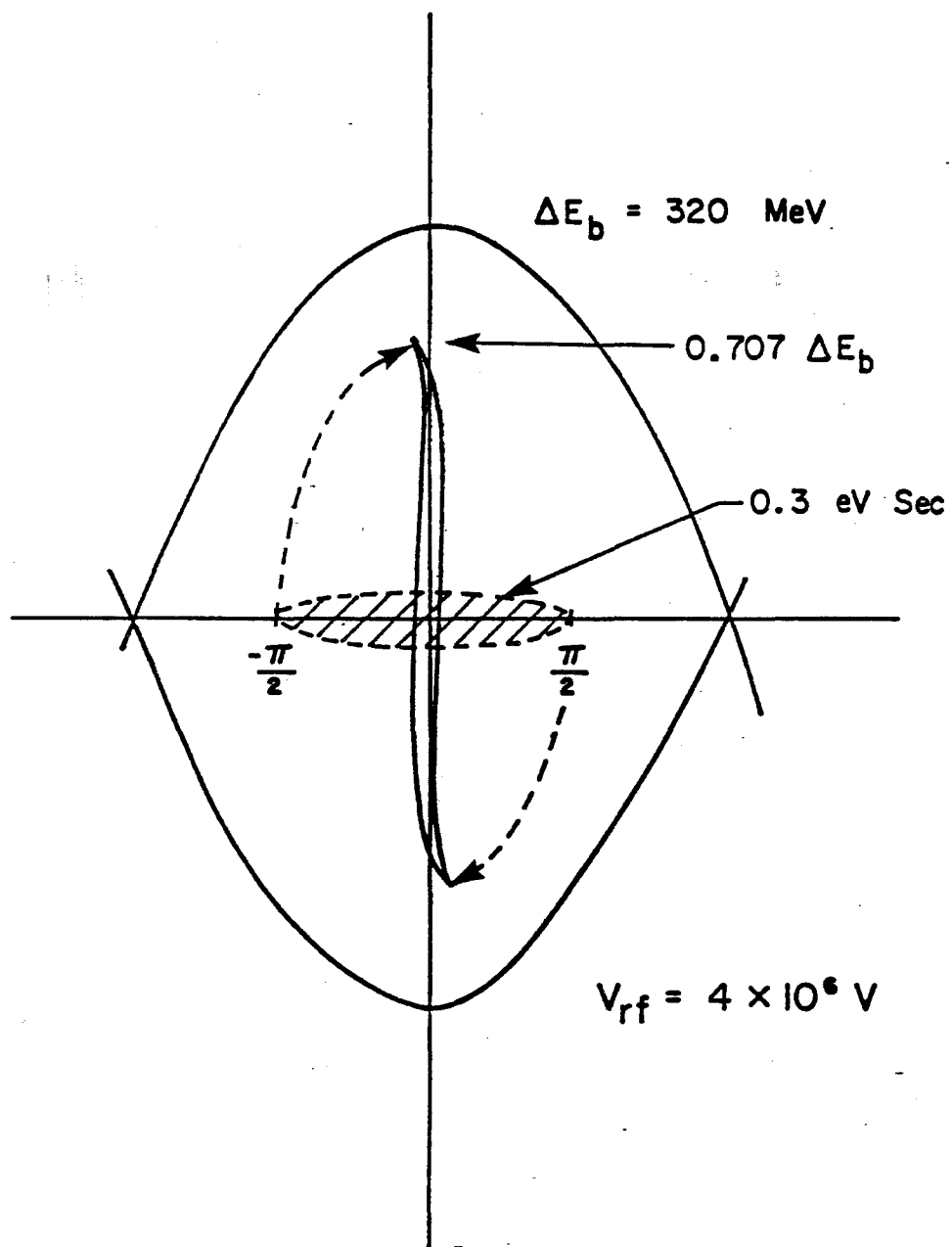


Fig. 2-1

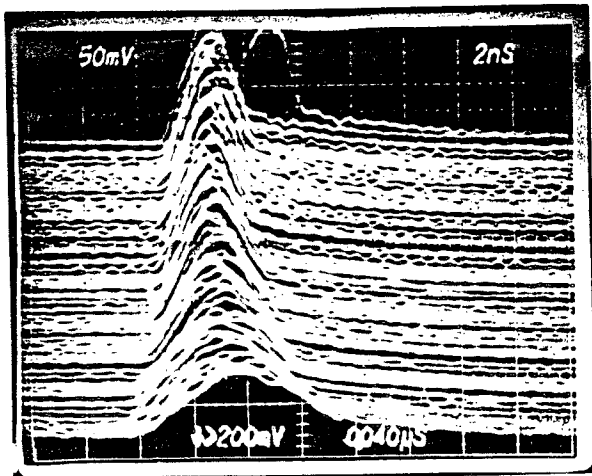


Figure 2-2

Bunch broadening resulting from slow reduction in rf voltage. Time progresses downward and total debunching time is 100 msec. Final bunch length is near 9 nsec.

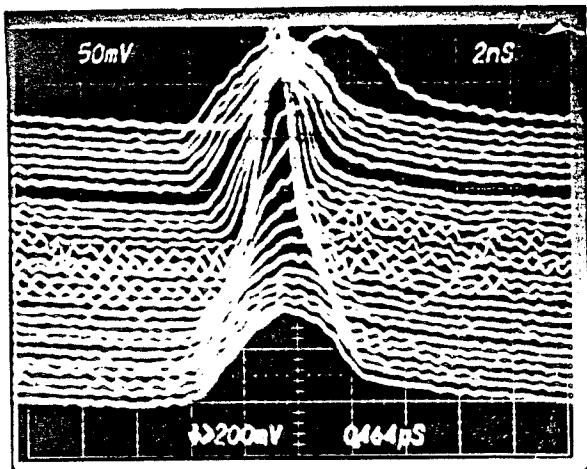


Figure 2-3

Rotation of mismatched bunch following sudden increase in rf voltage to 1 MV. Time progresses downward and traces are separated by about 100 msec. The displaced top trace is a mistrigger.

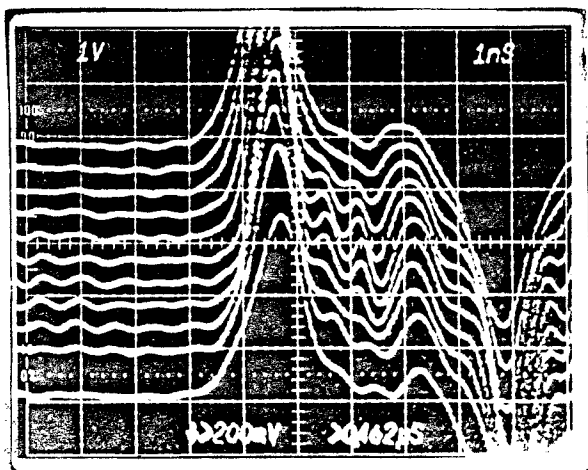


Figure 2-4

Bunch length pictures near the narrowest bunch time. Traces are separated by one machine turn, 20.9 μ sec. The narrowest bunch has length about 1 nsec. The beam pickup is a broadband transmission line pickup so inverted reflections from the downstream end of the pickup also appear. In this experiment the maximum rf voltage available was 3.6 MV. Narrower bunches can be obtained by using the full MV. A bunch with 95% full time width of 1 nsec corresponds to a physical length (one standard deviation) of 7.5 cm.

The bunch area can be expressed in terms of these quantities as

$$S = 6\pi\beta E \frac{\sigma_e}{c} \frac{\sigma_p}{p} .$$

The bucket area of a stationary bucket B and the phase oscillation period T_s are respectively

$$B = (0.34 \text{ eV-sec}) \sqrt{VE} \quad T_s = (1\text{msec}) \sqrt{E/V} .$$

In all these equations E is in GeV, V in MV and S in eV-sec.

For a fixed antiproton momentum spread, the bunch area of the antiprotons is minimized by making the time spread of the extracted proton bunches as narrow as possible. At the end of acceleration when the rf voltage is 4 MV the relevant beam parameters are $T_s = 5.6 \text{ msec}$, $\sigma_e = 16 \text{ cm}$, $\sigma_p/p = 2.4 \times 10^{-4}$.

The rf voltage is slowly reduced from 4 MV to 30 kV so that the bunch motion remains matched to the rf bucket shape. At 30 kV, the beam parameters are $T_s = 65 \text{ msec}$, $\sigma_e = 56 \text{ cm}$, and $\sigma_p/p = 6.8 \times 10^{-5}$. The adiabatic reduction of the rf voltage is accomplished in 100 msec. At that moment the synchrotron phase of the bunch extends to $\pm 90^\circ$.

The rf voltage is then raised abruptly to 4 MV within two revolutions or 42 μsec . The bunches are no longer matched to the buckets, so they start to rotate as in Fig 2-1. After a quarter of a phase oscillation or 1.4 msec, the time spread of the beam has been reduced by more than an order of magnitude. At that moment the beam parameters are $T_s = 5.6 \text{ msec}$, $\sigma_e = 5.0 \text{ cm}$, and $\sigma_p/p = 8.4 \times 10^{-4}$. After these operations are completed, a momentum spread of $\pm 0.4\%$ contains 95% of the beam.

The results of recent bunch narrowing experiments in the Main Ring at 120 GeV (March 1982)², are shown in Figs. 2-2, 2-3, and 2-4. In these experiments the maximum rf voltage was limited to 3.6 MV. Shorter bunches can be obtained by using the full available 4 MV.

Measurements made in the Main Ring³ have shown that the available momentum aperture is $\pm 0.27\%$ for 90% beam transmission at 120 GeV with extraction equipment for the Tevatron in place. The loss of beam due to the 0.4% momentum spread is expected to be small, since very little of the beam will extend into the bad-field region of the aperture. As soon as the bunch rotation is complete, all 82 bunches are ejected at F17 into the 120-GeV transport line.

Table 2-I. MAIN RING BEAM PARAMETERS

Proton Beam Kinetic Energy @ Extraction	120 GeV
Relativistic Factors: β	0.99997
γ	128.9318
B ρ , magnetic rigidity	4035.506 kG-m
Momentum, P	120.9347 GeV/c
Number of Booster batches accelerated	one
Number of Proton Bunches	82
Total number of protons per Batch	$<2.0 \times 10^{12}$
Main Ring Cycle Time	2.0 sec
Betatron Emittance, 95% of beam, (H and V)	0.2π mm-mrad
Longitudinal Emittance, 95% of beam at 120 GeV	0.3 eV-sec
RF harmonic number (h)	1113
RF Frequency @ 120 GeV	53.1035 Mhz
Revolution Period @ 120 GeV	20.96 μ sec
Booster Batch Time Length	1.56 μ sec
Transition Energy (γ_t)	18.75
Betatron tune number (H and V)	19.4
$\eta = \gamma^2 - \gamma_t^2$	-0.0028
Maximum RF voltage	4.0 MV
Average Radius	1000 m

2.2 Extraction at F17

Extraction of 120-GeV protons from the Main Ring for the production of antiprotons takes place at location F17. Two Lambertson magnets deflect the extracted beam vertically by 32.2 mrad into the transport line, which is located just above the Main Ring magnets. The geometry and expected beam sizes at the Lambertsons are shown in Fig. 2-5 and 2-6. The horizontal beam size at 120. GeV includes the contribution of the $\pm 0.2\%$ momentum spread of the tightly bunched proton beam. The large horizontal size of the bunched beam uses most of the available Main Ring aperture to the inside of the Ring at the extraction point. As seen in Figs. 2-5 and 2-6, the septum of each Lambertson will be located well within the Main Ring aperture, preventing parasitic extraction at F17 during the 400-GeV slow-extraction HEP program. The Lambertsons will be withdrawn from the aperture during 400-GeV operation.

The relevant parameters of the Main Ring lattice are listed in Table 2-II.

Table 2-II. PROPERTIES OF SELECTED MAIN RING MINISTRAIGHTS

Horizontal-Plane Lattice Functions

Location	β (m)	α	Phase Relative to F17 (Modulo	Space Available (in.)
----------	----------------	----------	--	-----------------------------

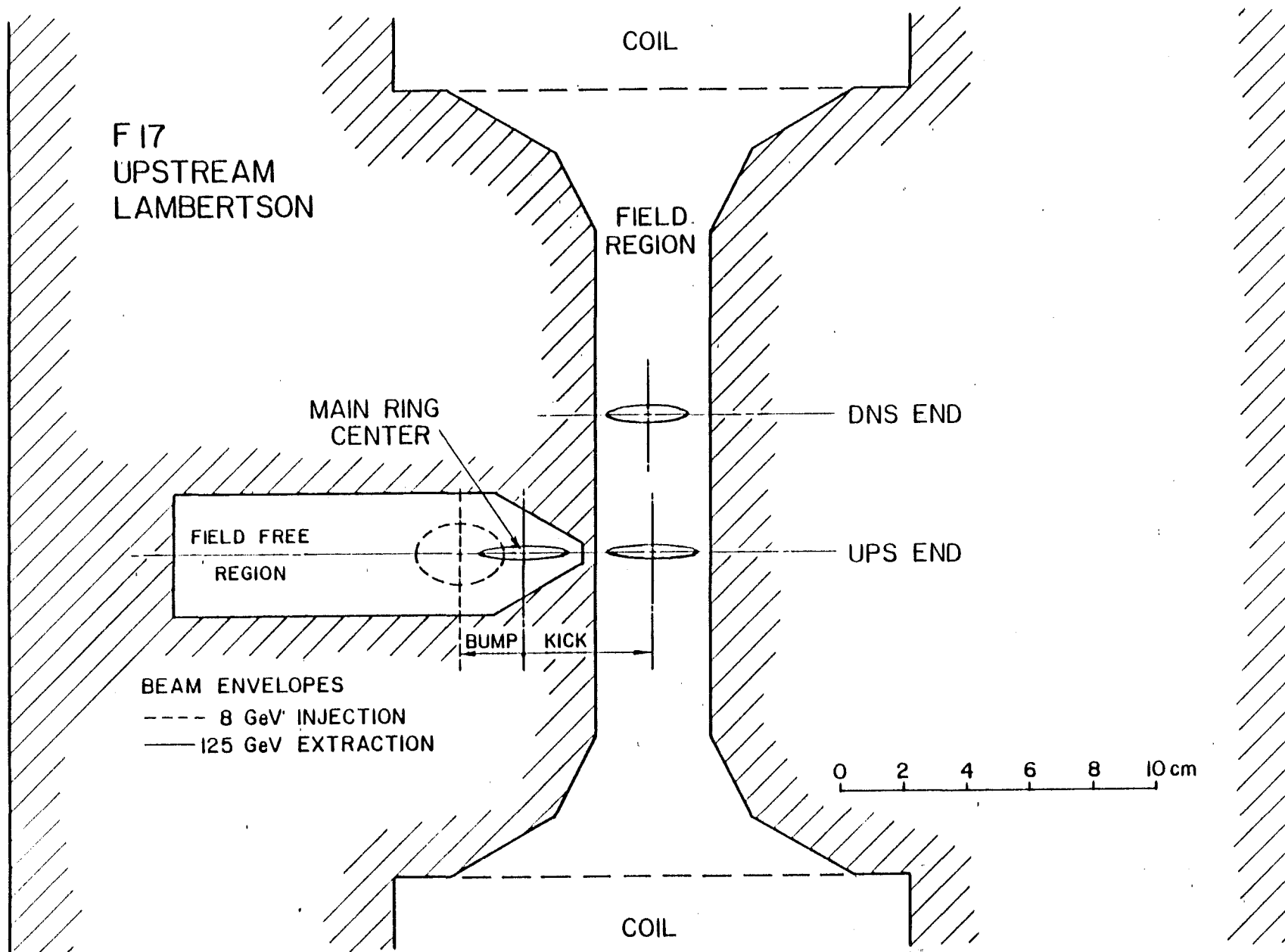


Fig. 2-5

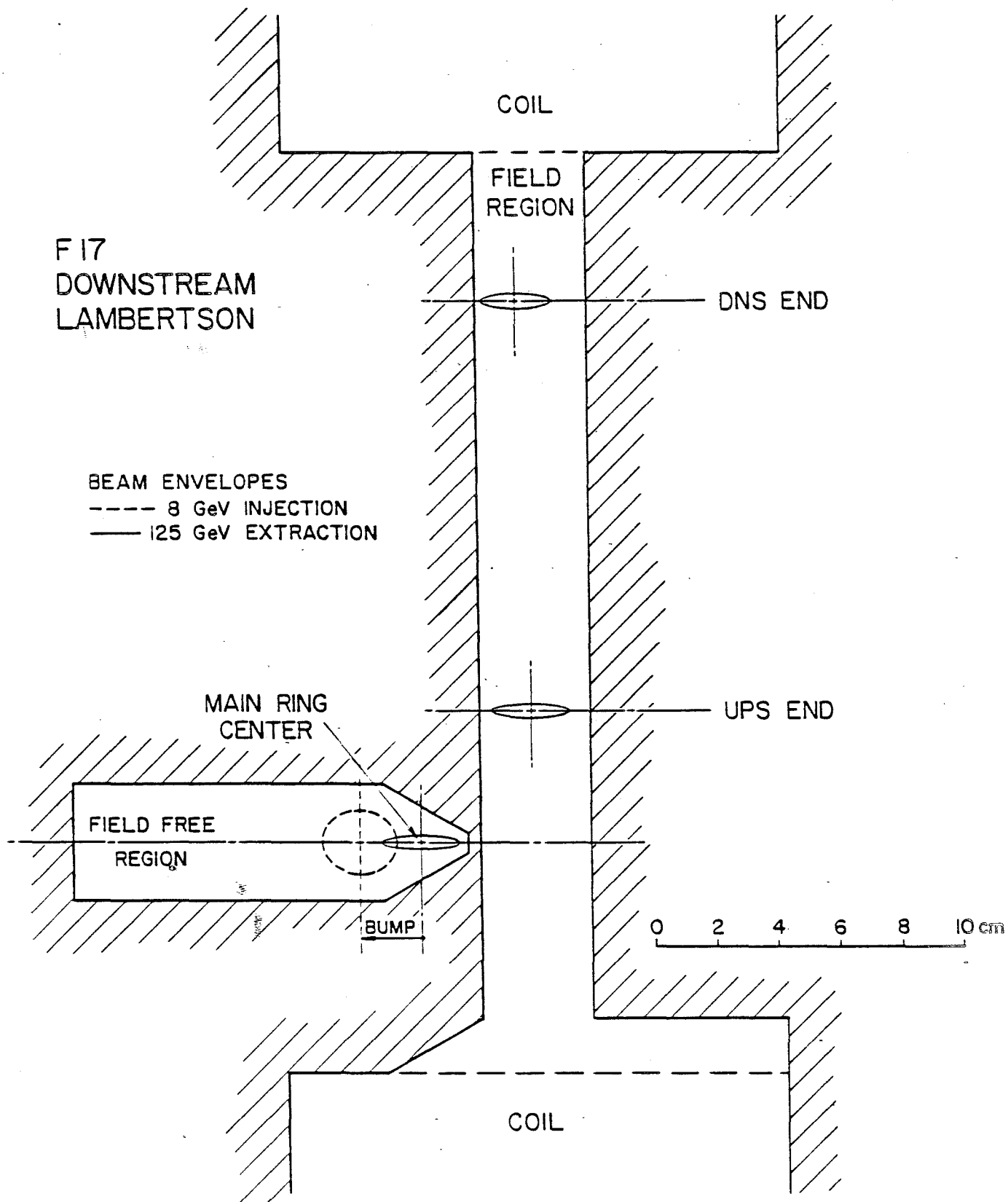


Fig. 2-6

360°)

C48 Kicker	102.4	0.467	-90.11°	(Existing)
F12	29.6	-0.573	-168.30°	0.0
F13	95.4	1.858	-135.74°	0.0
F14	28.4	-0.589	-99.29°	34.0
F15 (Bump 1)	97.3	1.839	-66.32°	42.5
F16	30.1	-0.624	-31.47°	42.0
F17 (Bump 2)				
(Extraction)	99.7	1.939	0.00°	32.0
F18 (Bump 3)	28.9	-0.558	35.20°	52.0
F19	94.3	1.816	68.42°	0.0
F21	28.9	-0.618	104.71°	28.0
F22 (Bump 4)	99.5	1.893	136.92°	27.5
F23	30.1	-0.598	171.32°	35.0
F24	97.4	1.906	203.21°	0.0
F25	28.4	-0.567	239.23°	35.0
F26	95.2	1.810	272.60°	43.5

The kicker at location C48 causes a -43 mm horizontal displacement at F17, which is sufficient to cross the Lambertson septum. The required angular deflection at C48 is obtained with a voltage of 60.0 kV, well within the present operating range of the device. Given the Main Ring lattice characteristics, the kick at C-48 results in an angular displacement of +0.847 mrad at F17 as well as the horizontal displacement. This residual angle can be cancelled with a 3° rotation of the first Lambertson extraction magnet.

A local four-magnet orbit bump at F17 is used to position the closed orbit during 8-GeV injection in the center of the restricted aperture at F17 and to move the orbit close to the Lambertson septa during 120-GeV extraction. Four standard 35-in. long bump magnets are placed at F15, F17, F18 and F22. The closed orbit at 120 GeV can be adjusted over a range of ± 37 mm at location F17.

Vertical extraction was chosen since it allows the extracted proton beam to clear the Main Ring magnet, F17-1, just downstream of the Lambertsons with a minimum deflection. The return coil on the upstream end of F17-1 has been modified to permit the beam pipe containing the extracted 120-GeV to be as close to the magnet steel as possible. The length of the medium straight section at F17 limits the maximum energy that can be extracted to 120 GeV.

The Lambertson magnets are 204 in. long and are excited to less than 13 kG at 120 GeV. The second Lambertson accommodates a vertical beam translation of 5 in.

References

1. C. Moore et al., Fermilab EXP Note 101, February 1980 (unpublished).
2. J. Griffin (unpublished).
3. J. Griffin, Fermilab Report, 7, July 1982.

3. ANTIPROTON PRODUCTION

3.1 Proton Transport from F17 to Target

The extraction energy for the protons to be used for antiproton production was 80 GeV in an earlier design. It was decided to raise this energy to 120 GeV in order to increase antiproton production. The earliest choice for a 120-GeV extracted beam was to upgrade the then-existing 80-GeV line, which extended 1000 feet from F17 to F25 within the Main Ring Tunnel. Although this design satisfied most of the project requirements, it possessed a number of undesirable features. Its estimated power consumption of 2 MW would place a heavy burden on the operating cost of the Antiproton Source. The elements of the 80 GeV line were placed immediately above the Main Ring magnets, below which the Energy Saver magnets have now been installed. As a consequence, difficult operational problems would be encountered wherever work had to be performed on the Main Ring or the Energy Saver. It was necessary to dismantle the 80-GeV beam in many locations in order to install the Energy Saver. The location of the original \bar{p} hall, which is very close to F25, limited the ability to vary the proton targeting. The 80-GeV line had been put in the Main Ring tunnel because the 400-GeV operating schedule in 1977 and 1978 did not allow the several-month interruption that was believed to be needed to modify the Main Ring Tunnel at F18 in order to build a more flexible beam. This constraint is no longer relevant. For these reasons, a more efficient and flexible beam design was developed.

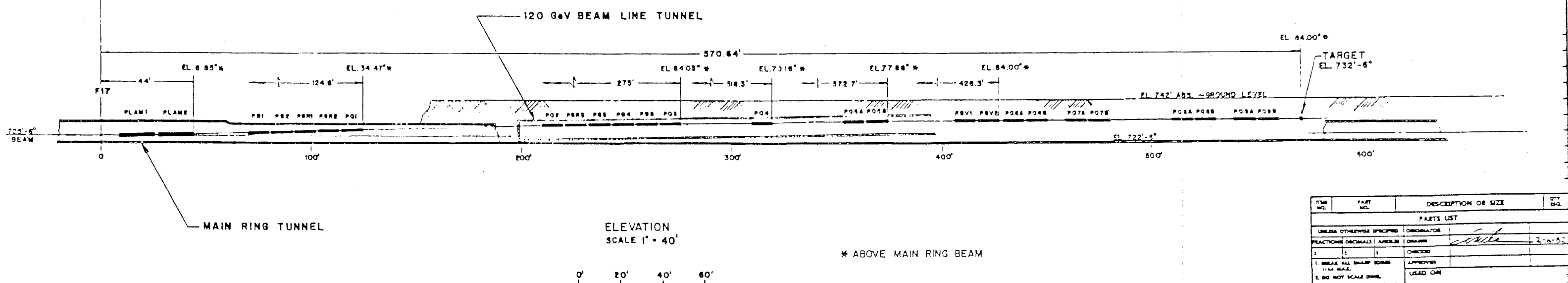
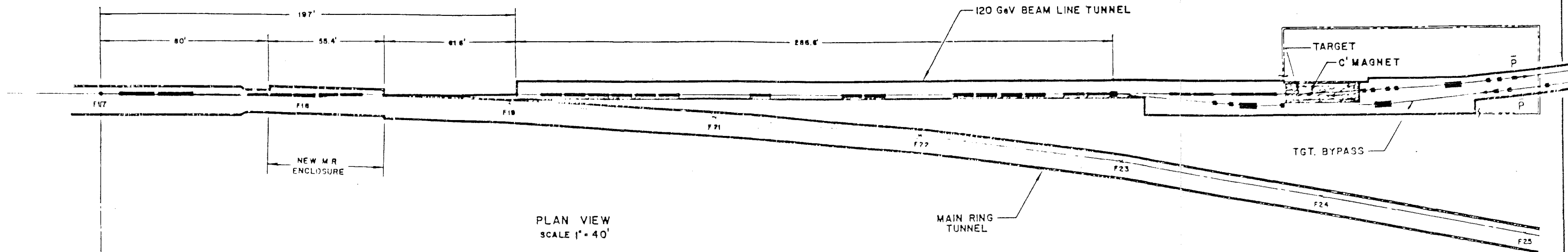
The design of the new 120-GeV proton transport line was based on the following requirements:

- (i) It must leave the Main Ring tunnel as close as possible to location F18.
- (ii) The target elevation is to be 7.0 feet above Main Ring beam height.
- (iii) It must transport a 120-GeV proton beam with a momentum spread of $\pm 0.2\%$.
- (iv) It must be possible to bypass the target and collection system in the reverse direction.
- (v) It must transport the 8.9-GeV/c cooled antiproton beam with an emittance of 2.0π mm-mrad.
- (vi) It must produce a round proton beam spot at the target which can be varied from 0.2 mm to 0.8 mm rms.
- (vii) It must have zero dispersion at the target.

(viii) The power consumption must remain below 500 kW.

A layout of the beam is shown in Fig. 3-1 and its parameters are tabulated in Table 3-I. In Fig. 3-2 we show the behavior of the monoenergetic β_y , β_x , η_y , and η_x through the system from extraction to the target. The beam consists of 10 EPB dipoles excited to a field of 13 kG or less and 14-3Q120 quadrupoles excited to a field gradient of 4.75 kG/in. or less. Three of the dipoles, indicated by (R), are rotated by 45° to achieve the necessary vertical and horizontal bends with the minimum number of magnets. The Main Ring Tunnel must be widened over a distance of roughly 18 m in order to accommodate the four EPB dipoles and one 3Q120. The length of the beam is 174 m, of which 41 m is located in the Main Ring Tunnel. The remainder of the beam elements are located in a new 115-m long enclosure. The new enclosure and the Main Ring Tunnel are connected by an 18-m long pipe.

A 4.5° bending magnet, which bends the reverse antiproton beam to the left, is placed within the final focus section between PQ7B and PQ8A in order to allow the target and antiproton collection lens to be bypassed whenever cooled antiprotons are transported back to F17. The total power consumption of the beam is estimated to be less than 390 kW. In Table 3-II the gradients of the four final focusing quadrupoles, which obtain the required range of beam sizes, are listed.



ITEM NO.	PART NO.	DESCRIPTION OR SIZE	QTY. REQ.
PARTS LIST			
UNLESS OTHERWISE SPECIFIED		ORIGINATOR	
REACTIONS ORIGINALS / ANGLES		ORIGIN	2-4-80
1	2	CHICK	
1. BREAK ALL SHARP EDGES 1/4" MAX.		APPROVED	
2. DO NOT SCALE DIMS.		USED ON	
3. DIMENSIONS IN ACCORD WITH JUNE 1974 STD.		MATERIAL	
✓ MAKE ALL MACHINED SURFACES			
FERMI NATIONAL ACCELERATOR LABORATORY UNITED STATES DEPARTMENT OF ENERGY			
120 GeV PROTON BEAM TRANSPORT LINE			
SCALE	PLANS	DATE	REV
NOTED			A

Figure 3-1

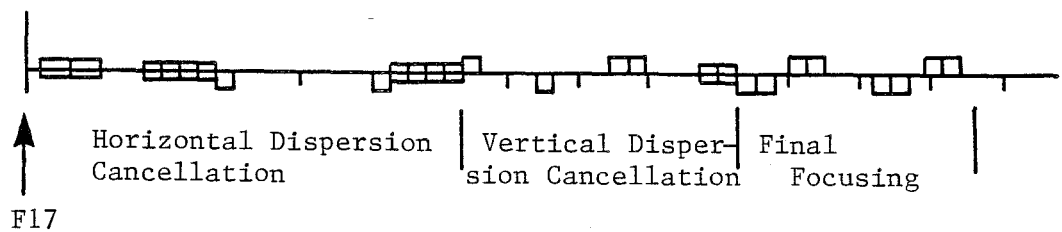
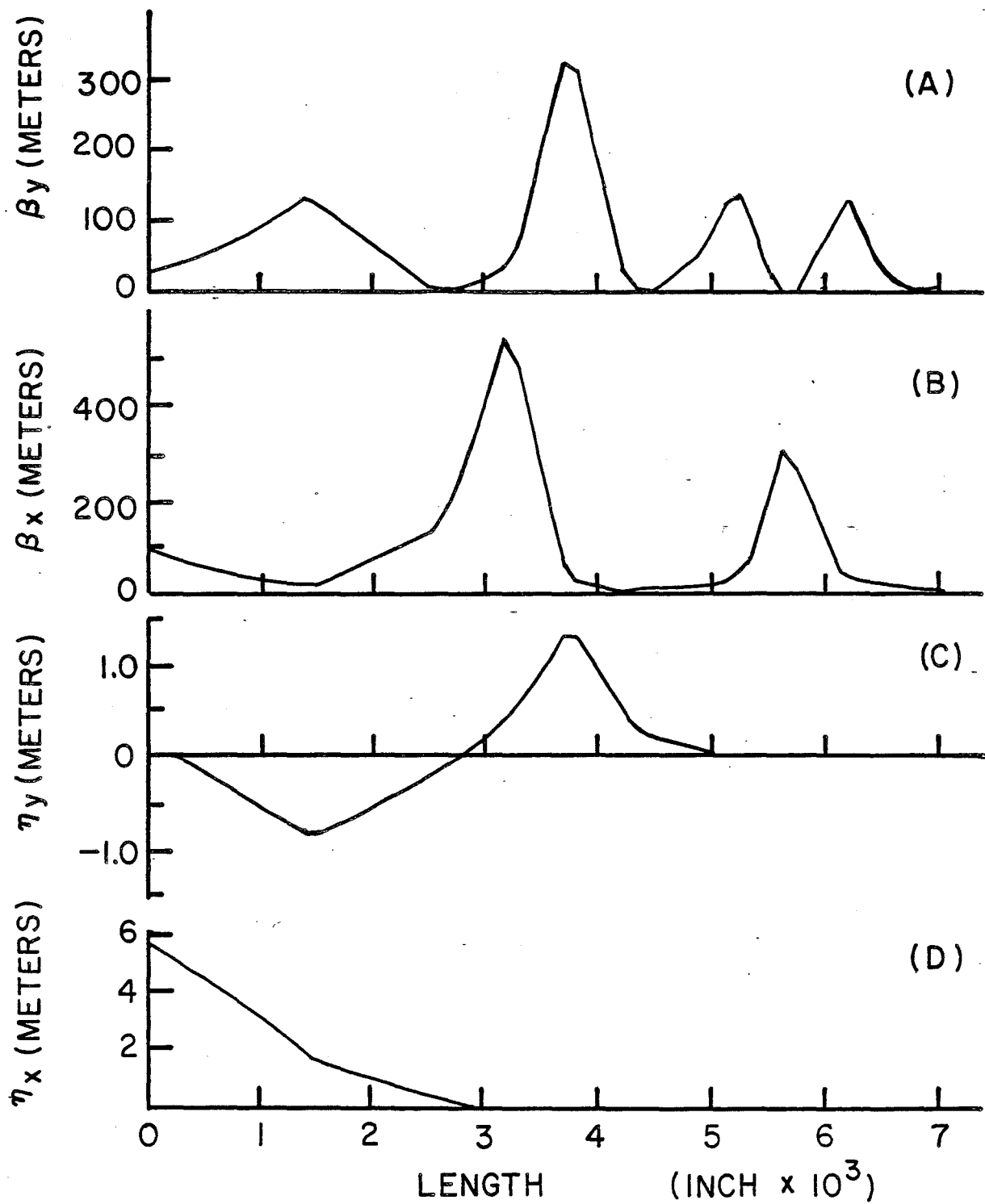


Fig. 3-2. Twiss parameters β_y , β_x and dispersion functions η_y , η_x through the 120^x GeV beam transport system.

Table 3-I. 120-GEV TRANSPORT ELEMENTS

NAME	DIST. TO F17(m)	TYPE	FIELD (T)	GRADIENT (T/m)	FUNCTION
P-LAM1	2.74	Lamberston	1.25		Bend up
P-LAM2	8.38	Lambertson	1.25		Bend up
PB1	21.7	EPB	1.271		Bend Left
PB2	25.0	EPB	1.271		Bend Left
PBR1	28.4	EPB (R)	1.271		Bend Left/Down
PBR2	31.7	EPB (R)	1.271		Bend Left/Down
PQ1	35.1	3Q120		6.59	Vertical Focusing
PQ2	64.2	3Q120		4.85	Vertical Focusing
PBR3	67.5	EPB (R)	1.271		Bend Right/Down
PB3	70.9	EPB	1.271		Bend Right
PB4	74.2	EPB	1.271		Bend Right
PB5	77.6	EPB	1.271		Bend Right
PQ3	80.9	3Q120		12.09	Horiz. Focusing
PQ4	94.1	3Q120		15.96	Vertical Focusing
PQ5A	107.3	3Q120		18.30	Horiz. Focusing
PQ5B	110.7	3Q120		18.30	Horiz. Focusing
PBV1	123.7	EPB	0.782		Bend Down
PBV2	127.0	EPB	0.782		Bend Down
PQ6A	130.7	3Q120		11.43	Vertical Focusing
PQ6B	134.1	3Q120		11.43	Vertical Focusing
PQ7A	139.6	3Q120		10.27	Horiz. Focusing
PQ7B	143.0	3Q120		10.27	Horiz. Focusing
PQ8A	154.9	3Q120		12.38	Vertical Focusing
PQ8B	158.3	3Q120		12.38	Vertical Focusing
PQ9A	163.9	3Q120		9.27	Horiz. Focusing
PQ9B	167.2	3Q120		9.27	Horiz. Focusing
TARGET	174.1				

Target Location in Site Coordinates

x = 585.94 feet
y = -2064.26 feet
z = 728.50 feet

Table 3-II. GRADIENT OF FINAL FOCUSING QUADRUPOLES
AS A FUNCTION OF BEAM SIZE AT THE TARGET, IN T/m.
(MAXIMUM GRADIENT 18T/m)
QUADRUPOLES

$\beta^*(m)$	$\sigma(mm)$	PQ6A/B	PQ7A/B	PQ8A/B	PQ9A/B
1.17	0.20	-13.2	+10.3	-12.1	+13.2
4.69	0.40	-11.4	+10.3	-12.4	+ 9.3
18.75	0.79	-10.3	+ 9.7	- 9.8	+ 2.0

3.2 Antiproton Yields and Targeting

The choice of the antiproton energy and that of the protons for their production depend on the production cross sections and practical considerations relative to the existing facilities at the Laboratory. This section describes the present targeting scenario for the production of antiprotons, based on the discussion of the three following topics:

1. details of the production cross sections obtained from existing experimental data;
2. the choice of primary proton energy, antiproton momentum, antiproton longitudinal acceptance and antiproton transverse acceptance; and
3. limitations introduced by targeting and the antiproton collection system.

3.2.1 Antiproton Production Cross Sections. The available experimental data on the cross sections for the production of antiprotons have been described by a phenomenological formula that includes the dependence on the incident proton energy, the antiproton momentum and the target nucleus.¹ For example, the yields of antiprotons from a tungsten target collected within a laboratory angle of 60 mrad for various proton energies are shown in Fig. 3-3. It can be seen that there is a plateau at 120 GeV for the production of antiprotons between 8 and 13 GeV/c.

3.2.2 Proton Energy. The yield of antiprotons per unit volume of phase space per unit time changes very slowly with proton energy above 150 GeV, when the Main Ring cycle time is taken into consideration. Although some gain in yield could be obtained by going to a higher energy, a proton energy of 120 GeV was chosen because it is the maximum energy that can be extracted from a medium straight section such as F17. F17 provides a convenient location for the Antiproton Source. The choice was also influenced by the rapid increase in operating cost as the energy of the

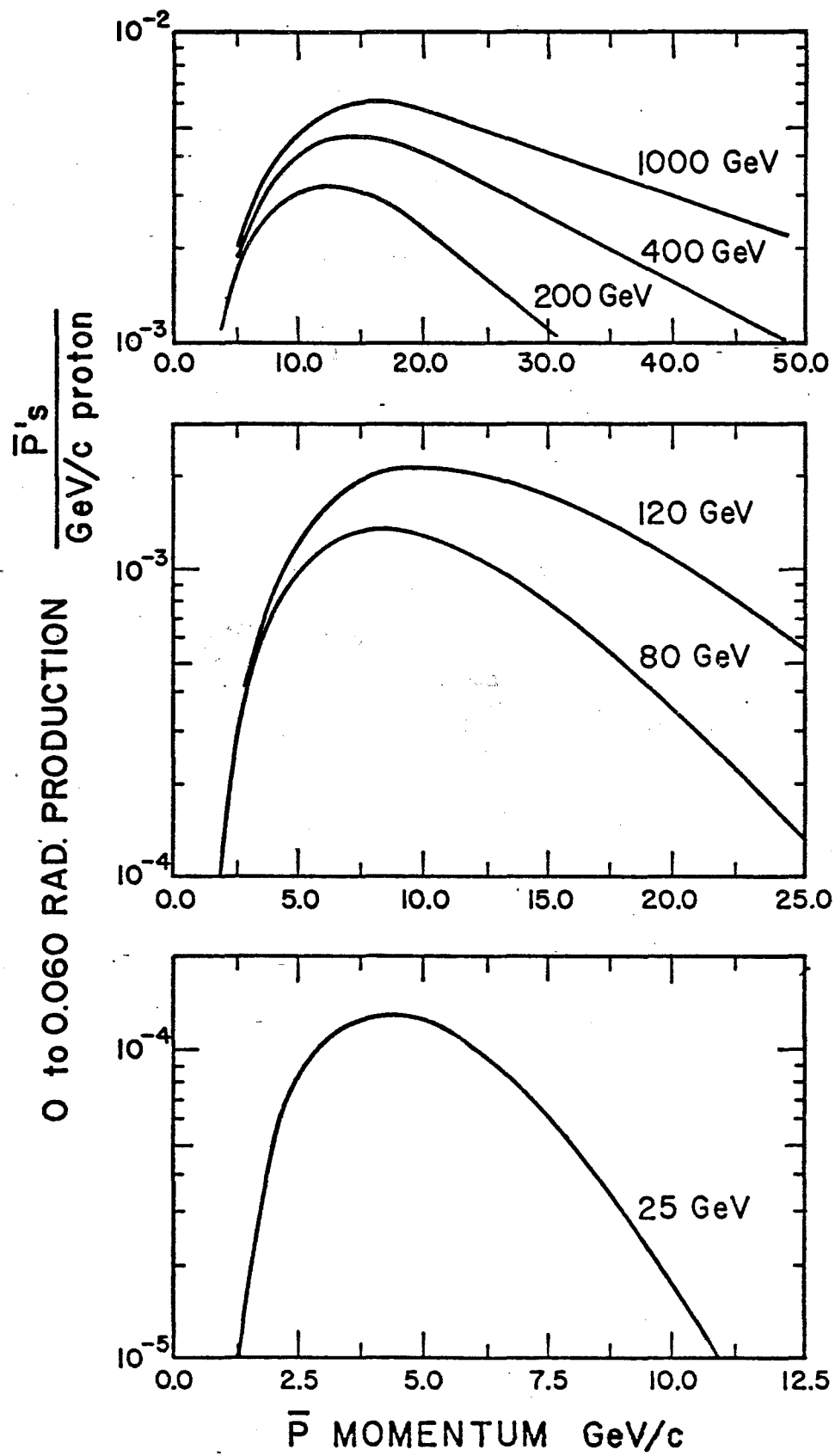


Fig. 3-3

Main Ring is increased. The energy of 120 GeV is also compatible with the Colliding Beams Detector overpass. The overpass, which is described in Chapter 7, will limit the maximum energy of the Main Ring to 200 GeV.

3.2.3 Antiproton Momentum. The optimum antiproton momentum is 10.0 GeV/c for an incident proton energy of 120 GeV. The yield is more than 90% of the optimum yield throughout the range from 7.5 GeV/c to 13.0 GeV/c. Since the normal injection momentum of the Main Ring, 8.89 GeV/c, is within this range of momenta, it is a reasonable choice. It has the advantage of permitting the transfer of antiprotons directly from the Accumulator to the Main Ring. In addition, it opens the possibility of utilizing protons directly from the Booster as an alternative source of particles during commissioning of the source.

3.2.4 Antiproton Longitudinal Acceptance. Stochastic cooling performance depends critically on the flux of \bar{p} 's injected into the Accumulator and on the particle density per unit of energy spread. This density, which is inversely proportional to the longitudinal emittance of the antiprotons, is determined in part by the time spread of the \bar{p} 's at production, as discussed in Chapter 2.

In the Debuncher, a total momentum spread of approximately 3% can be reduced to a momentum spread that can be accommodated by the Accumulator. Although a larger momentum spread will result in a larger flux the Accumulator is not able to cool the larger flux. The \bar{p} collection and transport system is designed to accept 4% total momentum spread. The momentum spread of the \bar{p} 's transported to the Debuncher will be adjusted by collimation in the beam transport.

3.2.5 Antiproton Transverse Acceptance. The calculation of expected antiproton yields depend crucially on the collection system downstream of the target. A comparison of different collection systems has been performed², taking into account the large momentum spread of the antiproton beam. The advantages of a device such as the lithium lens that was developed at the INP in Novosibirsk³ are clear. It has a very short focal length and it focuses in both transverse planes. Based on the INP experience, the parameters of the lithium lens collector were chosen to be: Radius = 1 cm, Gradient = 1000 T/m, Length = 15 cm. Within the present technology developed at Novosibirsk, a repetition rate of 1 Hz is feasible. The lens has a focal distance of 14.5 cm. The short focal distance requires the use of a dense target.

Antiprotons yields have been calculated with a Monte Carlo program¹ that includes the phenomenological description of the production cross section, the development of hadronic showers in the target and \bar{p} production by secondaries, multiple scattering and absorption. The result of these calculations is shown in Fig. 3-4 for two different rms proton beam spot sizes, $\sigma_x = \sigma_y = 0.038$ cm and $\sigma_x = \sigma_y = 0.22$ cm. The number of antiprotons

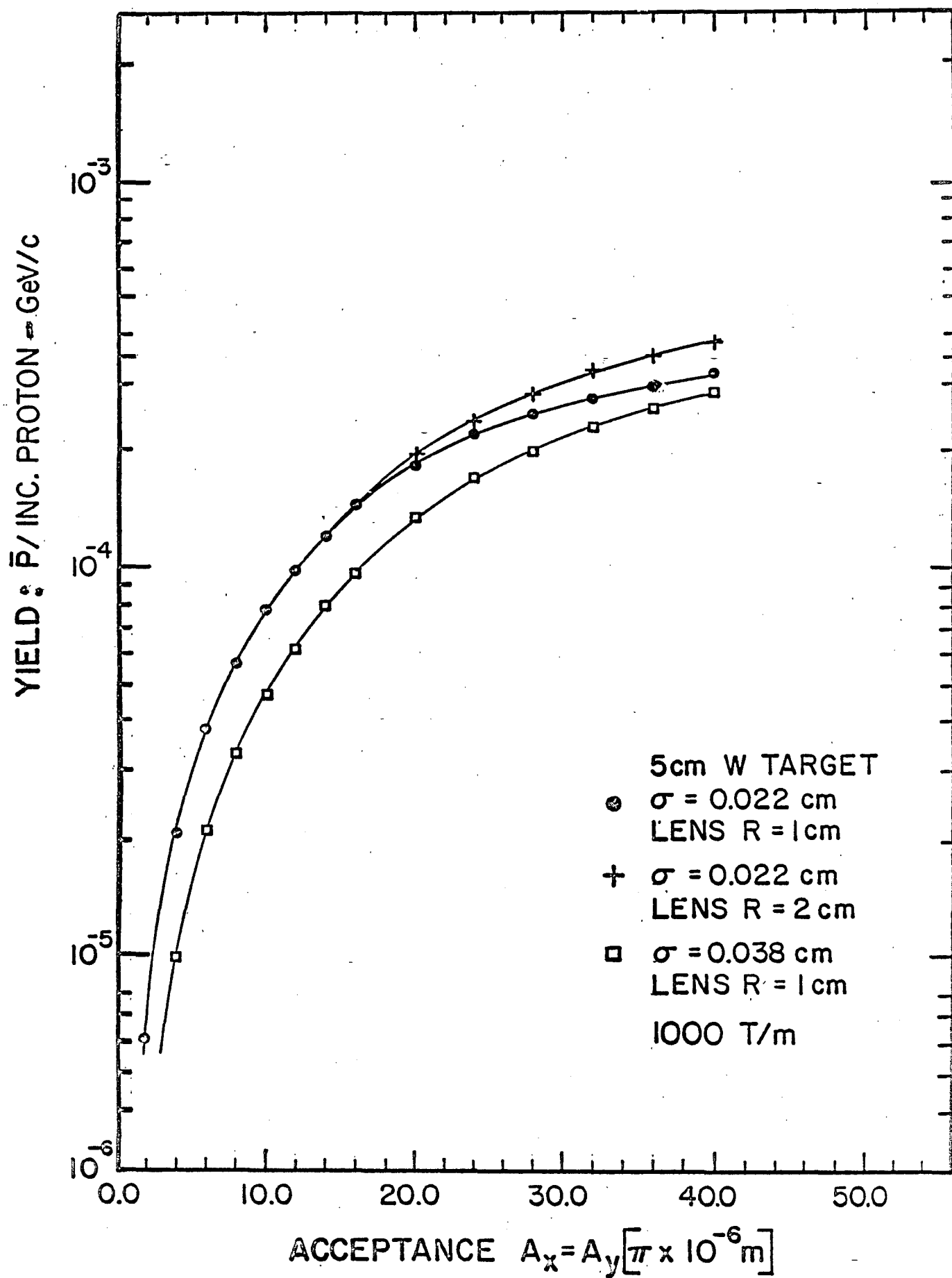


Fig. 3-4

increases approximately linearly with the transverse acceptance above 20π mm-mrad for $\sigma=0.038$ cm. For the smaller beam size, the departure from linearity above 20π mm-mrad is caused by the lithium lens radius and its gradient. The optimum target length is approximately 5 cm.

3.2.6 Targeting Limitations. Decreasing the proton beam size at the target increases the transverse phase-space density of the produced antiprotons, resulting in a larger yield within a given acceptance. The diameter of the proton beam cannot be reduced arbitrarily since the energy deposited by the beam per unit volume increases as the beam area decreases, causing the target to overheat.

The subject of high energy density deposition in targets was the subject of a Fermilab Workshop³. It was generally agreed that metal targets can sustain energy density deposition up to 200 Joules gm^{-1} before the apparently onset of shock waves that could result in the destruction of the target. Calculations indicate that the CERN Antiproton Accumulator target sustains a maximum energy deposition of approximately 185 Joules/gm for tungsten. Both copper and rhenium (instead of tungsten) have been used at CERN for some time with no failures. The energy density deposited by a 120-GeV proton beam in tungsten has been calculated using the program MAXIM⁴. The maximum energy density deposited within a 5-cm long target is shown in Fig. 3-5 versus the rms size of the proton beam, σ . Within the errors of the calculation, it varies as σ^{-2} . Also shown is the maximum number of protons per pulse vs rms beam size, under the condition that the maximum allowable energy density is 200 Joules/gm.

Table 3-III shows the expected number of antiprotons per pulse as a function of beam size and maximum permissible proton intensity.

A feasibility study was carried out⁶ on sweeping the proton beam across the target to decrease the energy density deposited in the material. The antiproton acceptance must be simultaneously swept to track the proton beam spot. If the sweeping covers several proton-beam diameters, it is possible to target 3×10^{12} protons on beam spots corresponding to $\beta < 3$ m, which will give an increased number of antiprotons accepted per proton. The design of the target area makes it possible to incorporate a beam-sweeping system in the future.

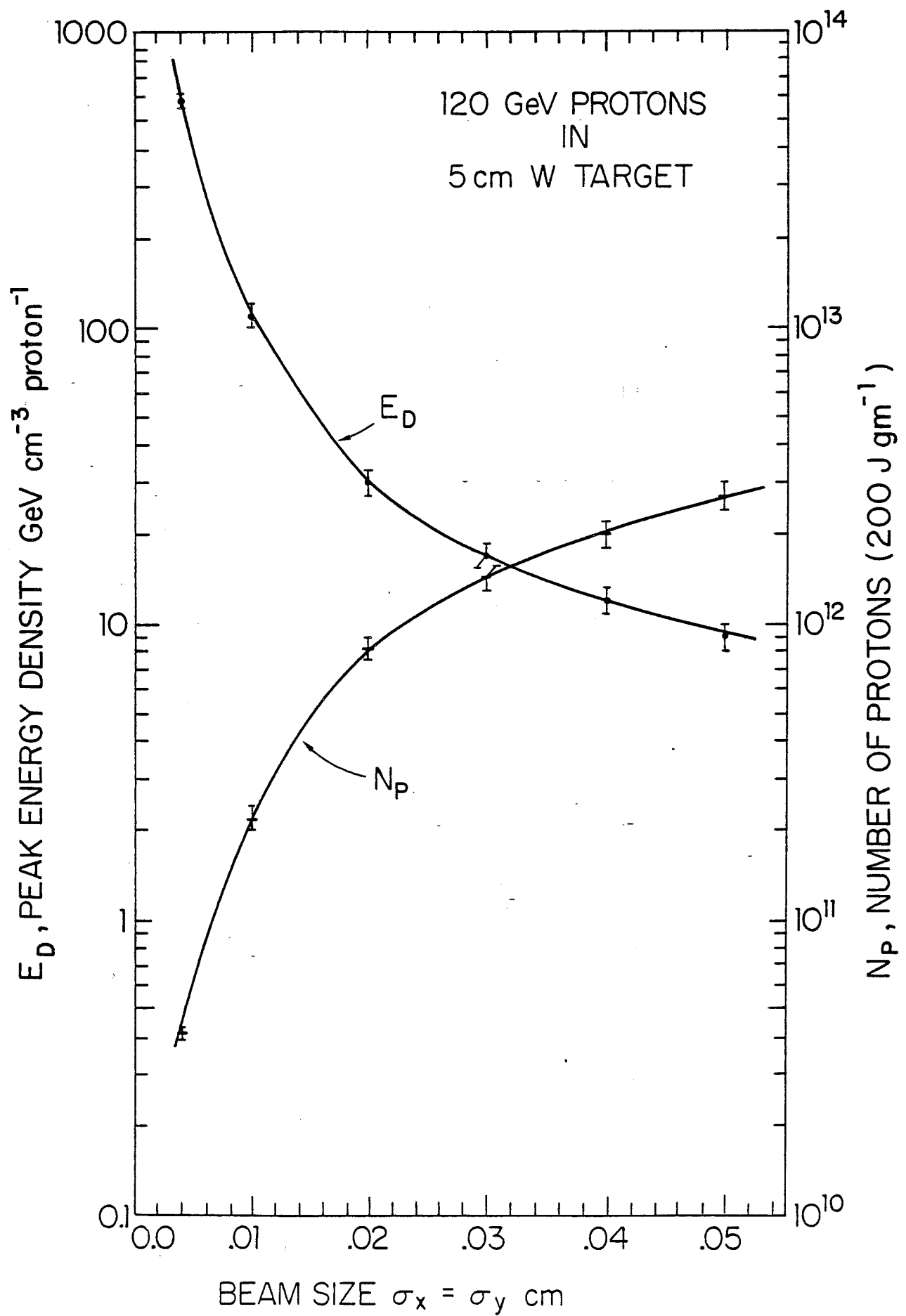


Fig. 3-5

Table 3-III. NUMBER OF ANTIPROTONS PER PULSE

$\beta^*(m)^+$	$\sigma_x = \sigma_y$ (cm)	N_p Max.	\bar{p}/p^{++}	\bar{p}/pulse
1.55	0.023	6.0×10^{11}	5.1×10^{-5}	3.1×10^7
3.07	0.032	1.2×10^{12}	4.3×10^{-5}	5.2×10^7
4.62	0.039	1.8×10^{12}	3.7×10^{-5}	6.7×10^7
8.00	0.052	3.0×10^{12}	2.5×10^{-5}	7.5×10^7

Notes: + β^* is for the proton beam at the center of the target
 $(\beta_x = \beta_y = \beta^*)$. The yield in \bar{p}/proton is for 3% $\Delta p/p$ and 20π mm-mrad.

3.3 Antiproton Target System Components

The principal components of the target system are the target itself and the antiproton collection device. This section discusses the design and limitations of these two components.

3.3.1 Antiproton Production Target The computer code MAXIM* has been used to calculate radial and longitudinal energy density distributions in a stationary tungsten target for an rms beam size of 0.038 cm. The results are plotted in Fig. 3-6. The temperature rise of tungsten corresponding to an energy deposition in Joules/gm may be estimated from the enthalpy reserve curve given in Fig. 3-7. As is shown in Fig. 3-6 it is anticipated that local peak energy densities will be approximately 200 Joules/gm for the present design parameters $\sigma = 0.038$ cm and 2×10^{12} protons per pulse. To decrease the number of thermal and stress cycles in the volume of material struck by the beam, the target will be rotated continuously, exposing a new volume of material to each beam pulse. Two possible configurations are shown in Figs. 3-8 and 3-9. During the target development stage the wedges shown in Fig. 3-8 will contain different materials to allow for comparative testing. Provision is also being made to test stationary targets of the CERN design.

The target must have a high density and high melting point. A compilation of mechanical properties for different materials was performed. A figure of merit to compare the mechanical properties is given by the yield stress divided by the coefficient of thermal expansion and the modulus of elasticity. On this basis rhenium, tungsten and tungsten-rhenium alloys are in increasing order for this figure of merit. The coefficient of heat conductivity could also be included in the figure of merit without significantly altering the choice of material.

The high-temperature behavior of tungsten-rhenium alloys shows considerable increase of yield stresses with respect to tungsten, but little change in the coefficient of thermal expansion or the modulus of elasticity. Tungsten-rhenium alloys are utilized in industry for

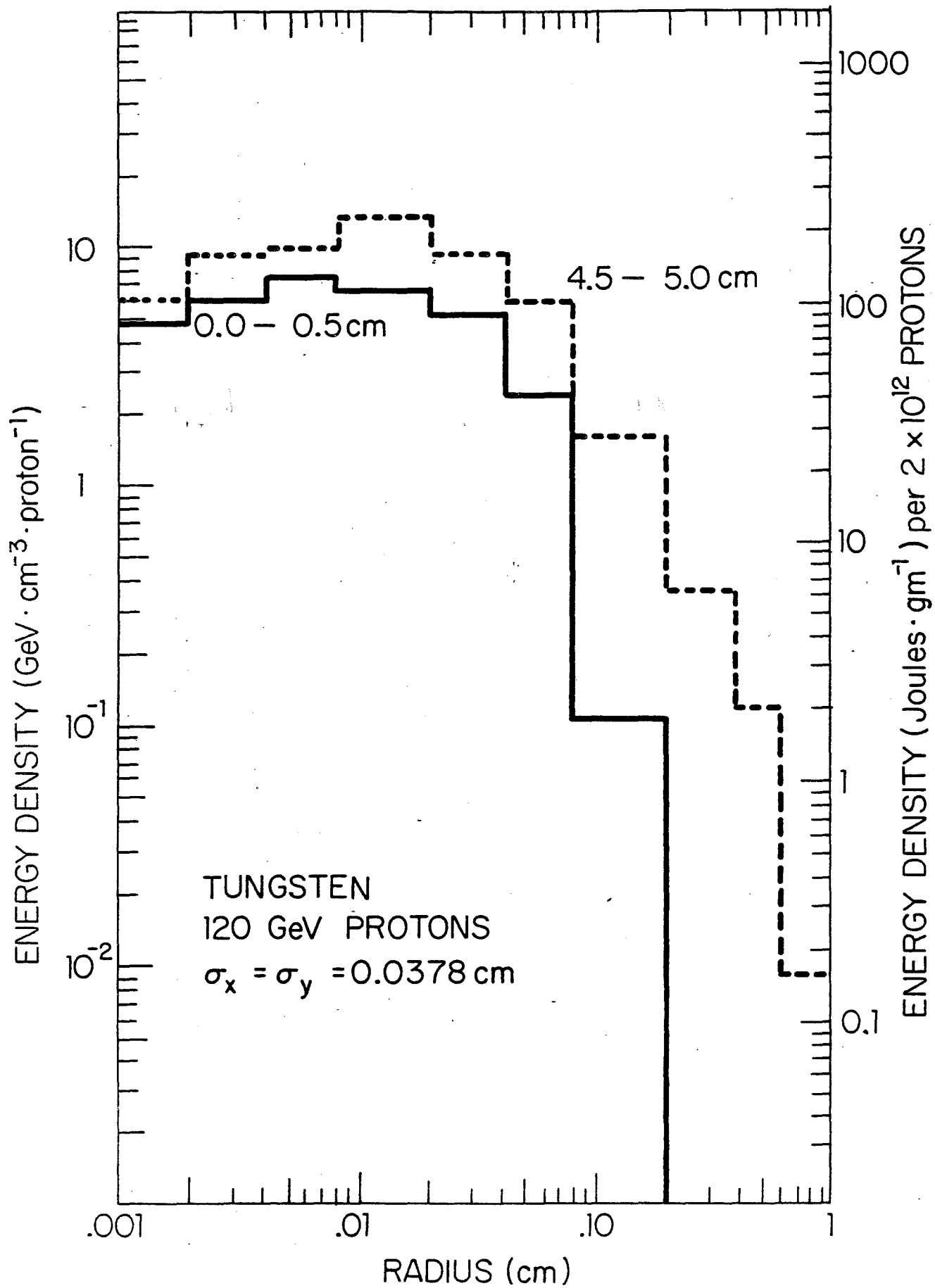


Fig. 3-6

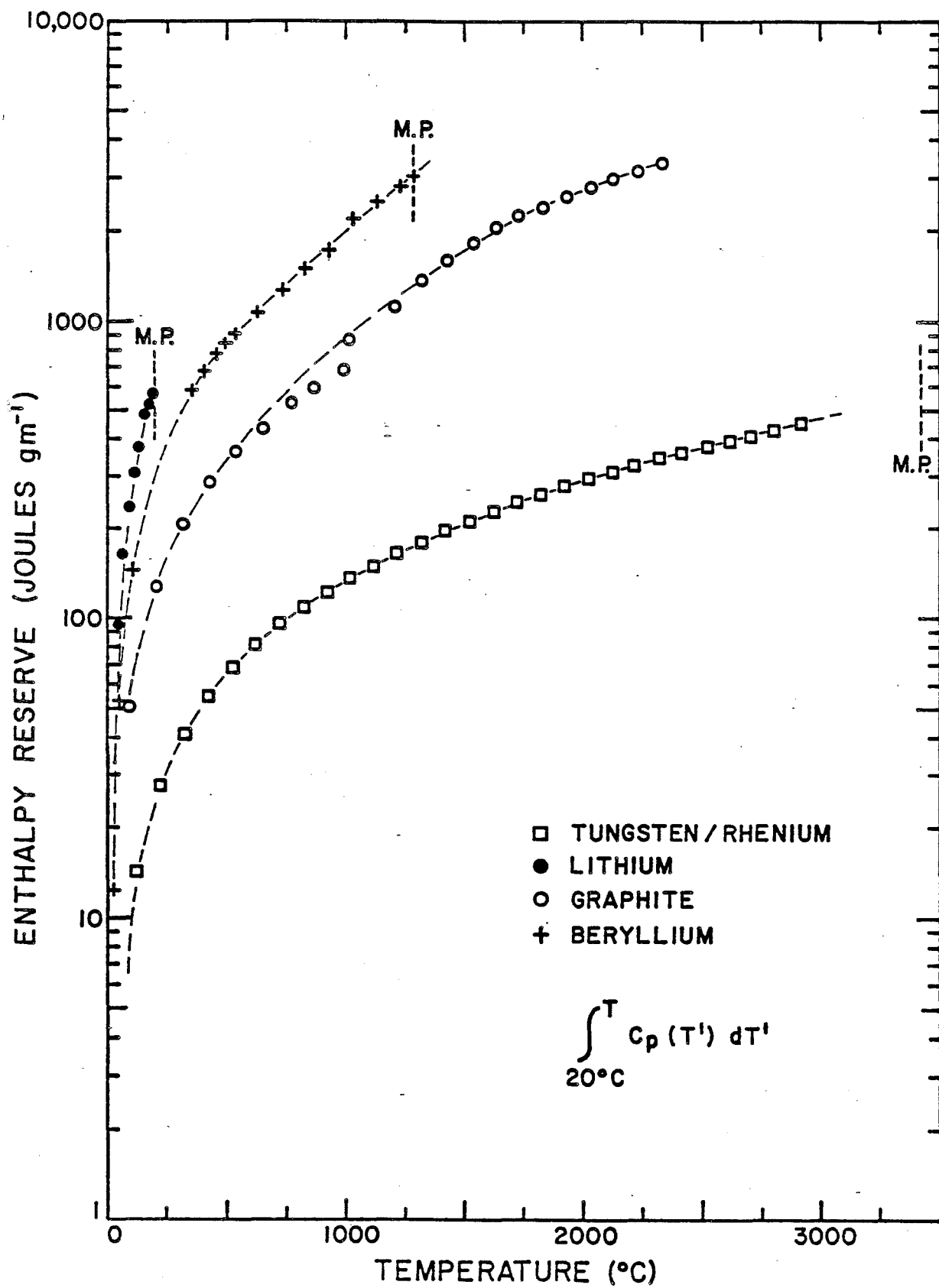
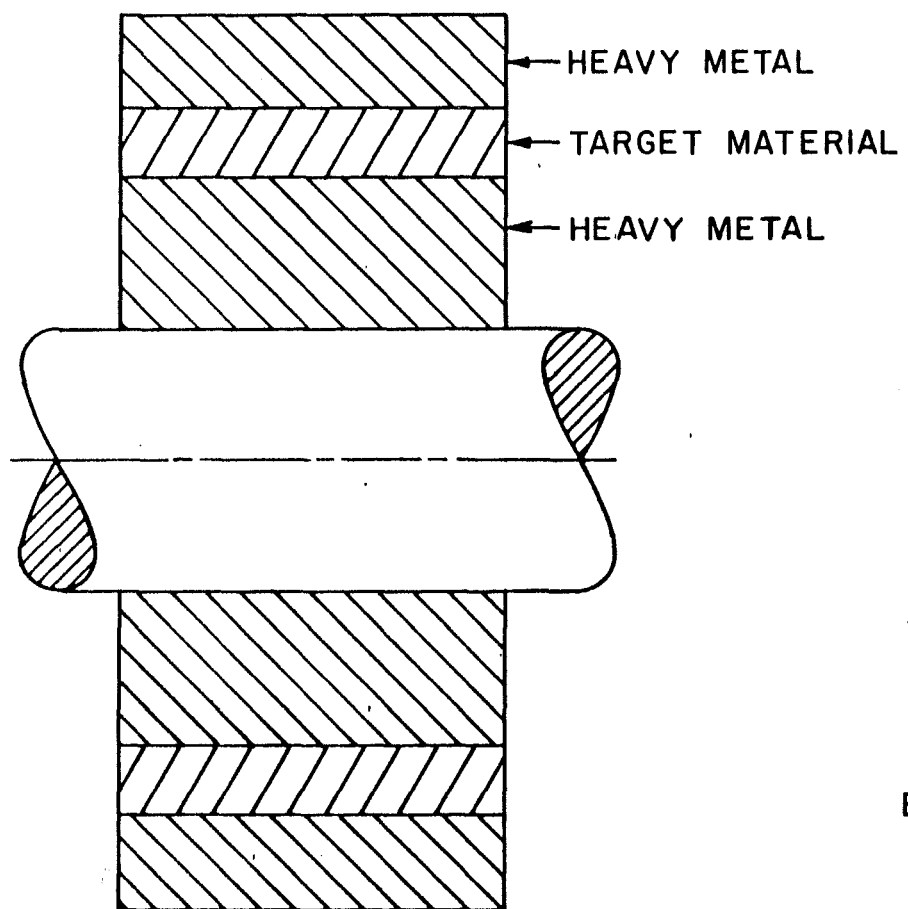


Fig. 3-7



0 1 2 3 4 5 cm

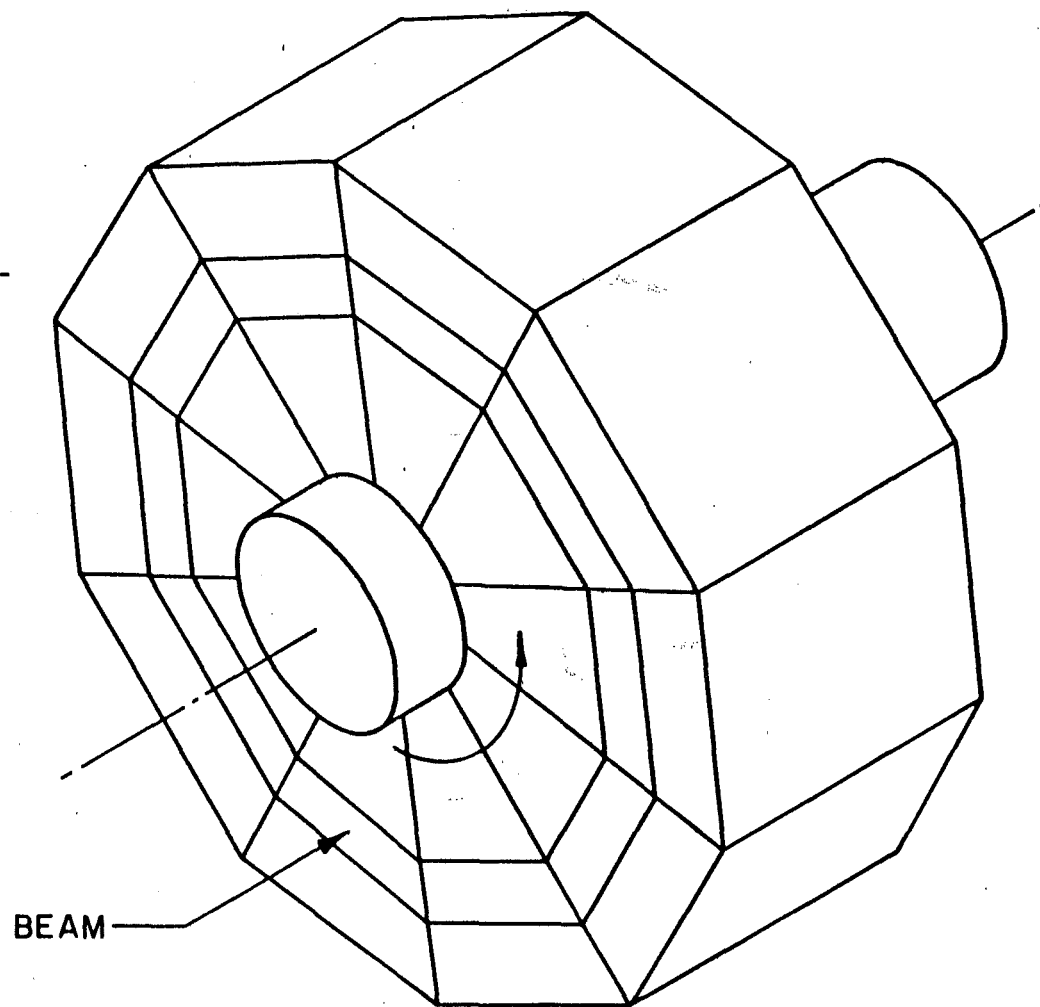


Fig. 3-8

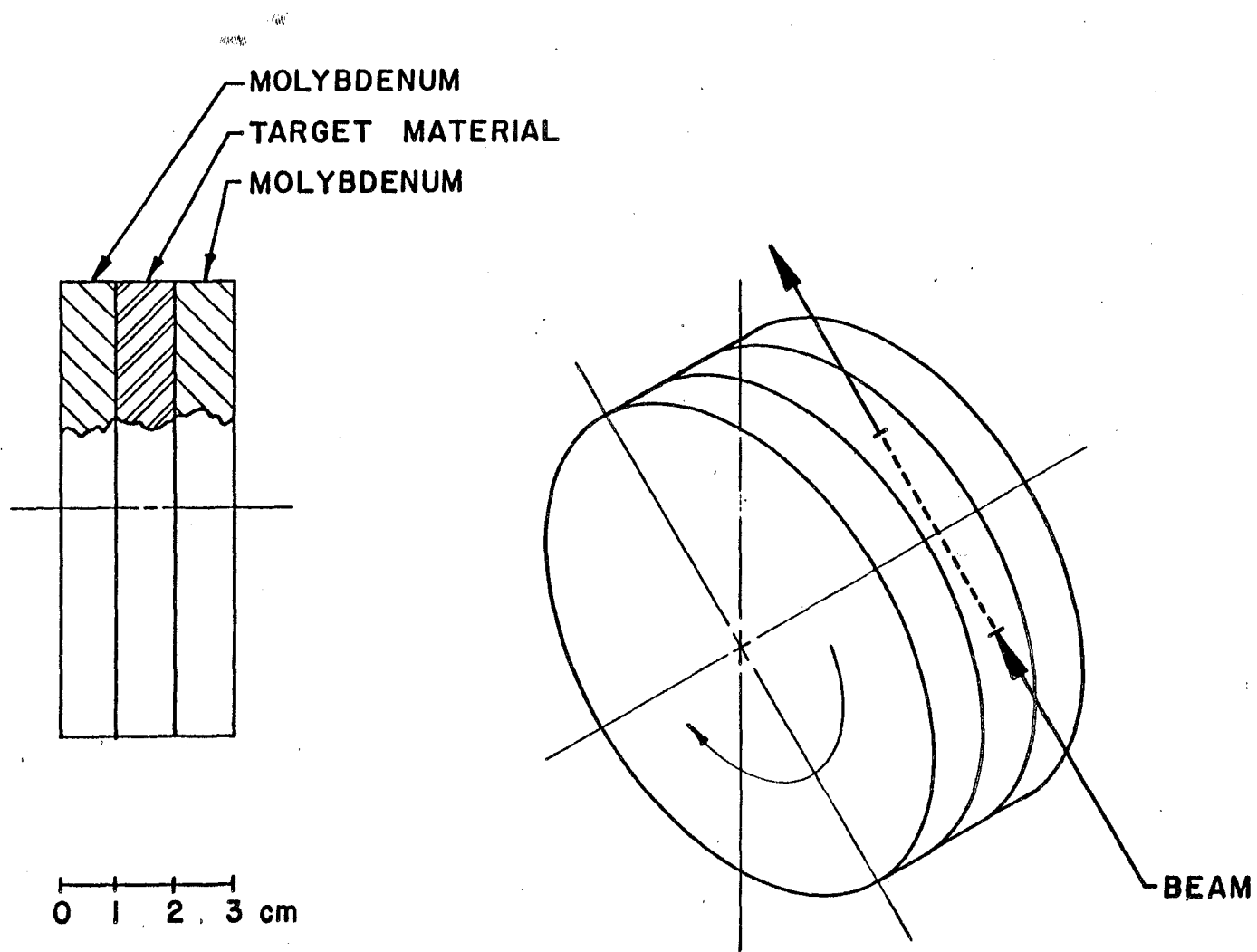


Fig. 3-9

high-temperature applications such as incandescent-lamp wire and targets for high-power x-ray tubes. A significant amount of experience with the technology for their fabrication exists. Tungsten has been used for all \bar{p} yield calculations, although a number of target configurations will be tested during the R & D phase of the target-station development. A summary of the target parameters is given in Table 3-IV.

Table 3-IV. TARGET PARAMETERS

Target Material	Tungsten/Tungsten Alloys
Length	5 cm
120 GeV protons/pulse	2.0×10^{12}
Total Beam Energy	3.46×10^4 Joules
Repetition Rate	0.5 Hz
Beam Pulse Duration	1.6×10^{-6} sec
Energy Deposited/proton	1.26 GeV (1.81×10^{-10} Joules)
Energy Deposited/pulse	346 Joules
Power Deposited	173 Watts
Average Temperature	100°C
Beam Size ($\sigma_x = \sigma_y$)	0.038 cm
Peak Energy Density/proton	13.4 GeV/cm ³
Peak Energy Density/pulse	200.0 Joules/gm
Peak Temperature Rise	<1500.0°C
<u>CERN</u>	
Peak Energy Density [†]	>185 Joules/gm
Peak Temperature Rise	1500°C
Average Temperature	800°C

[†]This rhenium target has been used for some time with no failures.

3.3.2 Antiproton Collection - the Lithium Lens A study has been made of the relative merits of \bar{p} collection schemes that utilize a lithium lens, a pulsed quadrupole multiplet, or a conventional quadrupole triplet.² Since it was found that the lithium lens is far more efficient for the collection of \bar{p} 's, this section concentrates on the lens. The other options which are discussed will be pursued if the lens development lags.

The basic physical principle of the lithium lens is that a uniformly distributed electric current in a cylindrical conductor produces an azimuthal magnetic field with a constant radial gradient. Charged beam particles traversing the length of such a conductor experience a force that focuses them toward the axis. Lithium is an appropriate material for such a focusing device because it is the least dense solid conductor, thereby minimizing \bar{p} absorption and multiple scattering.³ The lens under development uses a 15-cm long lithium cylinder of radius 1 cm and requires a current of 0.5 MA to produce the desired gradient of 1000 T/m. Joule heating caused by direct current in the lithium is prohibitively large, so

a 0.6 msec full-width unipolar sine-like pulse of amplitude 0.5 MA will be applied every two seconds. Each pulse will generate about 6000 Joules of heat and the problem of removing this heat dominates the mechanical design of the lens. It is desirable to keep the average temperature well below the 180°C melting point of lithium because the 1.5% volume expansion that occurs upon melting could shorten the lifetime of the lens. The magnetic induction H created by the pulsed current does not have a constant radial gradient, due to the skin effect. Fig. 3-10 shows the variation of H/H_{\max} during one pulse.⁷

Energy deposition in a lithium lens located 14.5 cm (one focal length) downstream of a 5-cm tungsten target was calculated using the program MAXIM. Contributions from secondaries emerging from the target as well as from non-interacting 120 GeV protons were included. The heating due to the beam was found to be small compared to Joule heating.⁸

In case the lithium-lens development lags, linear and non-linear horns of the types developed for the CERN AA ring could be utilized. To optimize the \bar{p} rate, they require significantly longer targets. Preliminary results indicate that horns would not provide as good a collection efficiency as the proposed lithium lens at our \bar{p} energy. The larger currents required for the 8.89 GeV/c \bar{p} 's, as compared with 3.5 GeV/c at CERN, may make the horn construction very difficult. Another option would be to install a 5Q36 triplet.² This would limit the \bar{p} production system to small momentum spreads and emittances, but could be useful in the early stages of running.

3.4 Target Hall

The antiproton production target, proton beam dump and the lithium lens for antiproton collection will be located in a vault downstream of the final quadrupole focusing system in the 120-GeV proton line. The dimensions of this vault are planned to be 7 ft by 33 ft with the floor located at 17 ft below grade, as shown in Fig. 3-11a and 3-11b.

The upstream end of the hall is separated from the proton-beam transport tunnel by 3 ft of steel shielding. Further shielding is placed around the external walls of the vault in the earth. Below the vault two separate impermeable membranes are used to collect irradiated ground water. Shielding configurations that limit the irradiations of the soil and the above-ground fluxes to permissible values have been designed to allow operation at an intensity of 10^{13} protons per second.

Downstream of the upstream end of the shield, within the target vault, a 3 ft high by 8 ft long and 2 ft wide volume of space is available for components. The space between this volume and the concrete walls and floors of the vault is filled with steel shielding. Access to the target station components is accomplished by raising one of a set of solid steel elevators into the Target Service Building. Each elevator segment extends 10 in. along the beam direction and 24 in. transverse to the beam. Each is 7 ft long in the vertical direction. The components are suspended from the bottom of the elevator. The 7 ft length makes it possible to place

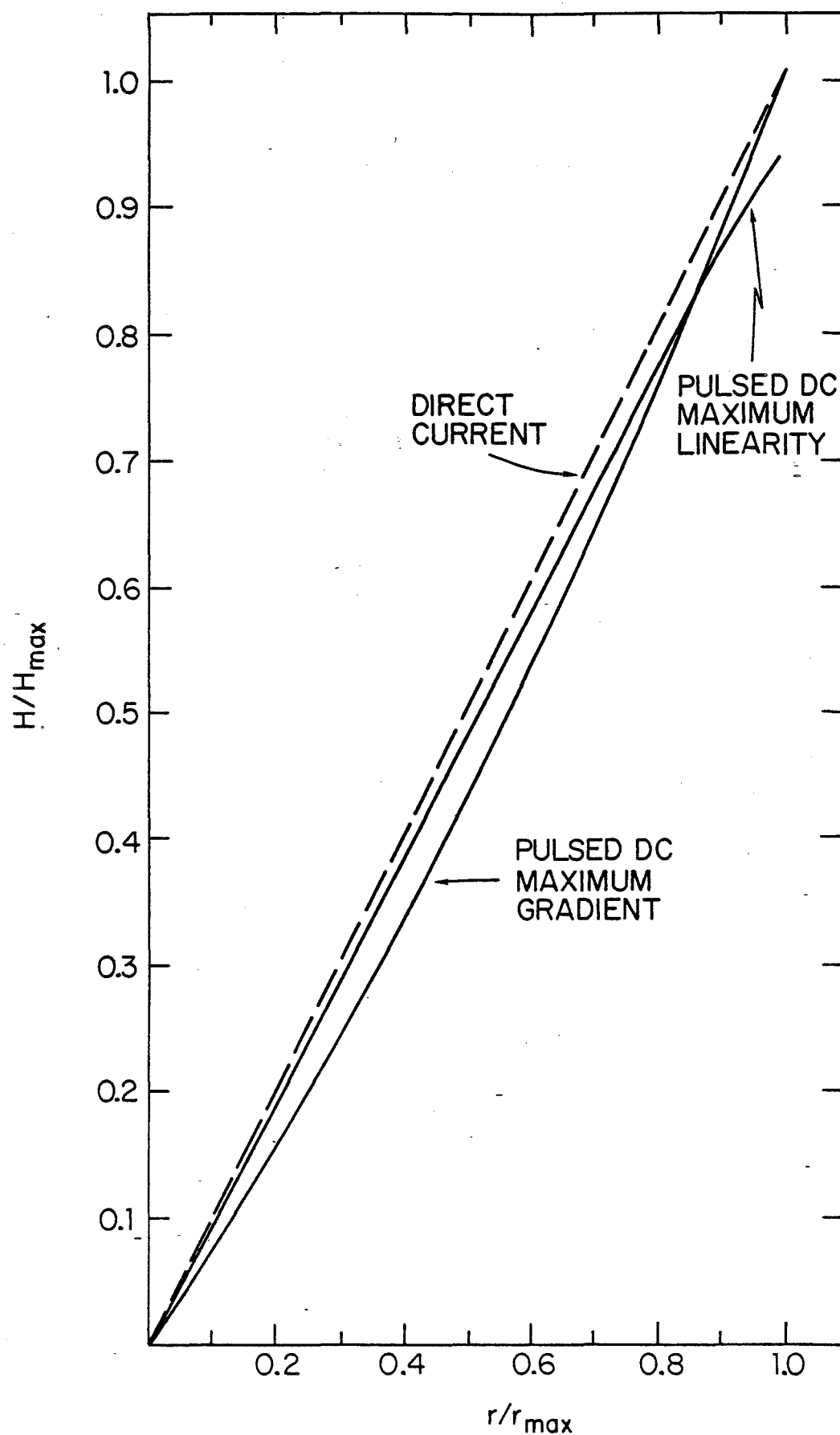


Fig. 3-10

electronics and control systems immediately above each elevator segment without danger of radiation damage. An additional 3 ft of concrete is required to keep the above-ground radiation levels within the Target Service Building below the maximum permissible level. Within the Target Service Building and surrounding the vault, a shielded area incorporating thick windows will be used to exchange elevator segments remotely. Work will be performed on components with remote manipulators. The manipulators will be used to exchange targets routinely. Access to the electronics at the top of the elevator segments will be possible when beam is not being delivered to the target station.

The last component in the beam before the dump is a pulsed magnet to bend the \bar{p} 's to the right by 3° , in order to separate them from the protons. The dump is a water-cooled graphite core 6 ft long surrounded by a steel jacket which fills the inside of the vault. The steel extends for 22 feet along the proton beam. The construction is similar to the dump developed for the Tevatron abort system.

3.5 Antiproton Transport to Debuncher

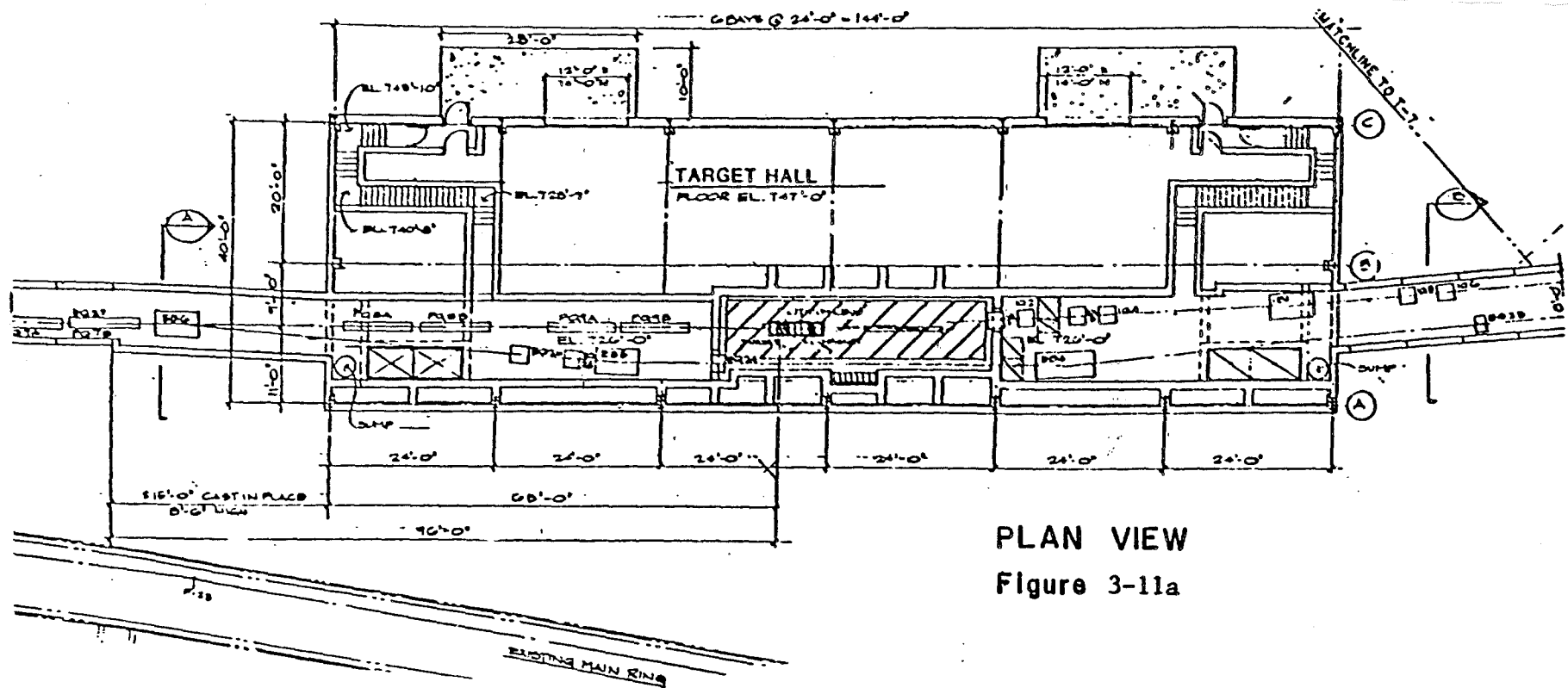
The antiproton transport line is shown symbolically in Fig. 3-12. This beam line can transport an 8-GeV beam with 20π mm-mm transverse emittance and $|\Delta p/p| < 4.0\%$. The match to the Debuncher is accomplished with an integrated efficiency of 80% over the 4.0% passband in $\Delta p/p$. Independent controls for emittance definition in both x and y planes and $\Delta p/p$ selection are possible using collimators. The detailed design can be found in Reference 9.

The "source" for the beam line is the center of the 5.0 cm \bar{p} production target. For the purpose of the transport calculations we have assumed a circular spot and a β^* of 2.25 cm. The lithium lens collector then performs point to parallel optics for negatives with a momentum of 8.9 GeV/c (8 GeV \bar{p}). The beam line consists of five basic sections: (i) cleanup, (ii) long transport, (iii) left bend, (iv) long transport, and (v) injector. Section (i) uses a pulsed C magnet to bend the 8 GeV \bar{p} 3° left, and two quadrupole doublets and another 3° bend left in order to complete the achromatic transformation. Charge, central momentum and vertical emittance ϵ_y are selected within this section using collimators. The long transport sections (ii) and (iv) consist of 90° FODO quadrupole cells and matching quadrupole lenses. The periodic structure has a cell length of 88.8147 feet with $\beta_{\max}/\beta_{\min} = 45.93\text{m}/7.98\text{m}$. The left bend (iii) which deflects the antiproton by 36.54° , consists using of six dipoles. Horizontal emittance (ϵ_x) selection is performed at the entrance and exit of this section where β_x is nearly 80 m. The fine $\Delta p/p$ selection is performed in the center of the left bend section where $\beta^* = 5.0$ m and a maximum in the dispersion $\eta_x^* = 2.62$ m is obtained. The first-order momentum resolving power is $1.3\beta_x^*$ for $\epsilon_x = 20\pi$ mm-mr and $\Delta p/p = 1.0\%$ and 2.62 for $\epsilon_x = 5\pi$ mm-mr. The injector (v) is an achromatic vertical translation ending at the downstream end of the 2.0 m long Lambertson septum. The beam is deflected downward by 48 inches using 2.658° bends.

The components for the beam line are listed in Table 3-V and shown in Fig. 1-1.

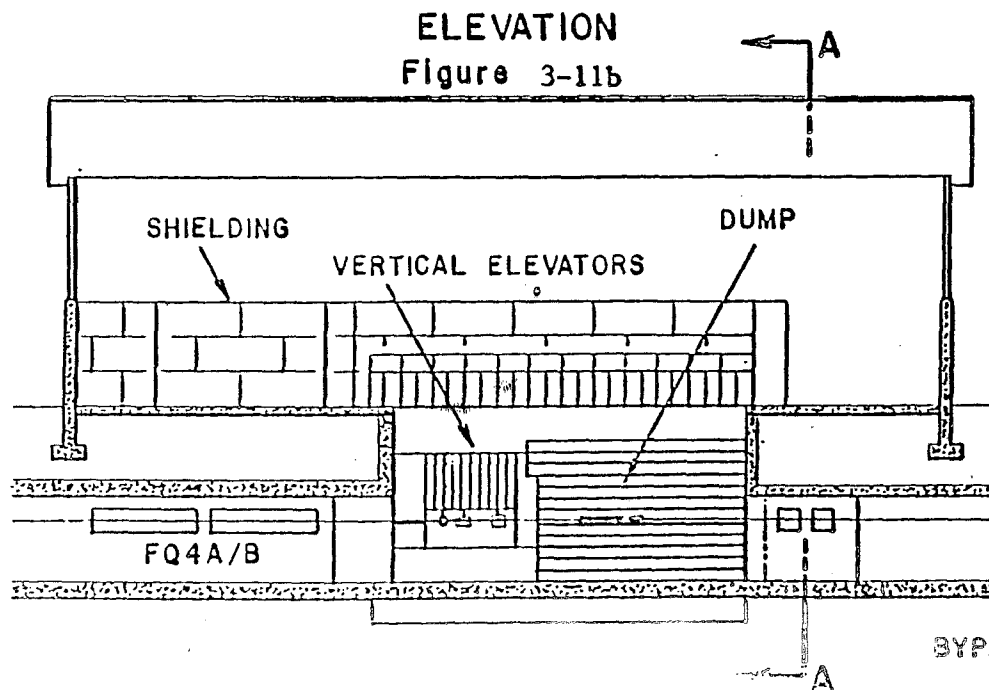
TABLE 3-V XYZ SITE COORDINATES OF BEAM
TRANSPORT ELEMENTS

NAME	LENGTH (IN)	FIELD (KG KG/M)	X (FT)	Y (FT)	Z (FT)
TARGET			585.943	-2064.261	732.500
LITHIUM LENS	5.9055	9760.6	585.217	-2063.593	
C-MAGNET	11.811	51.78	581.937	-2060.618	
IQ1	27.60	154.81	561.186	-2043.488	
IQ2	27.60	-130.54	557.883	-2040.759	
IQ3	27.60	-130.54	552.253	-2036.112	
IQ4	27.60	154.81	548.949	-2033.383	
IB1	75.00	8.16	527.082	-2015.544	
IQ5	27.60	155.54	515.241	-2006.769	
IQ6	27.60	-155.54	510.815	-2003.489	
IQ7	27.60	45.01	481.532	-1981.791	
IQ8	27.60	-45.01	445.852	-1955.354	
IQ9	27.60	45.01	410.172	-1928.916	
IQ10	27.60	-45.01	374.492	-1902.479	
IQ11	27.60	45.01	338.811	-1876.041	
IQ12	27.60	-45.01	303.131	-1849.604	
IQ13	27.60	45.01	267.451	-1823.166	
IQ14	27.60	-45.01	247.465	-1808.356	
IQ15	27.60	15.24	215.307	-1784.529	
IQ16	20.80	-90.56	185.257	-1762.262	
IQ17	32.00	90.56	179.901	-1758.292	
IB2	98.42	12.61	171.457	-1752.576	
IQ18	20.80	-78.10	166.507	-1749.666	
IB3	98.42	12.61	155.773	-1743.861	
IB4	98.42	12.61	144.491	-1739.232	
IQ19	20.80	78.10	139.031	-1737.429	
IQ20	20.80	78.10	132.637	-1735.319	
IB5	98.42	12.61	120.912	-1731.907	
IB6	98.42	12.61	108.908	-1729.761	
IQ21	20.80	-78.10	103.198	-1729.152	
IB7	98.42	12.61	91.026	-1728.292	
IQ22	32.00	85.46	86.359	-1728.292	
IQ23	18.00	-85.46	80.859	-1728.292	
IQ24	27.60	13.92	41.059	-1728.292	
IQ25	22.50	-46.82	-1.684	-1728.292	
IQ26	27.60	46.82	-38.689	-1728.293	
IQ27	27.60	-46.82	-82.014	-1728.293	
IQ28	27.60	147.76	-119.731	-1728.293	
IQ29	32.00	-160.34	-126.397	-1728.293	732.500
IBV1	75.00	7.25	-135.145	-1728.283	732.355
IQ30	32.00	-159.94	-161.620	-1728.192	731.127
IQ31	27.60	119.56	-167.561	-1728.171	730.850
IQ32	27.60	119.56	-184.960	-1728.111	730.043
IQ33	32.00	-159.94	-191.268	-1728.090	729.750



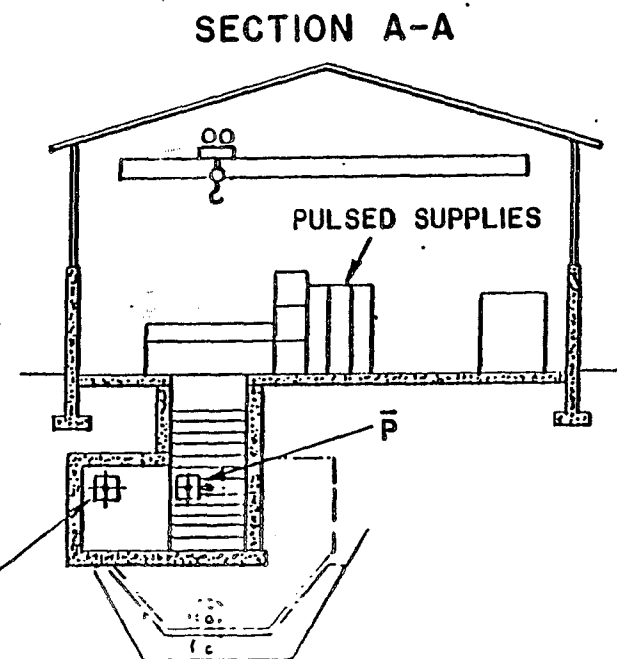
PLAN VIEW

Figure 3-11a



ELEVATION

Figure 3-11b



SECTION A-A

I-LAMBERTSON 78.74 6.88 -221.477 -1727.986 728.500
DEBUNCHER RING

Fig. 3-12 shows the evolution of the monoenergetic β_y and β_x envelope functions and the beam dispersions η_y and η_x through the transport line from the target to the downstream end of the injection Lambertson. We have studied the match to the debuncher lattice as a function of $\Delta p/p$ by evaluating the transmission efficiency as a function of p with a Monte-Carlo calculation. We find the useful efficiency drops to near 50% at $\Delta p/p = \pm 2.0\%$. The integrated transport efficiency is greater than 80% over the full momentum spread of 4%. The loss is due to chromatic aberration effects in the transport line which cause an effective emittance growth.

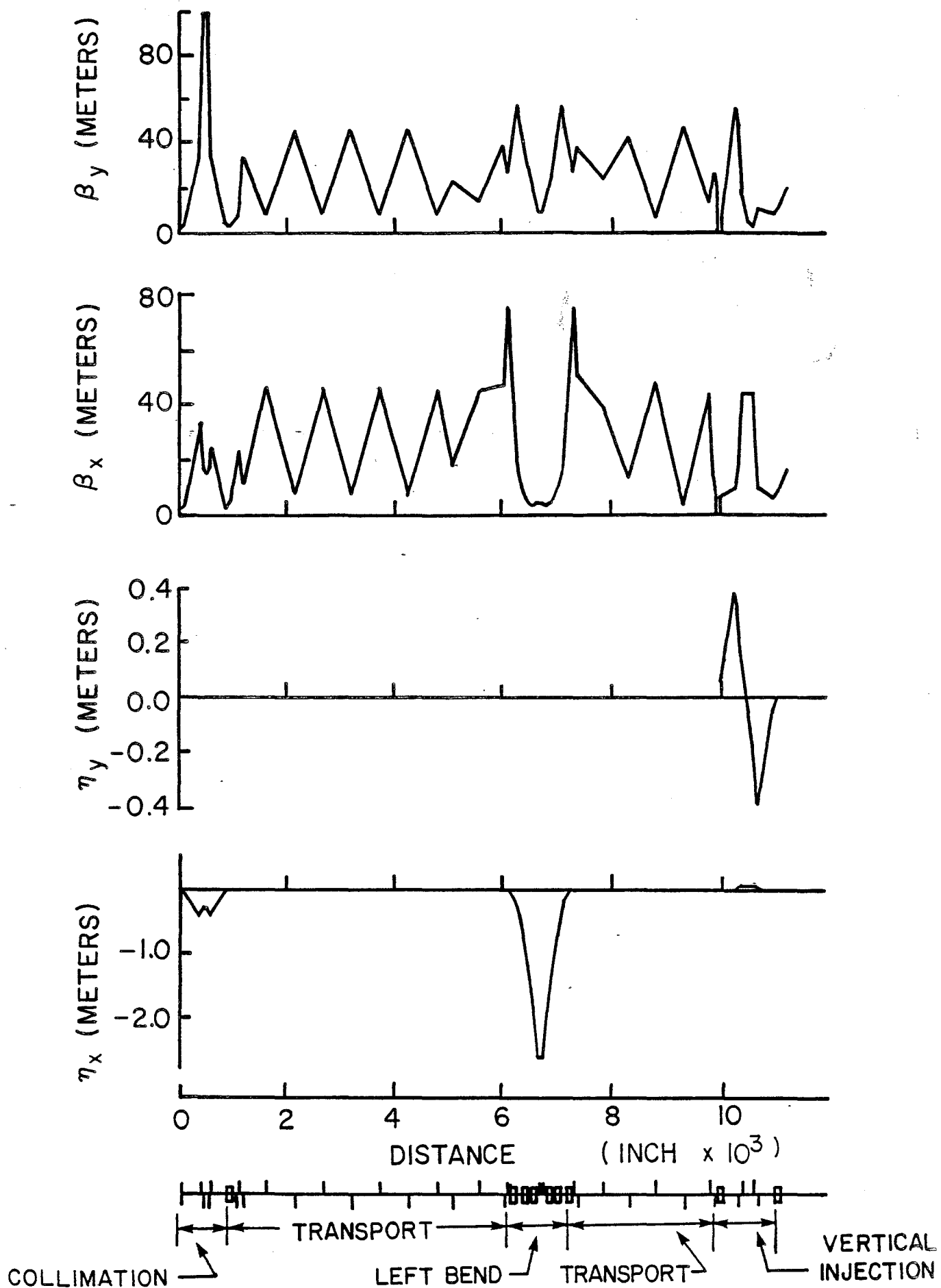


Fig. 3-12. The antiproton transport line to the Debuncher monoenergetic envelope functions β_y , β_x and dispersion functions η_y , η_x .

REFERENCES

1. "Calculation of Yields for the Fermilab Antiproton Source" Carlos Hojvat and A. Van Ginneken, Fermilab-Pub-82/43, 1982 (submitted to Nucl. Inst. Meth.)
2. E. Colton, "More on Antiproton Collectors," \bar{p} note #120, Fermilab (unpublished).
3. B. F. Bayanov et al., "A Lithium Lens for Axially Symmetric Focusing of High Energy Particle Beams," Nuc. Inst. Meth., 1909(1981).
4. "MAXIM - Program to Simulate Cascades in Bulk Matter." A. Van Ginneken, Fermilab FN-272 (January 1975).
5. "High Intensity Targeting Workshop," Fermilab April 28-30, 1980.
6. F. Krienen and F. Mills, Spreading the Hot Spot on the Target, \bar{p} Note 70.
E. Colton, \bar{p} Note 107.
7. "Electromagnetic Properties of a Pulsed Cylindrical Conductor," A.J. Lennox, (in preparation).
"Optical Properties of Cylindrical Lenses," T.A. Vsevolozhskaya et al, Sov. Phys. Tech. Phys., Volume 20, No 12, 1556 (1976).
8. "Energy Deposition in the Lithium Lenses," A.J. Lennox, \bar{p} Note 204, Fermilab 1982 (Unpublished).
9. E. Colton, \bar{p} Notes 224 and 225, Fermilab, 1982 (unpublished).

4. DEBUNCHER RING

4.1 Purpose of the Debuncher

The primary purpose of the Debuncher is to reduce the large momentum spread of the 8-GeV \bar{p} beam at production to 0.2% or less prior to injection into the Accumulator. This reduction is done by rf bunch rotation and adiabatic debunching after the \bar{p} beam is injected into stationary 53-MHz buckets in the Debuncher. The debunching time is only slightly longer than 10 msec, and there are therefore nearly two seconds available for cooling before the beam is transferred to the Accumulator. Stochastic cooling of betatron amplitudes was found to be feasible, and a betatron cooling system to reduce the emittance by a factor 3 in both planes in 2 sec is included in the design. Table 4-I gives parameters of the Debuncher.

Table 4-I. THE DEBUNCHER RING

Kinetic Energy	8.0 GeV
$\eta = \gamma_t^{-2} - \gamma^{-2}$	-0.0047
γ_t	12.6
Average Radius	83.1 m
RF Frequency	53.1035 MHz
Maximum RF Voltage	5 MV
Number of \bar{p} -bunches injected	80
Harmonic Number	93
Beam Gap for Injection Kicker	230 nsec
Momentum Aperture, $\Delta p/p$	4%
Betatron Acceptance, h and v	20π mm-mrad
Betatron Tunes, h and v	14.28
Natural Chromaticity, h and v	-22
Periodicity	3, each with mirror symmetry
Max β -values, regular cells	19 m
long straight sections	39 m
Max Dispersion Value	1.0 m
Phase Advance Regular Cells, h	120°
v	110°

4.2 Rotation and Debunching¹

In order to evaluate the effectiveness of the debunching process and thus to determine the momentum spread of \bar{p} 's that can be accepted at production, extensive computer simulations of the rotation and debunching sequences have been carried out. The following features have been included:

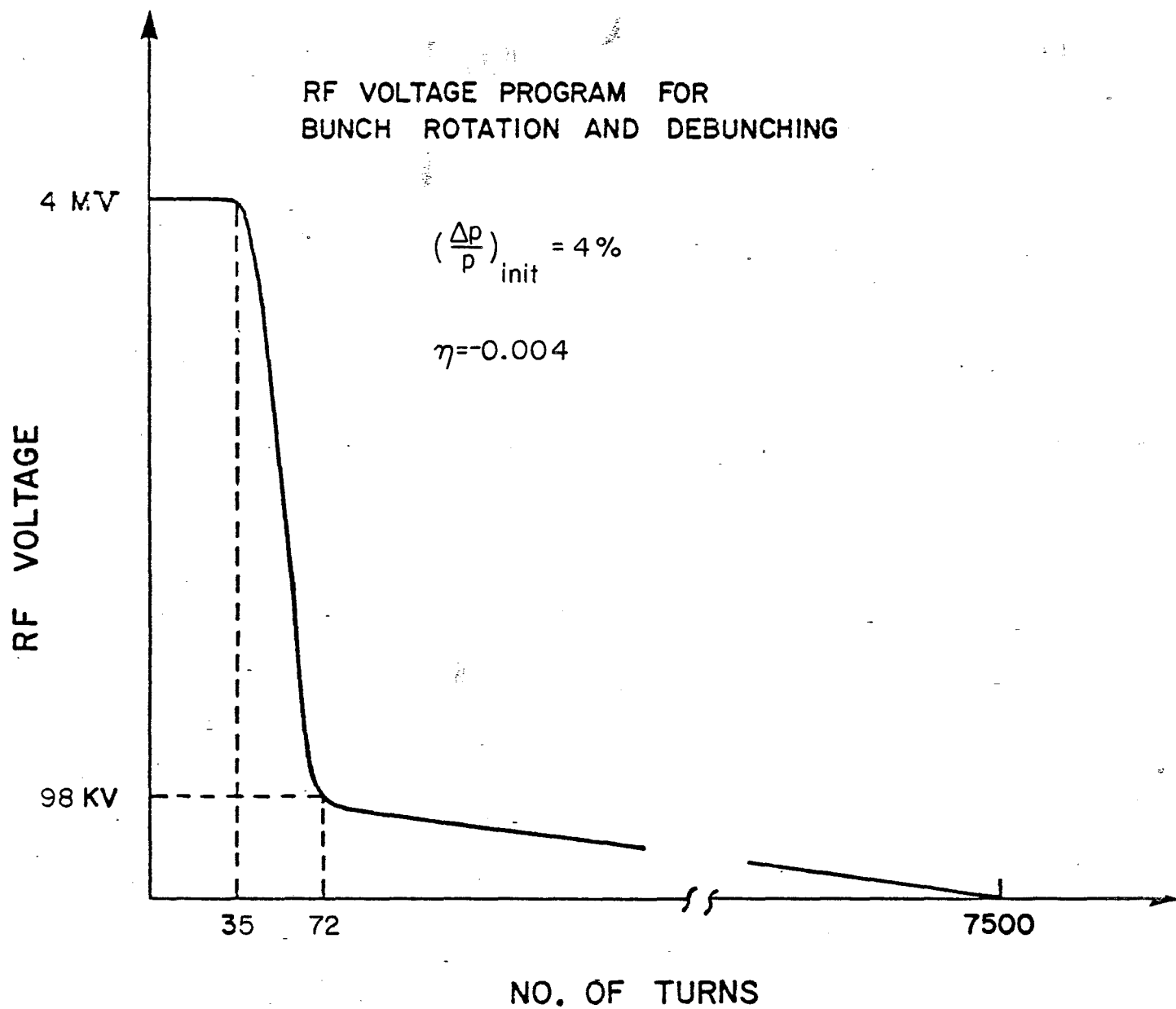


Fig. 4-1

- (i) The antiproton bunches, at the moment they have been generated at the target, have the same longitudinal distribution as the proton bunches, that is, an rms bunch length of 5 cm.
- (ii) The \bar{p} 's traverse a dispersionless drift of 100 to 400 m between the target and the first rf cavity. The rf voltage is generated by a single cavity.
- (iii) Two values of η were used. A value of -0.002 was used with an rf voltage of 2 MV and a value of -0.004 was used with an rf voltage of 4 MV. The results do not depend very much on the value of η although the case of $\eta=-0.002$ is somewhat worse.
- (iv) The bunches were allowed to rotate for 35 turns while the voltage was kept constant. The rotation was about 45° .
- (v) The voltage was then dropped to 98 kV in 35 turns (or 56 μ sec) to form a bucket matched in shape to the beam bunch, which had evolved into a grossly distorted S-shape that extended over $\pm 90^\circ$ in synchrotron phase.
- (vi) The voltage was slowly reduced to 5 kV or less.

A debunching time of 12 msec was chosen, since longer times did not significantly reduce the momentum spread while shorter times did increase the momentum spread. The final momentum spread is not sensitive to the other details of the time dependence of the rf voltage except during the early stage of rotation. The rf voltage program for the rotation and debunching operations is shown in Fig. 4-1 for the case of $\eta=-0.004$ and $\Delta p/p=4\%$. Figures 4-2 through 4-5 show the beam shape at the end of some of the steps for $\Delta p/p=3\%$. If the debunching could be done without dilution, 95% of the beam would be contained within a momentum spread of 0.11%. Computer simulations show that the debunched momentum spread is 0.2%. The factor of two dilution has several causes. It is caused in part by nonlinearities of phase oscillations of particles captured within rf bucket and in part by the variations of γ^{-2} of the particles and the momentum compaction factor γ_T^{-2} with energy. These variations and the presence of sextupole corrections in the ring lattice were taken into account in the simulations.

Calculations were done with smaller initial momentum spreads. The initial rf voltage of 4 MV and the final rf voltage of 5 kV were kept fixed for these calculations. These results, which are shown in Fig. 4-6, establish that the final momentum spread can be reduced significantly if the initial momentum spread is reduced by a relatively small amount. These calculations show that the debunched beam momentum spread is 0.2% if the bunched beam momentum spread is limited to 3%. The momentum spread of the \bar{p} beam will be limited to 3% by collimation prior to injection into the Debuncher. The Debuncher itself has a momentum aperture of over 4%. It may be possible to reduce the debunched beam momentum spread further if the rf voltage can be reduced adiabatically to a value much less than 5 kV.

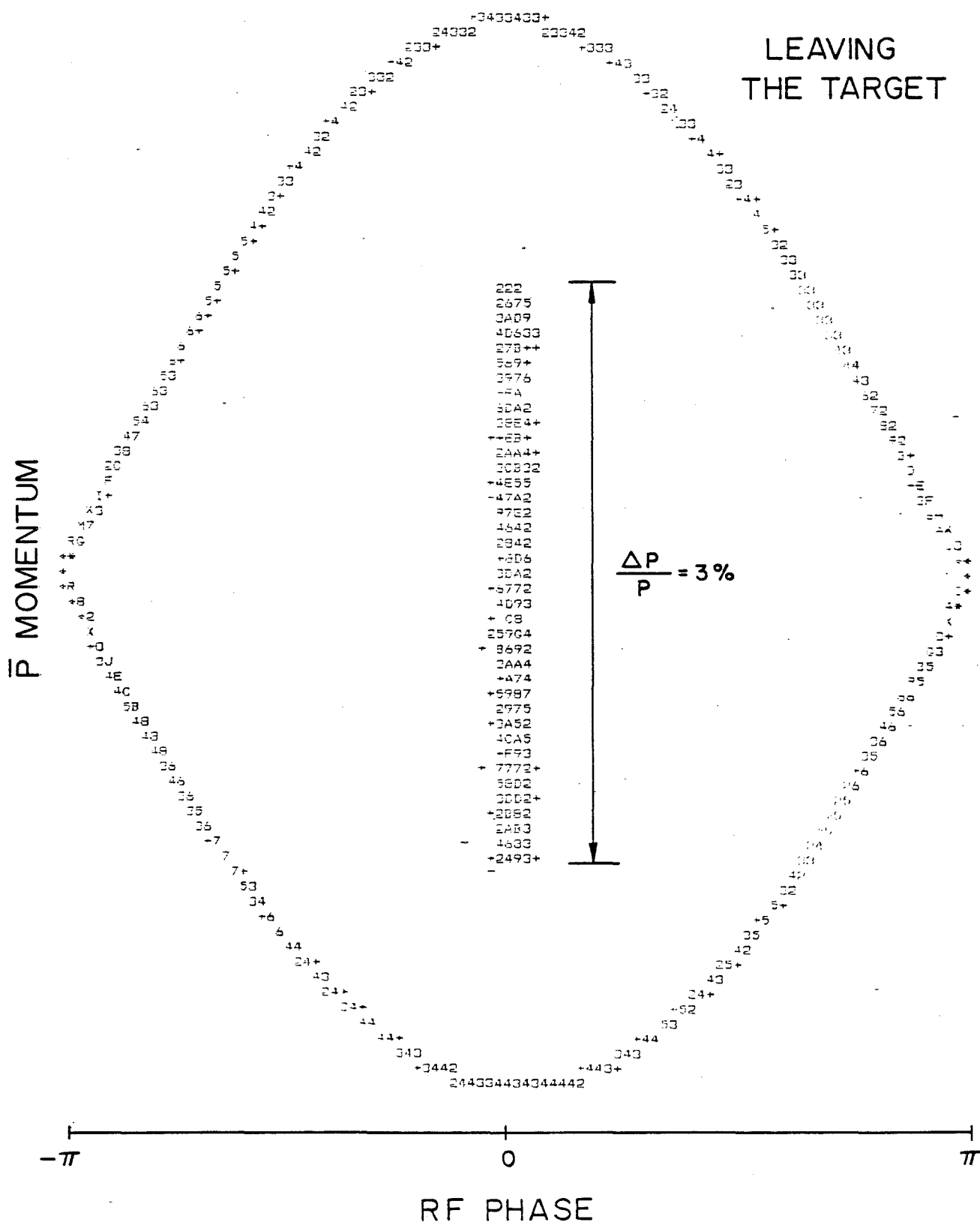


Fig. 4-2

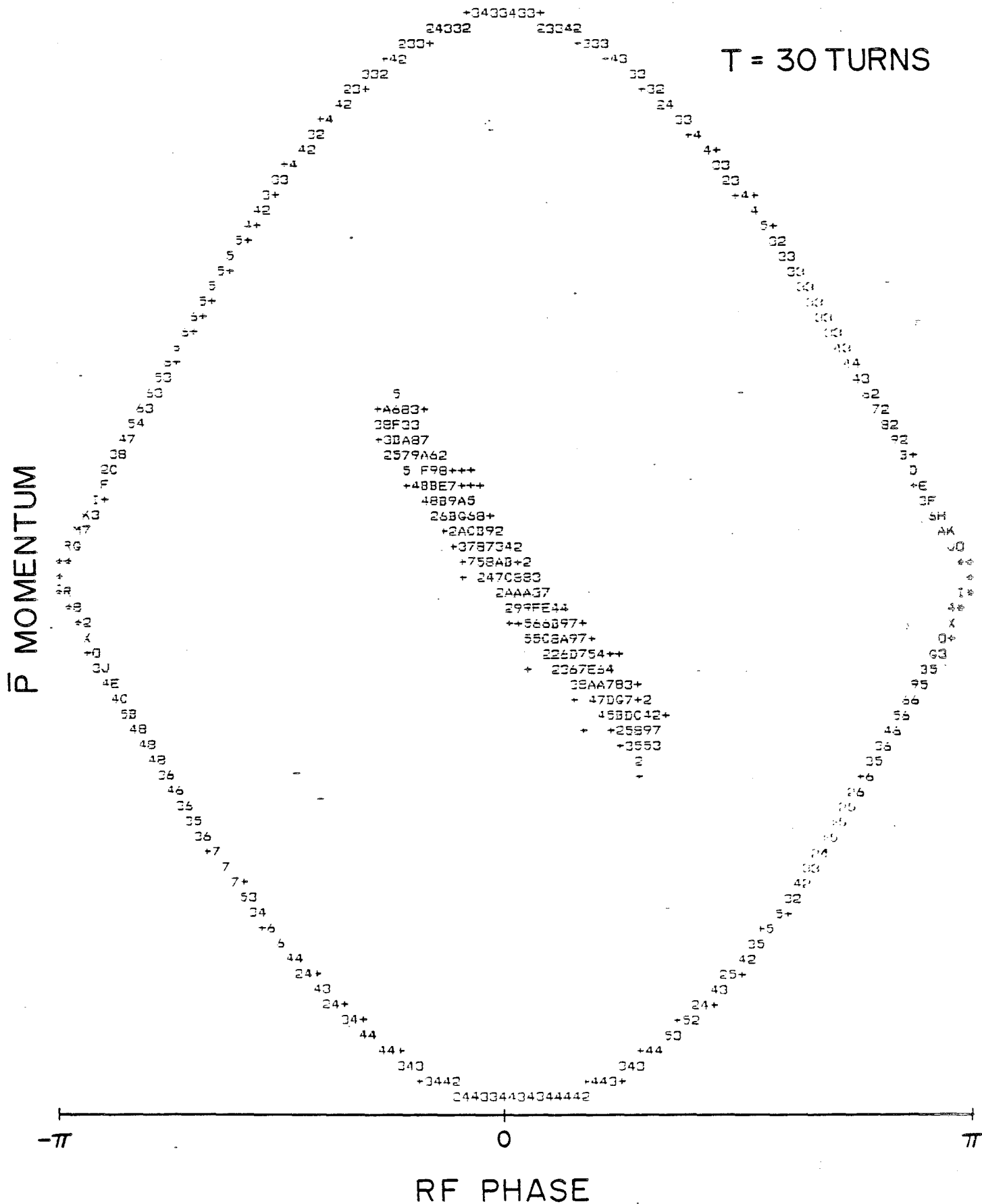


Fig. 4-3

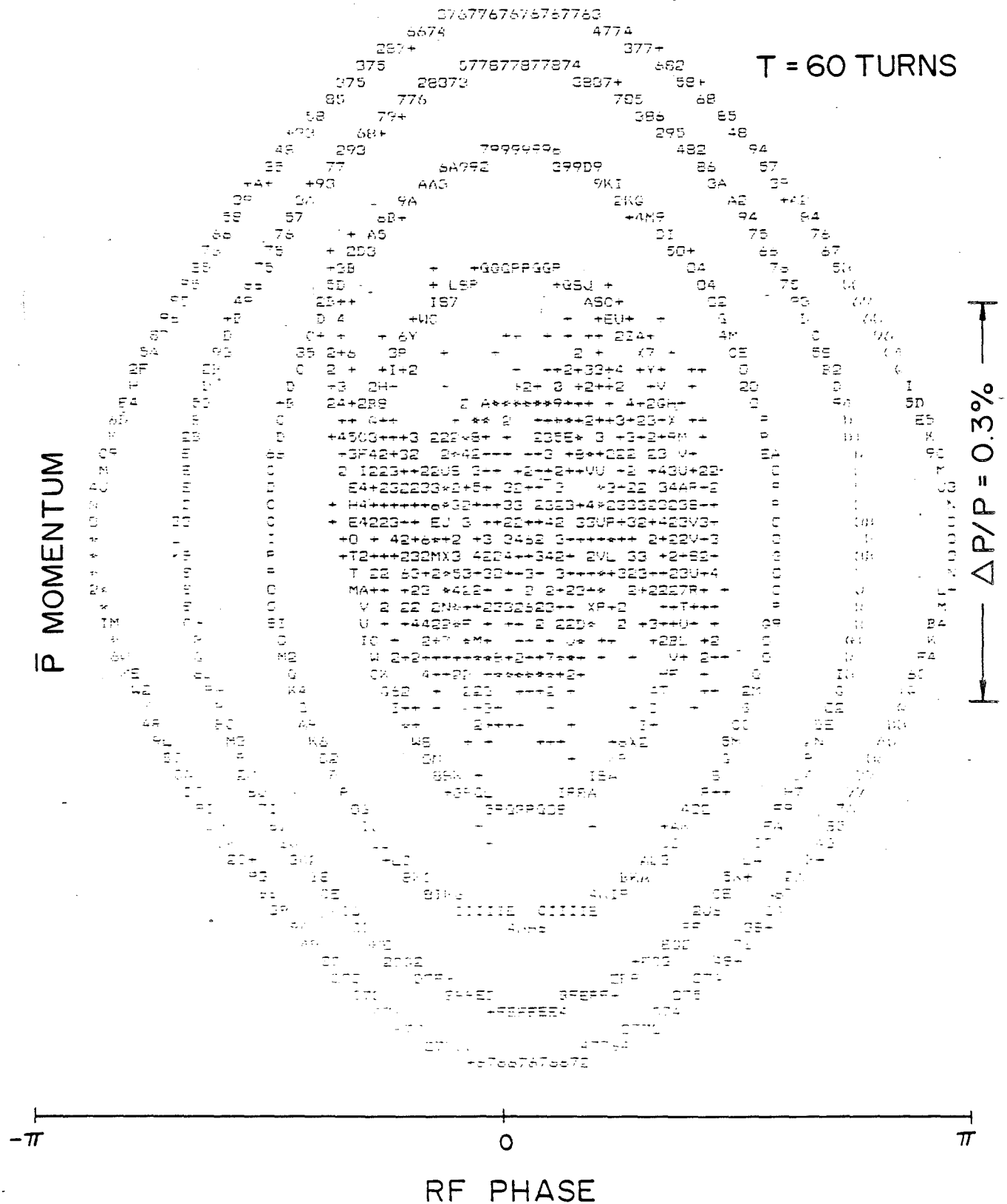


Fig. 4-4

60
50
56
54
52
50
48
46
44
42
40
38
36
34
32
30
28
26
24
22
20
18
16
14
12
10
8
6
4
2

95% OF BEAM
 $\frac{\Delta P}{P} = 0.2\%$ FULL WIDTH

T = 7500 TURNS
(5 KV)

2/2

[illegible]

Fig. 4-5

Debunched Beam Spread
vs.
Initial Beam Spread
for $V=4\text{MV}$ and a Final $V=5\text{KV}$

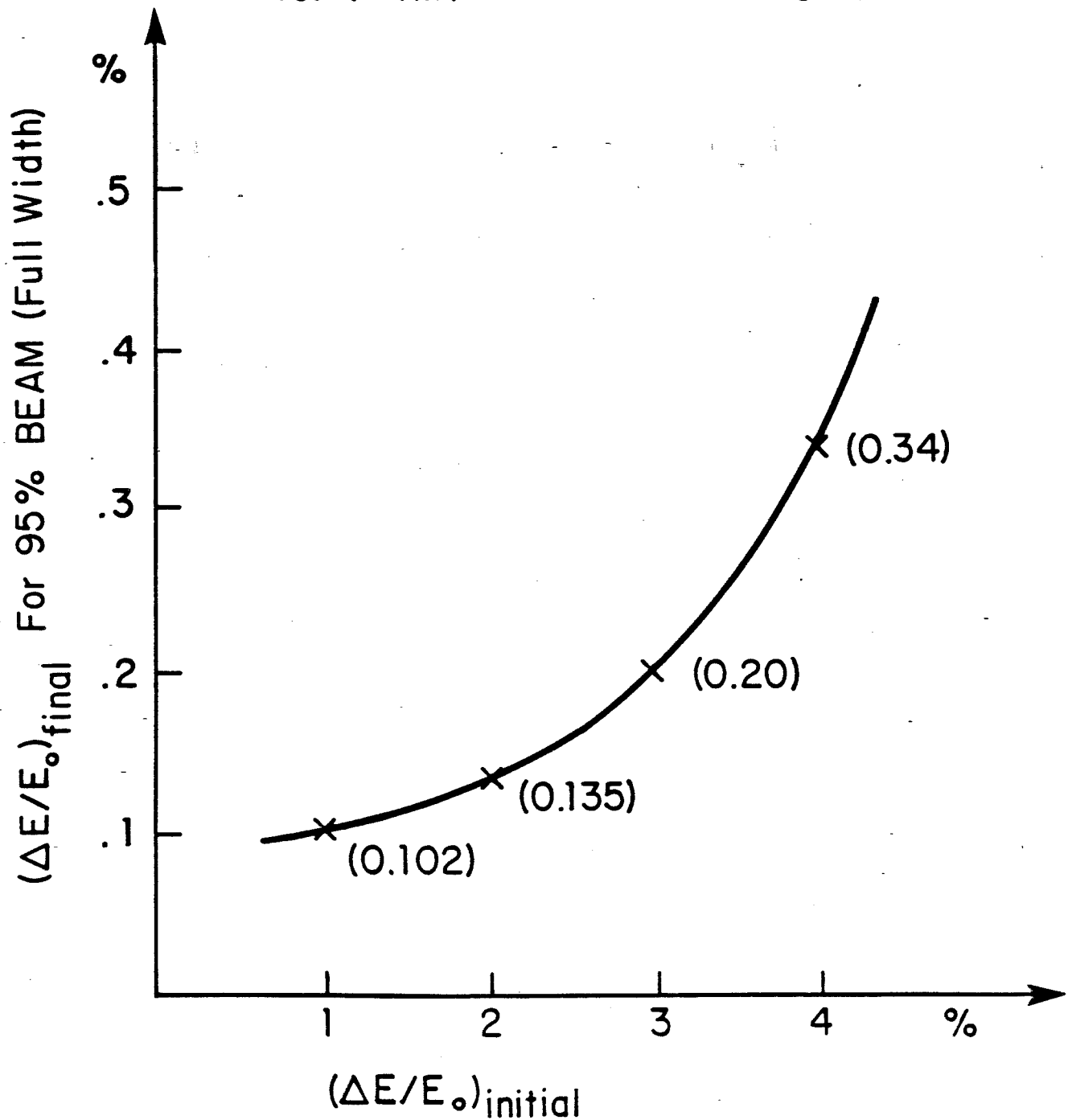
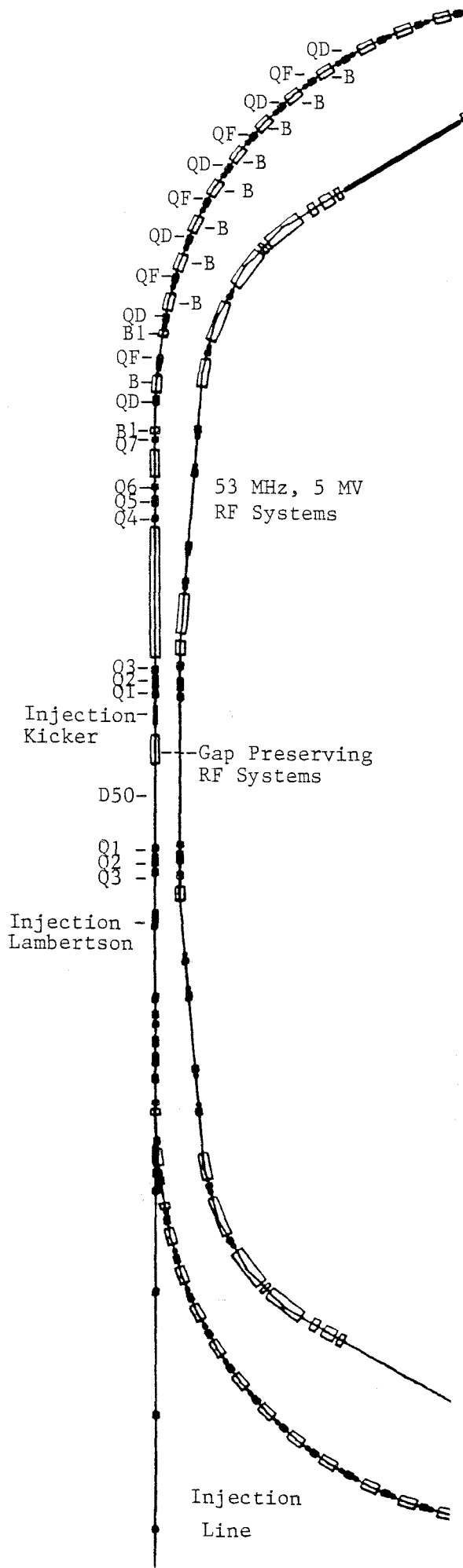


Fig. 4-6



DEBUNCHER LAYOUT
Fig. 4-7

The final momentum spread was not changed when a higher-harmonic rf voltage was added¹. Harmonics of twice and three times the fundamental frequency were added in the simulations.

After the 53 MHz rf is turned off, a broad-band, low-frequency rf system is turned on to preserve the gap in the otherwise debunched beam. A 200-nsec gap is needed if the beam is to be transferred to the smaller Accumulator without loss. The rf system to make this gap is described in Section 4.5.2.

4.3 The Debuncher Ring Lattice

The rf voltage needed for bunch rotation is proportional to $|\eta|$. If $|\eta|$ is less than 0.002, the variation of $|\eta|$ with momentum will degrade the final momentum spread. On the other hand, a larger value of $|\eta|$ helps the betatron cooling and is needed if momentum precooling is to be done in the future. As a compromise η was chosen to be -0.0047. This choice makes γ_T close to 12. Choosing γ_T above the operating energy is desirable because it leads to strong focusing, which in turn leads to magnets with small apertures. The Debuncher Ring is made of 24 FODO regular cells, each of which is about 9 m long. Long straight sections with zero dispersion have been included to accommodate pickups and kickers for stochastic cooling. These sections also provide the space for rf cavities and injection-extraction magnets.

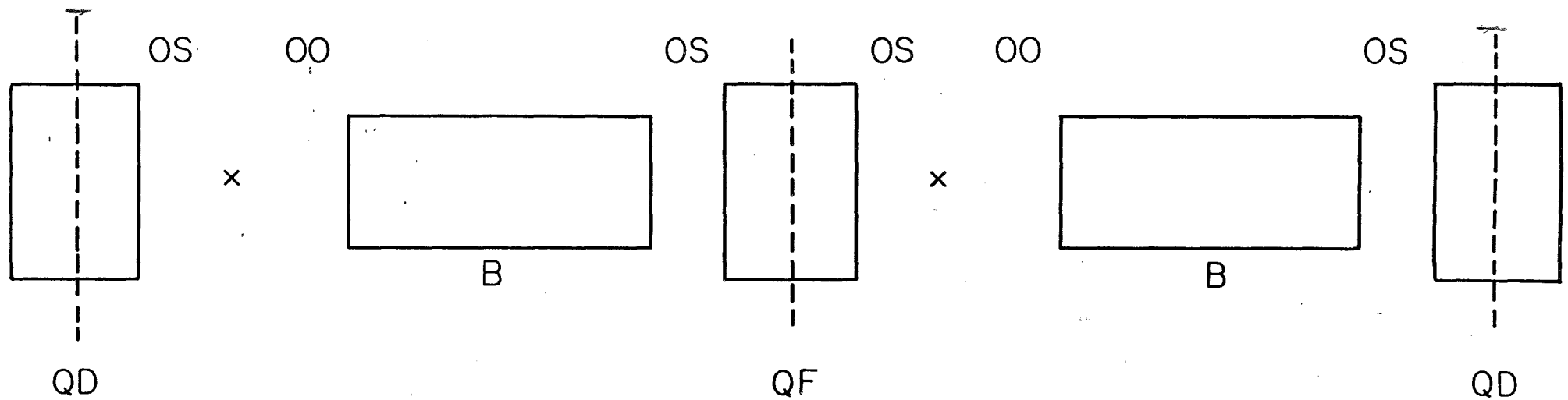
A threefold symmetry for the lattice was chosen because it closely matches the Accumulator Ring, which has threefold symmetry. This allows a reasonably convenient arrangement of straight sections with common equipment galleries. Figure 4-7 shows the overall Debuncher lattice. Figure 4-8 summarizes the parameters for a single cell. Locations around the ring are keyed with standardized code numbers. Figure 4-9 describes the dispersion-killer section. The packing factor, the ratio of bending length to circumference, is 21.3%.

The three long straight section are symmetric about the center and are made of three low-beta insertions, each about 16 m long. The low-beta values are 6-7 m in both planes, created with triplets on both sides. One half of a long straight section is shown in Fig. 4-10. The purpose for the low-beta is to maintain the beam size in both horizontal and vertical direction within 20 mm for stochastic cooling. This is also the purpose of zero dispersion.

Each regular cell consists of a focusing quadrupole, a defocusing quadrupole, two dipoles and a correction package. The correction packages consist only of two families of sextupoles.

Steering dipoles will be located only in the long straight sections to steer the beams through the pickup and kicker systems for stochastic cooling. We do not expect much closed orbit distortion in the rest of the ring. We plan to compensate for any such distortion by moving quadrupoles. Steering dipole specifications are given in Table 4-II.

DEBUNCHER REGULAR CELL



$B = 16.75 \text{ kG}, 1.905\text{m}$

QF, 0.4064m , $B' / B_p = 0.4947\text{m}^{-2}$

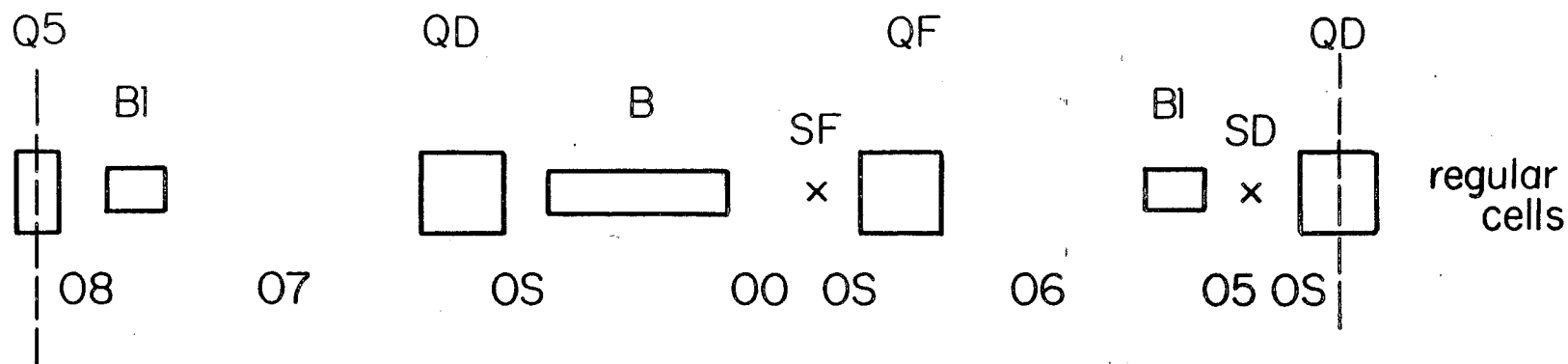
QD, 0.4064m , $B' / B_p = -0.46842\text{m}^{-2}$

OO = 0.85623m .

OS = 0.5m

Fig. 4-8

low β
insertions



OS	0.5 m
00	0.85623
05	0.4315141
06	2.1363695
07	2.5758275
08	0.4822375

Length = 13.5385 m
(1 and 1/2 regular cells)

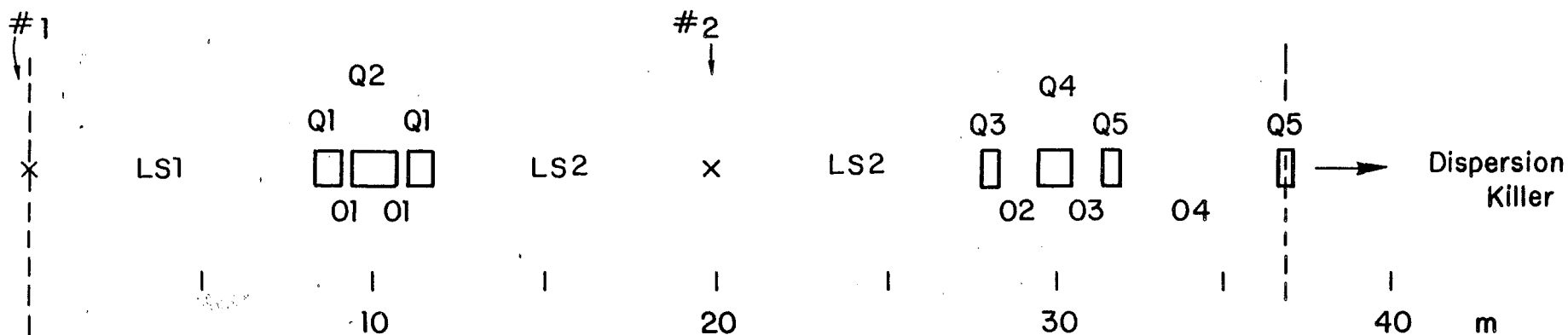
BI: Length = 0.695323m

Field = 16.75 kG

Dispersion-Killer Section

*what is SF + SD?
Why are x's there?
in diagram?
sextupole (focus + defocus)*

Fig. 4-9



O1	0.354525 m	#1	β_H^*	=	6.64 m	α_H^*	=	0.0
O2	1.1620		β_V^*	=	6.16 m	α_V^*	=	0.0
O3	0.8183		α_p^*	=	0.00 m	α_p^*	=	0.0
O4	4.8410							
LS1	8.2930 m	#2	β_H^*	=	6.35 m	α_H^*	=	0.018
LS2	8.0676		β_V^*	=	6.54 m	α_V^*	=	0.066
			α_p^*	=	0.00	α_p^*	=	0.000

Long Straight Section (One Half)

For the quadrupole specifications
see table 4-IV

Fig. 4-10

Table 4-II. STEERING DIPOLES

	Horizontal	Vertical
Maximum closed orbit dist.	± 5	± 3 mm
Deflection	0.44	0.16 mrad
Effective Length	0.30	0.30 m
Maximum Field	440	160 G
Gap	40	80 mm
Ampere-turns	1400	1020 A-turns
Current Density	1.0	1.0 A/mm ²
Current	10	10 A
Turns	140	102 turns/mag
Resistivity	0.2	0.15 Ohm/mag
Voltage	2.0	1.5 V/mag
Thermal Loss	20	15 W/mag
Total Number	24	24

The basic function of the sextupoles is to flatten the chromaticity in both planes so that the variation in tune across the aperture is less than 0.03. Sextupoles 50 cm long are located next to each quadrupole in a region of significant dispersion. The sextupole specifications are given in Table 4-III. The variation of $\alpha = 1/\gamma_T^2$ with momentum spread is displayed in Fig. 4-11. Figure 4-12 shows the variations of the betatron tunes and Fig. 4-13 the variations of the maximum values of β and α_p . Figure 4-14 gives the lattice functions across one-half period. Figure 4-15 shows the tune diagram with the range of tunes for a momentum spread of $\pm 2.2\%$. The heavy dot at the center is the tune of the beam after the rotation and beam debunching.

Table 4-III. SEXTUPOLE MAGNETS

	SF	SD
Number	30	30
Strength for zero chromaticity $B''/B\rho$	1.2 m	-2.2 m ⁻²
Bore Radius	50.0	50.0 mm
Estimated Effective Length	0.50	0.50 m
Maximum Field, B''	71.3	131 T/m ²
Ampere-turns	1182	2170 AT/pole
Current	100	100 A
Turns	12	22 Turns/pole
Conductor Size		
Current Density		
Resistance	0.07	0.120 ohm/mag
Voltage Drop	7.0	12 V/mag
Thermal Loss	0.7	1.2 kW/mag
Power Supply		
Current	100	100 A
Voltage	130	360 V
Power	21	36 kW

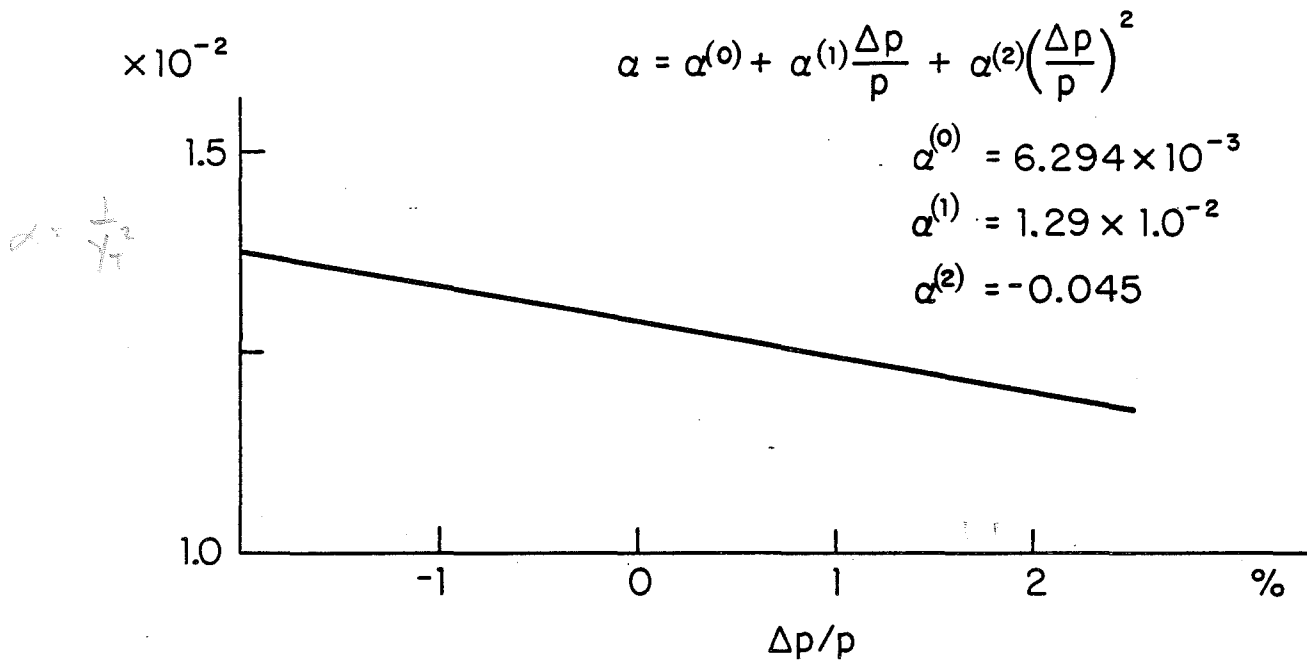


Fig. 4-11

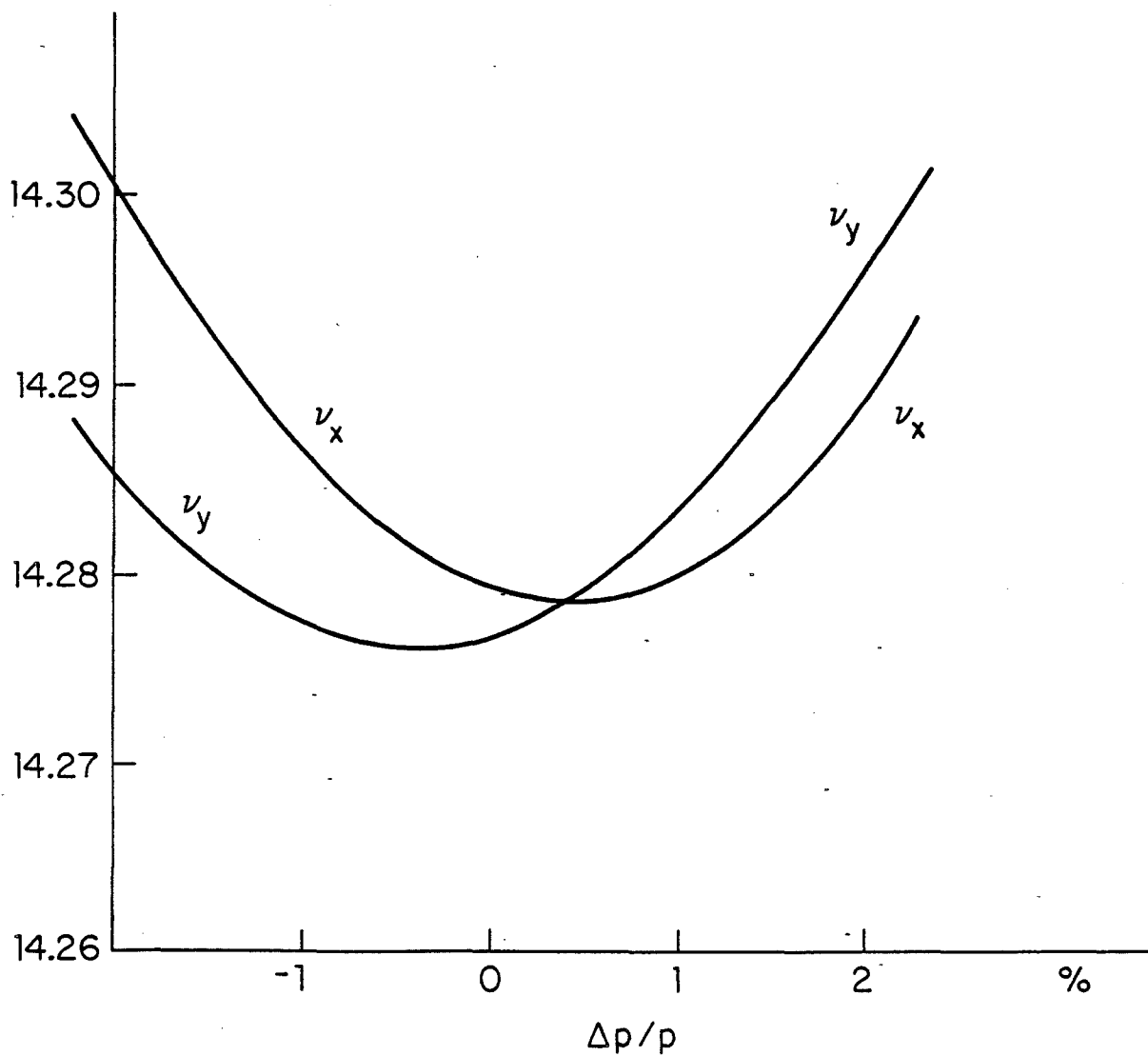


Fig. 4-12

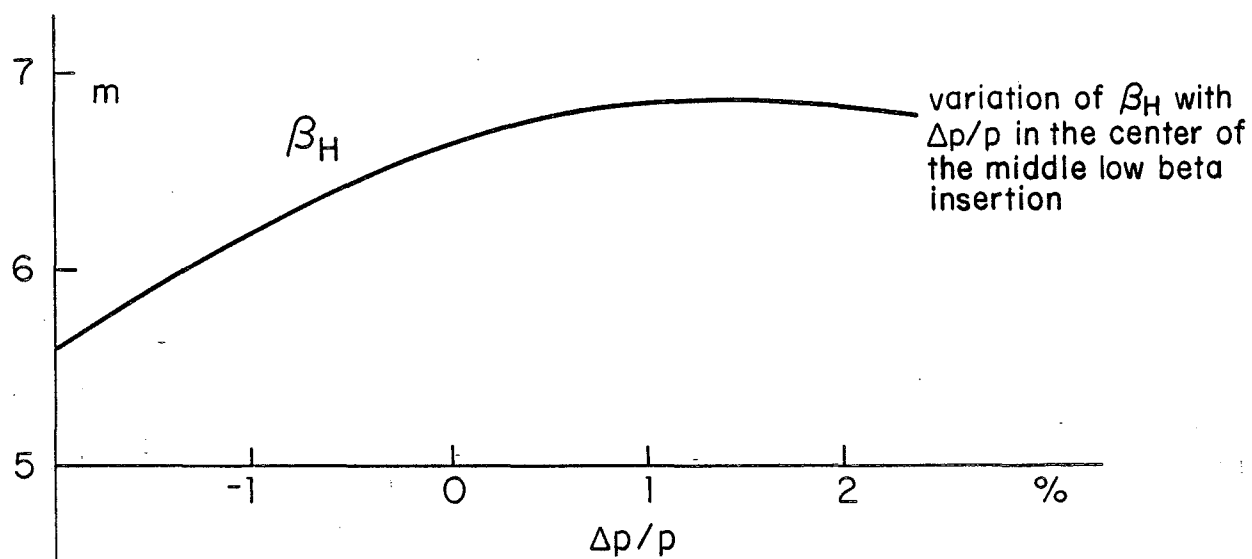


Fig. 4-13a

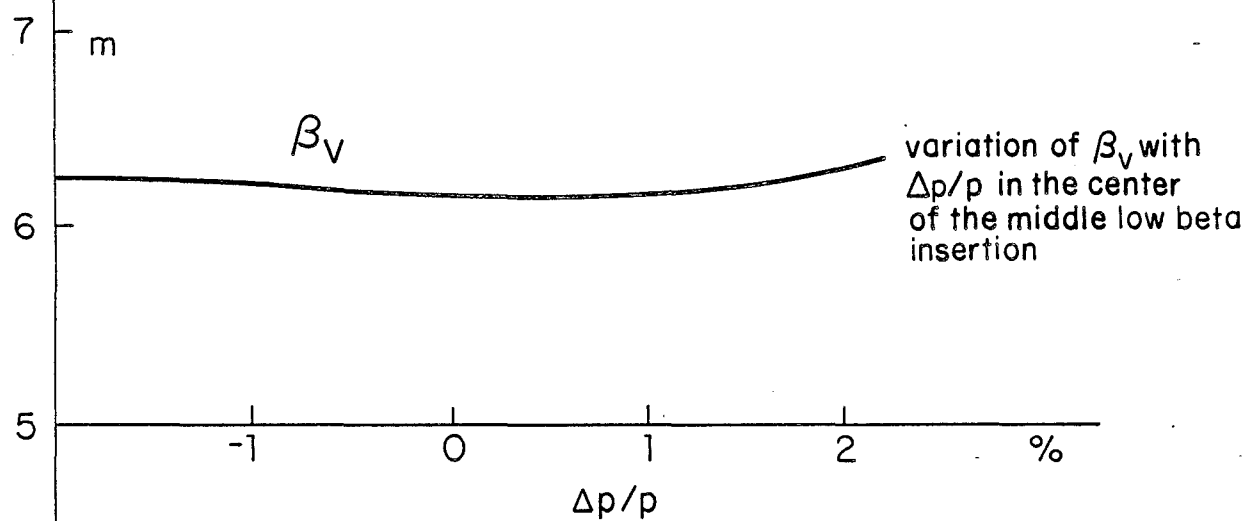


Fig. 4-13b

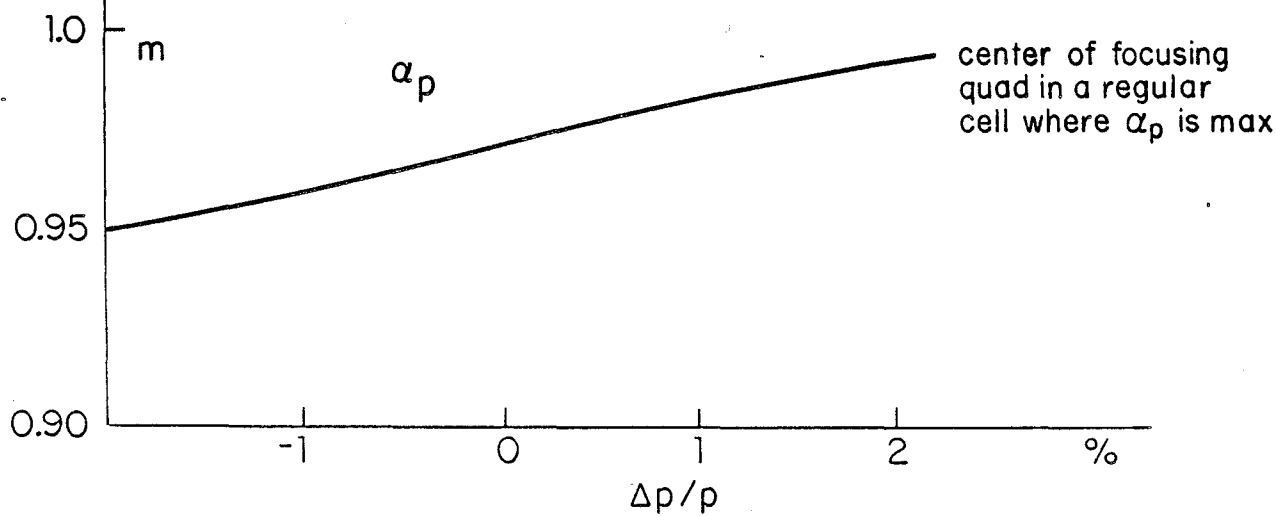


Fig. 4-13c

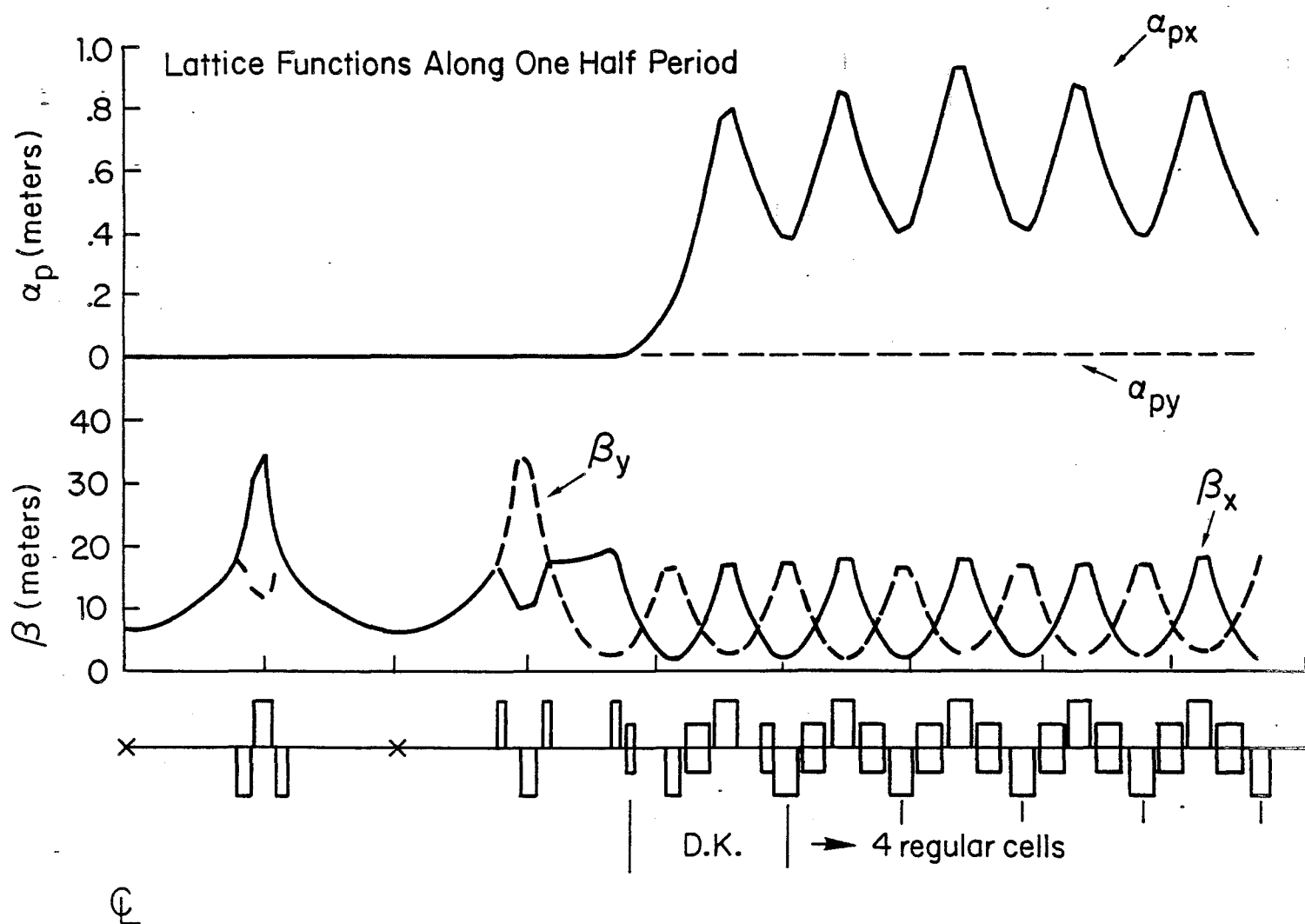


Fig. 4-14

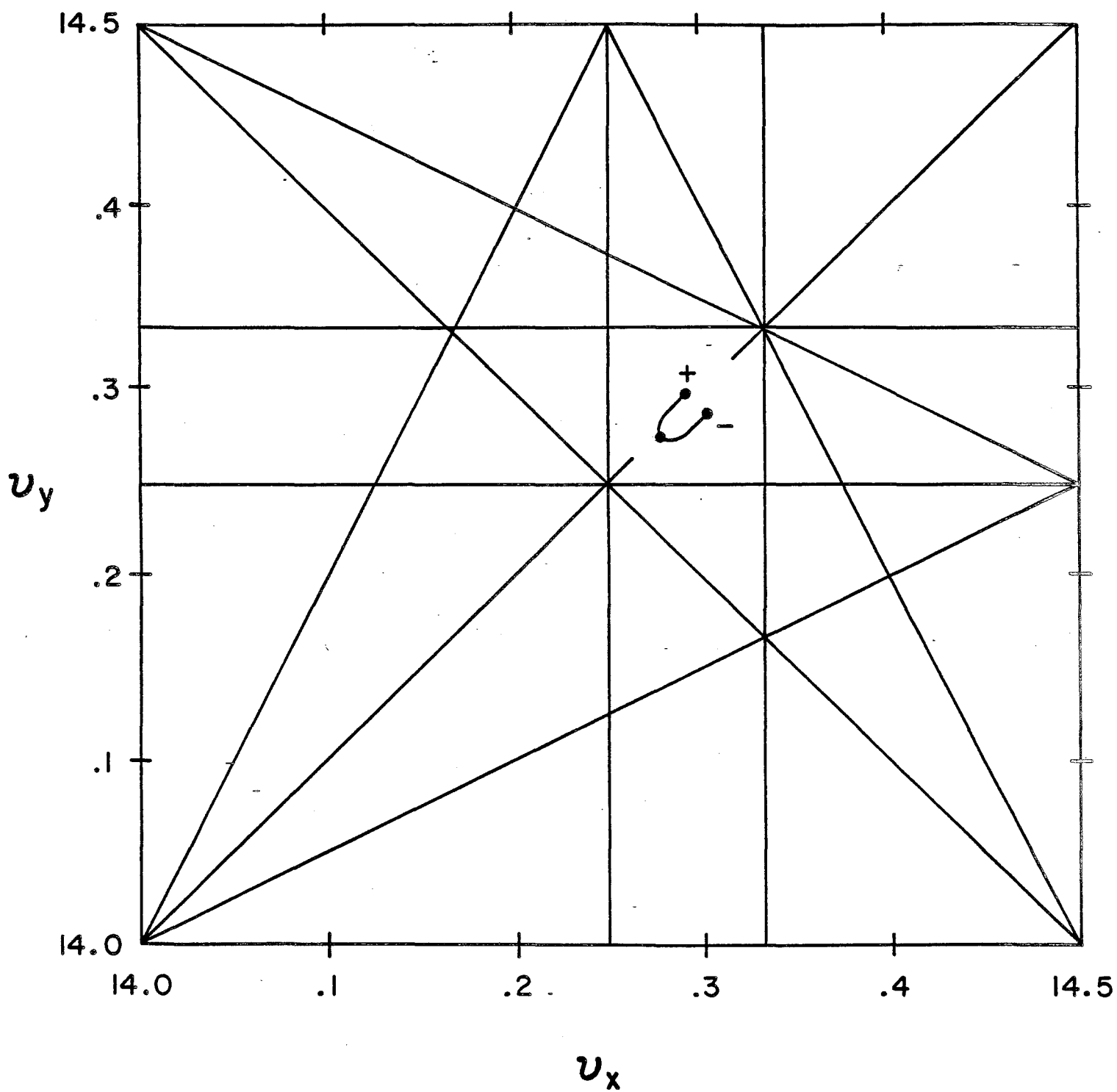


Fig. 4-15

Vacuum pumps will be distributed around the ring every few tens of meters. The lifetime for an 8.9-GeV/c beam is calculated to be few hours when the average vacuum pressure is 10^{-8} Torr. This vacuum can be achieved without baking the chamber, so no provisions for baking are included in the design. The vacuum pipe will be carefully treated and cleaned during construction and the vacuum is expected to be close to 10^{-8} Torr. Beam-position monitors are located next to each quadrupole.

4.4 Beam Injection and Extraction

4.4.1 Injection. The beam enters the Debuncher in the vertical plane at an angle of 50 mrad to the closed orbit. A Lambertson magnet located in a zero-dispersion region deflects the beam vertically onto an orbit parallel to the reference orbit and horizontally displaced by 40 mm at the downstream end of the magnet. A kicker in a zero-dispersion location 60° in betatron phase away from the Lambertson kicks the beam onto the reference orbit. A schematic layout of these components is shown in Fig. 4-16. Figure 4-17 shows the envelope of the circulating and injected beam in the injection region. The injection channel has been designed to accommodate a beam with momentum spread of 4% and transverse emittances of 20π mm-mrad.

The Lambertson magnet specifications are:

Length	2.0 m
Bending Angle	50 mrad
Bending Radius	42.4 m
Magnetic Field	6.9 kG
Aperture	4 cm (h) x 17 cm (v)
Effective thickness	1 cm

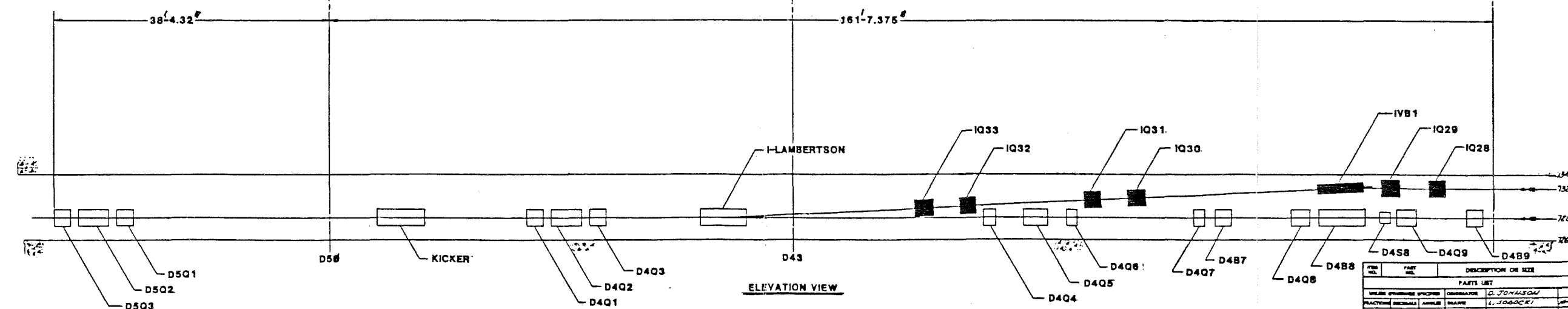
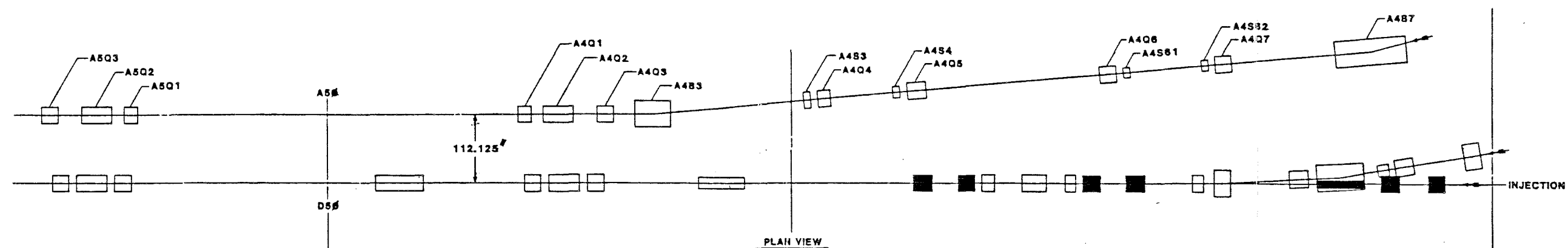
The magnet is located in the upstream low-beta insertion.

The kicker specifications are:

Length	3.4 m
Magnetic Field	525G
Fall-off Time	150-200 nsec
Aperture	5 cm (h) x 5 cm (v)

4.4.2 Debuncher to Accumulator Transfer

The beam transfer between the Debuncher and the Accumulator is a horizontal transfer taking place in the 10 straight section. Extraction from the Debuncher is accomplished with a 525 Gauss, 11 foot long kicker between quadrupoles D6Q7 and D6Q6, followed by a 8 kGauss, 12.5 foot long pulsed septum placed after D6Q4. The beam is then transported to the Accumulator through a string of two dipoles and six quadrupoles. At the Accumulator, the beam is injected onto a path displaced from the central momentum by $\Delta p/p = +0.775\%$ with an 11 kGauss, 12.5 foot long pulsed septum



DEBUNCHER/INJECTION STRAIGHT SECTION(elevation)

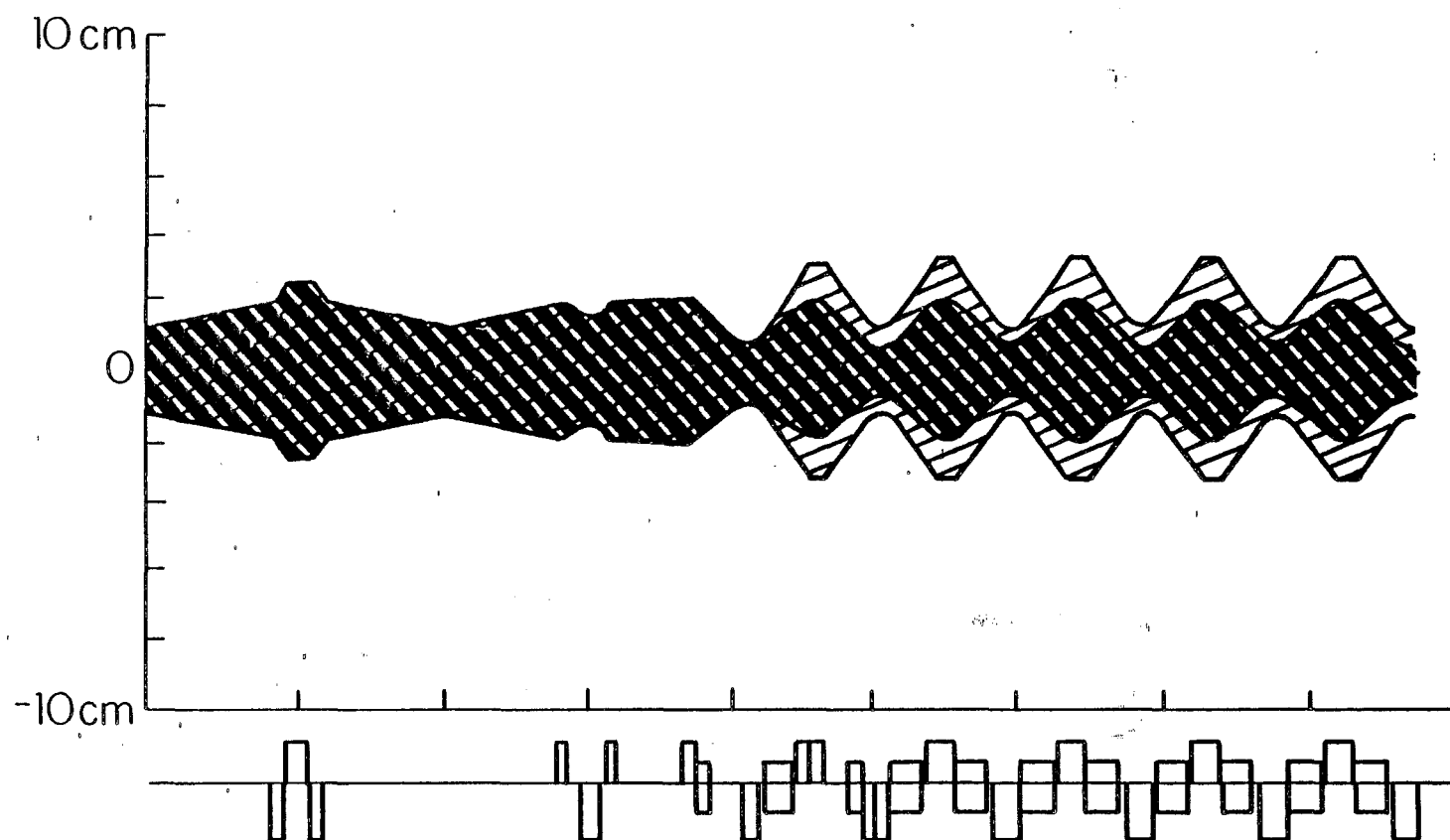
REV.	DESCRIPTION	DATE
1	ISSUED FOR CONSTRUCTION	10/1/68

PARTS LIST	
QUANTITY	DESCRIPTION OR SIZE
1	IVB1
1	IQ29
1	IQ28
1	D4B9
1	D4Q9
1	D4S8
1	D4B8
1	D4Q8
1	D4Q7
1	D4B7
1	D4Q6
1	D4Q5
1	D4Q4
1	D4Q3
1	D4Q2
1	D4Q1
1	KICKER
1	D5Q
1	D5Q3
1	D5Q2
1	D5Q1

DESIGNED BY	D. JOHNSON
CHECKED BY	L. JOHNSON
APPROVED BY	
DATE	10/1/68

PERMANENT NATIONAL ACCELERATOR LABORATORY
UNITED STATES DEPARTMENT OF ENERGY

Fig. 4-16



Horizontal beam envelope before & after debunching

$$\epsilon_H = 20 \pi \text{ mm-mrad}$$

$$\Delta p/p = \pm 1.5\% / \pm 0.1\%$$

Fig. 4-17

placed between A1B3 and A1S3. Finally the beam is kicked onto the proper orbit in the Accumulator with a 500-Gauss, 7 foot long shuttered kicker placed in the A20 straight section, as shown in Figs. 4-7 and 5-29. A plot of the lattice functions of the transfer line is shown in Fig. 4-18 and the list of elements is given in Table 4-IV.

Table 4-IV BEAM TRANSFER DEBUNCHER TO ACCUMULATOR

<u>Element</u>	<u>Length</u>	<u>Field</u>
Debuncher kicker	3.3528m	524.81 Gauss
Septum TS1	3.8100	7.78 kGauss
Drift	3.3236	
Quad TQ1	0.4572	78.78 kG/m
Drift	0.9624	
Dipole TB1	3.0480	-12.34 kG
Drift	1.8515	
Quad TQ2	0.5283	82.02 kG/m
Drift	3.5377	
Quad TQ3	0.5715	-86.84 kG/m
Drift	4.6976	
Quad TQ4	1.2903	+47.02 kG/m
Drift	1.2265	
Quad TQ5	1.2903	-59.13 kG/m
Drift	1.6596	
Quad TQ6	0.5715	72.89 kG/m
Drift	5.6385	
Dipole TB2	3.8100	15.90 kG
Drift	5.3563	
Septum TS2	3.8100	-10.25 kG
Accumulator Kicker	2.1336	500.00 Gauss

4.5 Radio Frequency Systems

4.5.1 Antiproton Debuncher RF. The design criteria for the antiproton debuncher rf are:

- (i) Voltage gain per turn ≥ 4.7 MV.
- (ii) Maximum pulse length 100 μ sec (duty factor 5×10^{-5}).
- (iii) RF voltage pulse fall time from ≥ 4.7 MV to 100 kV 30 μ sec.
- (iv) Pulse repetition rate 0.5 Hz.
- (v) Minimum voltage gain per turn ≤ 5 kV.
- (vi) Adiabatic reduction of voltage from 100 kV to ≤ 5 kV in a time of 5 to 20 msec under program control.

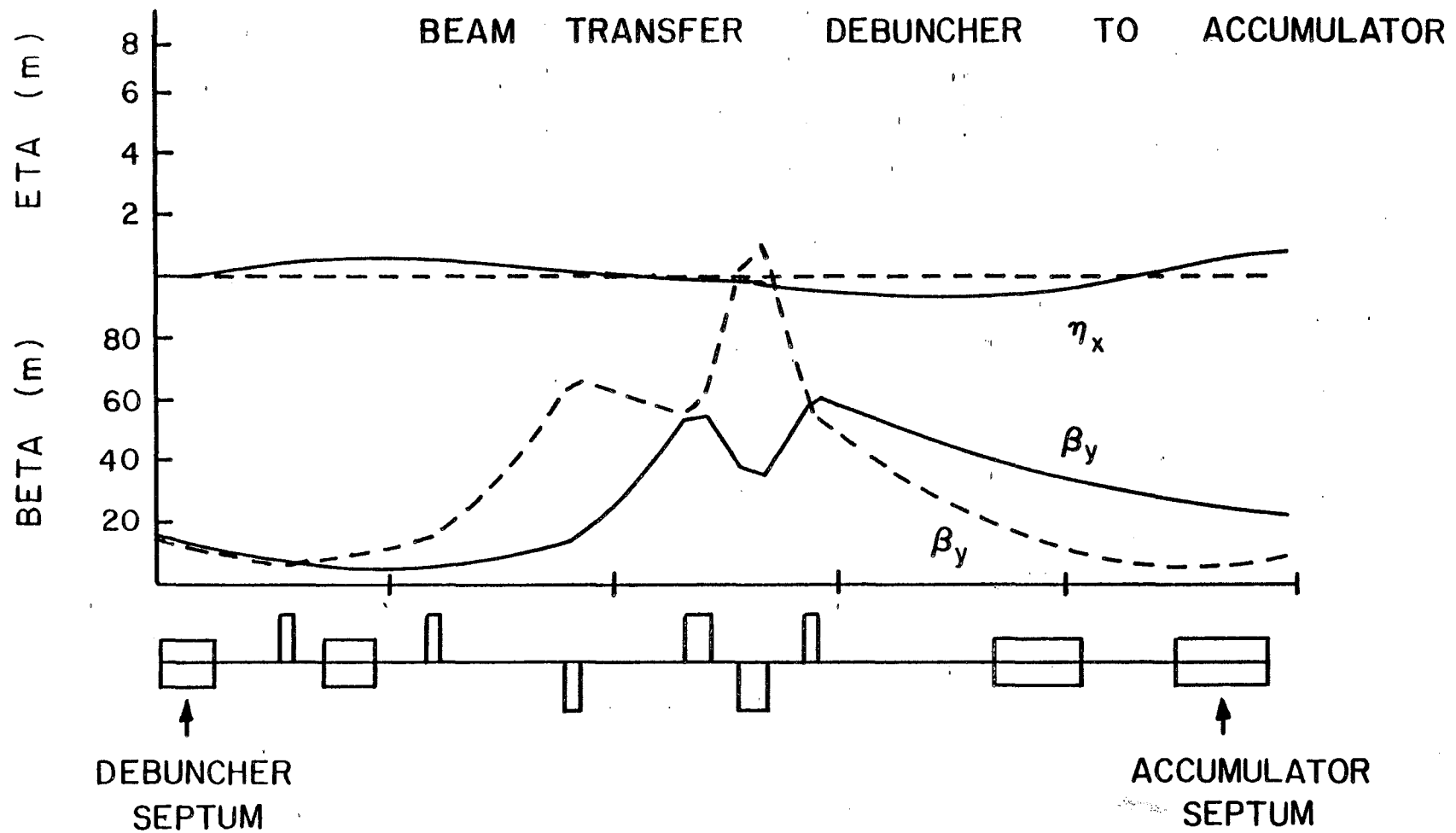


Fig. 4-18

A representative rf voltage waveform was shown in Fig. 4-1. The design is simplified by the fact that the beam intensity will not exceed 10^{10} particles when the rf voltage is on. Of the particles that emerge from the production target when it is struck by 2×10^{12} 120-GeV protons, approximately 2×10^{10} are within the acceptance of the beam transport and the Debuncher. Some 90% of these particles are mesons, of which 50% decay before reaching the injection straight section. After each successive turn, 63% of the remaining mesons decay. The remainder of the particles that reach the center of the injection straight section consist of muons, principally from pion decay, and electrons produced in showers in the target. The electrons lose 30 MeV per turn through synchrotron radiation and spiral out of the vacuum chamber within 20 turns.

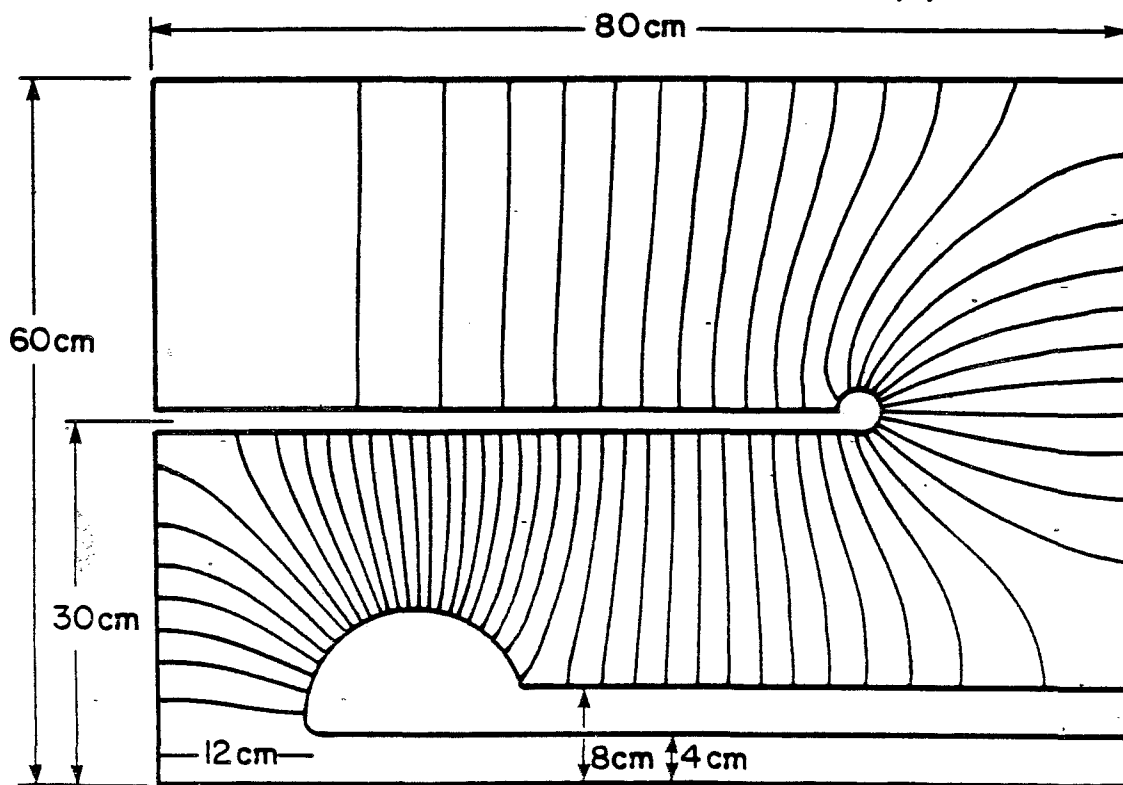
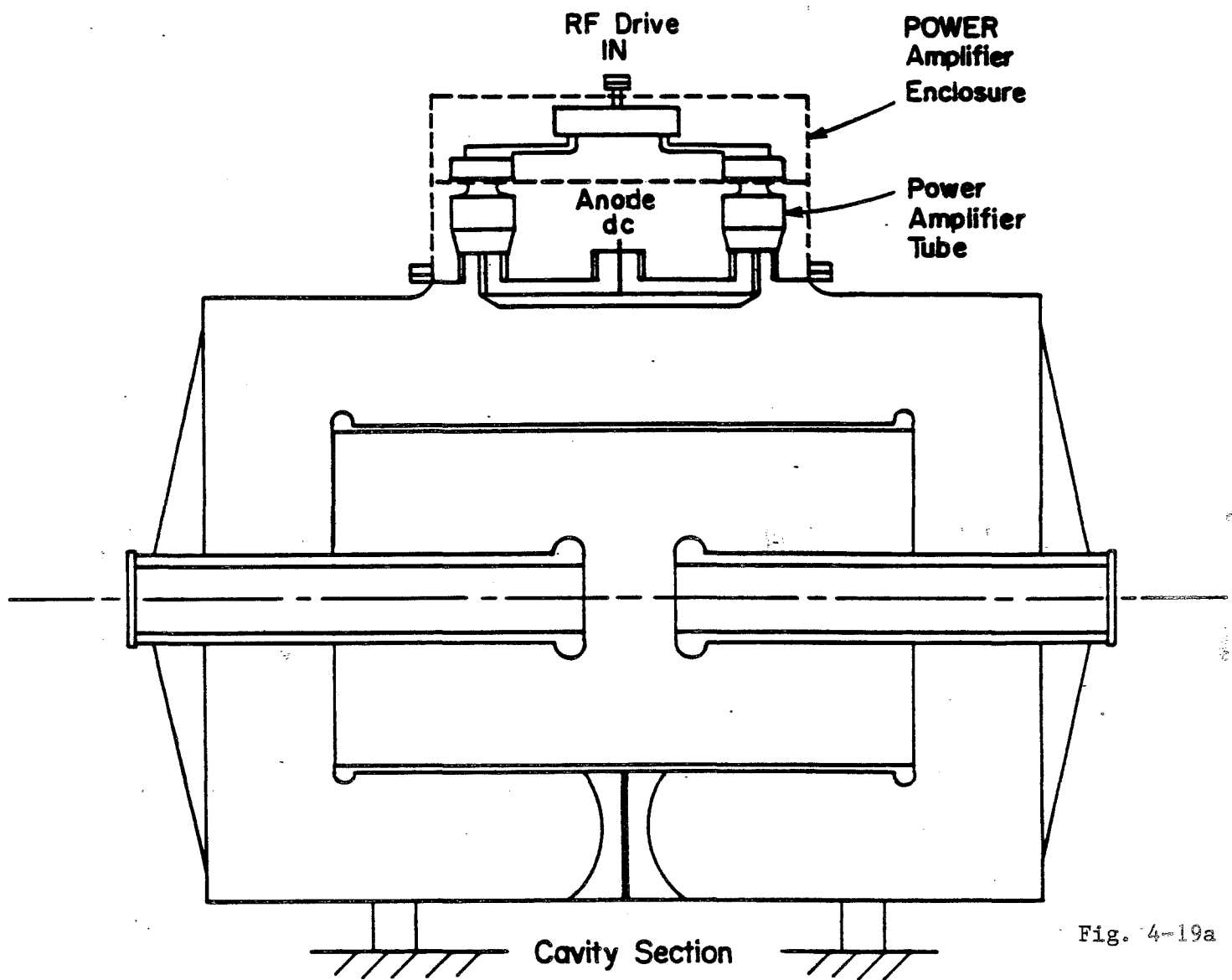
The large rf voltage, low beam loading and small duty factor favor an accelerating cavity with a very high Q, hence a high shunt impedance, which requires very little rf drive power. But the short fall time of the rf voltage pulse is not obtained easily with a high-Q structure. Moreover, the physical size of high Q structures operating in the 53-MHz region would require much larger enclosures than are under consideration.

A compromise structure, which contains an intermediate cylinder that reduces both the Q and the physical size, is shown in Figure 4-19a. Figure 4-19b shows a SUPERFISH plot of the electric fields within one-quarter of the structure. The entire volume of each cavity will be evacuated, with rf power coupled through two small ceramic windows at the top. The plate through which rf power is introduced serves as a bedplate for the high-power driver amplifiers, which are mounted directly on top of the cavity and are completely enclosed. Thus high-power rf transmission lines are not needed and rf leakage is less likely. This may be important because rf noise could adversely affect stochastic cooling. Each cavity is driven by two relatively small 10-kW triodes operating in a cathode-driven grounded-grid configuration. In this configuration, the tubes are capable of delivering very large peak rf currents during the short pulse. Because the pulse is short and the duty factor is low, the average anode dissipation is only a few hundred watts.

The rf voltage is reduced quickly by reversing the phase of the power-amplifier excitation and raising the excitation amplitude to a very high level. The high peak-power capability of the tubes is used to "drive" the cavities off, even though the cavity time-constant is longer than the required turn-off time of 50 μ sec.

The peak rf voltage which each cavity can develop has been calculated to be larger than 650 kV. Eight of these 1.8-m long cavities provide the required 5 MV. Six cavities can be installed in the downstream low-beta 16-m long insertion after the injection kicker and two more cavities can be installed in the following 4.8 m long drift.

In order to reduce the rf voltage down to 5 kV or less during the adiabatic-debunching part of the rf program, six of the cavities are turned off and two of the cavities are held at 50 kV and their relative phases



each changed by 90° in opposite directions. The resultant rf voltage gradually reaches a small value. This is done to avoid instabilities at low rf voltage that might arise from multipactoring.

In order to provide the structural rigidity necessary for complete evacuation and to reduce material costs, the cavities will be constructed from aluminum.

4.5.2 Gap-Preserving RF. Because the Debuncher circumference is larger than that of the Accumulator, antiprotons will be lost in the transfer to the Accumulator unless there is a gap in the Debuncher beam. Given the difference in circumference between the two rings and the need to allow for the fall time of the injection kicker, a gap greater than 200 nsec is needed.

An adequate gap can be created in the beam by a "barrier bucket" that excludes particles from its interior. It is created by a voltage that traces out a single complete sinusoidal oscillation for one-quarter of the rf period and then becomes zero for the remaining three-quarters of the period. A sketch of this waveform is shown in Fig. 4-20. The voltage waveform repeats itself every turn. The phase of the voltage is chosen so that it establishes an unstable fixed point between two back-to-back half-bucket separatrices. If the bucket height exceeds the beam energy spread, the beam will be forced away from the unstable fixed point by a distance determined by the ratio of the bucket height to the energy spread. The rf voltage is chosen so that the beam is excluded from a region between $\pm\pi/2$ radians in the "barrier bucket". This will create a gap of 221 nsec, as shown in Fig. 4-20. The peak amplitude required is 460 V. The Fourier series expansion of such a voltage waveform is given by

$$V(t) = 460 \frac{2h}{\pi} \sum_{n=1}^{\infty} \frac{\sin \pi n/h}{h^2 - n^2} \sin(n\omega_0 t)$$

where $\omega_0 = 2\pi f = 3.59 \times 10^6$ rad/sec and $h=4$. At frequencies above the 31st harmonic (17.7 MHz) the required amplitudes are reduced by more than three orders of magnitude. Amplifiers with a bandwidth between 0.1 and 30 MHz which are capable of delivering 300 W in a 50-ohm load are readily available. The required rf system can be broken into 150-V units, each consisting of a ceramic gap loaded with a 50-ohm resistor and surrounded by a shielding enclosure containing about ten large MnZn ferrite rings. The average power delivered to this system is very small. Since the physical size of each unit is dictated by the volume of ferrite required, each unit is 0.5 m in length.

An additional bonus associated with installation of the "barrier bucket" rf system is that it can be used in the "normal" $h=4$ mode to accelerate or decelerate 8 GeV protons across the ring aperture in tune-up testing of closed orbits and stochastic-cooling systems.

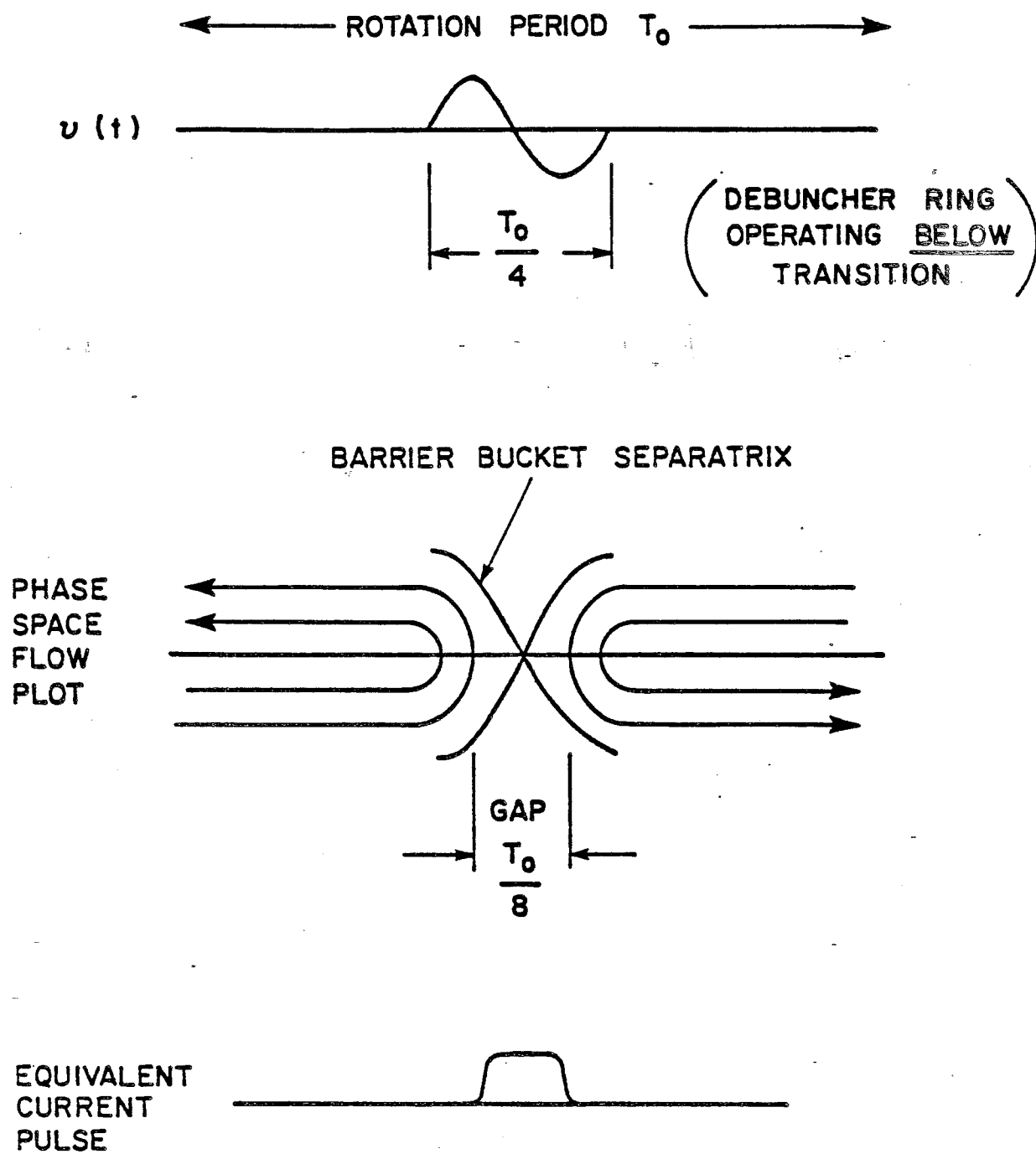


Fig. 4-20

4.6 Magnet and Power Supply Systems

The Debuncher magnet ring consists of 24 regular cells, 6 dispersion-killing units and 9 special low-beta insertions in the straight sections. There are two different-length dipoles that have the same profile. There are five different length quadrupoles, all having the same profile. All quadrupoles have the same profile as the small Accumulator quadrupole.

A beam with a 4% momentum spread and an emittance of 20π mm-mrad requires a good-field aperture of 75 mm (h) by 40 mm (v) in the dipoles and 80 mm by 50 mm in all quads. The good-field region of the dipole has been designed to be 100 mm x 60 mm. The sagitta of the beam is 22 mm and the long dipoles are therefore curved to match the orbit. The properties of these magnets are tabulated in Table 4-V.

The magnet ring is powered by five separate power supply buses, one for the dipole and one each for the regular focusing and defocusing quadrupoles. The two different kinds of triplets in the long straight sections are powered separately. The estimated power consumption of the ring is 2 MW.

Table 4-V. DEBUNCHER MAGNETS

Dipoles	Number	Arc length	Strength	Gap	Goodfield width
B	54	1.9050m	1.68T	60mm	100mm
B ₁	12	0.695323m	1.68T		

Quadrupoles

			Gradient	Poletip Radius
QF	30	.8128M	14T/m	44.5mm
QD	33	.8128	14 T/m	"
Q1	12	.7010	"	"
Q2	6	1.28778	"	"
Q3	6	0.5283	"	"
Q4(*)	6	1.0278	"	"
Q5	12	0.4572	"	"

(*) All the quadrupoles have a length and an aperture identical to the small quads for the Accumulator Ring. This magnet has a different length; identical magnets are used in beam-transport lines.

4.7 Betatron Cooling

4.7.1 Design Goal. The goal of the stochastic cooling in the Debuncher is to cool the beam emittance from 20π mm-mrad to 7π mm-mrad in both the horizontal and vertical planes. An emittance of 7π mm-mrad is the assumed beam size which can reliably be transferred into the 10π mm-mrad acceptance Accumulator ring with negligible beam loss. In addition to cooling the beam to fit into the Accumulator, it is desirable to make the beam injected into the Accumulator as small as possible. In the Accumulator the momentum stacking is done in part by a pickup that senses a particle's momentum by observing its position in a region of high dispersion. Betatron oscillations add undesired noise to this process².

4.7.2 Design Considerations. The betatron-cooling system is conceptually simple. It consists of a pickup that senses the positions and therefore the betatron amplitudes of the particles. The signal is amplified and applied to a kicker an odd multiple of 90° away in betatron phase. At the kicker, the position displacement that was sensed has been converted into an angular displacement. This angular displacement is decreased by a correcting kick, which thus decreases the betatron amplitude. As is well known, the cooling of a single particle is hampered by the presence of the other particles, which appear as a noise signal which heats the particle. For a properly designed system, the net effect over many turns is that cooling is achieved.

The process of betatron cooling is conventionally described by the equation³

$$\frac{dA}{dt} = -\frac{W}{2N}(2g-g^2(M+U))A, \quad (4.1)$$

where A is the betatron amplitude, W the amplifier bandwidth, N the number of particles, g the system gain, M the mixing factor and U the ratio of noise to signal power. The mixing factor M is given by

$$M = \frac{f^2 \psi(>)\Lambda}{2WN}, \quad (4.2)$$

where $\psi(f)$ is the density of particles (number per Hz), f is the revolution frequency, f_0 is the revolution frequency (0.578 MHz) of the central momentum, and Λ is a constant of order unity ($\Lambda=\ln 2$ if the gain is independent of frequency).

Stochastic cooling during the 2-sec Debuncher cycle is difficult for several reasons. The first reason is that the mixing factor M is large compared to 1. M is inversely proportional to η , where

$$\frac{\Delta f}{f} = \eta \frac{\Delta p}{p}, \quad (4.3)$$

The choice of the value of η was a compromise between the rf requirement for the bunch rotation (which favors a small η) and stochastic cooling (which favors a large η). The choice of $\eta = -0.0047$ leads to a mixing factor M of about 10 for the particles near the central momentum of the Debuncher, assuming a Debuncher momentum distribution which is parabolic with a full width of $\Delta p/p = 0.3\%$.

A second problem is that the noise-to-signal ratio U tends to be large. The techniques to make U small are: 1) increase the beam signal as much as possible by using a large number of high-impedance pickups and 2) decrease the noise temperature by cooling the pickup terminating resistors and the preamplifiers. The pickup system has been assumed to be loop couplers as described in 5.4.1. The parameters of the pickup and preamplifier system are given in Table 4-VI.

Table 4-VI. BETATRON COOLING SYSTEM PARAMETERS

Pickup Characteristic Impedance (Z_0)	75 Ω
Sensitivity (or coupling factor) (L_D)	1.6
Number of Pickups n_p	192

Maximum β at pickup β	10 m
Terminating resistor temperature θ_R	80K
Amplifier equivalent noise temperature θ_A	80K

A technical problem⁴ occurs when one tries to use a large number of pickups in a region of low β . The betatron phase advance becomes appreciable over the pickup array and there is a partial cancellation of signal. For example, in a straight section 10 m long with a minimum beta at the center of 5 m, a pickup array centered in the straight section would give the best signal-to-noise ratio if the array length were limited to 8 m. At this length, the effectiveness of the array is 0.85 of what it would be if the betatron oscillation could be turned off. For this reason, both pickups and kickers have been divided into two sections 180° apart in betatron oscillation. With this division, the betatron oscillation dilutes the sensitivity by 0.05. This effect has already been taken into account in the sensitivity factor quoted in Table 4-VI.

The criterion for the thermal noise to be negligible is $U \ll M$. With the parameters of Table 4-VI,

$$U = \frac{2K_{\beta}(\theta_R + \theta_A)h^2}{d^2 Z_0 e^2 f_0 n_p N \beta_p \bar{\epsilon}} \quad (4.4)$$

$$= 1.2 \text{ (initially)}$$

where $K_{\beta} = 1.38 \times 10^{-23}$ joules/°K, $f_0 = 1/T$ = revolution frequency, $\bar{\epsilon}$ = average beam size = 8π mm-mrad initially. However, as the beam is cooled to $\bar{\epsilon} = 0.8\pi$ mm-mrad, U will grow to 12, the same value as M , the mixing factor. Thus cooling will initially proceed not limited by thermal noise, but as the beam cools, the effect of the Schottky and thermal noise become comparable (note that the cooling equation (4.1) is written in a deceptive form because it does not explicitly show the dependence of U on $\bar{\epsilon}$).

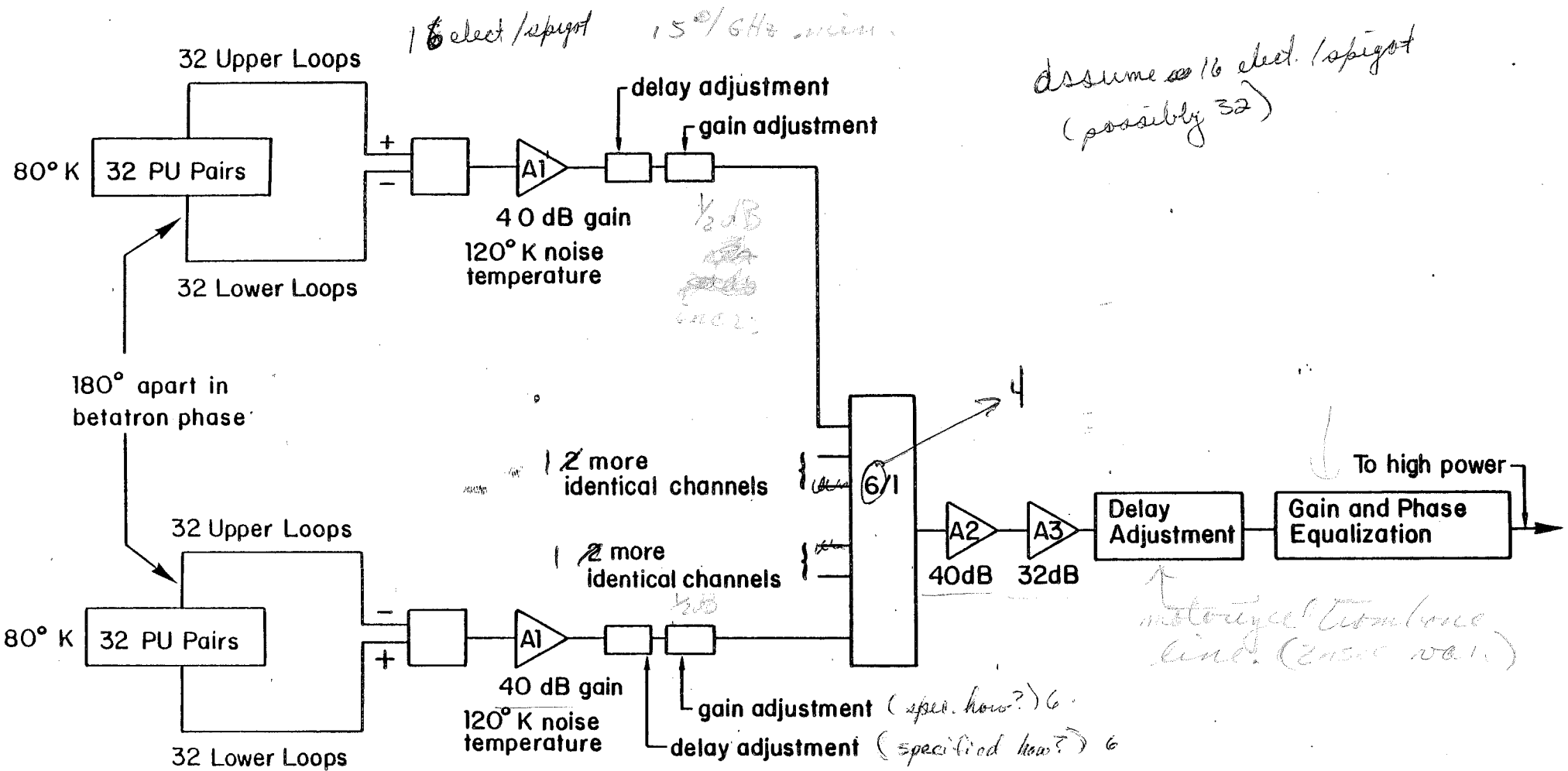
A practical problem that occurs in fast stochastic cooling is that the power requirements are often very high. In the Debuncher, the best cooling rate is obtained for a power level of 1700W. However, as can be seen from Eq. (4.1), the gain can be decreased by a factor of 2 and the cooling rate will be only $2g - g^2 = 3/4$ of the optimum rate. In the absence suppression, the power will decrease by a factor of 4. In the case that signal suppression is important, the decrease in power can be even greater because the system gain g increases more slowly than linearly with the amplifier gain. In a system with bad mixing like the Debuncher, most of the thermal power is between Schottky bands and is largely unaffected by signal suppression. In this case, the thermal power is therefore more nearly proportional to amplifier gain squared than to system gain squared (g^2).

4.7.3 Hardware. A block diagram of the betatron cooling system is shown in Fig. 4-21(a-b). In brief, the pickup signal from 32 upper plate pickups is combined with 32 lower plate signals to provide a difference signal proportional to the position displacement of the beam. The signals from each set of 32 pickups amplified 40 dB are combined in an 6-fold combiner. Each combiner input has an adjustment for amplitude and delay. After combination the signal is further amplified by 72 dB to a level of about 25 dBm. An overall delay adjustment is followed by a gain and phase compensating circuit, to partially cancel the variations in the TWT (traveling wave tube) gain characteristics. The power is then split to drive two sets of TWT's, each of which drives an array of 96 kickers. The hardware components are described in more detail in Section 5.4.

4.7.4 Computer Simulation⁵. A simulation of the betatron cooling in the Debuncher was made to calculate the expected system performance. Included in the simulation were the pickup and kicker response functions, transit-time differences of the electrical signal and particles between pickup and kicker, and signal suppression. The amplifier was modeled as a physically unrealizable ideal amplifier having a gain g_A from 2 to 4 GHz and zero elsewhere. It was assumed that g_A was purely real. While the amplifier model was not realistic, measurements of the TWT tube amplifiers in the 1-2 GHz range show that, when externally phase compensated, these tubes can provide gain and phase characteristics that lead to cooling rates equal to or better than the 1-2 GHz "ideal" amplifier. The initial \bar{p} distribution was taken from Fig. 3-4. It was assumed that the Debuncher had an emittance of 25π mm-mrad but that the transport line had already limited the beam size to 20π mm-mrad. The total output power was limited to 500W. The gain was continually adjusted to provide the best cooling within the 500W limit.

Figure 4-22 shows the initial and final beam distributions for particles at the central momentum. Ninety-nine per cent of the particles fall within an emittance of 7π mm-mrad. Also shown is the final curve for particles with a momentum offset of 0.075%, or halfway to the edge of the distribution. The cooling of these particles is somewhat better since they have a somewhat lower density, i.e., less Schottky noise. Since the noise figure assumed is somewhat speculative, Fig. 4-23 compares the final spectrum for design case $\theta_A = \theta_P = 100^\circ\text{K}$ and noise figures 2x and 3x worse. If the noise figures were worse because of the pickup sensitivity being less than supposed, the kickers would presumably be less sensitive in the same ratio. In this case, the total dissipated power would be larger than the design case of 500W. Figure 4-24 is a comparison of the final distribution for different power levels assuming the design case noise figure ($\theta_A = \theta_P = 80^\circ\text{K}$). As previously stated there is little advantage in running at power levels corresponding to the optimum gain.

The stochastic cooling system for the debuncher as designed will cool the beam emittance by about an order of magnitude. If the system fails to perform as designed, there is a substantial margin of safety in getting the beam to 7π mm-mrad for transfer into the accumulator.



128 PU (not 192)
Debuncher Betatron Cooling Systems

2-4 GHz Horizontal and Vertical Systems are Identical.

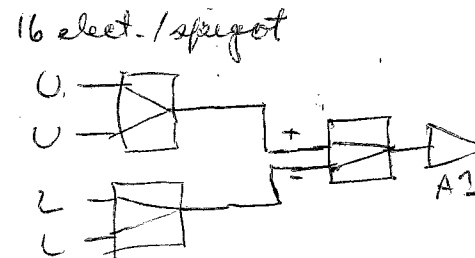
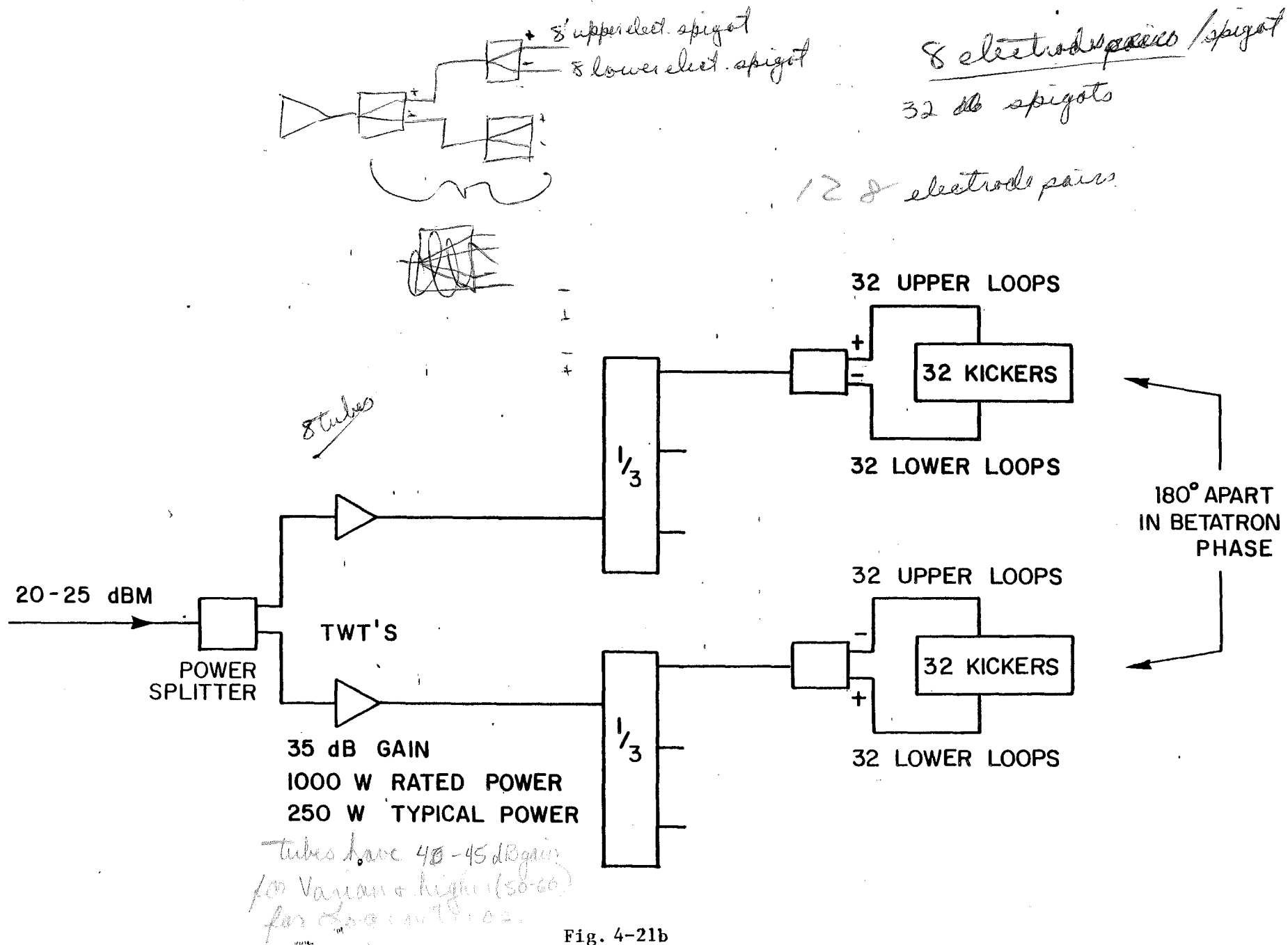


Fig. 4-21a

- for lower betatron phase



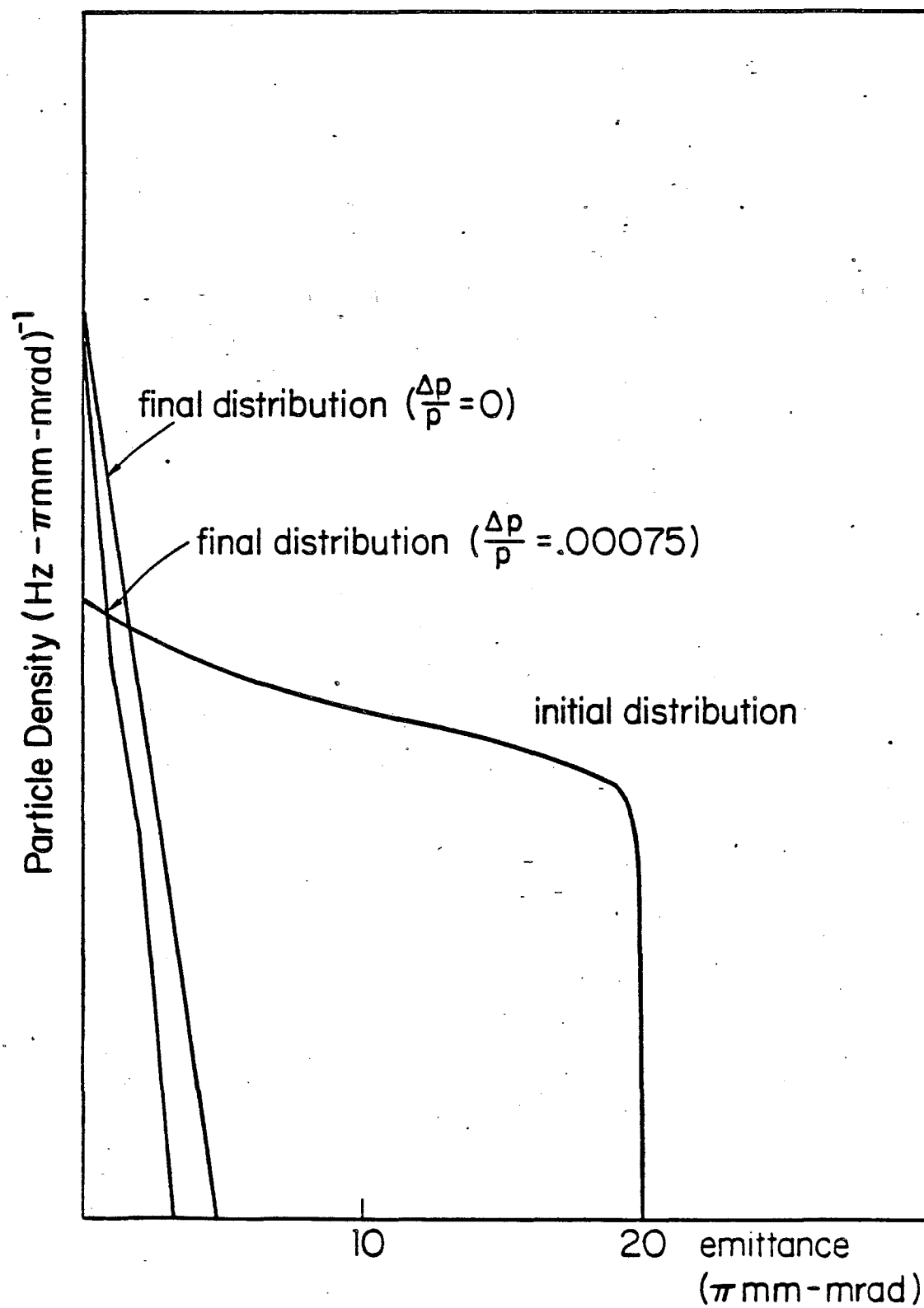


Fig. 4-22

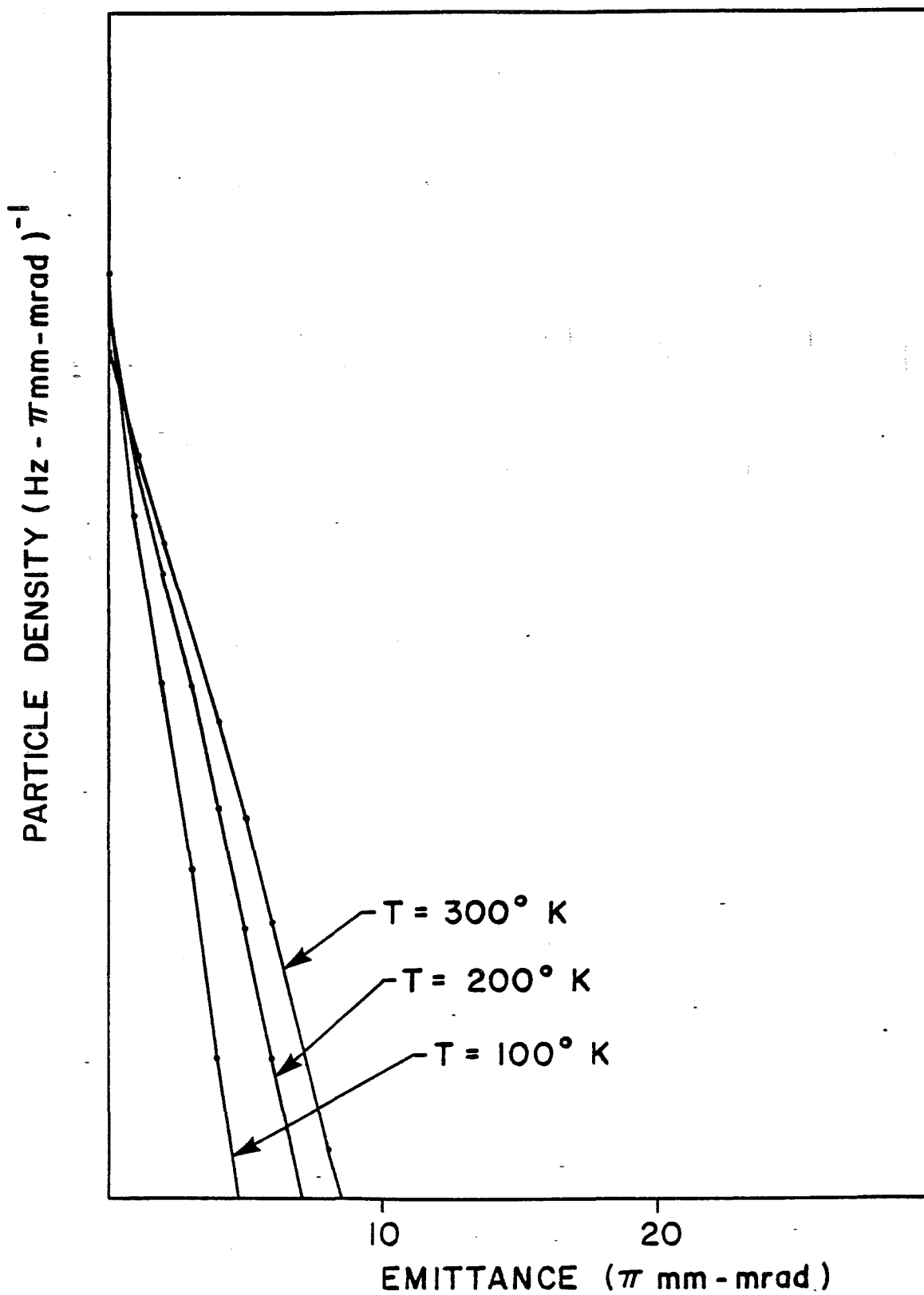


Fig. 4-23

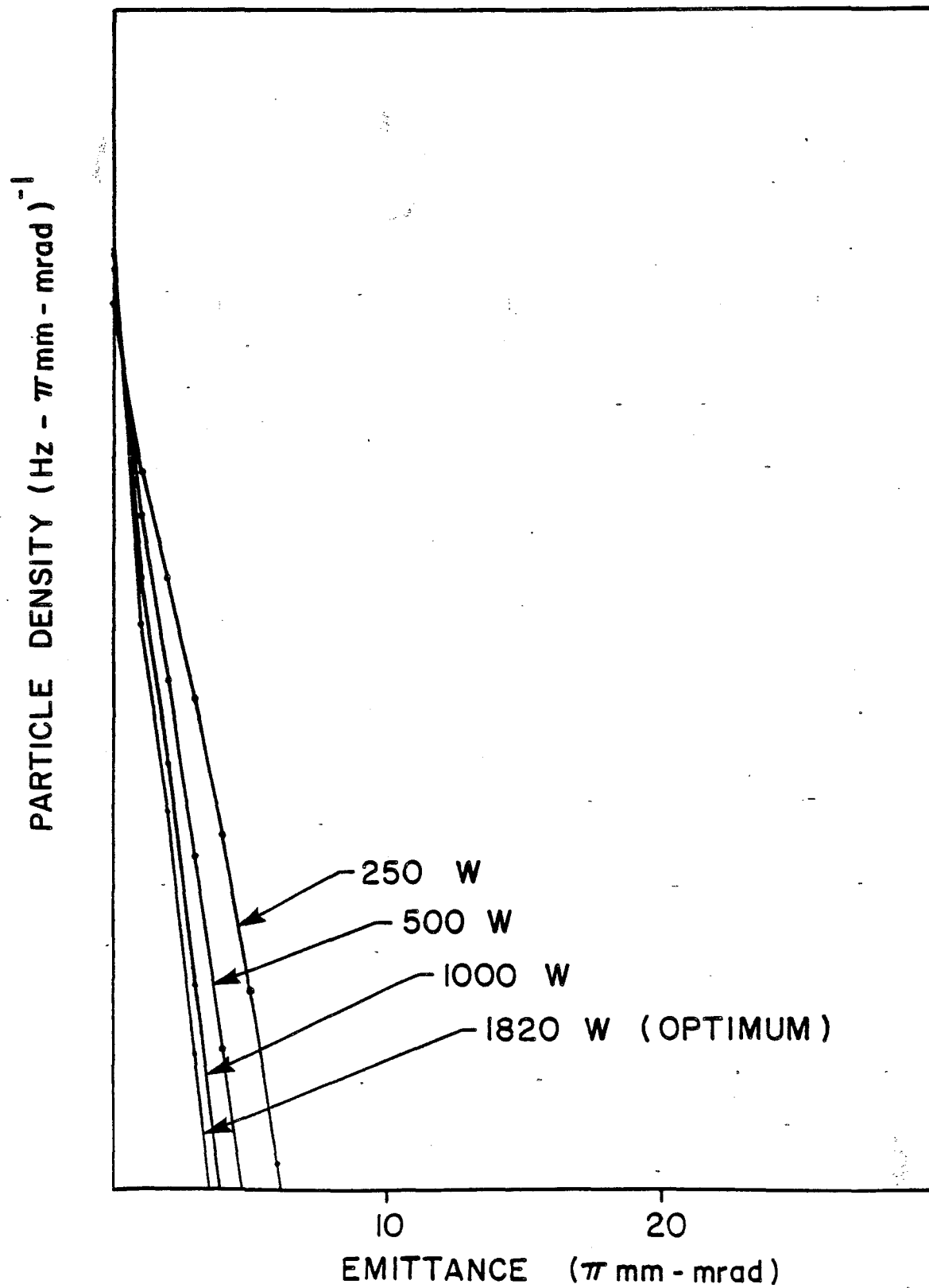


Fig. 4-24

4.7.5 Effect of the gap on betatron cooling. The effect of the "barrier bucket" on stochastic cooling has been considered. Recall that the "barrier bucket" establishes a gap in an otherwise-continuous debunched beam. The process of creating this bucket adiabatically after betatron cooling, is time consuming, it is planned to turn the barrier bucket on as soon as the debunching is completed. This raises the question of the effect that such a gap has on the betatron cooling. Excitation of a beam pickup by the gap in the beam is equivalent to excitation by a single bunch in the ring with a current distribution equivalent to the missing current in the gap, as shown in Fig. 4-20. If the current is described by a \cos^2 dependence where it is changing and if the gap length is related to the total bucket length by a factor k , then the Fourier series representing the current distribution is

$$i(t) = i_{dc} \left[1 + \frac{2h}{(k+1)\pi} \sum_{n=1}^{\infty} \frac{(\sin nk\pi/h + \sin n\pi/h)}{n(1-(1-k)^2(n/h)^2)} \cos n\omega_0 t \right]$$

For $h=4$, $k=0.5$, and $\omega_0=3.5 \times 10^6$, the maximum amplitude of signals in the region of 1 GHz ($n \approx 1800$) is about $2 \times 10^{-8} i_{dc}$, which is much smaller than the thermal noise.

References

1. A. Ando and K. Takayama, FNAL TM-1073 or \bar{p} Note 173 (1981).
2. J. Simpson, \bar{p} Note 207 (1982).
3. D. Mohl, G. Petrucci, L. Thorndahl, and S. van der Meer, Physics Reports C, 58, 73-119 (1980).
4. J. Marriner, \bar{p} Note 234 (1982); Fermilab.
5. J. Marriner, \bar{p} Note 229 (1982), Fermilab.

5. ACCUMULATOR RING

5.1 Accumulator - Functional Summary

The first function of the Accumulator is to accept a pulse of \bar{p} 's every 2 seconds. In order to make room for this pulse, the \bar{p} 's must be compressed (cooled) into a smaller area of phase space. A technique to accomplish the continuous \bar{p} accumulation and compression has been developed at CERN and is the basis of this design. The technique consists of establishing a stack of \bar{p} 's with an energy density that rises approximately exponentially from the injection density (the low-density end is referred to as the "stack tail") and then culminates in a roughly Gaussian high-density region (the "core"). The density profile of the proposed system is shown in Fig. 5-1. Betatron amplitudes are also cooled during the stacking process. The design criteria for the accumulation process are given in Table 5-I.

Table 5-I. ANTIPROTON STACK PARAMETERS

Injected Pulse

Number of \bar{p} 's	7×10^7
$\Delta p/p$	0.2%
Horizontal and vertical emittance	10π mm-mrad
Time between injections	2 sec
Fraction of beam accepted	~85% of injected pulse
Flux	3×10^7 \bar{p} /sec

Final Stack

Number of \bar{p} 's	4.3×10^{11}
$\Delta p/p$	0.1%
Horizontal and vertical emittance	2π mm-mrad
Peak density	1×10^5 eV ⁻¹
Core width (Gaussian part)	1.7 MeV (rms)
Total stacking time	4 hours

5.2 Momentum Cooling

5.2.1 Introduction to Stochastic Stacking The stochastic stacking system consists of pickup electrodes, an amplifier system with electronic filters and phase-compensation networks, and kicker electrodes. Each particle produces an electronic signal that, when applied to the kicker, changes its momentum in the direction of the core. The signal of each given particle thus produces a kick that tends to cool the beam into a small momentum width around the core. Other particles in the beam with

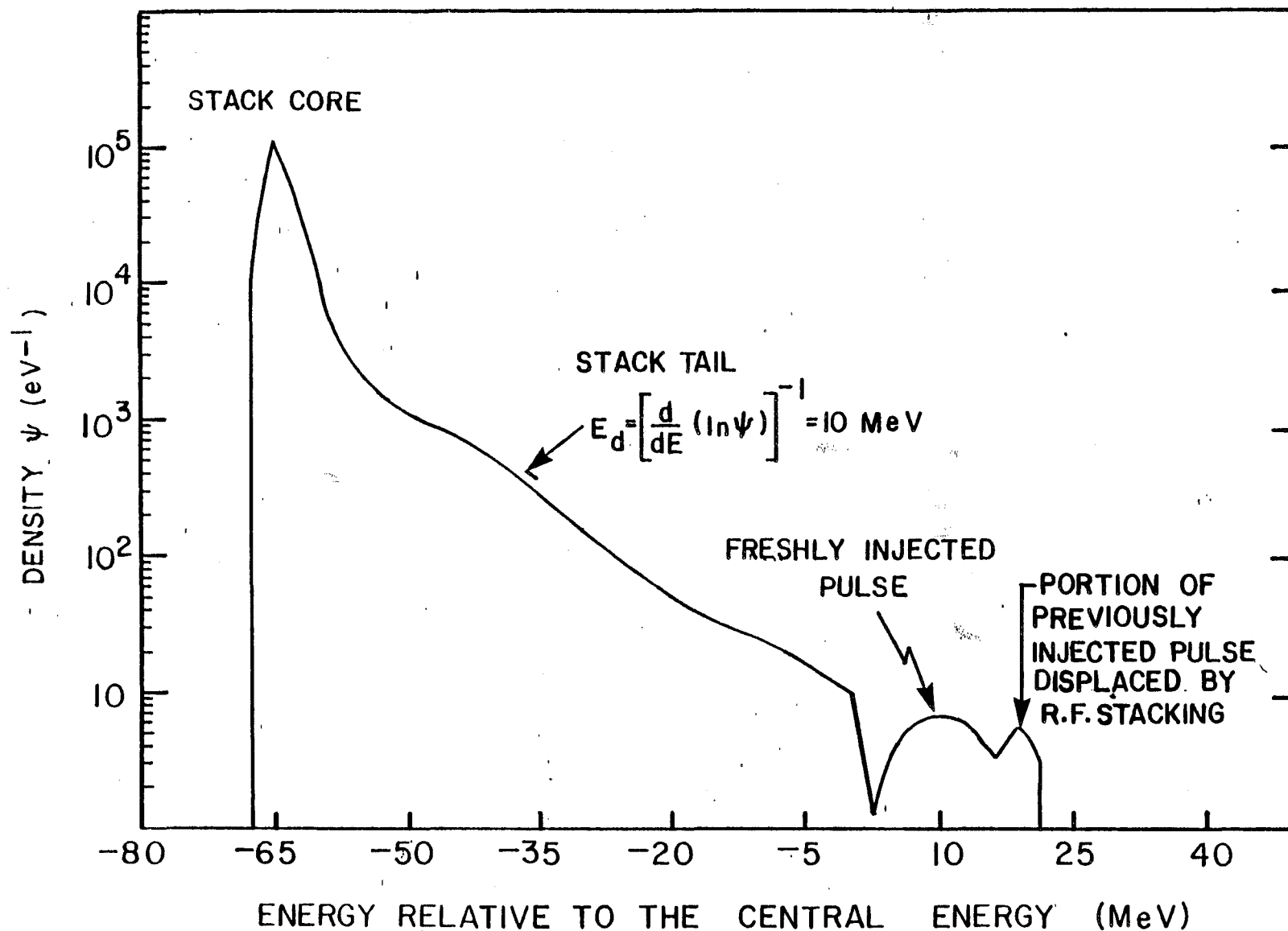


Fig. 5-1

approximately the same revolution frequency produce random kicks on the given particles and cause diffusion or heating. The interesting systems, of course, are those in which cooling dominates over heating.

Momentum cooling is usually described in terms of the Fokker-Planck equation

$$\frac{\partial \psi}{\partial t} = - \frac{\partial}{\partial E} \left[-F\psi + (D_0 + D_1 + D_2\psi) \frac{\partial \psi}{\partial E} \right]$$

where $\psi = \partial N / \partial E$ is the particle density, F is the coefficient of the cooling term, D_0 is the coefficient of the heating term due to intrabeam scattering (described later), D_1 is the coefficient of the heating term due to thermal noise, and D_2 is the coefficient of the heating due to other particles. A derivation and discussion of this equation are given by Mohl et al.¹

A simplified version of the Fokker-Planck equation has been used by van der Meer² to describe the stacking process. It is assumed that the voltage on the kicker is exactly in phase with the particles that created it, that there is no amplifier thermal noise or intrabeam scattering, the feedback gain is independent of harmonic number, and that there are no beam-feedback effects. A more general approach, including thermal noise, is possible.³ While none of these assumptions is justified in the proposed system, the simplified discussion yields semi-quantitative results that can form the basis of a design.³ Following van der Meer, the flux can be written as

$$\dot{\Phi} = - \frac{V}{T} \psi - AV^2 \psi \frac{\partial \psi}{\partial E},$$

cooling heating
term term

where $N(E, t)$ is the number of particles with energy less than E and

$$\Phi = \frac{\partial N}{\partial t}$$

$$\psi = \frac{\partial N}{\partial E} ,$$

from which the Fokker-Planck equation

$$\frac{\partial \psi}{\partial t} = \frac{\partial \Phi}{\partial E}$$

follows. Here $V = V(E)$ is the average energy loss per turn and T is the revolution period. The constant A describes the strength of the heating term and is given by

$$A = \frac{\beta p \Lambda}{4T^3 W^2 |\eta|} ,$$

where $\beta = v/c$, p is the momentum, T is the revolution period, W is the bandwidth $= f_{\max} - f_{\min}$, $\Lambda = \ln(f_{\max}/f_{\min})$, and $\eta = \gamma_t^{-2} - \gamma^{-2}$. If the amplifier gain is not independent of frequency, Λ is modified. The ideal gain profile, in fact, rises linearly with frequency, but the exact value of Λ is not important for this discussion.

The Fokker-Planck equation is nonlinear in ψ and it is therefore usually solved numerically. Stationary solutions, $\Phi(E,t) = \Phi_0 = \text{constant}$, can often be found by elementary methods. These solutions are useful because in the stack tail between the core region and the injection region, the actual time-dependent solution is normally very close to the steady-state solution.

Consider $\Phi_0 = \text{constant}$ and $\Psi(E,t) = \Psi(E)$, and ask what the shape of the voltage profile $V(E)$ should be. The answer, as given by van der Meer, is to maximize $d\psi/dE$ everywhere and thus minimize the energy aperture which is required. This choice also minimizes the total Schottky power in the amplifier. The solution is

$$V(E) = - \frac{2\Phi_0 T}{\Psi(E)} = - \frac{2\Phi_0 T}{\Psi_1} e^{-(E_1 - E)/E_d}$$

where Ψ_1 is the initial stack-tail density at E_1 and E_d is the characteristic energy

$$E_d = -4A\Phi_0 T^2 = - \frac{8p\Lambda\Phi_0}{TW^2|\eta|}$$

This equation exhibits the major design consideration. We know that $d\psi/dE$ is maximized by a gain profile $V(E)$ that is exponential in energy. The exponential slope $d\psi/dE$ is maximized by minimizing E_d . In the stack tail, we want a density increase of 1000, so we require a minimum momentum aperture of $\Delta p/p = \ln(1000) E_d/p = 6.91 E_d/p$. If we want to limit the aperture ($\Delta p/p$) required for the stack tail to 0.75%, then $E_d < 0.001 p \approx 10$ MeV for $p = 8.9$ GeV/c. Since we want to have Φ_0 as large as possible, we must make E_d small by choosing $TW^2|\eta|$ to be as large as possible.

We have chosen to work with a maximum frequency of 4 GHz for the purposes of this report, but we intend to use frequencies up to 8 GHz for core cooling if our research program indicates that 8 GHz cooling systems are practical. The stack-tail system was chosen to have a maximum frequency of 2 GHz. As described below, the choice of frequency dictates the choice of η . By limiting the stack-tail system to 2 GHz, we are able to use a relatively high η ($\eta = 0.02$). The high value of η is useful for the core-cooling systems, where the core cooling times are inversely proportional to η .

The maximum value of η is limited once we choose f_{\max} . For a number of reasons, it is required that $\eta(\Delta p/p) f_{\max} T < \delta$, where δ is some number of order unity. The reasons that determine the value of δ are:

- (i) The Schottky bands must not overlap in a system that uses electronic filters for gain shaping. In such a system, the particle energy is sensed in the electronics by the connection between energy and the harmonics of the revolution frequency. If the relationship is not unique, it is difficult and probably impossible to design appropriate filters. In this case, $\delta = 1$ and $\Delta p/p = 1\%$ so $\eta < 0.03$ with $T = 1.6$ μ sec.
- (ii) The phase shift between PU and kicker must not vary across the momentum band more than about $\pm 45^\circ$. If PU and kicker are exactly opposite in the Accumulator Ring, then $\delta = 0.5$. If the stack-tail system is divided into subsystems with $\Delta p/p = 1/3\%$, then this constraint applies to each system individually, so $\eta < 0.05$.

- (iii) For reasons described below, the filters must have the peak of their response at the tail end and a notch in the core. Between Schottky bands, of course, the response must rise from the notch in the core back to the peak value. Since the rise back to the peak value cannot be done infinitely sharply, at least without undesirable phase characteristics, this requirement is more severe than 1) above. We have found that $\eta = 0.02$ is a suitable value for a maximum frequency of 2 GHz.

We have chosen a Booster-sized ring ($T = 1.6 \mu\text{sec}$) because it is large enough to accommodate the cooling-system hardware and can run at 8 GeV, a good energy for production of p' 's and their injection into the Main Ring.

5.2.2 Summary of Design Considerations. We have chosen $E_d = 0.001p = 10$ MeV to keep the required momentum aperture sufficiently small. The product $Tf_{\max}\eta$ is fixed by the requirement of a minimum spacing between Schottky bands. We have chosen $W = 1$ GHz with $f_{\max} = 2$ GHz to yield a somewhat higher value of η (0.02) than would be the case if we chose a higher frequency. Higher frequencies also have the disadvantage that it is somewhat more difficult to build the quality of hardware that is required.

5.2.3 Building the Exponential Gain Profile. Once the parameters of the stack tail have been chosen, the next step is to build the required gain profile. We use a combination of two techniques. The first technique is to sense the particle momentum by sensing its position in a region of high momentum dispersion. The position sensitivity of the strip-line pickups we plan to use is given in Section 5.4.1. For large horizontal displacement x the sensitivity of these pickups becomes

$$s(x,0) \propto e^{-\pi x/h}$$

where h is the gap between plates. In our case, the momentum dispersion is $\alpha_p = 9$ m and we have chosen $h = 3$ cm. Thus for large ΔE ,

$$V(E) \propto e^{-|\Delta E|/E^*},$$

$$\text{where } E^* \sim \frac{\beta^2 E h}{\pi \alpha_p}$$

where $V(E)$ is the average (coherent) particle voltage gain per second ΔE is the difference between energy E and the energy where the pickup response is centered, and $E^* = 10$ MeV. In our system we use the pickups in the region where the falloff is not truly exponential, but the system can be characterized roughly by an E^* for the pickup response of approximately 15 MeV.

The second method of gain shaping is with filters. However, the main purpose of the filters is to reduce the thermal noise in the core. In order to maintain a flux of 3×10^7 into the stack tail, an amplifier system with very high gain (150dB) is required. Even with preamplifiers with low noise temperatures (80°K), the thermal noise produces an rms voltage of approximately 1500 V/turn. This noise voltage is (perhaps surprisingly) tolerable in the tail where the average (cooling) voltage gain is about 10 V/turn. In the core region, where the cooling voltage is a few mV/turn, this noise voltage must be reduced to a tolerable level. The filter does this by making a notch at all harmonics of the revolution frequency of the particles in the core. The filter also does some gain shaping in the tail region. The filters used are composed of a series of notch filters similar in concept to those used at CERN. A schematic diagram of the individual component filters is given in Fig. 5-2. The response of these filters is given by

$$\frac{V_{out}}{V_{in}} = (e^{-\gamma_1 l_1} - \xi e^{-\gamma_2 l_2})/2,$$

where γ_1 , γ_2 and l_1 , l_2 are the propagation constants and lengths of the cables and ξ is a variable attenuation of order unity. To get a clearer picture of the operation of this filter, consider the approximation $\xi = 1$, $l_1 = 0$, $\gamma_2 = \omega T_c / l_2$, where ω is the applied frequency and T_c the electrical length of the cable. In this case,

$$\left| \frac{V_{out}}{V_{in}} \right|^2 = (1 - \cos \omega T_c)/2$$

and the phase changes linearly with frequency except at the transmission zero, where it takes a discontinuous jump of 180°.

It is probably worth mentioning that the absence of amplifier noise would not necessarily eliminate the need for filters. Nonlinearities in the pickups, amplifiers and other components cause frequency mixing, as is well known to r.f. engineers. The input power at frequencies corresponding to the stack tail, where the power density is high, will mix in a nonlinear device and produce output power at frequencies corresponding to the core where the power density must be low. The filters suppress the most dangerous part of the unwanted distortion because of the notch at the frequency of the core particles. (These particles are cooled by a separate system without filters, as will be described later.) It will be advantageous to place some of the filtering after the final amplifier to reduce the sensitivity to the nonlinear distortions from that source.

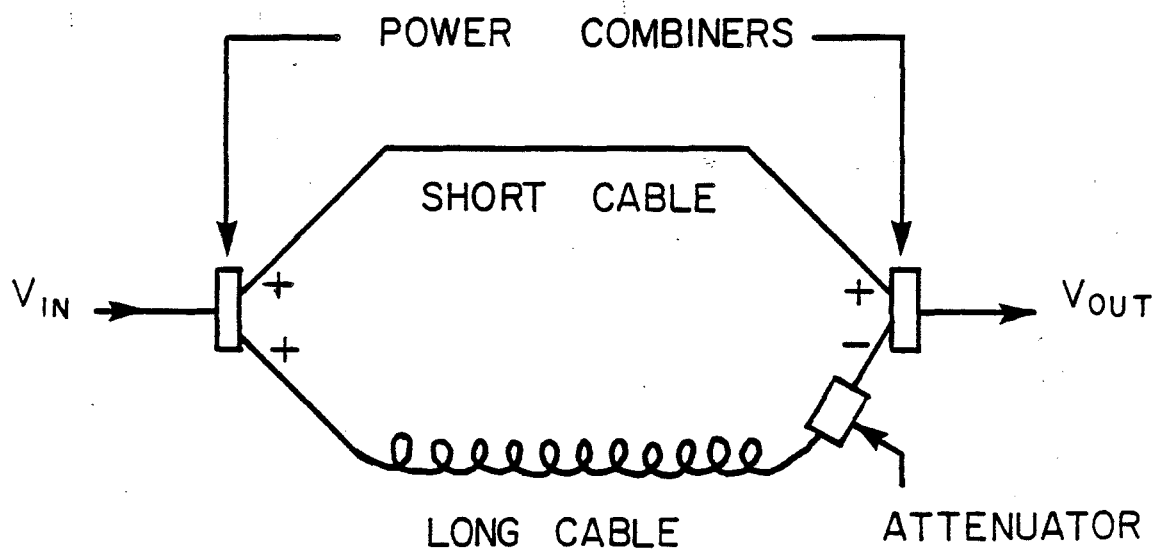


Fig. 5-2

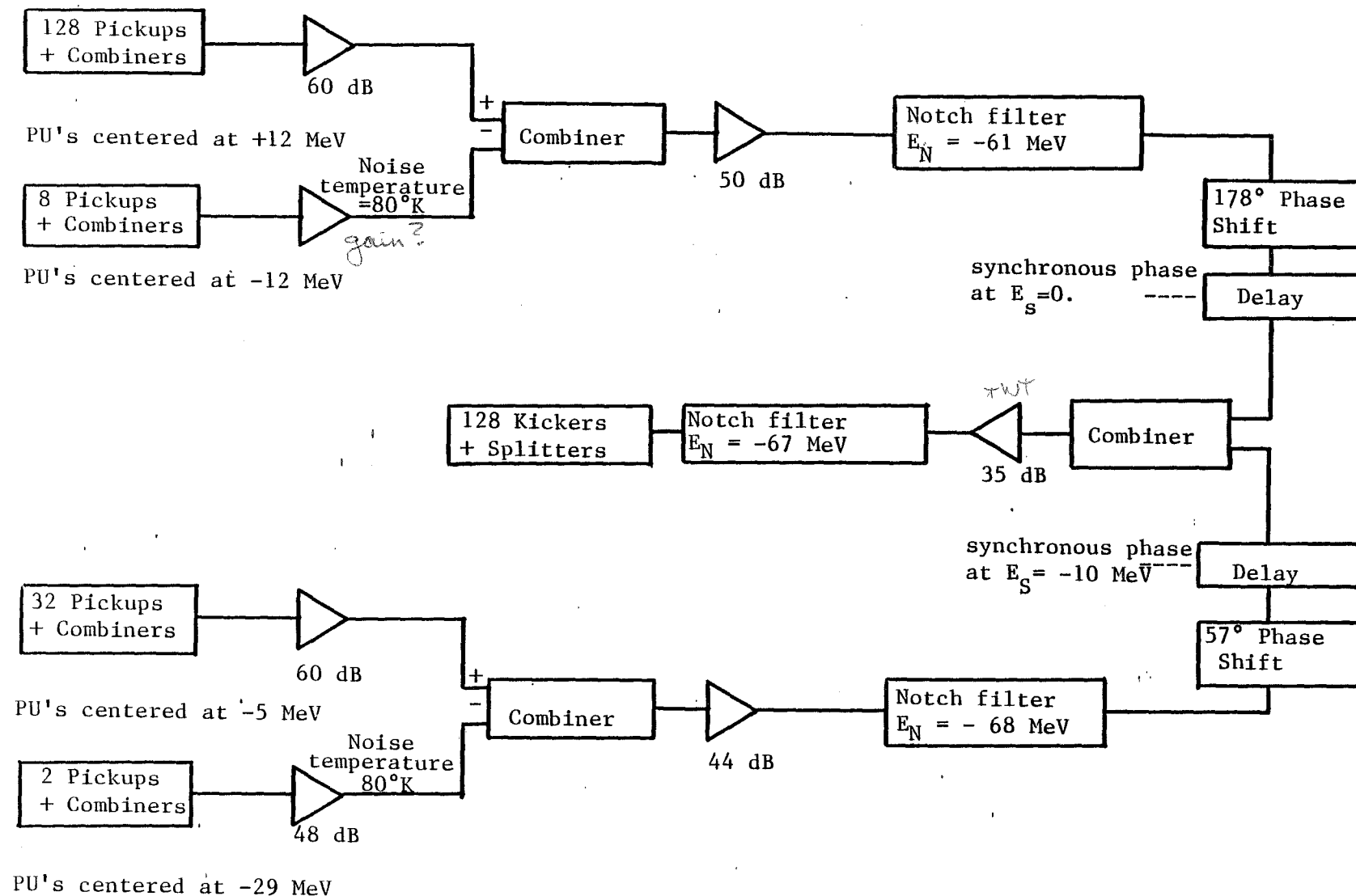
The shape of the gain curve at the injection end is purposely different than the ideal exponential curve, becoming flat in the injection region because of several practical considerations:

- (i) It is desirable to keep the electronic gain between Schottky bands as low as possible. The gain between Schottky bands does not affect the cooling process, but the thermal power between Schottky bands is significant.
- (ii) To maximize the ratio of Schottky signal to thermal noise, it is desirable to place the pickups so they have maximum sensitivity to the freshly injected beam, i.e., so they operate in the non-exponential region.
- (iii) The exponential gain profile minimizes Schottky power only in the approximation that beam is injected in a steady state manner. In fact, each newly injected pulse substantially alters this picture since the density of particles will differ by factors of 2 or 3 from the steady state situation. By making the gain profile flatter in the injection region, we can reduce the required Schottky power immediately after a new pulse is injected.

The stack-tail system we have designed consists of two sections of pickups and associated amplifiers and filters. The two sections make it possible to control undesirable phase shifts and thermal noise in the tail. A block diagram of the system is shown in Fig. 5-3. The number of pickups was chosen to be as large as possible to minimize the thermal-noise to Schottky-signal ratio and to minimize the total thermal power. In order to keep the betatron oscillations from substantially affecting the momentum cooling, the betatron amplitudes must be limited. To achieve the desired gain profile, the pickups have a plate separation of 3 cm. Calculations indicate that the beam size should be less than 2.4 cm to avoid trouble with betatron motion. For an emittance of 10π mm-mrad, the β function at the pickup must be 15 m or less. This requirement limits the pickup straight section to 15 m in length and a total of 200 pickups. The function of the subtracting pickups is discussed in the next section. The number of kickers was chosen to fill the straight section across from the pickups to minimize total power (inversely proportional to the number of kickers). The gain profile achieved with this system is shown in Fig. 5-4 abc for the Schottky bands at 1.1, 1.5 and 1.9 GHz.

5.2.4 Signal Suppression and Stability. An important aspect of the cooling process, when using high-gain cooling systems, is signal feedback via the beam. A signal of frequency ω will modulate the beam at frequency ω , and this modulation will be sensed at the pickup. Thus the cooling system forms a closed-loop feedback system. This feedback system is analogous to amplifier systems with conventional electronic feedback. An expression for the beam feedback has been given by van der Meer⁵ and independently by Ruggiero.⁶ An approximate expression is

STACK TAIL MOMENTUM COOLING SYSTEM 1-2 GHz



ENERGIES ARE GIVEN RELATIVE TO THE CENTRAL ENERGY

Fig. 5-3

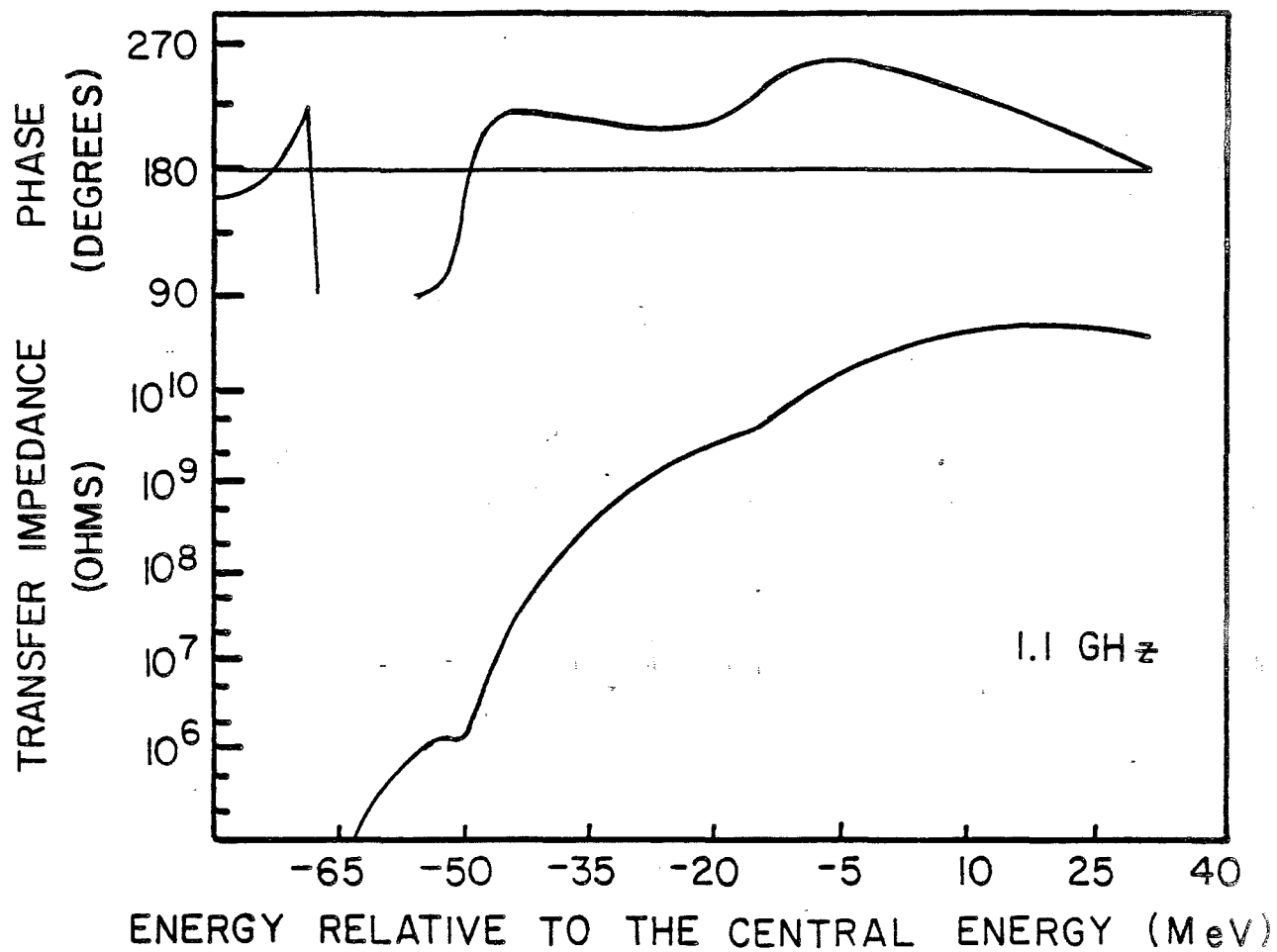


Fig. 5-4a

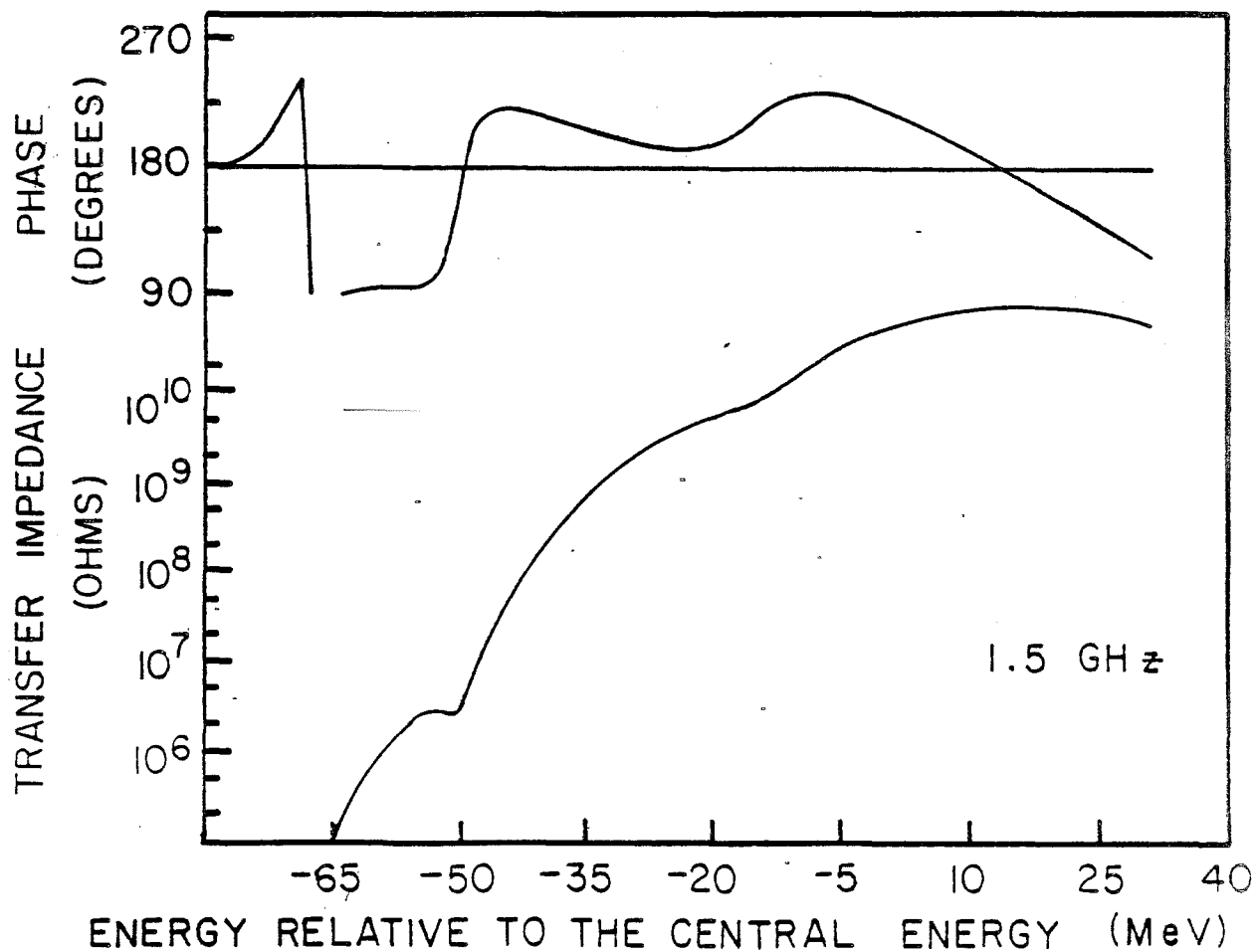


Fig. 5-4b

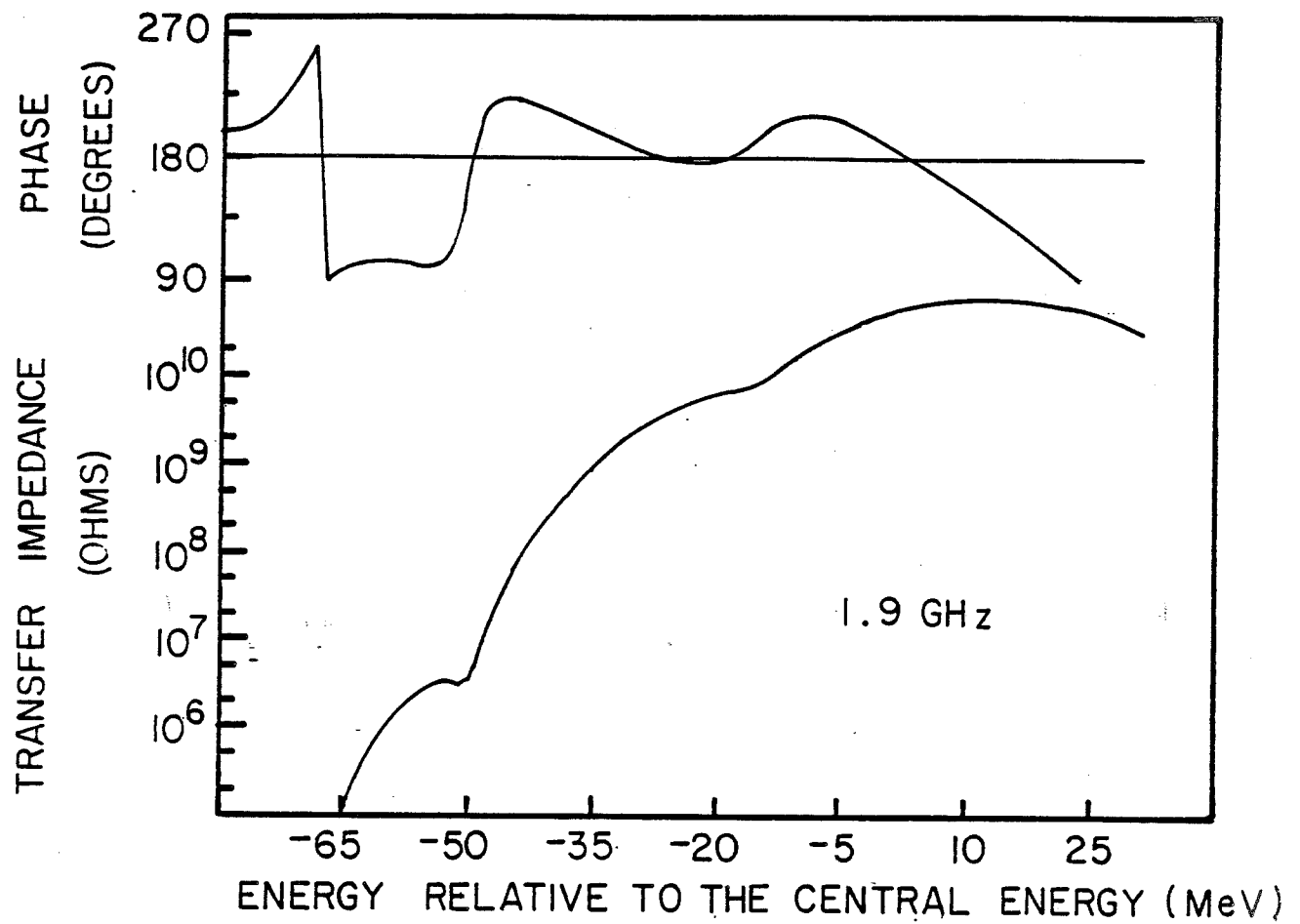


Fig. 5-4c

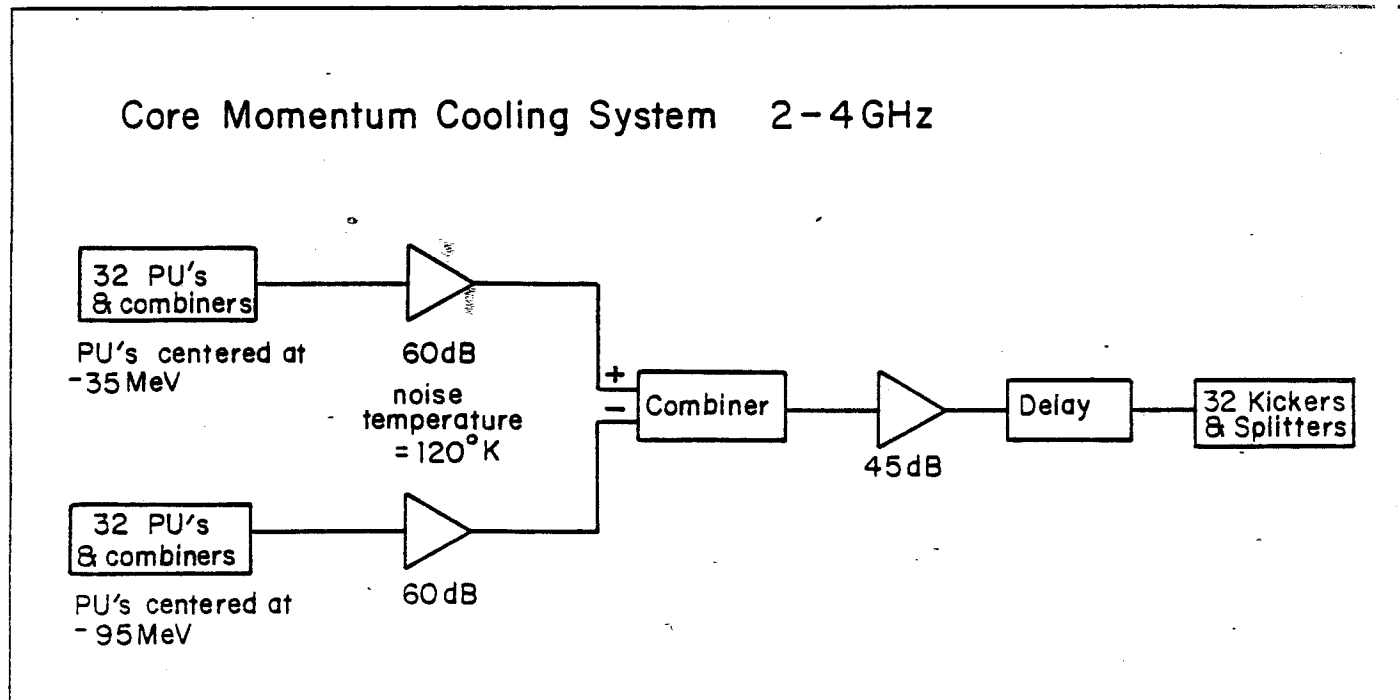


Fig. 5-5

$$F = \frac{I_p}{V} = j e f_0^2 P \int \frac{C P}{n k (E - E')} \frac{d\psi}{dE'} dE' \approx - \frac{\pi e f_0^2}{n |k|} C P \frac{d\psi}{dE},$$

where F denotes the principal value of the integral, I_p = induced current at the frequency $f = n f_0$ in the pickup due to modulation caused by voltage V on the kicker, f_0 is the revolution frequency corresponding to energy E , n is the harmonic number, e is the unit charge, $j = \sqrt{-1}$, $k = 2\pi df_0/dE$, C is the phase factor due to transit time differences between pickup and kicker, and $P = P(f, E')$ is the pickup sensitivity. P depends on E' because P depends on particle position, which depends on E' (usually exponentially). The dependence of P on f comes from electrical properties and is usually weak.

This approximation is valid when the Schottky bands are well separated, but is a poor approximation for quantitative results for the system described here. Nonetheless, it is sufficient to expose the main features of the physical process.

The closed-loop gain of the system is given by $G' = G/(1 - FG)$, where G is the open-loop gain ($G = V/I_p$) of the electronics going from pickup to kicker. If the real part of FG is less than zero, then $G' < G$ and the cooling signal is suppressed. If the real part is greater than zero, the signal may be enhanced. If the real part of $FG > 1$, when the imaginary part is zero, the system is unstable. (This situation is completely analogous to the case of conventional electronic circuits with feedback).

In the approximate expression for F , one sees that there is a resistive (energy-absorbing) component of the beam response proportional to the gradient of the density at the driving frequency and a reactive component that depends on the asymmetry of the gradient about the driving frequency. It would be wrong to conclude, however, that the resistive term is the more important when looking at system stability. Both terms must be considered because the open-loop gain function G is a complex quantity; it unavoidably contains phase shifts from the filters and differences in time delays between pickup and kicker.

In fact, in the stack tail, the feedback can be dominated by the contribution from the particles in the core where $d\psi/dE$ is very large - 10^4 times larger than in the tail. Fortunately, $d\psi/dE$, which is increasing exponentially, is multiplied by the pickup response, which is decreasing exponentially. The rate of exponential increase of $d\psi/dE$ depends on the total gain profile, i.e., the product of pickup and filter response. The damping of $d\psi/dE$ in the feedback integral, however, depends only on the pickup response. Thus, it is important that the filter gain profile not be too sharp compared with the pickup in order to avoid severe problems with stability and signal suppression. The importance of the relative amounts of the gain profile derived from filters and pickups has been pointed out previously by Sacherer.⁷

An additional suppression of signal from particles in the core is provided by the subtracting pickups in each section. These pickups are placed closer to the core and normalized so that their sensitivity to the core region is equal and opposite to the sensitivity of the main pickups. In the stack tail, however, they subtract less than 10% of the signal. Several subtracting pickups followed by substantial attenuation are required to avoid having the subtracting pickups appreciably affect the amount of thermal noise in the pickups. Immediately after injection, the signal suppression is substantially larger because of the large values of $d\psi/dE$ created by the RF stacking process. The gradients quickly (after 200 msec) smooth out because of the diffusion terms in the Fokker-Planck equation. It appears that during the first 200 msec of the injection cycle, it may be necessary to reduce the amplifier gain in order to maintain beam stability. This gain reduction has been taken into account in computer simulations and, in any event, is only of minor importance.

5.2.5 Core Cooling. The same Fokker-Planck equation that describes the stack-tail system also describes the core system. In fact, the distinction between core and tail cooling systems is somewhat arbitrary. The asymptotic distribution is given by

$$\Phi = F\psi + (D_0 + D_1 + D_2\psi) \frac{\partial \psi}{\partial E} = 0$$

The cooling coefficient F has a zero at the peak of the core and a slope proportional to $g(E - E_c)$ where g is the electronic gain and E_c is the energy at the peak of the core. The other terms are heating terms. D_0 is the contribution of intrabeam scattering (via the Coulomb force) to the diffusion and has been calculated by Ruggiero⁸ to be $D_0 = 0.0015 N_p^2 (eV)^2/\text{sec}$, where N_p is the total number of antiprotons in the Accumulator. This value of D_0 corresponds to a momentum heating time of 2 hr. D_0 is independent of both g and E . D_1 is the contribution of thermal noise and is proportional to g^2 . D_2 is the Schottky heating term and is proportional to $g^2 (E - E_c)^2$. In our system D_1 is small compared with D_0 . Optimum performance occurs when g is adjusted so that intrabeam scattering dominates in the central part of the core and the Schottky heating term dominates at the edges of the core. Smaller values of g leave the cooling term F less than optimum ($g = 0$ means no cooling) and larger values of g mean that Schottky heating is larger than the cooling. Computer calculations show that densities in excess of $1 \times 10^5/\text{eV}$ can be reached.

The choice of 1 - 2 GHz bandwidth (and $\eta = 0.02$) for the tail system was made because of the desire to optimize core cooling. Since D_2 is proportional to $1/\eta$, a larger gain can be used to counteract intrabeam scattering in the core. Choosing a higher maximum frequency and the same momentum width for the stack tail system would have required a lower η for the lattice. This would have reduced the core cooling effectiveness.

A block diagram of the core cooling system is shown in Fig. 5-5. The zero in gain is obtained by subtracting the signals from two sets of pickups placed in a region of high momentum dispersion. One set of pickups is centered above the core energy and one is centered below. The signal is then applied to a kicker placed in a region of zero momentum dispersion. The gain profile for the core system Schottky bands at 2.2, 3.0, and 3.8 GHz is shown in Fig. 5-6 abc.

5.2.6 Numerical Calculations of Momentum Cooling. A computer simulation of the combined core and stack-tail momentum cooling systems has been made. These calculations use the full theory developed by van der Meer et al. and not the simplified models given here. It has been found that a core density of $1 \times 10^5/\text{eV}$ can be obtained after 4 hours of stacking with a flux of $3 \times 10^7 \text{ sec}^{-1}$. Figure 5-7 shows the stack profile as a function of time. Figure 5-8 shows the cooling term (F) including the effects of beam feedback after 3 hours. Figures 5-9 and 5-10 show the heating term coefficients $D_0 + D_1$ and D_2 . Figures 5-11 and 5-12 are stability plots: the real versus the imaginary part of the cooling system gain G times the beam feedback F . In this plot the system is stable if the curve does not enclose the point (1,0).

5.3 Betatron Cooling

5.3.1 Introduction. Betatron cooling is accomplished by using a pickup sensitive to the transverse displacement of the particles. In going from pickup to kicker the particle oscillates in betatron phase by an odd multiple of $\pi/2$, converting the position displacement to an angle displacement. Each given particle creates a signal in the pickup which, when applied to the kicker, decreases the angle displacement. Other particles with similar revolution frequencies contribute noise that tends to increase the betatron amplitude. This situation is similar to the momentum-cooling discussed earlier.

Betatron cooling is conventionally described in terms of the time decrease of the betatron emittance⁹

$$\frac{d\epsilon}{dt} = \sum_{n=n_{\min}}^{n_{\max}} \sum_{\pm v} \frac{-2G_{n+v\epsilon} + \alpha G_{n+v\epsilon}^2}{|S|^2} \quad (5.1)$$

The first term in the numerator describes the effects of the Schottky signal. (In the case of betatron cooling, the heating and cooling terms may be combined into a single term as has been done in Eq. (5.1) above.) The signal-suppression factor S is given approximately by

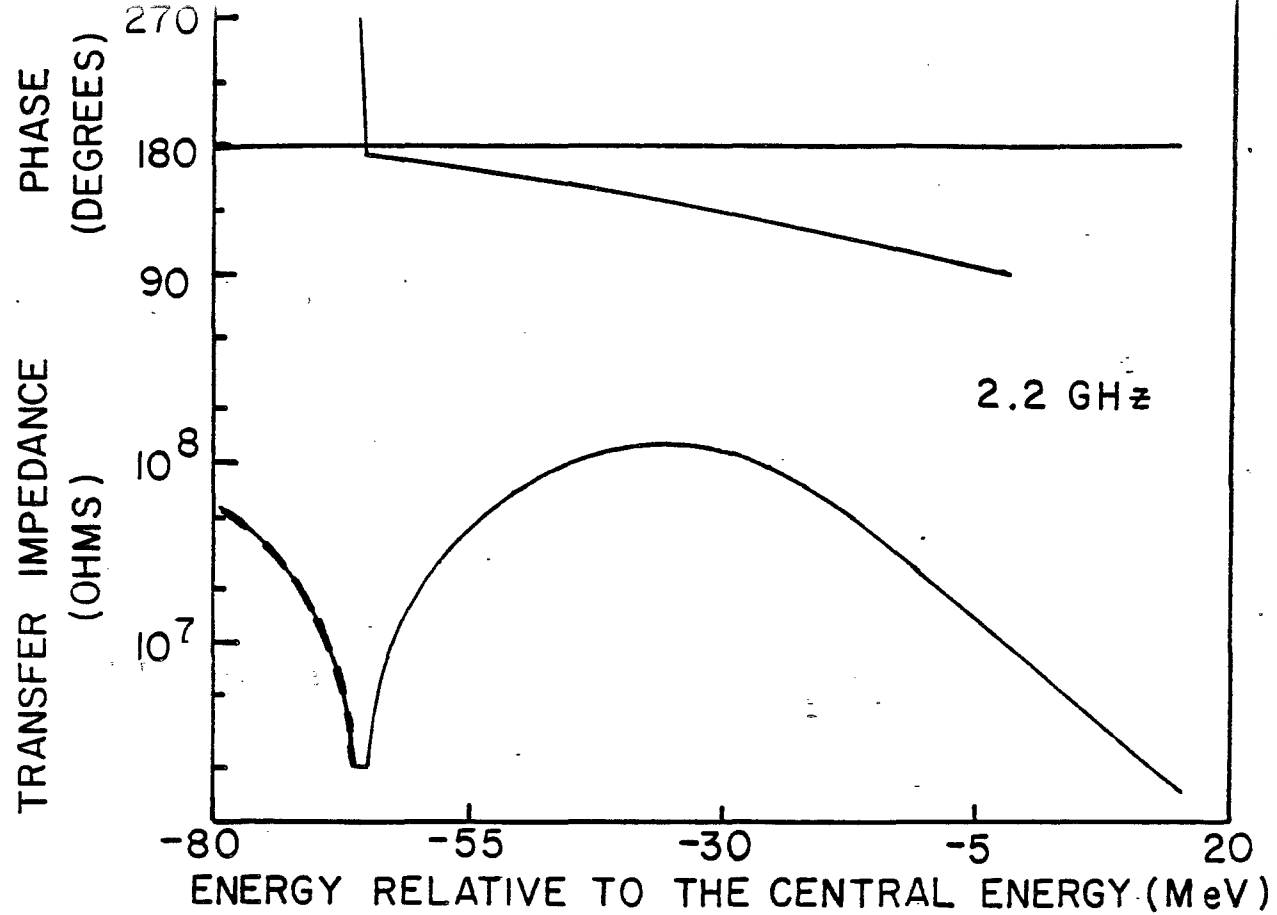


Fig. 5-6a

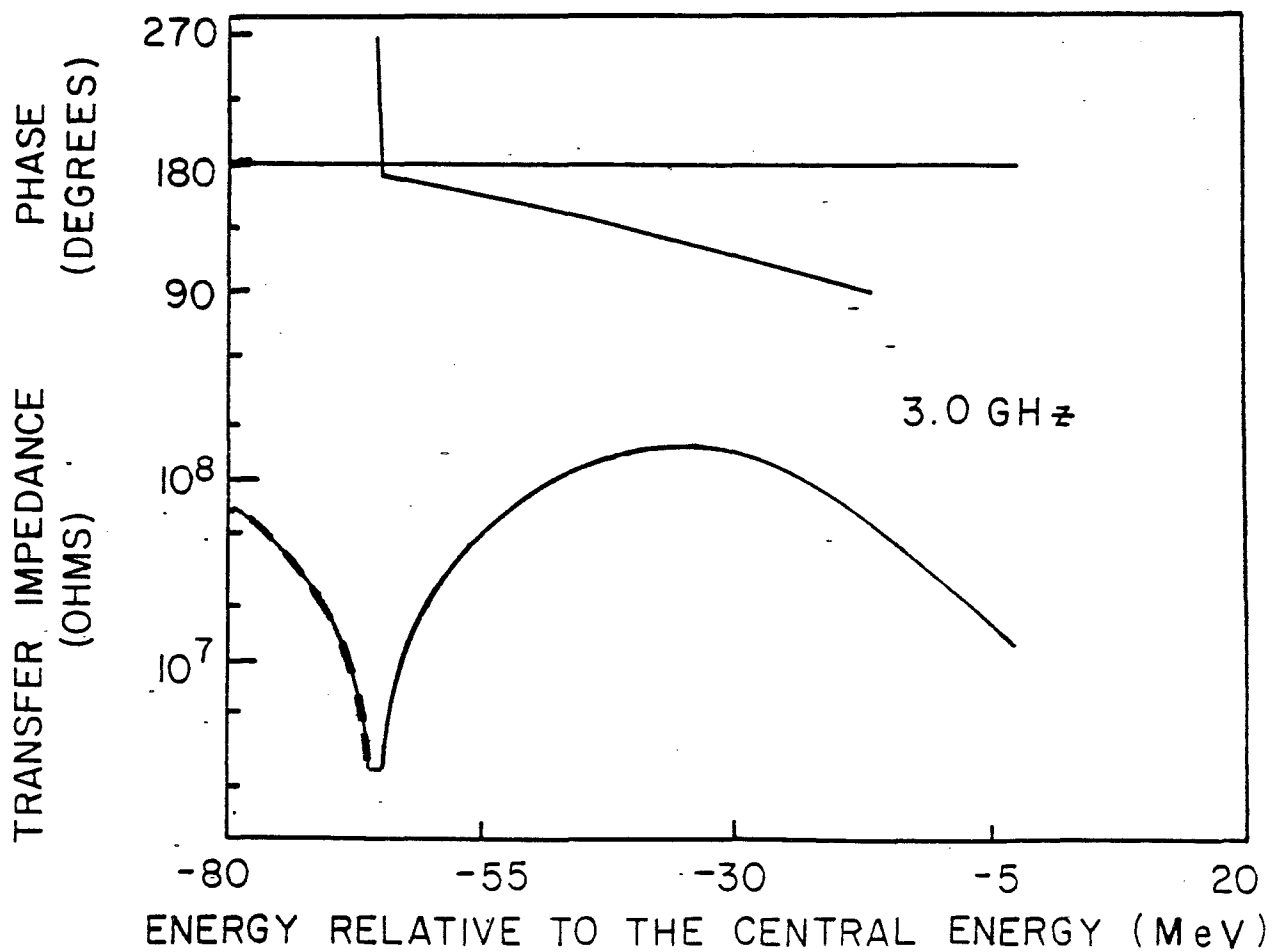


Fig. 5-6b

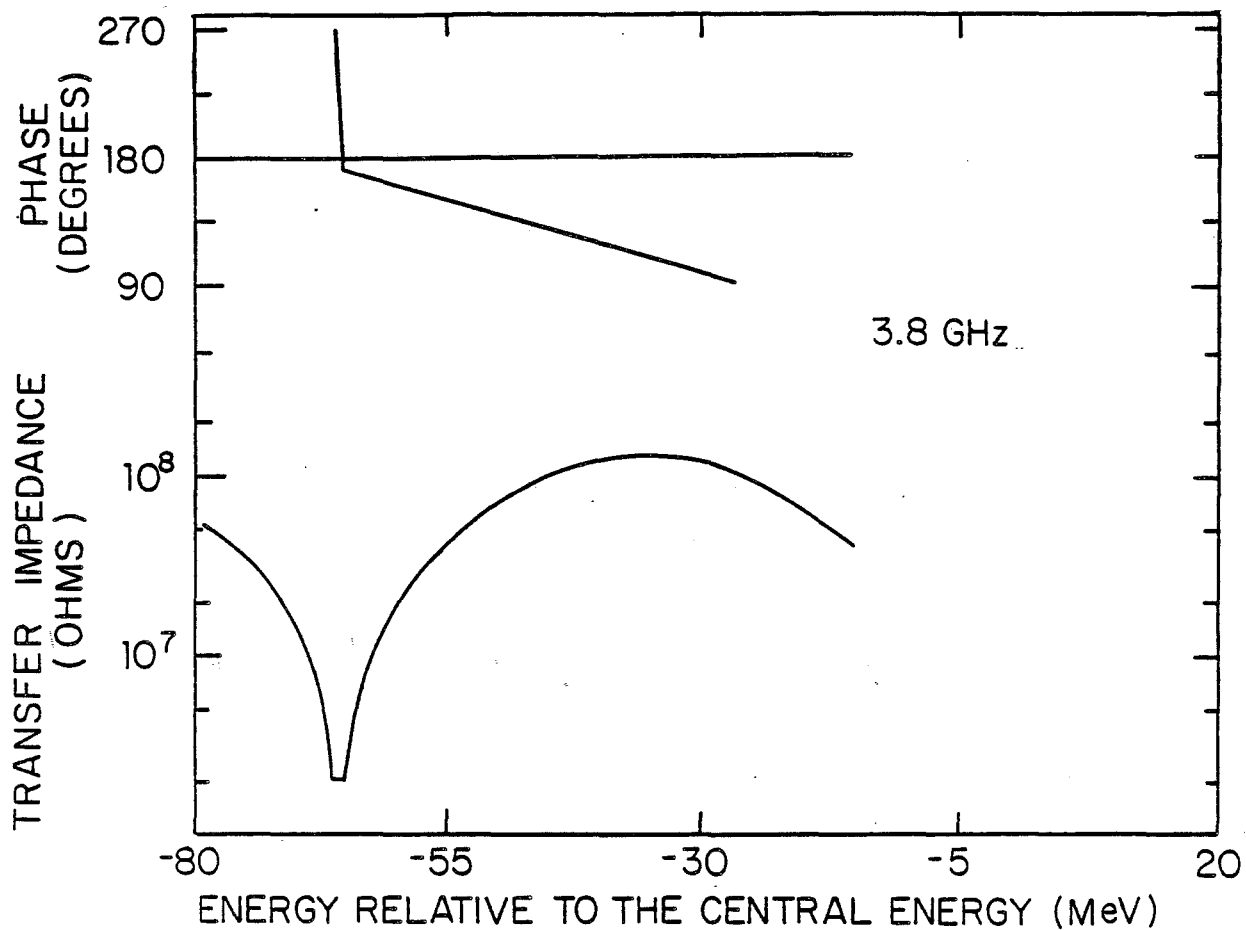


Fig. 5-6c

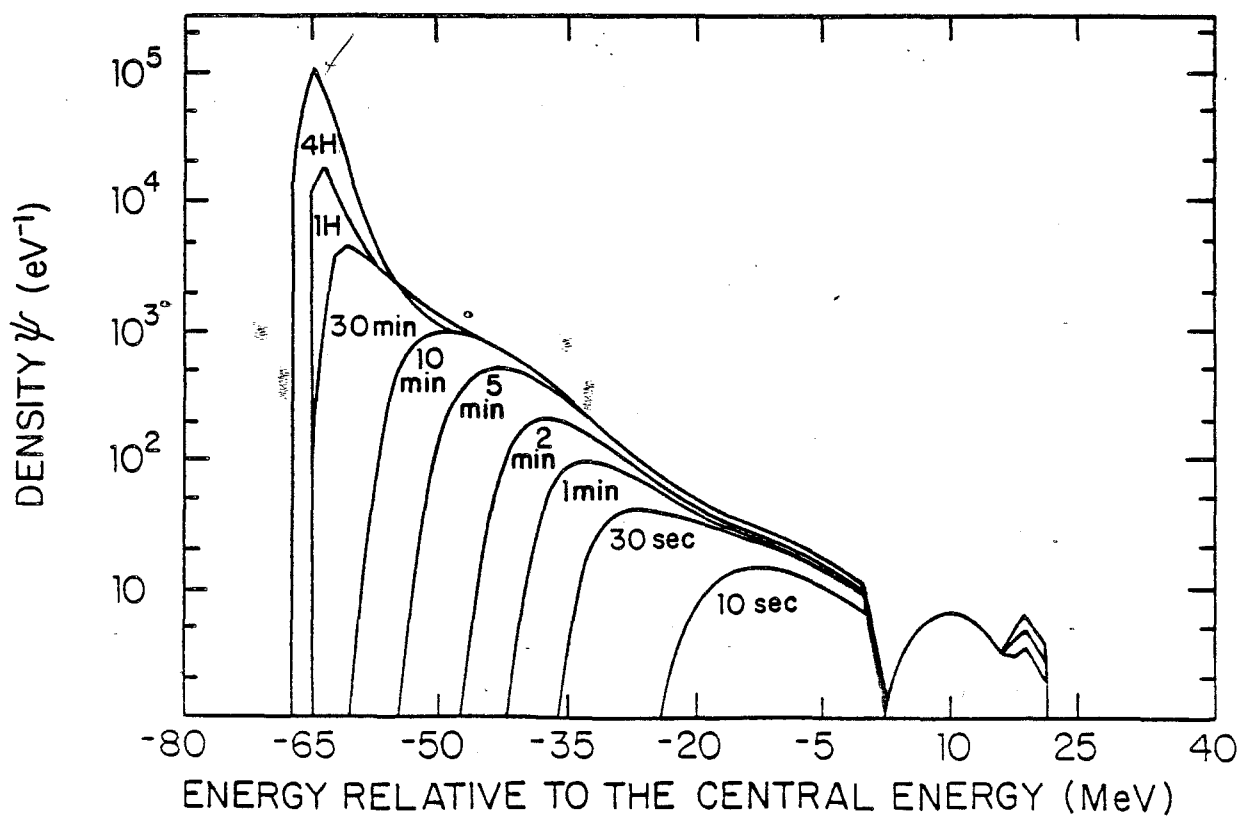


Fig. 5-7

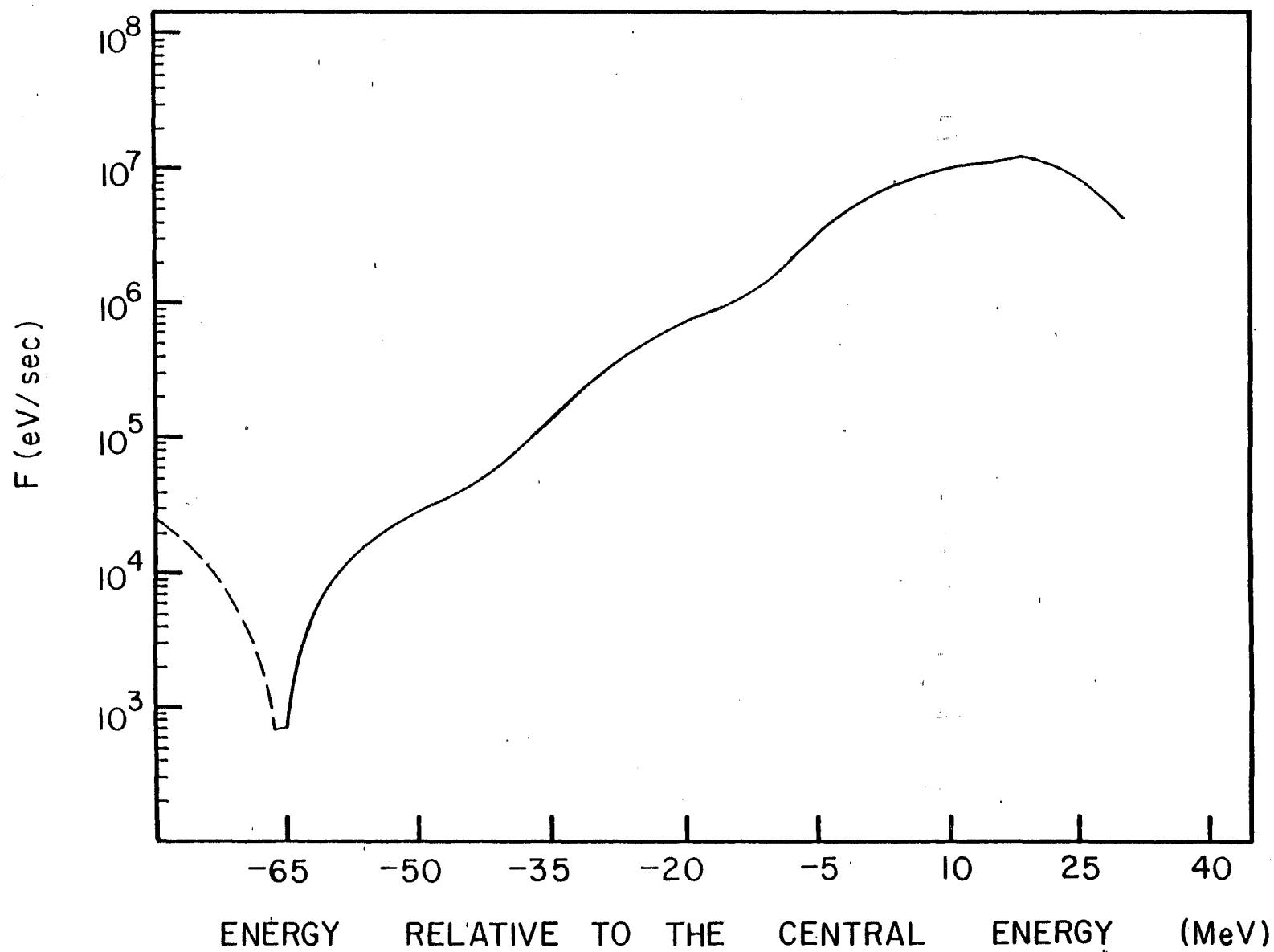


Fig. 5-8

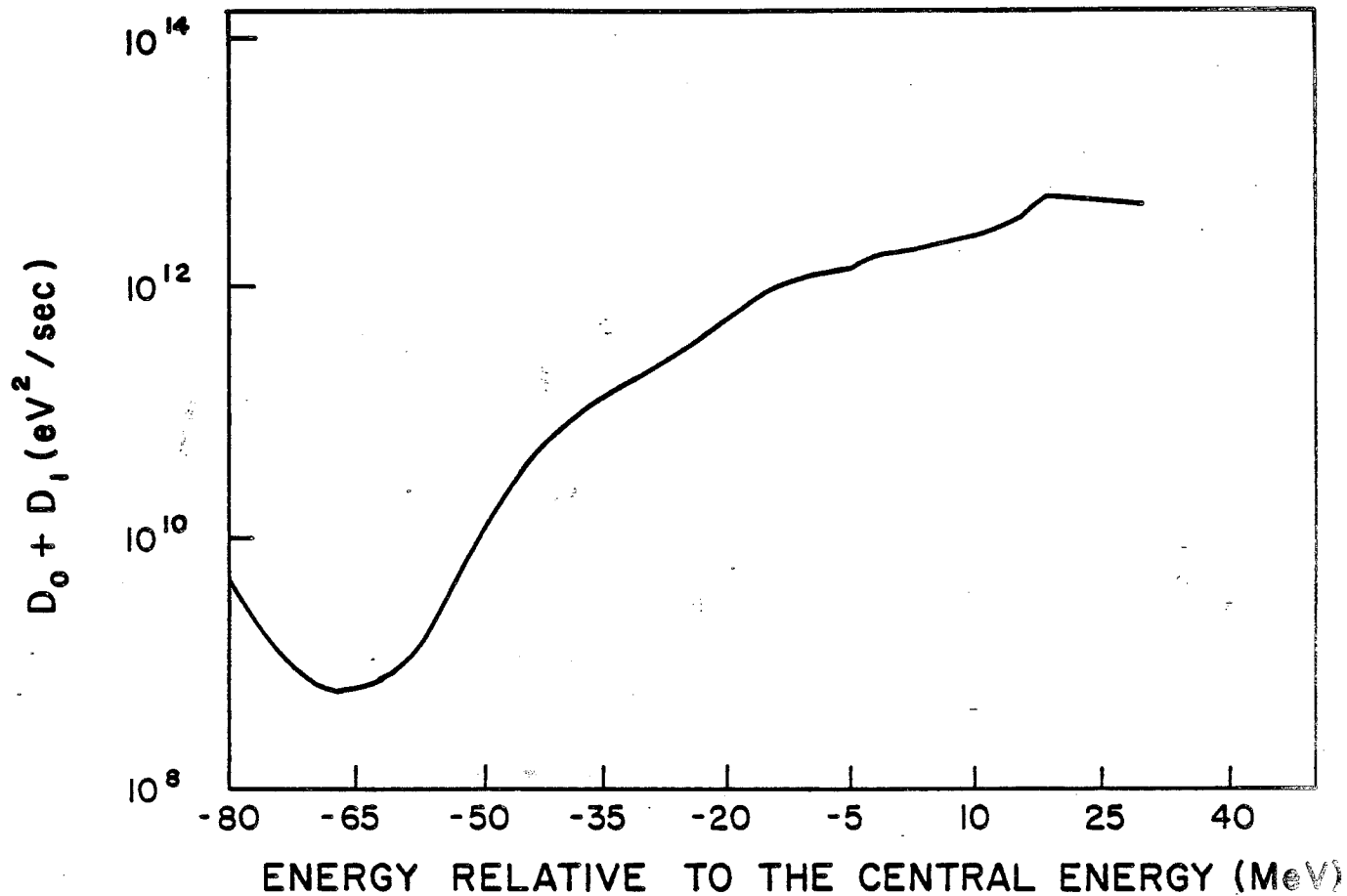


Fig. 5-9

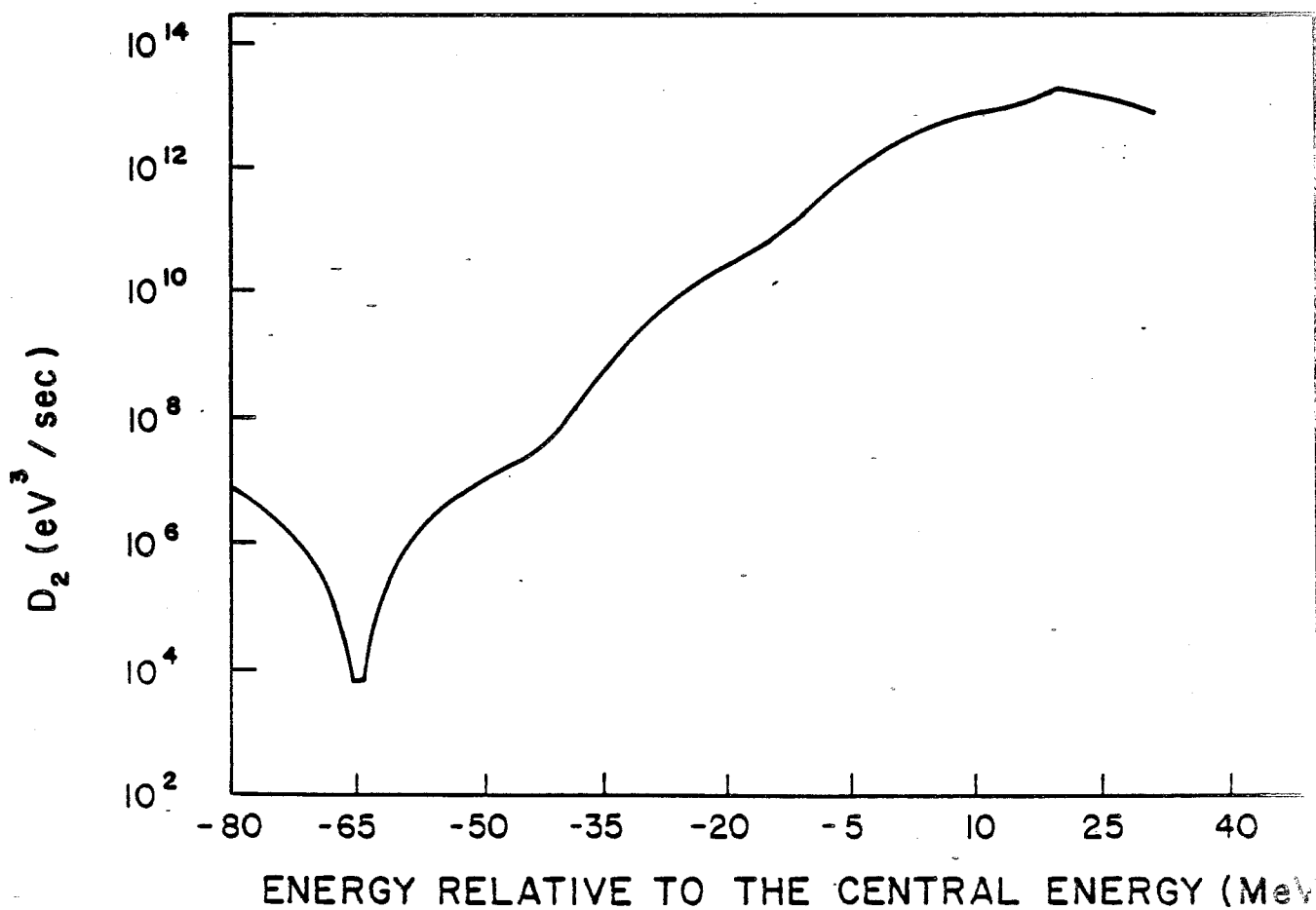


Fig. 5-10

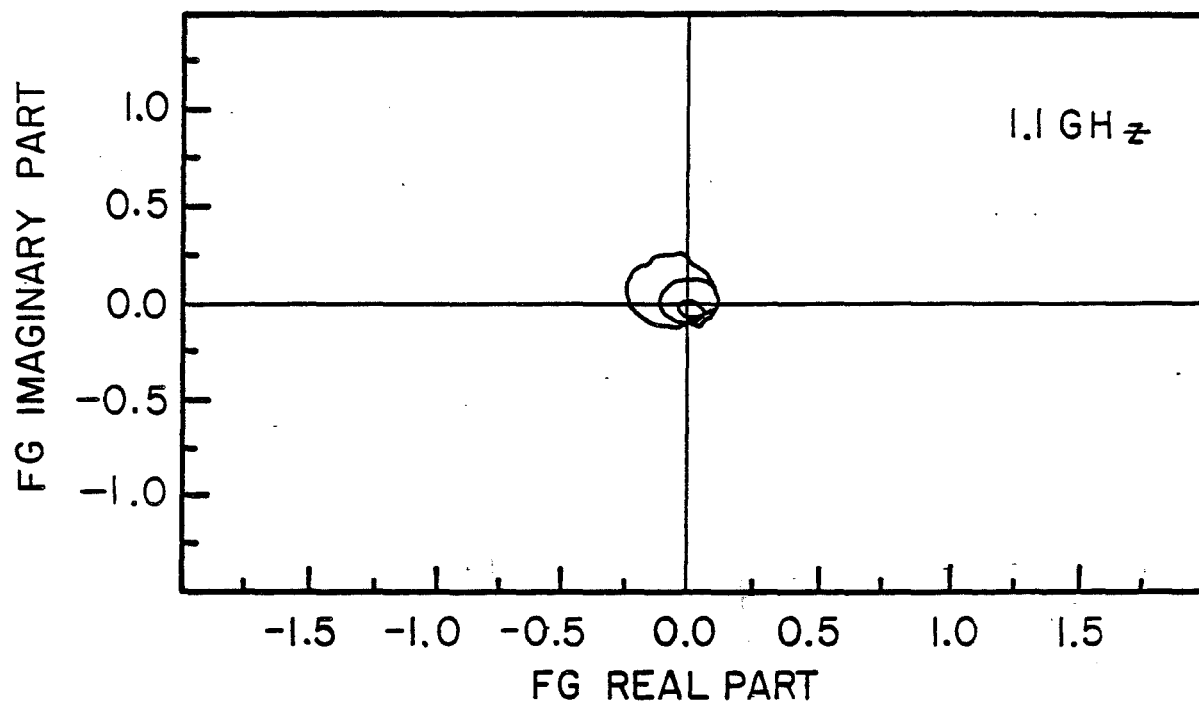


Fig. 5-11a

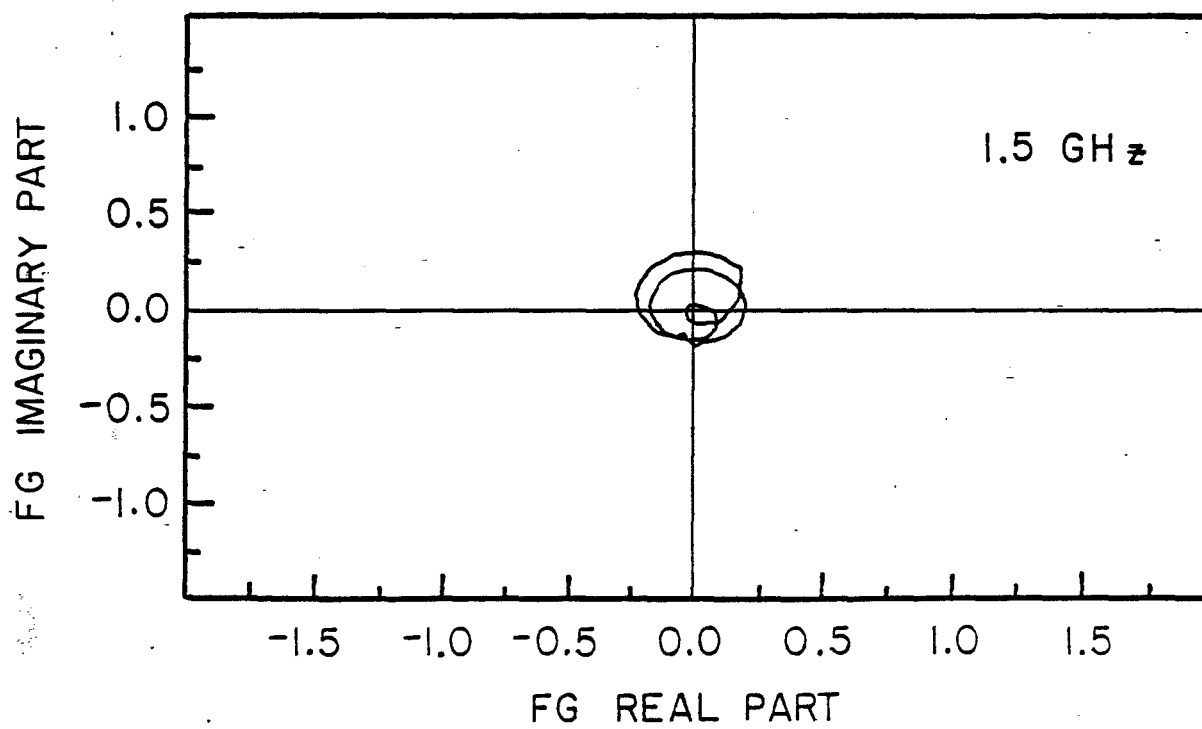


Fig. 5-11b

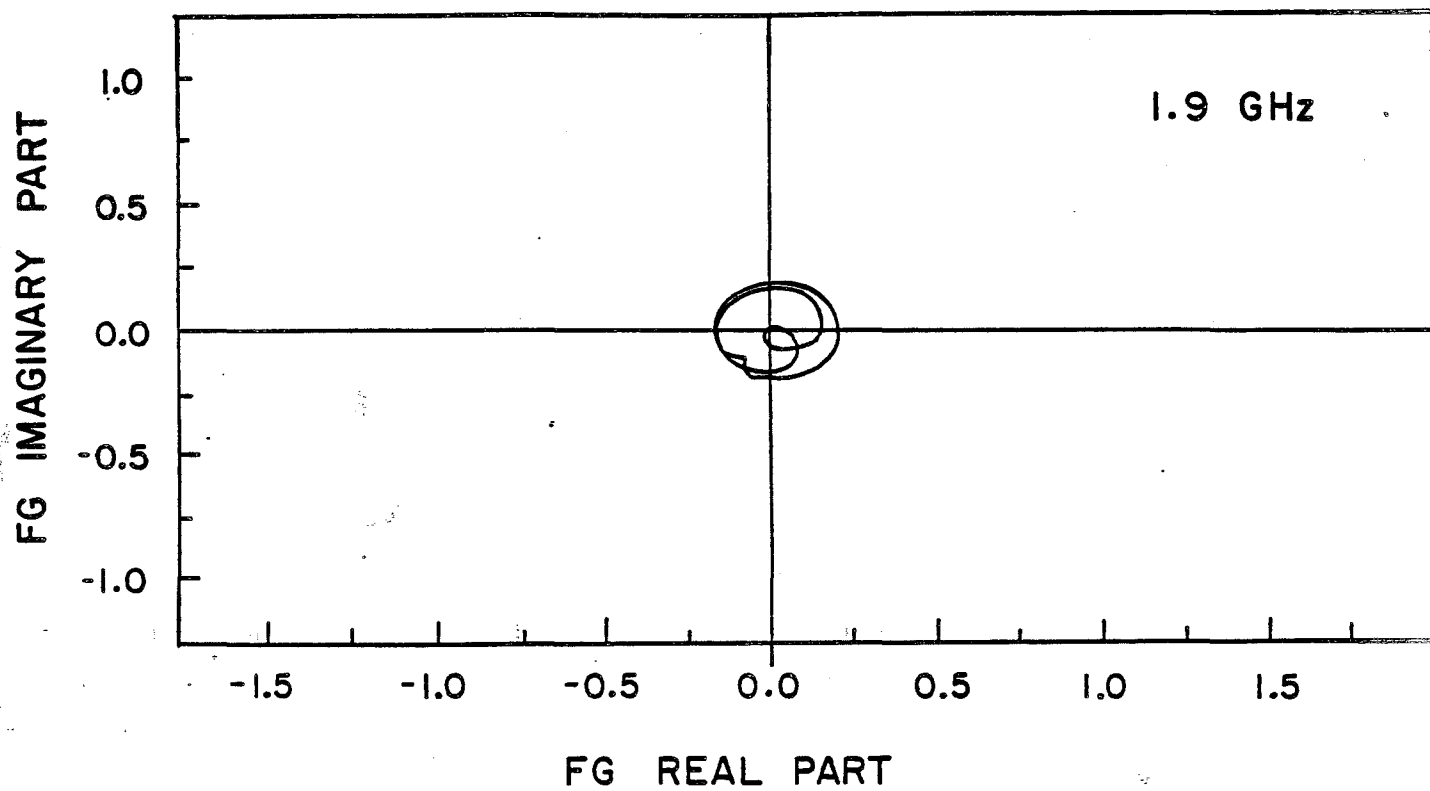


Fig. 5-11c

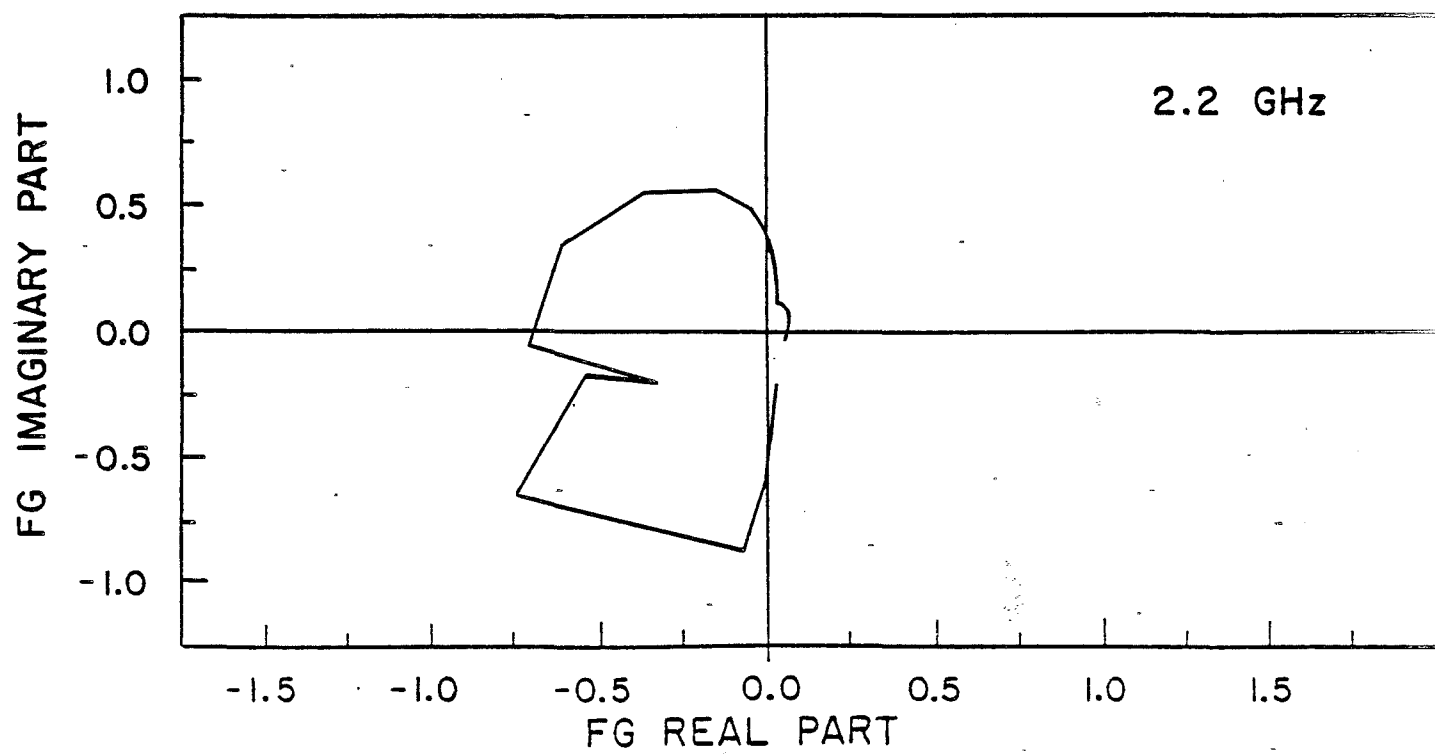


Fig. 5-12a

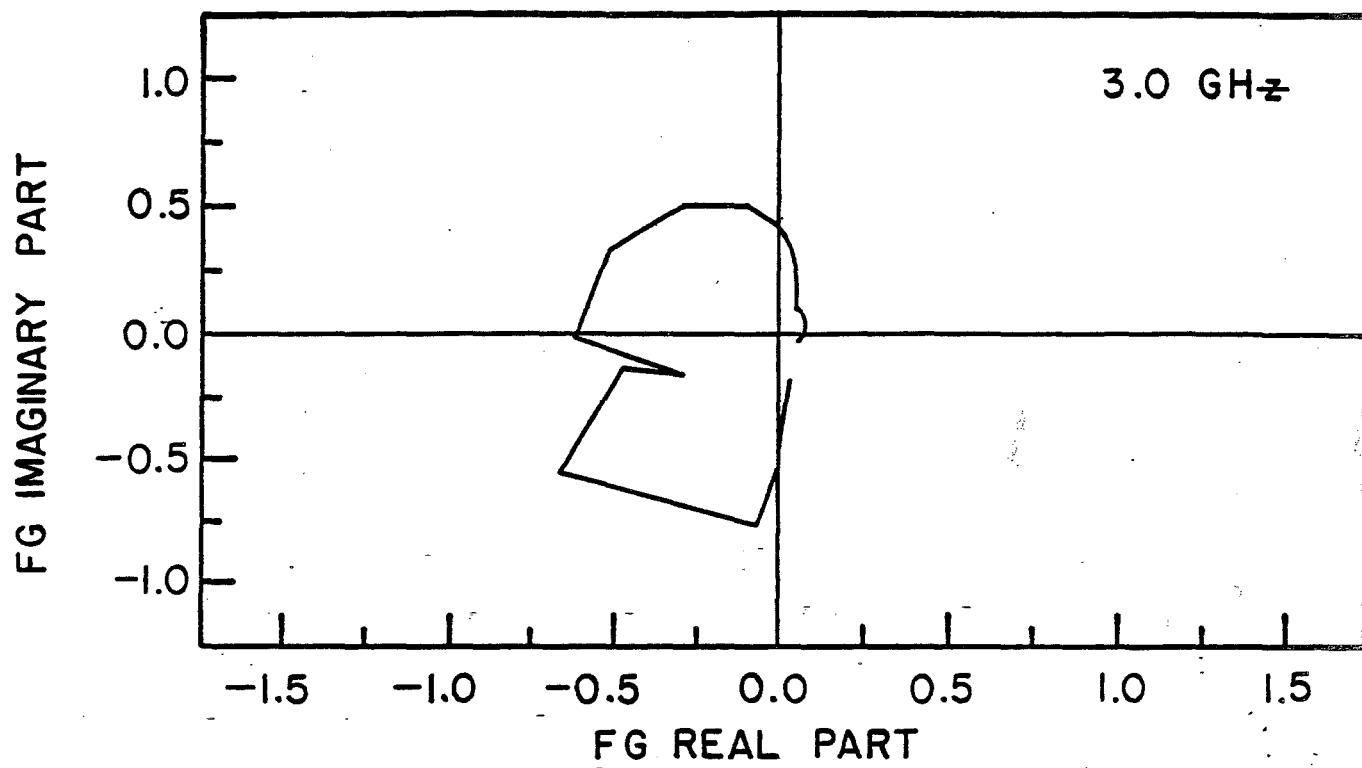


Fig. 5-12b

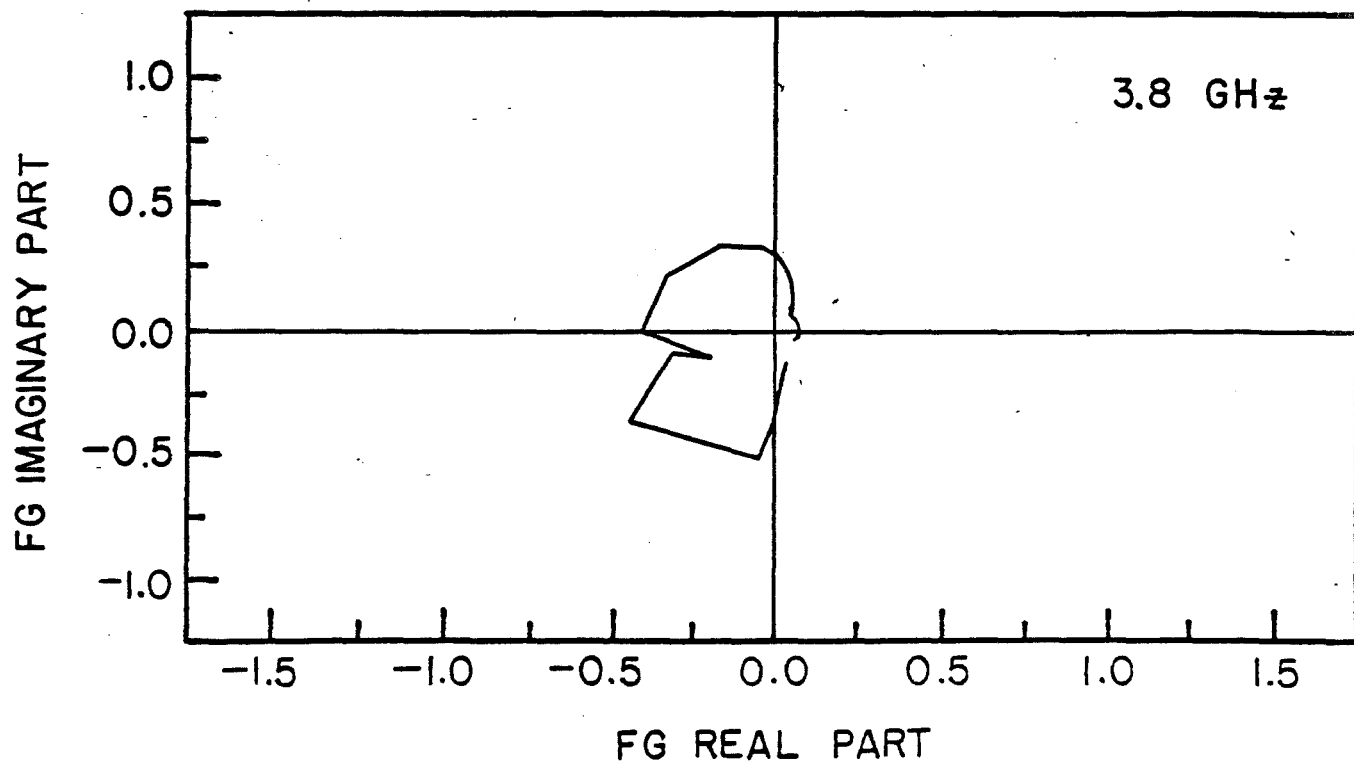


Fig. 5-12c

$$S = 1 + \frac{G_{n \pm v}}{n \pm v} \psi(E) \frac{\beta^2 E}{\eta} T. \quad (5.2)$$

The exact expression for S contains, in addition to the "pole term" given above, a principal-value integral over the distribution $\psi(E)$. At the center of a symmetric distribution, the principal-value integral vanishes. Away from the center, $|S|$ tends to be smaller than S at the center of the distribution. Thus, we can get approximate, but slightly pessimistic, results for betatron cooling in the core by considering only particles at the peak of the distribution. In the case of betatron cooling in the tail, the gain $G_{n \pm v}$ is sufficiently small that S can be set to 1.

The second term in the numerator of Eq. (5.1) describes the heating by thermal noise. Here

$$\alpha = 2TU_0, \quad (5.3)$$

where T is the revolution period, U_0 is the ratio of thermal noise power to Schottky signal power per particle at time $t = 0$, and ϵ_0 is the emittance at $t=0$. The total thermal power is given by

$$P_{th} = k(\Theta_R + \Theta_A) g_A^2 W, \quad (5.4)$$

where k is Boltzmann's constant, Θ_R is the pickup termination temperature, Θ_A is the amplifier equivalent noise temperature, g_A is the amplifier voltage gain and W is the bandwidth.

The Schottky power per pickup per particle is

$$P_{sch} = \frac{1}{2} e^2 r_0 Z_{pu} \frac{d^2}{h^2} \beta_p \epsilon_0 g_A^2 W, \quad (5.5)$$

where Z_{pu} is the pickup impedance, s is the pickup sensitivity, h is the pickup gap, β_p is the β function at the pickup. The ratio of thermal to Schottky power is

$$U_0 = \frac{2k(\Theta_R + \Theta_A)}{e^2 r_0 Z_{pu} (d/h)^2 \beta_p \epsilon_0}$$

The solution of Eq. (5.1) may be written as

$$\epsilon = (\epsilon_0 - \epsilon_\infty) e^{-t/\tau} + \epsilon_\infty \quad (5.7)$$

with

$$\epsilon_\infty = U_{0GT} \epsilon_0 \quad (5.8)$$

and

$$\frac{1}{\tau} = \frac{TW}{\xi} R(\xi G) \quad (5.9)$$

$$\xi = \frac{\psi(E) \beta^2 E}{rW} \quad (5.10)$$

$$R(x) = \int_1^2 \frac{4xdt}{(1+x/t)^2} \quad (5.11)$$

Equations (5.8) through (5.11) have assumed that the gain G_{n+y} is constant and equal to G . Equation (5.11) is an approximation to the sum from Eq. (5.1); the limits of integration assume an octave bandwidth. The gain G is related to pickups, kickers, and amplifier gain by

$$G = \frac{2\sqrt{\beta_k \beta_p}}{3\pi} \frac{s_p s_k}{h_p h_k} \frac{e^2 f_o^2 Z_{pu} \sqrt{N_p N_k}}{Wp} g_A, \quad (5.12)$$

where $\beta_k(\beta_p)$ is the betatron function at the pickup (kicker), $s_p(s_k)$ is the pickup (kicker) sensitivity, $h_p(h_k)$ is the gap height in the pickup (kicker), $N_p(N_k)$ is the number of pickups (kickers), e is the electric charge, $f_o = 1/T$ is the particle revolution frequency, Z_{pu} is the pickup and kicker impedance, and p is the momentum.

We will build two betatron cooling systems: a stack-tail system and a core-cooling system. The stack-tail system has both pickups and kickers

placed in dispersive regions and has a low sensitivity to particles in the core. The core-cooling system has both pickups and kickers placed in regions of zero dispersion and is therefore equally sensitive to particles in the core and tail. The gain of the core system is so low, however, that it has little effect on the tail. The core cooling system is somewhat simpler and will be discussed first.

5.3.2 Betatron Cooling in the Core. In the case of the core cooling, the gain of the system is determined by the energy density of particles in the core.

The function R has its maximum of 1.5 at about $x = 1.5$. The gain G is therefore

$$G = \frac{1.5 \eta W}{\beta^2 E \psi(E_c)}$$

$$= 7 \times 10^{-8} \text{ sec}^{-1},$$

where $\psi(E_c) = 10^5/\text{eV}$ is the peak core density, $W = 2 \text{ GHz}$ (from 2 to 4 GHz) $\eta = .02$, $\beta^2 E = 8.8 \times 10^3 \text{ eV}$. Then ϵ_∞ is $0.06 \pi \text{ mm-mrad}$ and negligible compared to a final emittance of $2 \pi \text{ mm-mrad}$. Thus, as might have been expected, thermal noise can be neglected.

The cooling time τ is found from Eq. (5.9) to be 1 hour. Particles that have an emittance much larger than the average emittance of the core will be cooled considerably faster however since the cooling correction is proportional to betatron amplitude. The intrabeam scattering diffusion times have been calculated to be 9 hr horizontally and large and negative (corresponding to slight damping) vertically. The amplifier power gain (90 dB) and power level (5 W) are modest. A block diagram of the system is shown in Fig. 5-13.

5.3.3 Stack-Tail Betatron Cooling. The stack tail betatron cooling system uses the same pickups as the second section of the tail momentum-cooling system. The pickup plates are centered at -5 MeV relative to the central energy. For horizontal signals the pickup is most sensitive at its edges at +15 MeV and -25 MeV. Most of the cooling takes place at the -25 MeV edge because the momentum cooling system is pushing particles much more slowly past the -25 MeV edge than the +15 MeV edge. The pickup is most sensitive at its center (-5 MeV) for signals in the vertical direction. The kickers are also placed at -5 MeV in a region with high dispersion. A block diagram of the system is shown in Fig. 5-14.

Approximate calculations of the system performance have been made with Eq. (5.1) except that the time variable has been replaced with the energy variable, using the relationship

CORE BETATRON COOLING SYSTEM 2-4 GHz

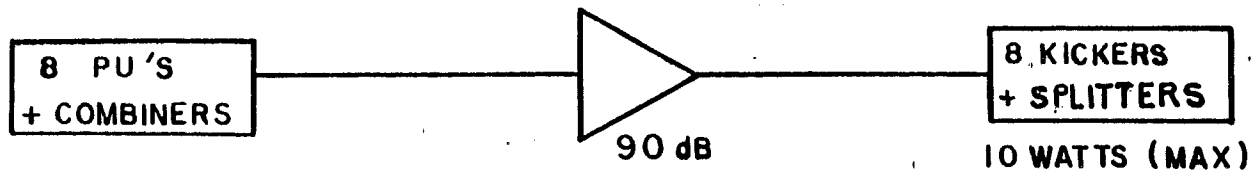


Fig. 5-13

STACK TAIL BETATRON COOLING 1-2 GHz

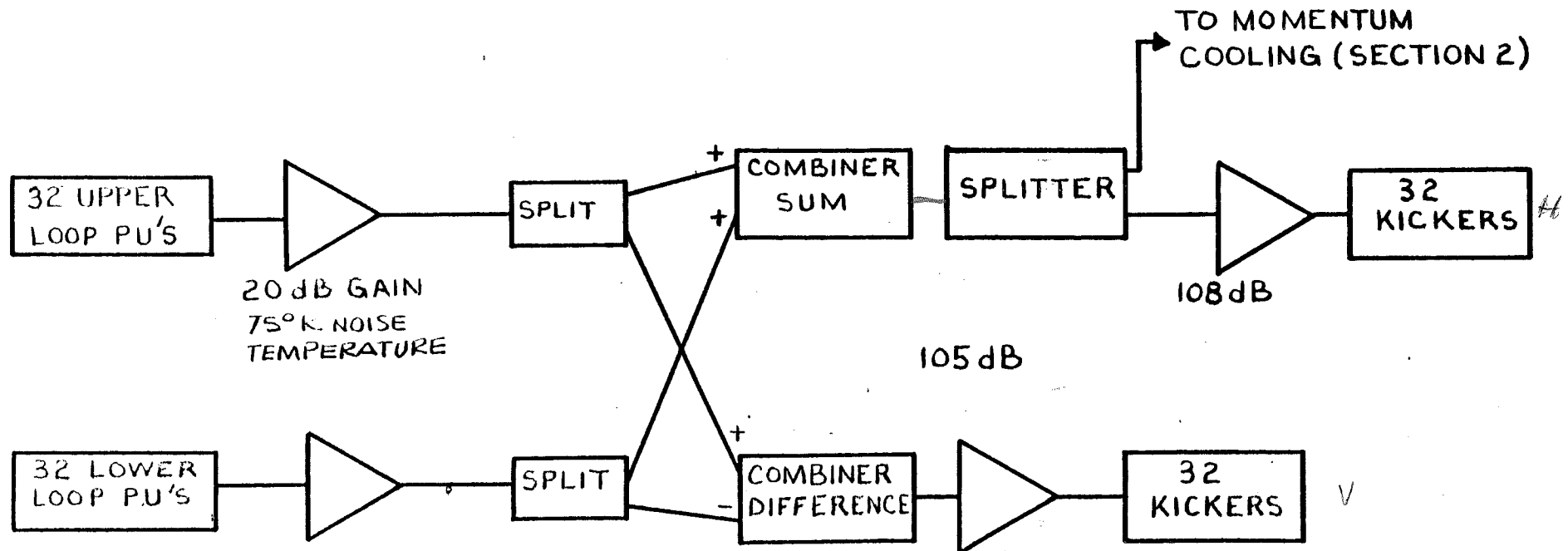


Fig. 5-14

$$\frac{dE}{dt} = \frac{\Phi}{\psi(E)},$$

where Φ is the flux of particles and $\psi(E)$ is the density of particles. This approximation ignores fluctuations in energy gain in the stacking process. With this approximation, Eq. (5.1) is easily integrated numerically. Figure 5-15 shows the emittance reduction as a function of energy. The power in each system is less than 20 W.

5.3.4 Operation of Betatron Cooling Systems. In the Accumulator we have available two betatron cooling systems, either of which is capable, or nearly capable, of cooling the beam emittance from 10π to 2π mm-mrad. The core system is clearly required so that a core of p's may be held for several hours without diffusion. The tail system serves two functions: 1) to cool the betatron amplitudes in a system with a low particle density (it is not necessary to wait one half to one hour for the core cooling system to do its work) and 2) to counteract possible betatron heating by the momentum-cooling system. The size of the latter effect is difficult to estimate; it depends on how well we are able to build the momentum kickers for the stack-tail system. If the effect is larger than expected, the gain of the stack-tail system can be raised to achieve better cooling, but, of course, the power requirements will be greater. Tentatively, however, we would plan to use the stack-tail system to reduce the beam emittance from 10π to 3π or 4π mm-mrad and use the core system to reduce it below 2π mm-mrad.

5.4 Stochastic Cooling Hardware

The purpose of this section is to outline the hardware and techniques we expect to use in order to meet the design requirements presented above. Although the design is not complete, it has been carried out in sufficient detail to make reliable cost estimates. In several instances alternative designs are possible. We present here the design which is most sound technically. Research and development are presently in progress to investigate alternatives which could lead to better system performance, reliability, or cost reduction.

Each stochastic cooling system is composed of 5 basic parts: beam pickup electrodes, low level electronics (including preamplifiers), medium level electronics (including gain and phase correction circuits, filters etc.), high level electronics (including travelling wave tubes), and kicker electrodes. As several of the cooling systems share common elements in their design, and the performance of these elements is necessary for the proper functioning of the cooling system, they are discussed below.

5.4.1 Pickup Electrodes The design of the 1 to 2 GHz and the 2 to 4 GHz

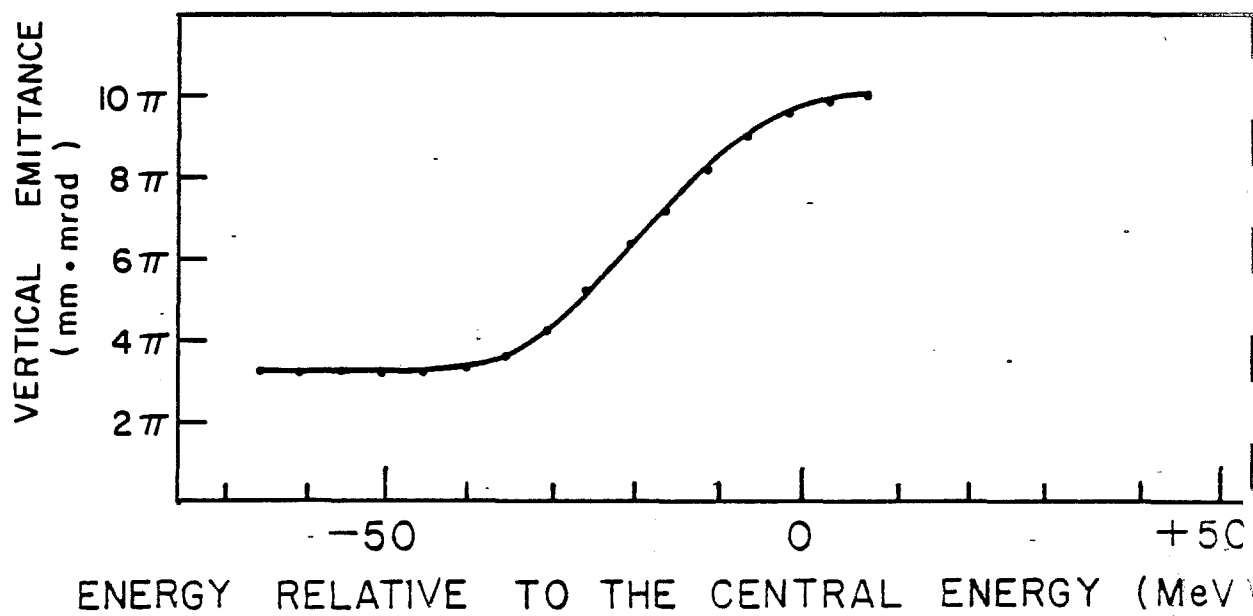
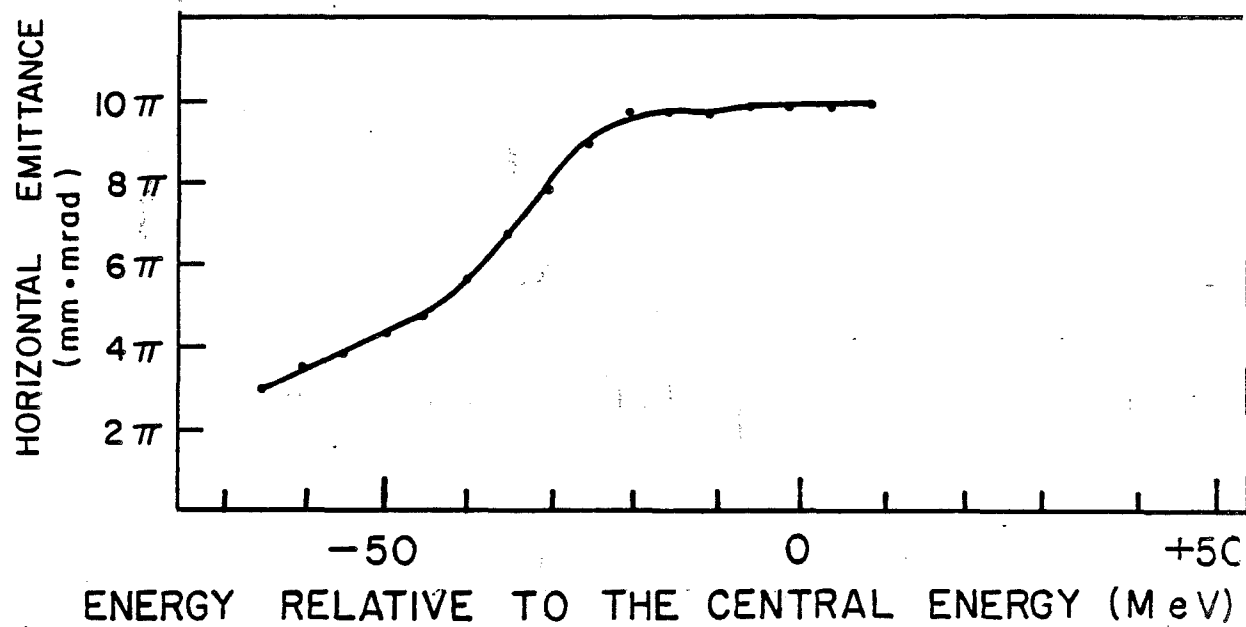
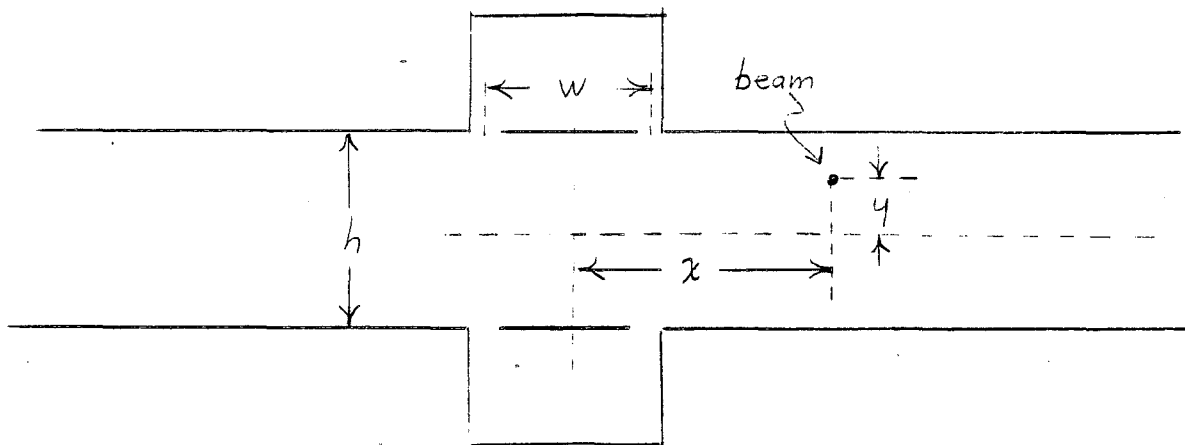


Fig. 5-15

stochastic cooling systems is based on the known^{4,11} and measured¹² performance of quarter-wave loop (directional coupler) pickups. The loop pickup is a segment of transmission line of well defined characteristic impedance on which beam wall (image) currents can be induced. The magnitude of the voltage induced on it depends on its characteristic impedance Z_{pu} , its effective length l , its geometrical coupling $e(x,y)$ (which depends on the transverse beam location as well as the height of the vacuum chamber, and the amplitude of the beam current $i_b(\omega)$):

$$V_{pu}(\omega) = e(x,y) Z_{pu} \sin\left(\frac{l\omega}{c}\right) e^{i\pi/2} i_b(\omega)$$

where the 90° phase shift at the reference plane (the center of the loop) is due to the inductive nature of the coupling. The geometry of a typical pickup pair is shown below:



Here, h is the full height of the gap between the electrodes and w is their effective width. If the signals are added in a microwave power combiner circuit and the output signal is referenced to a transmission line of impedance Z_o , the output voltage is

$$V_{out}(\omega) = s(x,y) \sqrt{\frac{Z_{pu}Z_o}{2}} \sin\left(\frac{l\omega}{c}\right) e^{i\pi/2} i_b(\omega)$$

where $s(x,y) = e(x,y) + e(x,-y)$

$$= \frac{1}{\pi} \left[\tan^{-1} \left(\frac{\sinh \frac{\pi}{h}(x + w/2)}{\cosh(\pi y/h)} \right) - \tan^{-1} \left(\frac{\sinh \frac{\pi}{h}(x - w/2)}{\cosh(\pi y/h)} \right) \right]$$

For $x = y = 0$:

$$s(0,0) = \frac{2}{\pi} \tan^{-1} \{ \sinh(\pi w/2h) \}$$

Transfer impedances of pickup pairs in sum mode are defined with a centered beam at center frequency ($\omega = \pi c/2\ell$) and in a $Z_0 = 50$ ohm transmission line,

$$Z_s = s(0,0) \sqrt{25 Z_{pu}}$$

At large x , $s(x,0) \rightarrow \frac{4}{\pi} e^{-\pi x/h} \sinh(\pi w/2h)$

If the differences of the signals in the pickup electrode pair are combined into a transmission line of impedance Z_0 , the output voltage is

$$V_{out}(\omega) = d(x,y) \frac{y}{h} \sqrt{\frac{Z_{pu} Z_0}{2}} \sin\left(\frac{\ell \omega}{c}\right) e^{i\pi/2} i_b(\omega)$$

$$\text{where } d(x,y) = \{e(x,y) - e(x,-y)\} \frac{h}{y},$$

and the difference mode transfer impedance at $x = 0$ is

$$Z_d(o,y) = d(o,y) \frac{y}{h} \sqrt{25 Z_{pu}}$$

where $d(o,y) \approx 2 \tanh(\pi w/2h) \approx \pi s(o,o) [1 - 1/3 s^3(o,o)]$

As microwave power combiners add power of coherent signals, the coupling

impedance of η_0 loop coupler pairs is $\sqrt{\eta_0}$ times the impedance for a single pair, in both sum and difference modes. Figures 5-16 and 5-17 show a typical electrode assembly.

Based on calculations, as well as measurements with both wires and electron beams, the loop coupler characteristics shown in Table 5-II are the values we use in the Design Report.

Table 5-II LOOP COUPLER CHARACTERISTICS

Characteristic		1-2 GHz band	2-4 GHz band
characteristic impedance	Z_{pu}	100	75 ohms
height (gap) typical	h_{pu}	3.0	3.0 cm
effective width	w	4.0	2.5 cm
pairs per meter		15	25 per m
<u>Sum Mode</u>			
$s(o,o)$.843	.664
transfer impedance	Z_s	42.2	28.8 ohms
<u>Difference Mode</u>			
$d(o,y)$		1.94	1.73
transfer impedance	Z_d	3230	2500 ohms/m

The electrode assemblies shown in Figs. 5-16, 5-17, and 5-18 are approximately 2.5 meters long (for the 1-2 GHz band) and contain 32 pickup pairs. The signals are combined separately for top and bottom electrodes using a double-sided Teflon printed circuit board. The air-spaced ground plane yields a group velocity of about 0.98c. The electrodes are back-terminated in their characteristic impedance, and the whole assembly is cooled to liquid nitrogen to reduce the thermal noise power from the back termination, the skin effect losses in the circuit board, and teflon outgassing. In the 2-4 GHz band, it is quite possible that slot couplers will have a higher coupling impedance per unit length than loop couplers. A research and development program is underway in this area.

5.4.2 Preamplifiers Commercial gallium-arsenide field-effect transistor (GaAsFet) amplifiers are available in the microwave frequency bands required for stochastic cooling. Although their thermal noise characteristics are relatively low (a 2.0 db noise figure amplifier, available in the 1-2 GHz band¹³, has an equivalent noise temperature of 170 K) it would still contribute nearly 70% of the total thermal noise power. The design therefore includes preamplifiers cooled to liquid nitrogen temperatures. We expect equivalent noise temperatures of 75 K (NF = 1.0 db) and 120 K (NF = 1.5 db) for 1-2 GHz and 2-4 GHz amplifiers respectively. Minimization of thermal noise is not only important in relation to beam heating, but also in relation to the cost of extra travelling wave tube installed power required to amplify it.

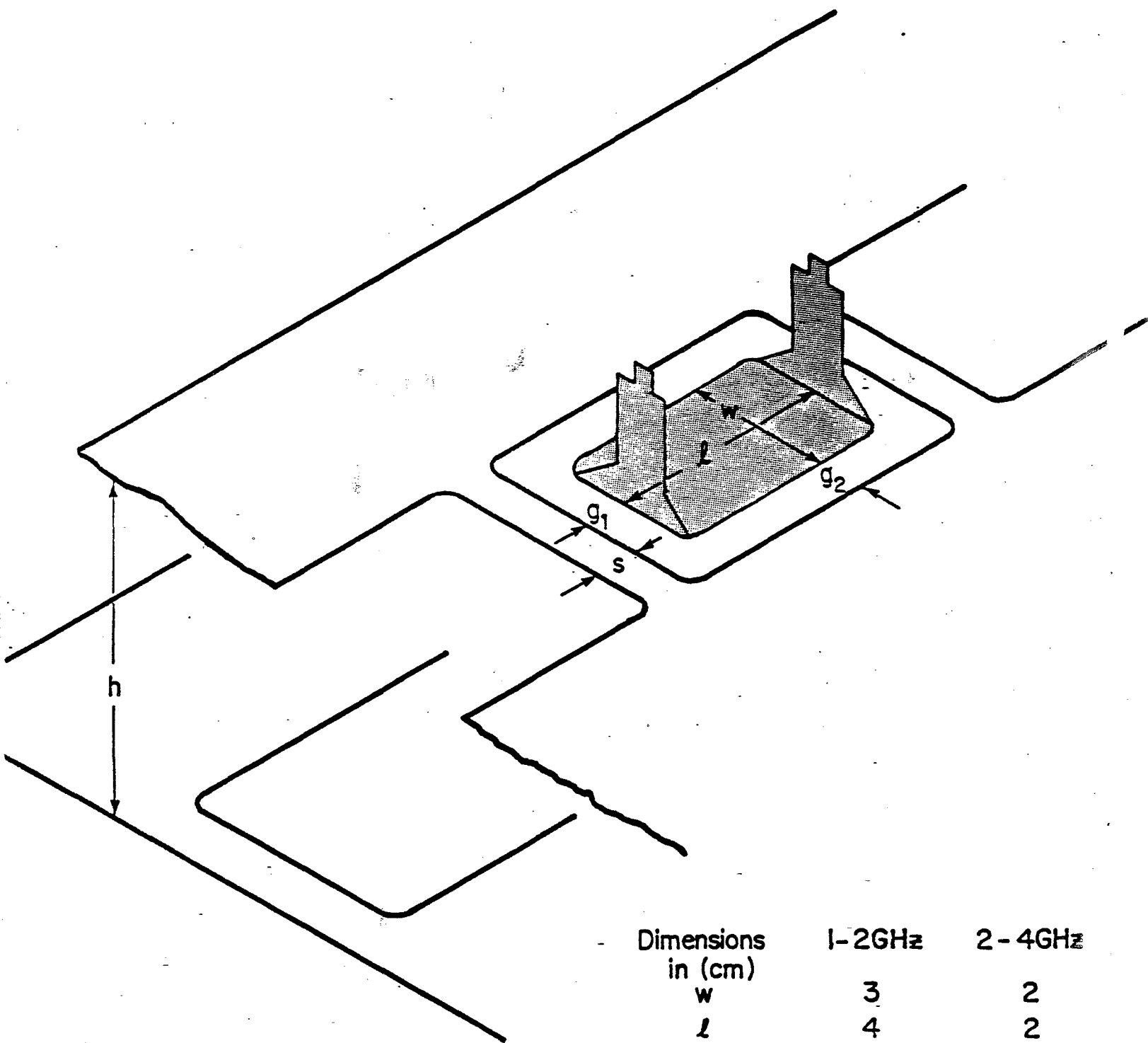
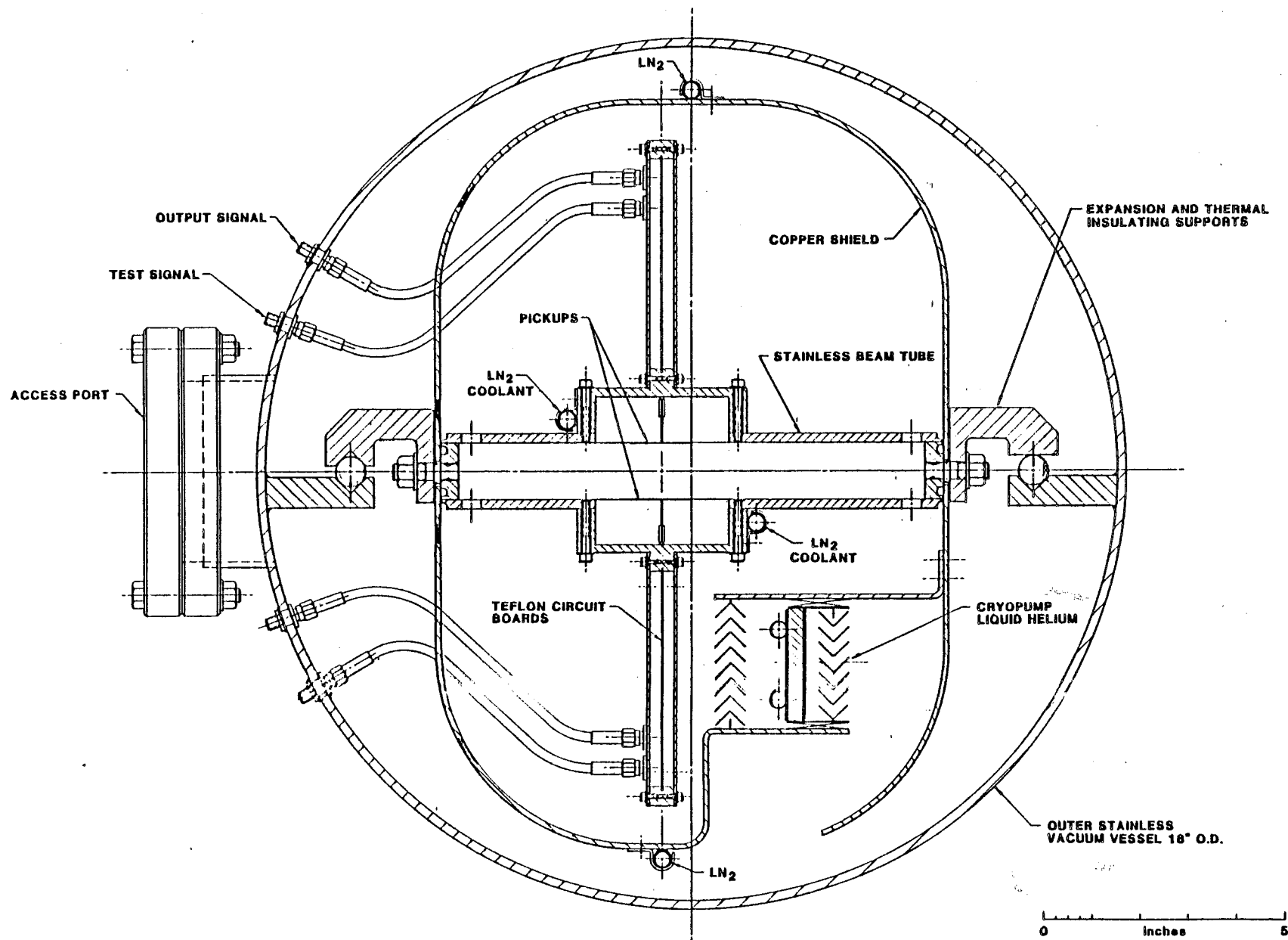


Fig. 5-16

Dimensions in (cm)	1-2GHz	2-4GHz
w	3	2
l	4	2
g_1	1	0.5
g_2	1	0.5
g_3	1	0.5
h	3	3
s	1	1

g_3 is the distance to the ground plane (not shown) above the pickup electrode



1-2 GHz PICKUP ELECTRODE ASSEMBLY CROSS SECTION

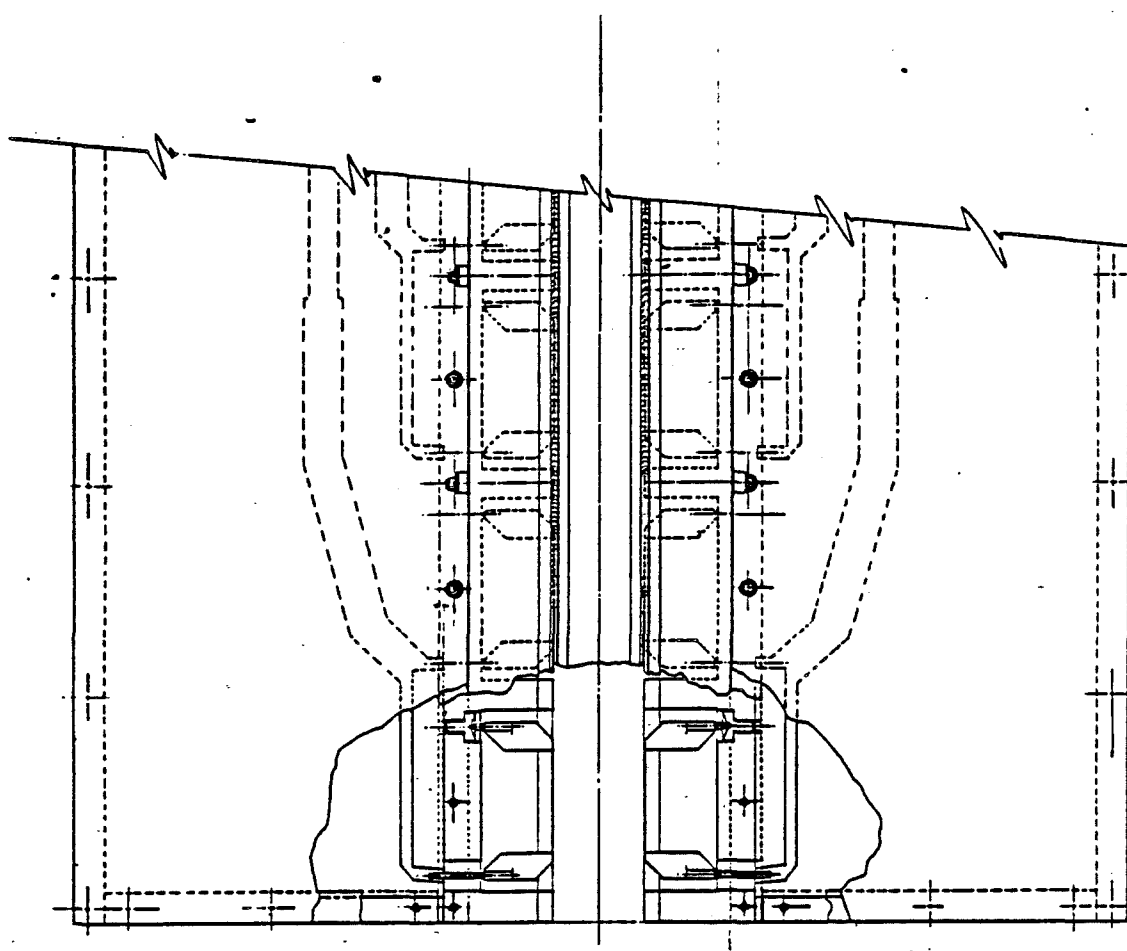
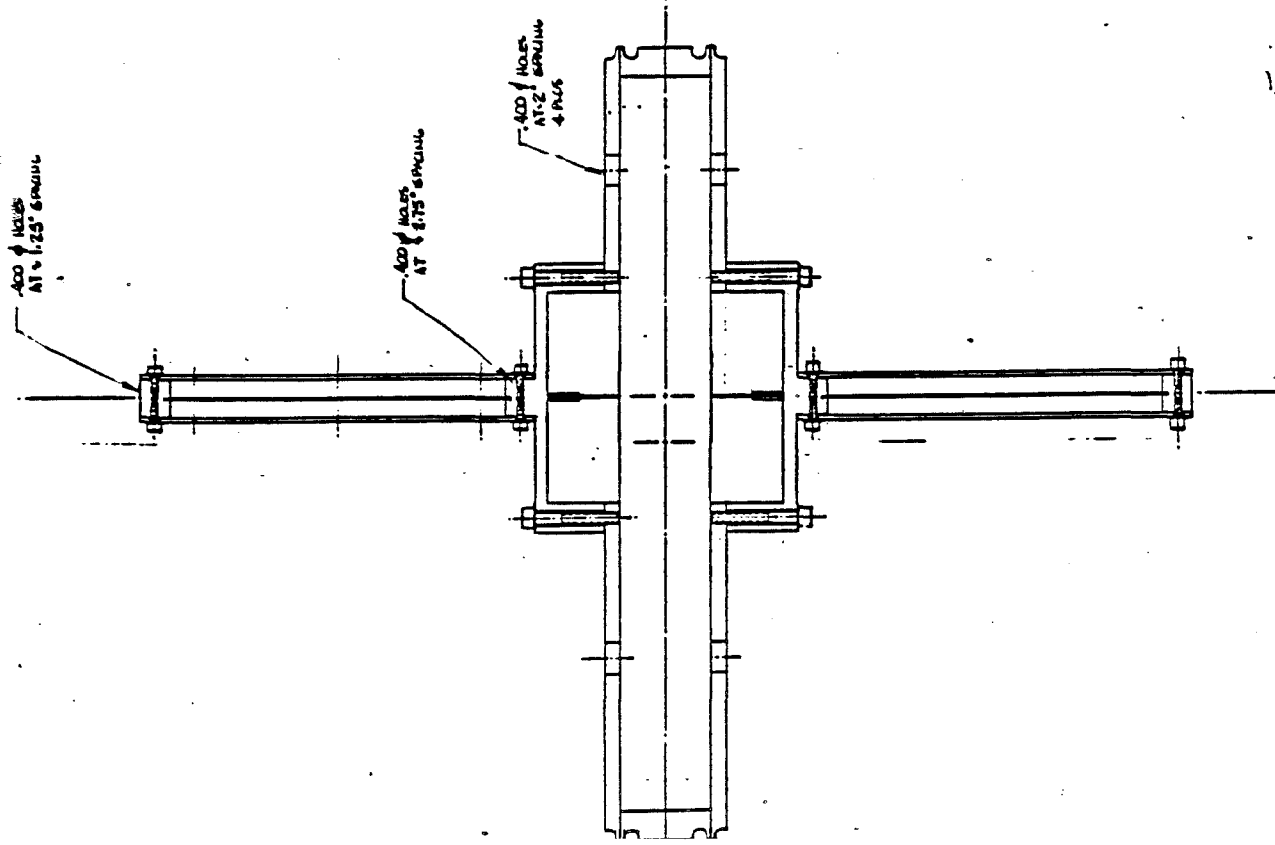


Figure 5-18

ANTIPROTON SOURCE 3H ₂	
U.S. DEPARTMENT OF ENERGY NEWM NATIONAL ACCELERATOR LABORATORY	
PROJECT NO. 10-2KEL-11 DATE 10-1-79	
DRAWN BY: [blank] CHECKED BY: [blank] APPROVED BY: [blank]	
MATERIAL: [blank]	
USED ON: [blank]	
COMMENTS: [blank]	

Commercially available GaAsFet amplifiers designed to operate in the Mil spec temperature range (-55 C to 70 C) have been successfully operated as low as 77 K¹⁴. In this case a 1-2 GHz amplifier achieved an equivalent noise temperature of 120 K (NF = 1.5db). GaAsFet amplifiers have been specially designed for operation at liquid helium temperatures, and equivalent noise temperatures of 20 K (NF = .2 db) have been achieved in narrow band operation¹⁵ (0.5 GHz bandwidth at 1.5 GHz). We are undertaking parallel R&D efforts to test commercially available amplifiers at liquid nitrogen temperatures, and to develop our own design. The amplifiers will be housed in separate vacuum systems closely coupled to the electrode assemblies shown in Fig. 5-17.

5.4.3 Notch Filters Notch filters are needed in our design of the stochastic cooling system for several reasons. In one system, the stack tail momentum cooling system, notch filters are used both for reducing the microwave power at frequencies corresponding to particles in the core, and to assist in shaping the gain vs momentum (frequency) in the stack tail. In systems with poor signal to thermal noise ratio, notch filters are useful in reducing the extra travelling wave tube installed power required to amplify it. If momentum cooling is implemented in the debuncher, a notch filter would be used to produce a phase inversion of the pickup sum signal at the harmonics of the central revolution frequency. The tolerance on the frequency deviation of the notch centers at each harmonic of the revolution frequency ω_0 in the frequency bandwidth is of the order of (for the accumulator)

$$\left| \frac{\omega_n - n\omega_0}{n\omega_0} \right| < \frac{\delta p}{\eta p} \sim 0.5 \times 10^{-5}$$

Where $\eta = 0.02$, p is 8.9 GeV/c and δp is about 2 MeV/c.

Filter designs include both shorted stubs, which use reflections from the shorted end of a long transmission line (nominally half the circumference of the accumulator ring), and correlator types, which use the constructive and destructive interference of the same signal transmitted over two transmission lines (whose lengths differ by about the circumference of the accumulator ring).

In our application here, the large circumference of the accumulator ring, in combination with the very high frequencies used in the electronics, impose severe restrictions on the selection of transmission lines. In room temperature transmission lines, the skin effect conductor resistance causes dispersion as well as attenuation. This is reduced by using larger diameter transmission lines. However, the maximum size of the transmission line is limited as higher order modes are excited, and affect the dispersion. In particular, in a 7.5-cm diameter 50-ohm transmission line, the TE₁₁ mode propagates at frequencies above 2.0 GHz. These effects are only marginally better at 76.6 ohms, the impedance at which skin effect losses are minimized.

Our design is based on superconducting transmission-line correlator type notch filters. We have achieved notch dispersion of less than 1×10^{-5} in the 1-2 GHz band using a 1.6-mm diameter 50-ohm superconducting transmission line about 86 m long. Early measurements using the line in the shorted stub mode showed that small discontinuities in the line created voltage standing waves (VSWR's) which added to the dispersion. In the correlator circuit, the reflected power is absorbed by the matched source impedance (or the isolated port of a hybrid splitter) and is only re-reflected forward by additional discontinuities. Hence a correlator design is less sensitive to discontinuities than is the shorted stub design. A schematic of the 86 m superconducting line is shown in its liquid helium cryostat in Fig. 5-19. The superconducting line is wound into a coil 40 cm long and 10 cm diameter. In the present design, the helium cryostat must be refilled every two days. Figure 5-20 shows the notch dispersion obtained with this line in the 1-2 GHz band and the 2-4 GHz band. It has been found, for example, that the notch dispersion can be improved by use of carefully matched hybrid splitters and combiners. Research and development in superconducting transmission lines is in progress.

5.4.4 Travelling Wave Tubes (TWT's). The power amplifier stages in all our cooling systems are travelling wave tube amplifiers. Several commercial units are available in the 1-2 and 2-4 GHz bands with saturated output power ratings up to 200 watts. Travelling wave tubes are also available with power ratings above 1 kW.

Numerical studies show that in the stack tail momentum cooling system, the depth of the notches between the Schottky bands must be at least 40 db deep in order not to excessively heat the core. Even though notches of this depth can be obtained with the filters discussed above, the intermodulation distortion which occurs at higher power levels in TWT's can rapidly fill these in. Second-order intermodulation distortion can occur at the edges of the operating band of octave bandwidth TWT's. Operation of the TWT's in a push-pull mode however can reduce the second order IM products effectively. However, third order IM distortion can occur at midband frequencies and is not reduced by operating the TWT's in push-pull mode. Measurements using a single TWT and a notched white noise source show that the remaining notch depth at the TWT is only 13 db at full power (200 watts), but improves to about 30 db at 10 watts per TWT. This is shown in Fig. 5-21. The highly peaked Schottky spectrum produces a third order intermodulation distortion which is naturally peaked in rather than between the Schottky bands, providing another 12 db of notch depth at core frequencies. Hence we would need to use of the order of 160 TWT tubes to provide an estimated 1.6 kW to 160 kicker electrode pairs.

The potential cost saving of being able to run the TWT's at 100 W rather than 10 has stimulated interest in using superconducting correlator filters on the output of the TWT's. In principle, the filter need only provide a notch depth of the order of 20 db, the remainder being provided by the TWT IM distortion reduction of 13 db, and the IM form factor of the Schottky bands of the order of 12 db. As a correlator filter using a

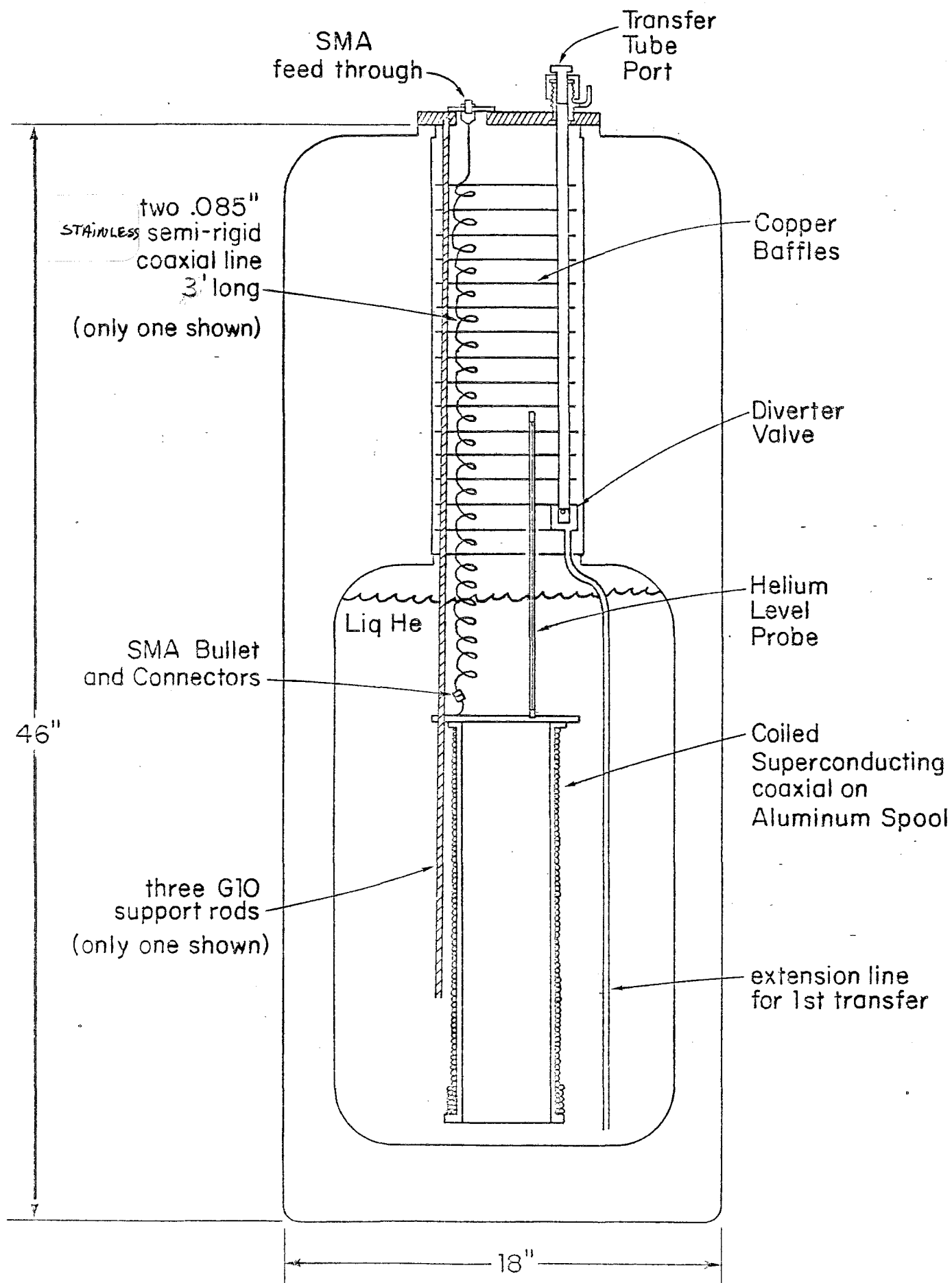


Fig. 5-19

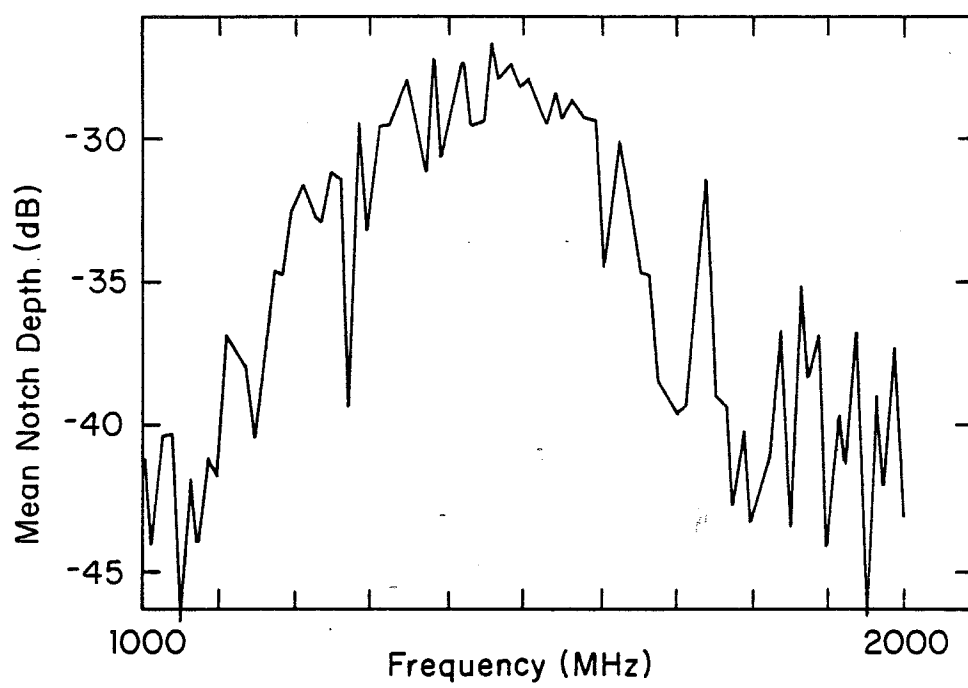
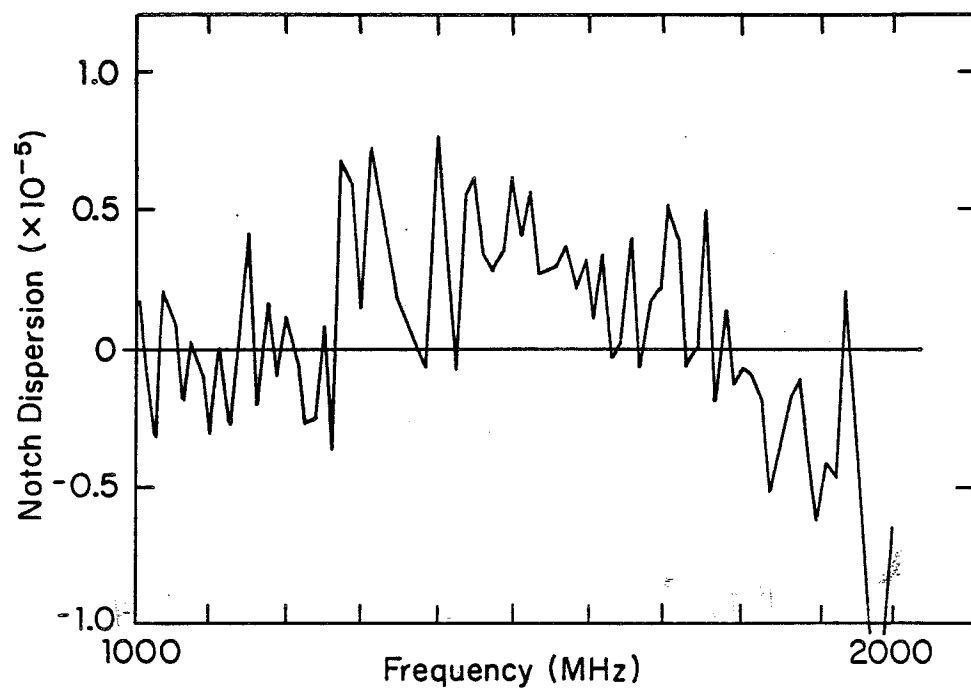


Fig. 5-20a

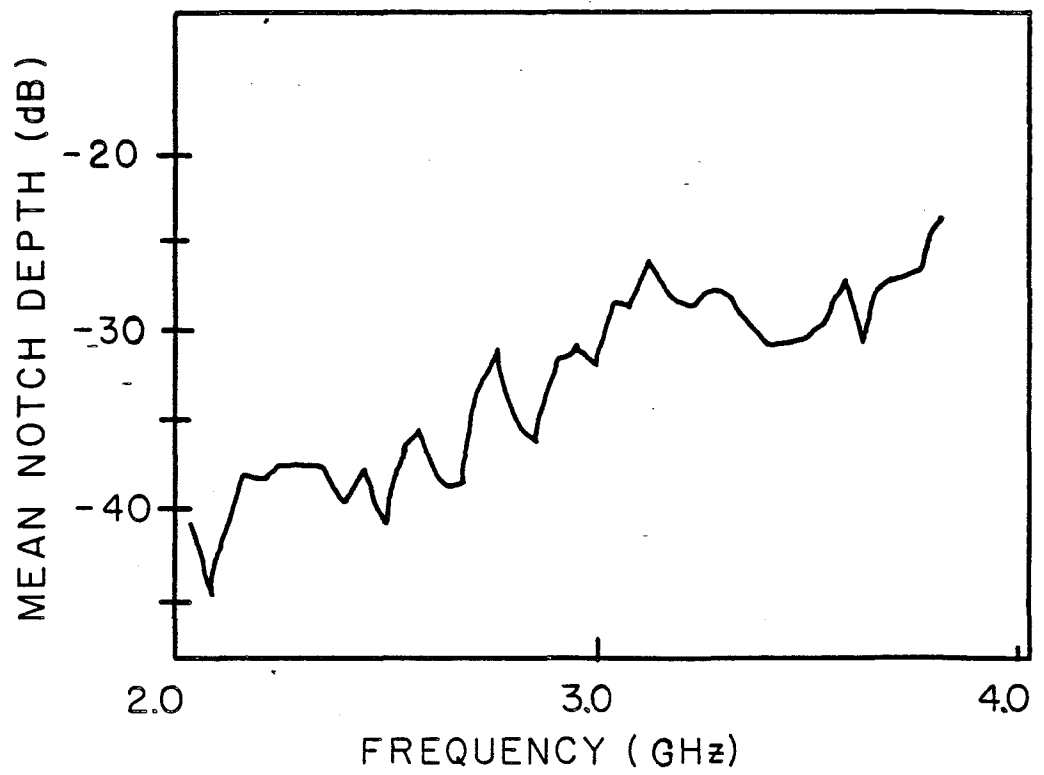
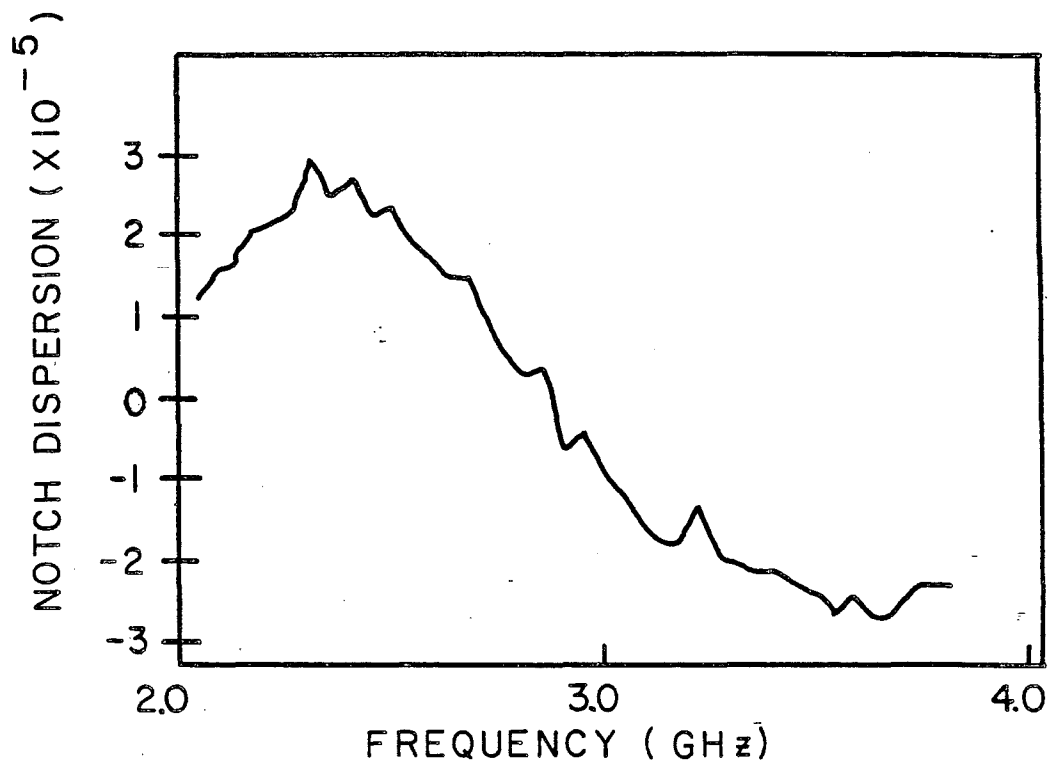


Fig. 5-20b

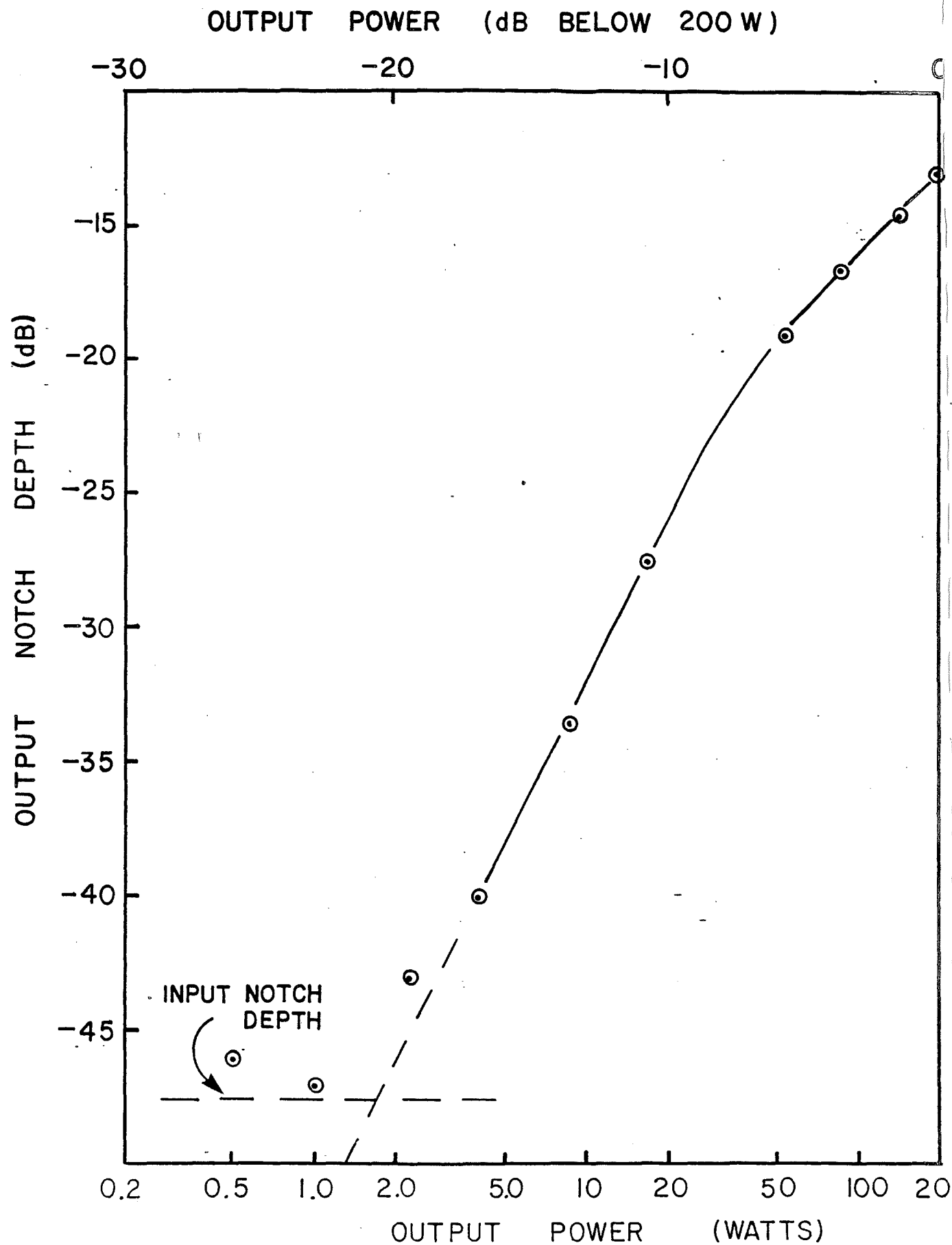


Fig. 5-21

superconducting transmission line is nearly lossless, we are investigating the possibility that such a filter could be used on the TWT outputs. Calculations show that the superconducting line could dissipate about 0.7 W/meter without quenching. Measurements presently show that attenuation in a 80-m line is less than 0.5 db at low power levels (corresponding to 0.3 W per meter at 200 W forward power). Calculations of the anomalous skin effect and dielectric losses yield similar values. Hence a research and development program is going on in this area. The present design is based on using the post TWT filters with each tube in a push-pull pair operating at about 40 watts. The circuit arrangement is shown in Fig. 5-22.

5.4.5 Kicker Electrode Assemblies The kicker electrode assemblies are conceptually similar to the pickup electrodes except that the printed circuit combiner board is now a power divider, and the terminating resistors must dissipate 5 to 7 W each (into a heat sink). Cryogenic pumping does not appear to be needed if the teflon circuit board is prebaked at 150 C, hence allowing the terminating resistors to be water cooled rather than liquid nitrogen cooled.

5.4.6 Other Considerations Most of the components in the stochastic cooling electronics have a limited bandwidth of about an octave, and this normally causes the frequency derivative of the phase delay to be frequency dependent. This leads to two parameters which need to be known for each element. The group delay (the slope of a straight line fit to the phase delay vs frequency data in the operating band) and the phase intercept (the zero frequency intercept of the above straight line) need to be measured for each component and accounted for the final system. Deviations from the average group delay at particular frequencies, as well as gain nonuniformity may have to be corrected. Special circuits to cause gain shaping and constant phase offset will need to be designed and built. In brief, the group delay is adjusted using cables so that the information signal arrives at the kicker at the correct time. The phase intercept correction assures that it arrives with the correct phase angle. The gain correction assures that the signal power is properly apportioned to each Schottky band.

The dispersion in the transmission lines carrying the signals across the ring also needs to be considered. In the 1-2 GHz stack tail systems, the largest diameter coaxial line which we can use is 1-5/8-in. diameter rigid line (air dielectric) as the TE_{11} mode propagates above 3.5 GHz. Calculations show that the expected dispersion is about 8° over the 1-2 GHz band for 150 m of line, based on the known skin effect losses. Preliminary measurements indicate that it may actually be somewhat larger, possibly due to excitation of evanescent modes at 2 GHz. In the 2-4 GHz range, the transmission line diameter would have to be limited to about 7/8", and the calculated dispersion would be about 18°. This line will probably be of the foam dielectric type, as the time delay requirements are not overly restrictive.

Stack Tail P,H,V pickups
Core P pickups

Core H and V pickups

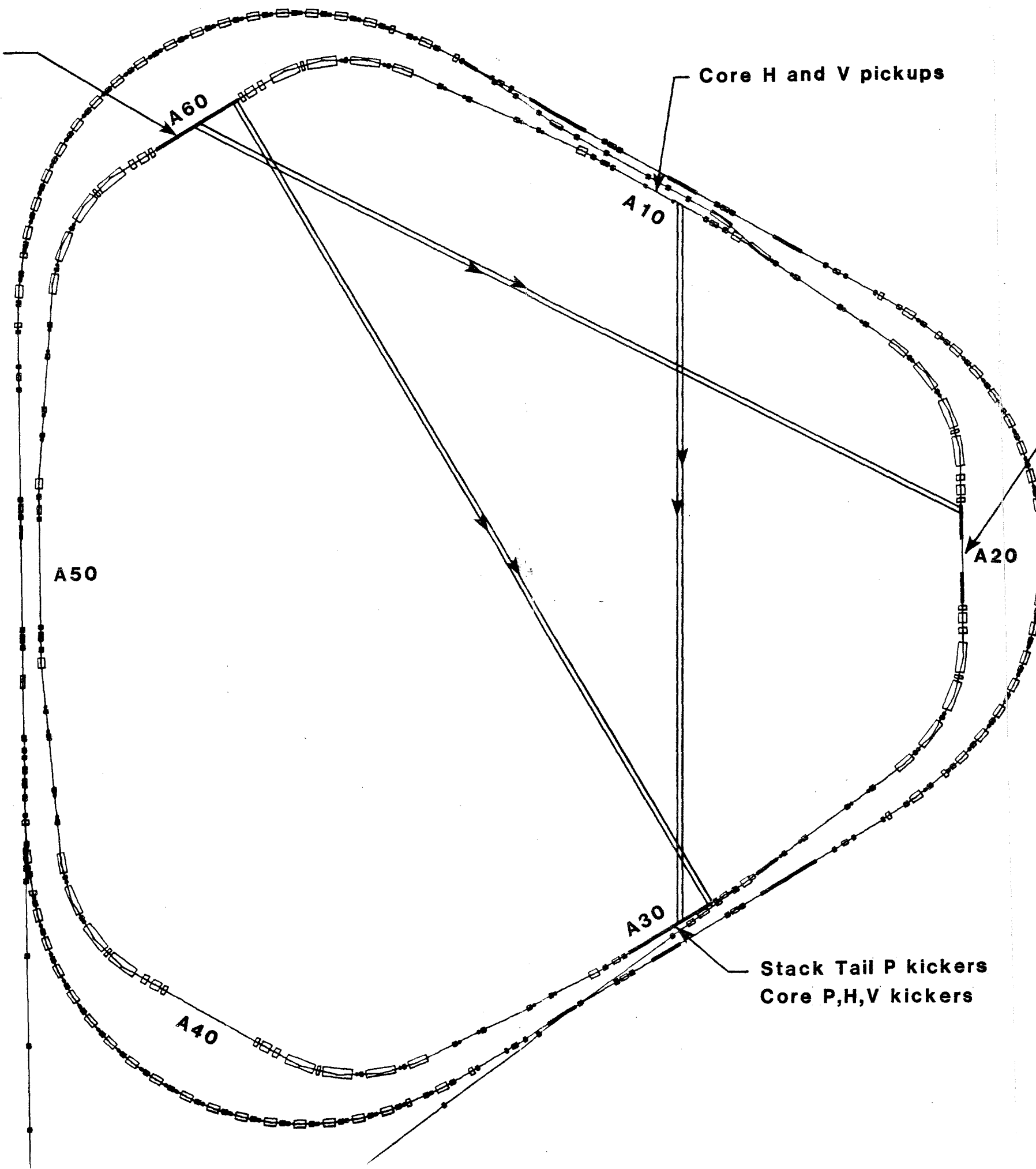
Stack Tail V and H kickers
10m dispersion

N ➤

Stack Tail P kickers
Core P,H,V kickers

**ACCUMULATOR STOCHASTIC
COOLING SYSTEM LAYOUT**

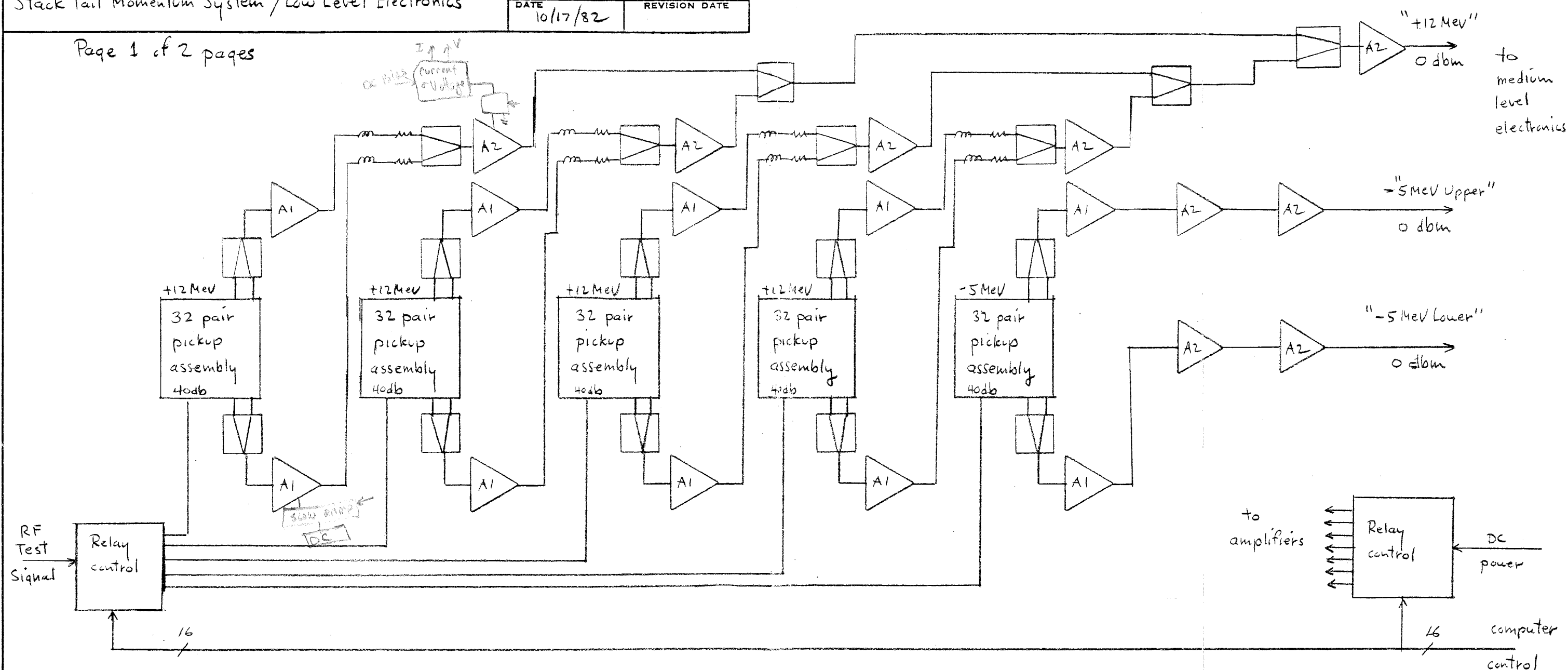
Fig. 5-23





SUBJECT
Stack Tail Momentum System / Low Level Electronics

Page 1 of 2 pages



Notes

32 pair pickup assembly

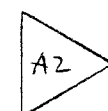
= 2.4 m long module containing 32 pair of 1-2 GHz loop couplers cooled to 77°K. Upper and lower electrode signals are separately brought to cooled GaAs fet amplifiers through vacuum chamber wall. A 40 db coupler built into assembly allows insertion of test signal.



= 2:1 power combiner



low noise GaAs fet amplifier cooled to 77°K. Gain about 30db. Equivalent noise temperature about 75°K



Commercial bipolar 1-2 GHz amplifier, Avantek # UTC-20-104 or equiv [gain = 23 db; equiv noise temp = 500°K]

m manually adjusted linear delay pad

m manually adjusted attenuator pad.

Fig. 5-24a

Figure 5-24a - Stack Tail Momentum Low Level Electronics

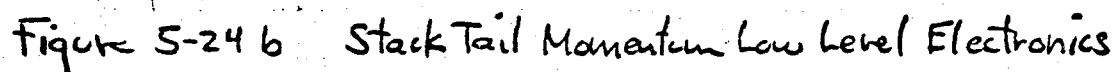
NAME	DATE	TIME	LOCATION	REMARKS
1				
2				
3				
4				
5				
6				
7				
8				
9				
10				
11				
12				
13				
14				
15				
16				
17				
18				
19				
20				
21				
22				
23				
24				
25				
26				
27				
28				
29				
30				
31				
32				
33				
34				
35				
36				
37				
38				
39				
40				
41				
42				
43				
44				
45				
46				
47				
48				
49				
50				
51				
52				
53				
54				
55				
56				
57				
58				
59				
60				
61				
62				
63				
64				
65				
66				
67				
68				
69				
70				
71				
72				
73				
74				
75				
76				
77				
78				
79				
80				
81				
82				
83				
84				
85				
86				
87				
88				
89				
90				
91				
92				
93				
94				
95				
96				
97				
98				
99				
100				

DATE _____

10/17/82

REVISION DATE

page 2 of 2 pages



5.4.7 Accumulator Stochastic Cooling System Layout There are 6 specific cooling systems in the Accumulator. Their location is shown in Fig. 5-23. Their basic operating parameters are outlined in Table 5-III. All 3 stack tail systems operate in the 1-2 GHz band, while the 3 core systems operate in the 2-4 GHz band. All kicker assemblies have been located remotely from the pickup electrodes to minimize coupling and feedback.

The largest system is the stack-tail momentum-cooling system, requiring about 1600 W of microwave power. The pickup electrodes are located in the 10 m dispersion short straight section A60, and the kickers in the zero dispersion long straight section A30. A block diagram of the low-level electronics is shown in Fig. 5-24a and b. Groups of 32 pickup electrodes are summed on an internal edge-supported teflon printed circuit board into low noise preamps. Signals are separately amplified for the upper and lower electrodes to allow for gain and phase correction, as well as for forming both sum and difference signals. Signal processing is done in the medium level of electronics as shown in Fig. 5-25. This includes 3 notch filters (superconducting correlators) with notch minima set at +4, -2, and -3 MeV relative to the core. After gain and phase corrections, the signals are amplified to about +20 dbm and transmitted across the ring to the high level electronics (TWT's). At present we estimate that 40 TWT's are needed if we can operate them at 40 W each and maintain a 30 db notch depth at the core frequency (this number includes the Schottky form factor of about 12 db). Post-TWT filters (superconducting correlators) would have to provide about 10 db additional.

The stack-tail betatron cooling systems derive their pickup signals from the stack tail momentum system as shown in Fig. 5-26. The kickers, however, are in straight Section A20, where the dispersion is about 10 m. These systems each require only about 20 W, and can be powered by a pair of TWT's without filtered outputs.

The core momentum system pickups are located in the high dispersion straight Section A60 along with the stack tail pickups. As indicated in Section 5.2.5 and Fig. 5-5, the core momentum pickups are double rows of pairs, each pair in sum mode. The difference signal of the two rows is then formed. These signals are processed as shown in Fig. 5-27 and sent to kickers in the zero dispersion straight section shared with the stack tail momentum kickers. This system requires about 10 W.

The core betatron system pickups are located in the zero dispersion straight section A10. The signals are processed as per Fig. 5-28 and also sent to kickers in zero dispersion straight section A30. Each system requires about 10 W.

Fig. 5-25

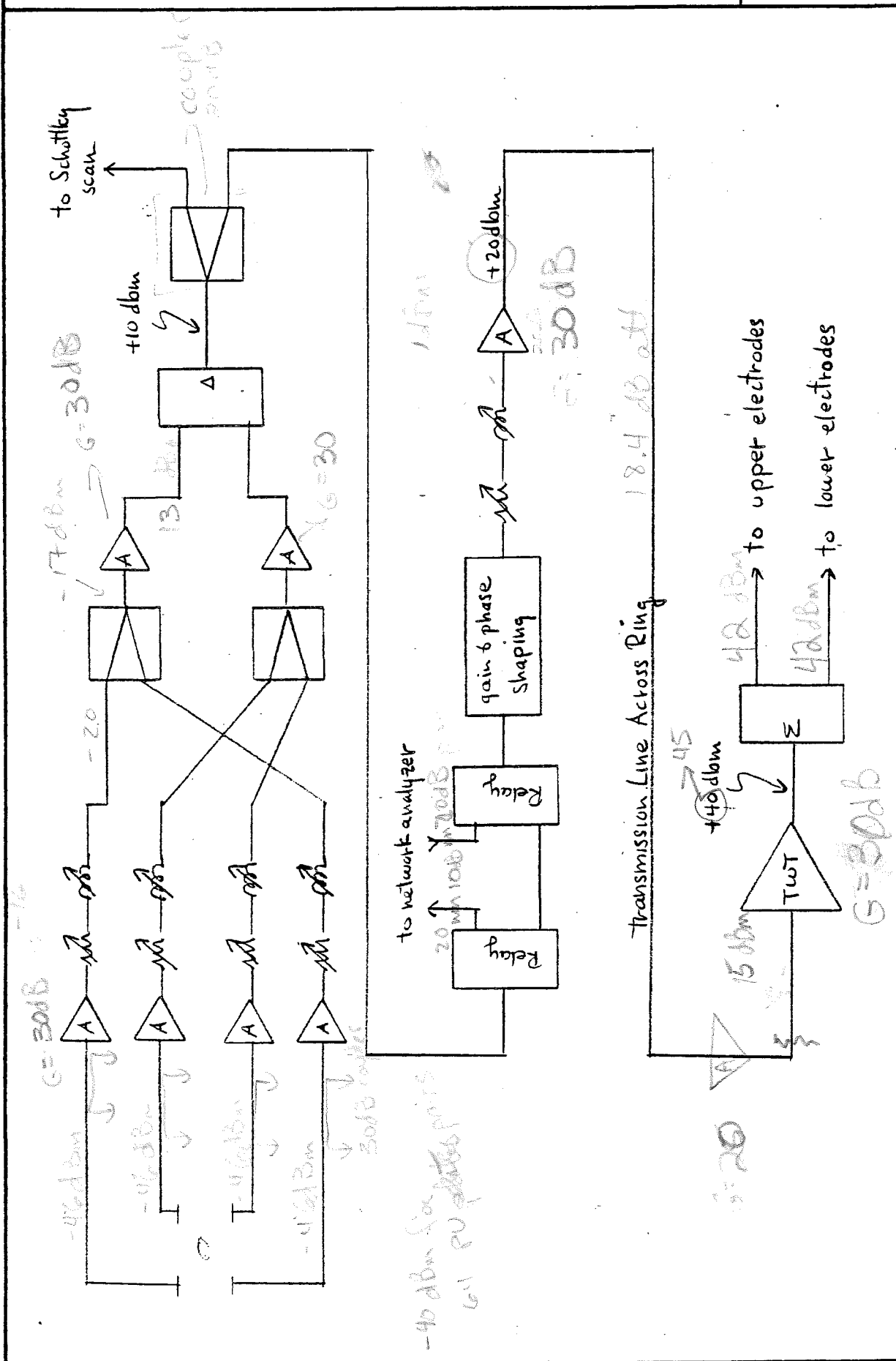


Figure 5-27. 2-4 GHz Core Momentum Cooling System

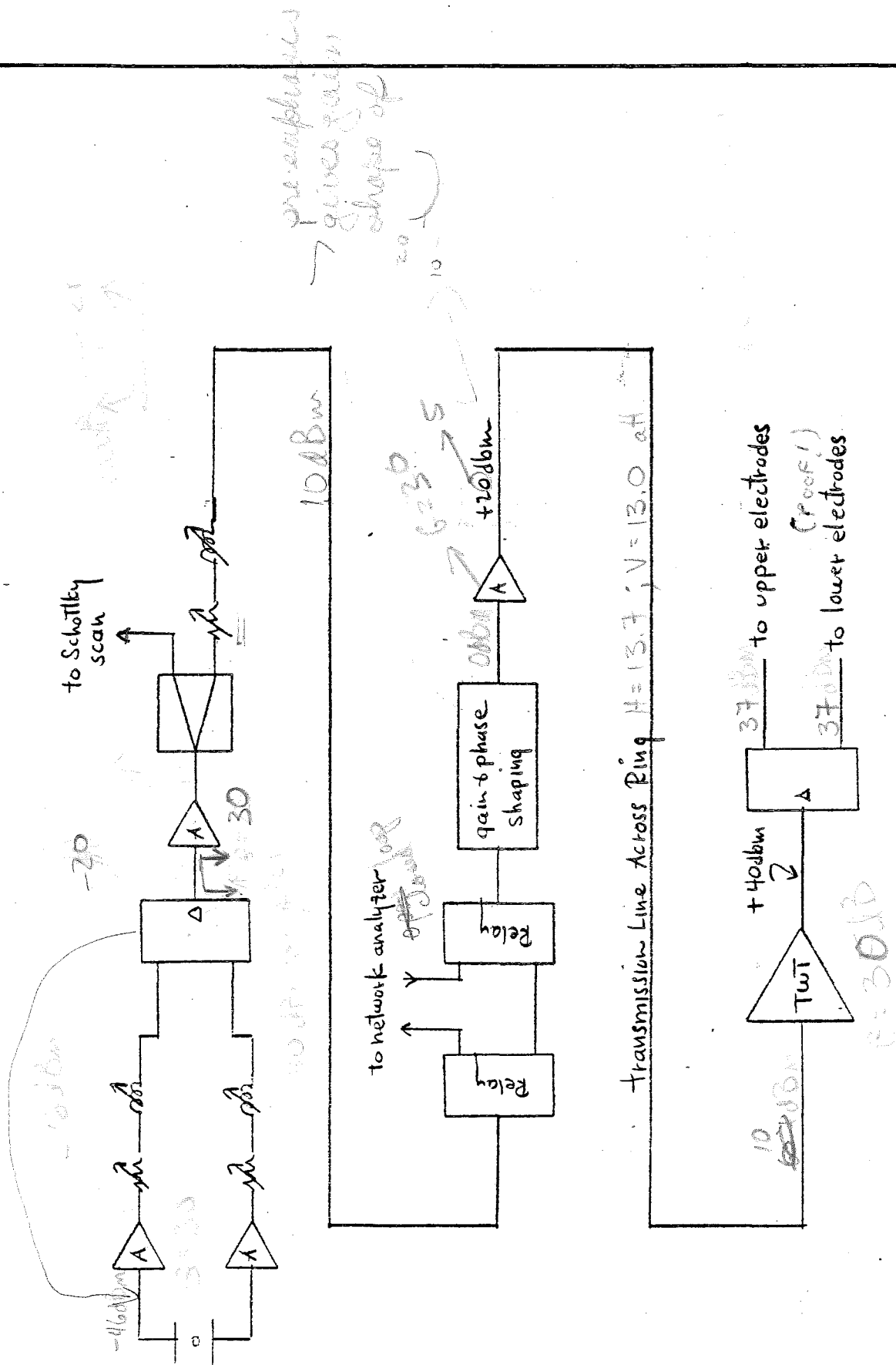


Figure S-28. 2-4 GHz Core Betatron Cooling System (2 systems required)

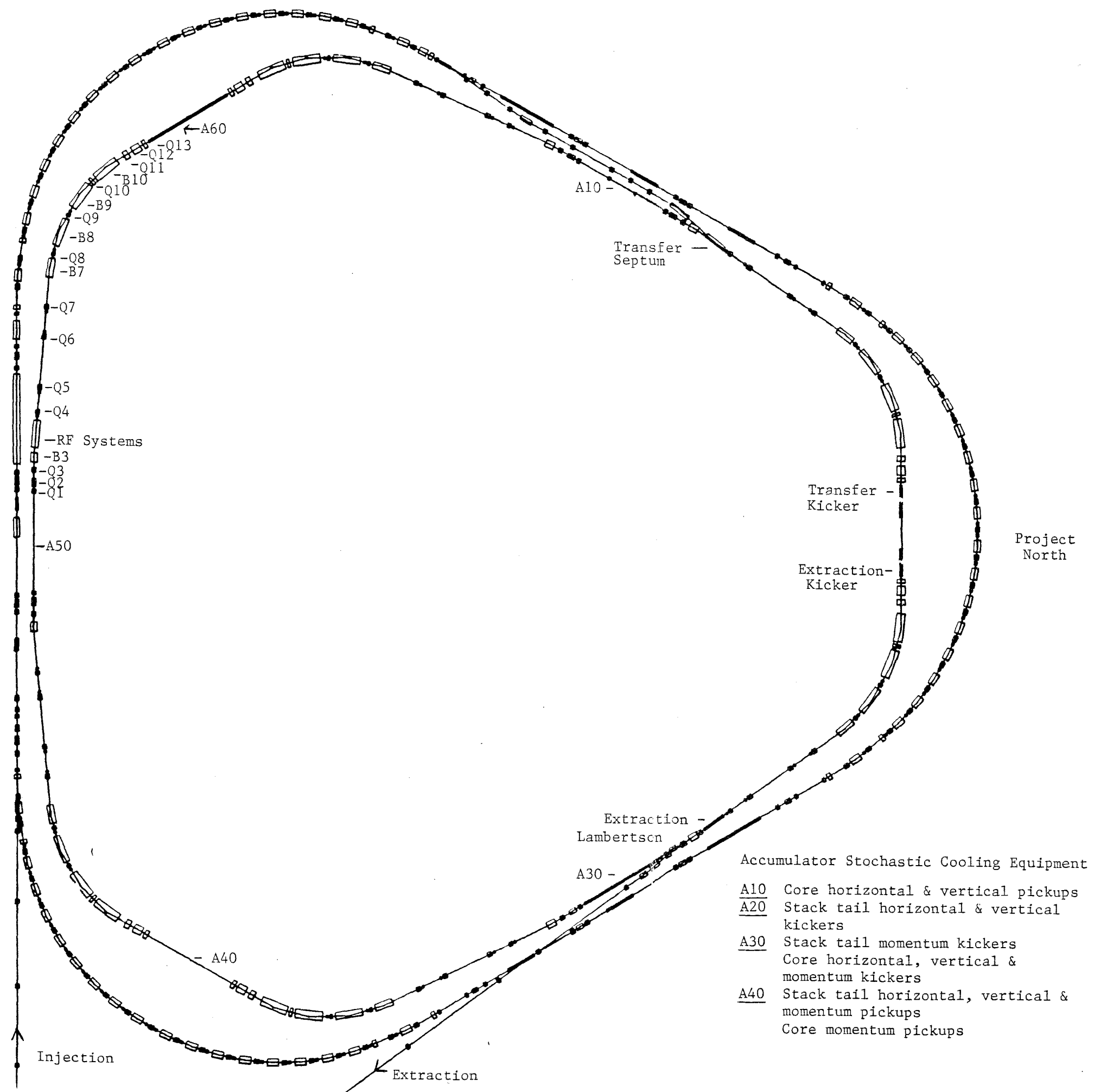
Table 5-III ACCUMULATOR STOCHASTIC COOLING SYSTEMS

	<u>Stack tail Momentum</u>	<u>Stack tail Betatron</u>	<u>Core Momentum</u>	<u>Core Betatron</u>
Frequency band	1-2GHz	1-2GHz	2-4GHz	2-4GHz
Number of pickup pairs (loops)	128+32+8+2	(32)	32 + 32	8(x2)
Pickup characteristic impedance	100 ohms	100 ohms	75 ohms	75 ohms
Pickup sensitivity s(0,0) or d(o,y)	.84(s)	1.94(d)	.66(s)	1.73(d)
Back termination thermal noise temperature	80 °K	80 °K	80 °K	80 °K
Amplifier equivalent thermal noise temperature	75 °K	75 °K	120 °K	120 °K
Amplifier gain (net)	145db	125db	95db	90db
Number of filters (superconducting correlators)	22(3)*	0	0	0
Output power				
-Schottky	1400W	10W(x2)	10W	10W(x2)
-thermal	200W	10W(x2)	0	0
-total	1600W	20W(x2)	10W	10W(x2)
Number of TWT's (200 watt saturated power)	40(160)*	1(x2)	1	1(x2)
Number of kicker pairs (loops)	160	32(x2)	32	8(x2)
Kicker characteristic impedance	100 ohms	100 ohms	75 ohms	75 ohms
Kicker sensitivity s(0,0) or d(o,y)	.84(s)	1.94(d)	.66(S)	1.73(d)
Spare time delay with air dielectric line ($\beta=.998$)	205 nsec	23 nsec	230 nsec	110 nsec
Spare time delay with heliax ($\beta=0.89$)	197 nsec	-34 nsec	166 nsec	63 nsec

*If post TWT filters are not used.

5.5 Accumulator Lattice

The lattice of the Accumulator has been designed to accept the injection of antiprotons every few seconds at an energy of 8 GeV, momentum stack and stochastically cool the antiprotons, accumulate over a period of several hours a very dense core of antiprotons, and, finally, extract a high-intensity beam to re-inject into the Main Ring and Tevatron. The requirements on the lattice are twofold. The Accumulator must be a high-class storage ring capable of reliable operation, and it must accommodate all the conditions imposed by the stochastic cooling systems. The second set of requirements has led to the general design of this ring and its somewhat unusual appearance, while those of the first set have also been incorporated. These general conditions are listed below:



ACCUMULATOR LAYOUT
Fig. 5-29

- (i) The momentum mixing factor must be correct.

$$|1/\gamma_T^2 - 1/\gamma^2| = 0.02$$

where γ_T is the transition gamma of the ring and γ is the relativistic gamma factor of the particle. Thus for 8-GeV kinetic energy the ring must have

$$\gamma_T = 5.4 \text{ or } 10.6$$

- (ii) There must be several long straight sections, some 16 meters long, with very small transverse beam sizes. Some of these must have zero dispersion, and the rest dispersion of ~ 10 m. This requirement leads to the lower choice of transition gamma.
- (iii) Betatron-cooling straight sections must be an odd multiple of $\pi/2$ apart in betatron phase. Pickup and kicker straight sections must be far enough apart physically so that a chord will be at least 75 nsec shorter than the arc for signal-transfer purposes.
- (iv) The β values of the lattice should be about the same for the horizontal and vertical planes in the straight sections.
- (v) The ring should match the Booster circumference.
- (vi) There should be easy injection and extraction schemes.
- (vii) The beam everywhere should be as small as possible, consistent with the large-dispersion straight sections.
- (viii) The ring must have very good chromaticity corrections, be situated far from any resonances, have tuning flexibility, and generally be a good storage ring.

The result of the above criteria is given below. The ring is a six-sided figure in which the bending has been concentrated to produce high values of dispersion in some straight sections and zero dispersion in others. This gives a machine of superperiodicity three with six 16-meter long straight sections, alternating between zero and ten meter dispersion. The machine is mirror symmetric about each straight section. The straight sections have small beta-functions in each plane, consistent with the aperture requirements needed for the stochastic cooling equipment and have the necessary phase relations. A plan view of the ring is shown in Fig. 5-29, the lattice functions for one sixth of the ring are plotted in Fig. 5-30 and the structure and lattice parameters are listed in Table 5-IV.

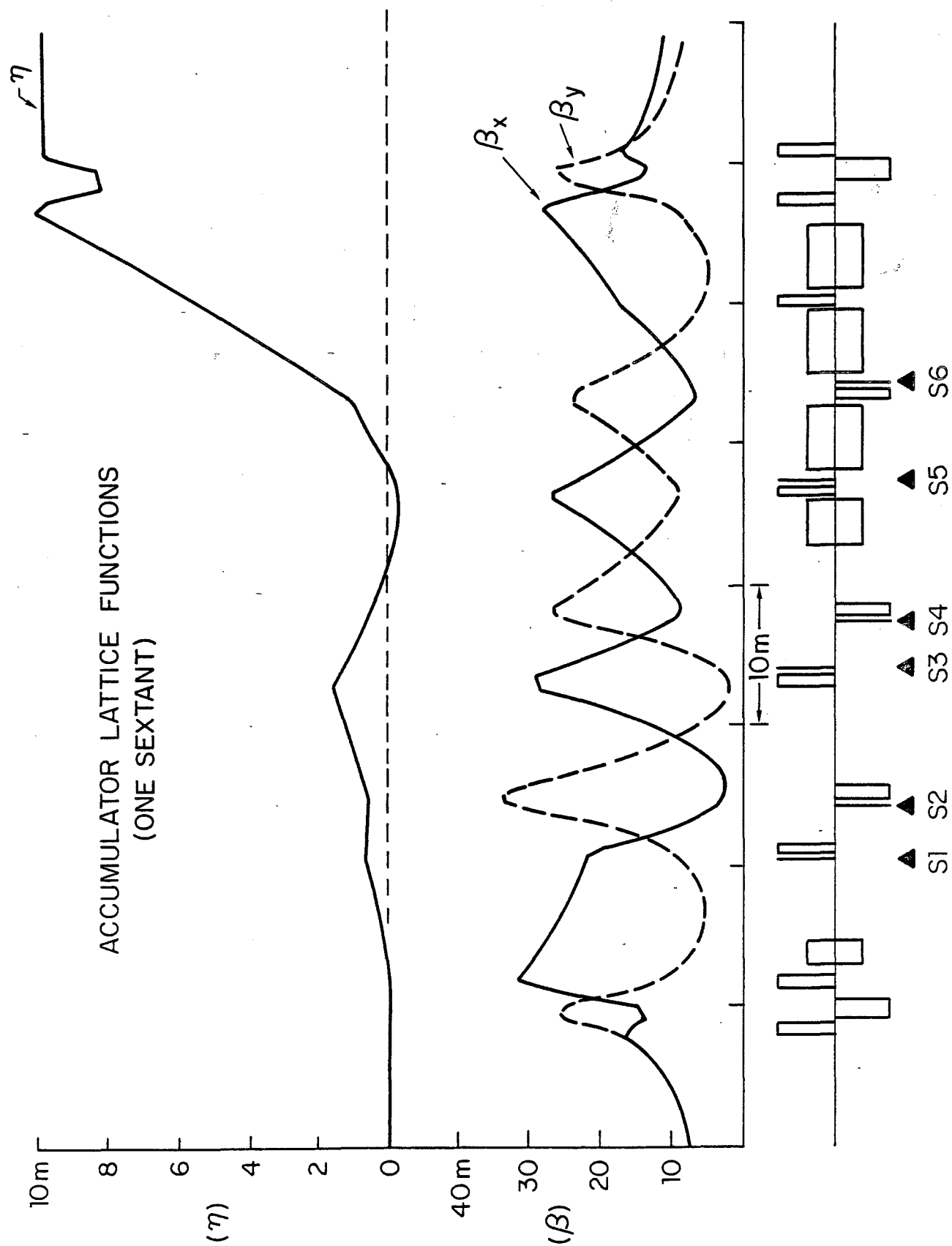


Fig. 5-30

Injection into and extraction from this machine are done in a similar manner. The injection orbit is displaced radially outward by approximately 0.8% in $\Delta p/p$. The shuttered kicker in the high-dispersion straight section is closed just before the p's are injected. The momentum displacement is enough to allow the injected beam to clear the shutter. Beam is transferred from the Debuncher ring via the 4-m long, 8-kG current septum magnet located at the upstream end of a zero-dispersion straight section. It arrives at the kicker and is kicked onto the injection orbit. The kicker is 2 m long and has a field of 500 G. The shutter is then opened and the beam is rf stacked. A drawing of the injected, stacked and accumulated beams at the position of the shuttered kicker is shown in Fig. 5-31. The injection and extraction positions are shown on Fig. 5-29.

Extraction from the Accumulator is essentially identical to the injection except the beam is extracted vertically with a Lambertson magnet, raising the beam four feet above the ring level to be transported back to the Main Ring. A layout of the extraction straight section is shown in Fig. 5-32.

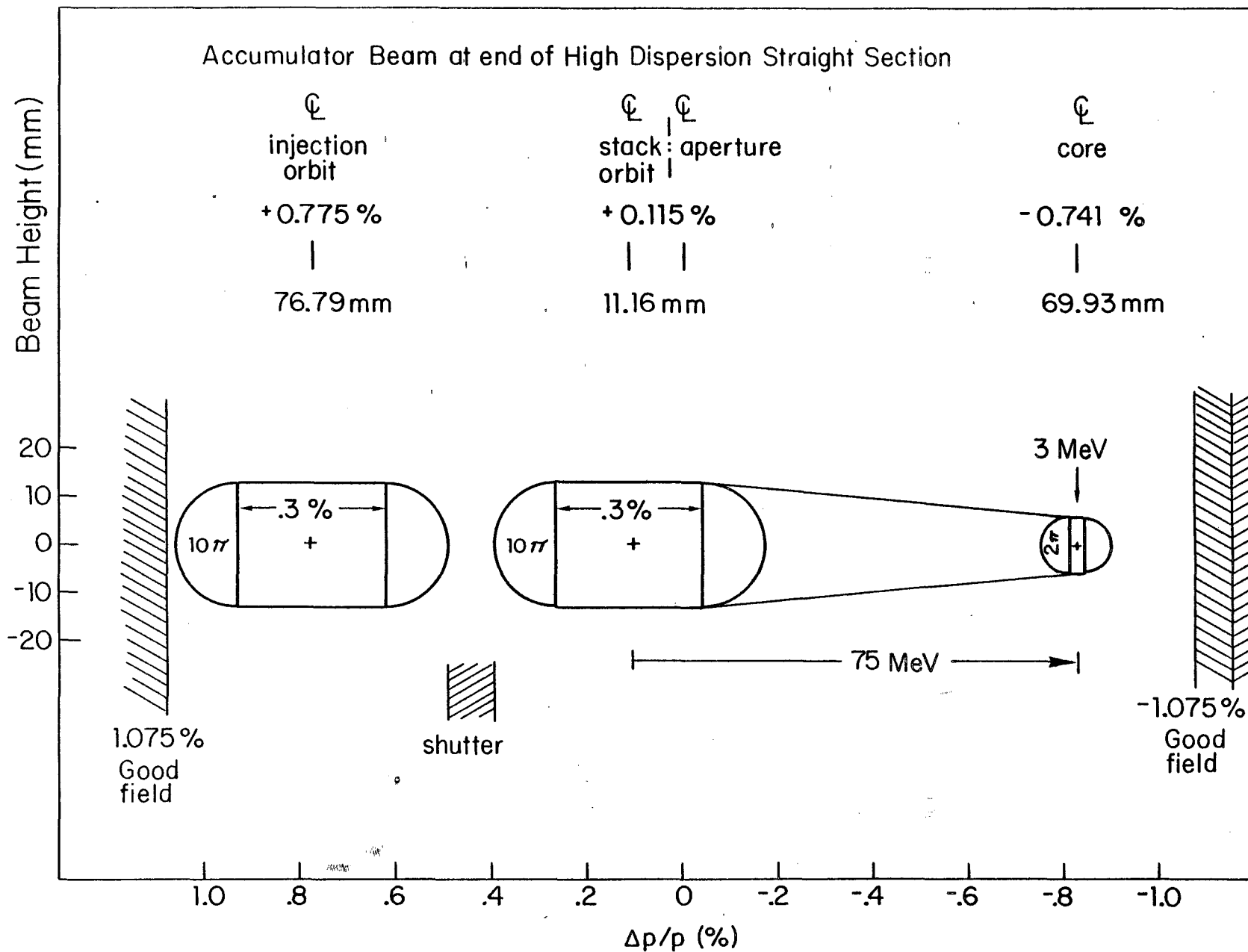


Fig. 5-31

- (i) The momentum mixing factor must be correct.

$$|1/\gamma_T^2 - 1/\gamma^2| = 0.02$$

where γ_T is the transition gamma of the ring and γ is the relativistic gamma factor of the particle. Thus for 8-GeV kinetic energy the ring must have

$$\gamma_T = 5.4 \text{ or } 10.6$$

- (ii) There must be several long straight sections, some 16 meters long, with very small transverse beam sizes. Some of these must have zero dispersion, and the rest dispersion of ~ 10 m. This requirement leads to the lower choice of transition gamma.
- (iii) Betatron-cooling straight sections must be an odd multiple of $\pi/2$ apart in betatron phase. Pickup and kicker straight sections must be far enough apart physically so that a chord will be at least 75 nsec shorter than the arc for signal-transfer purposes.
- (iv) The β values of the lattice should be about the same for the horizontal and vertical planes in the straight sections.
- (v) The ring should match the Booster circumference.
- (vi) There should be easy injection and extraction schemes.
- (vii) The beam everywhere should be as small as possible, consistent with the large-dispersion straight sections.
- (viii) The ring must have very good chromaticity corrections, be situated far from any resonances, have tuning flexibility, and generally be a good storage ring.

The result of the above criteria is given below. The ring is a six-sided figure in which the bending has been concentrated to produce high values of dispersion in some straight sections and zero dispersion in others. This gives a machine of superperiodicity three with six 16-meter long straight sections, alternating between zero and ten meter dispersion. The machine is mirror symmetric about each straight section. The straight sections have small beta-functions in each plane, consistent with the aperture requirements needed for the stochastic cooling equipment and have the necessary phase relations. A plan view of the ring is shown in Fig. 5-29, the lattice functions for one sixth of the ring are plotted in Fig. 5-30 and the structure and lattice parameters are listed in Table 5-IV.

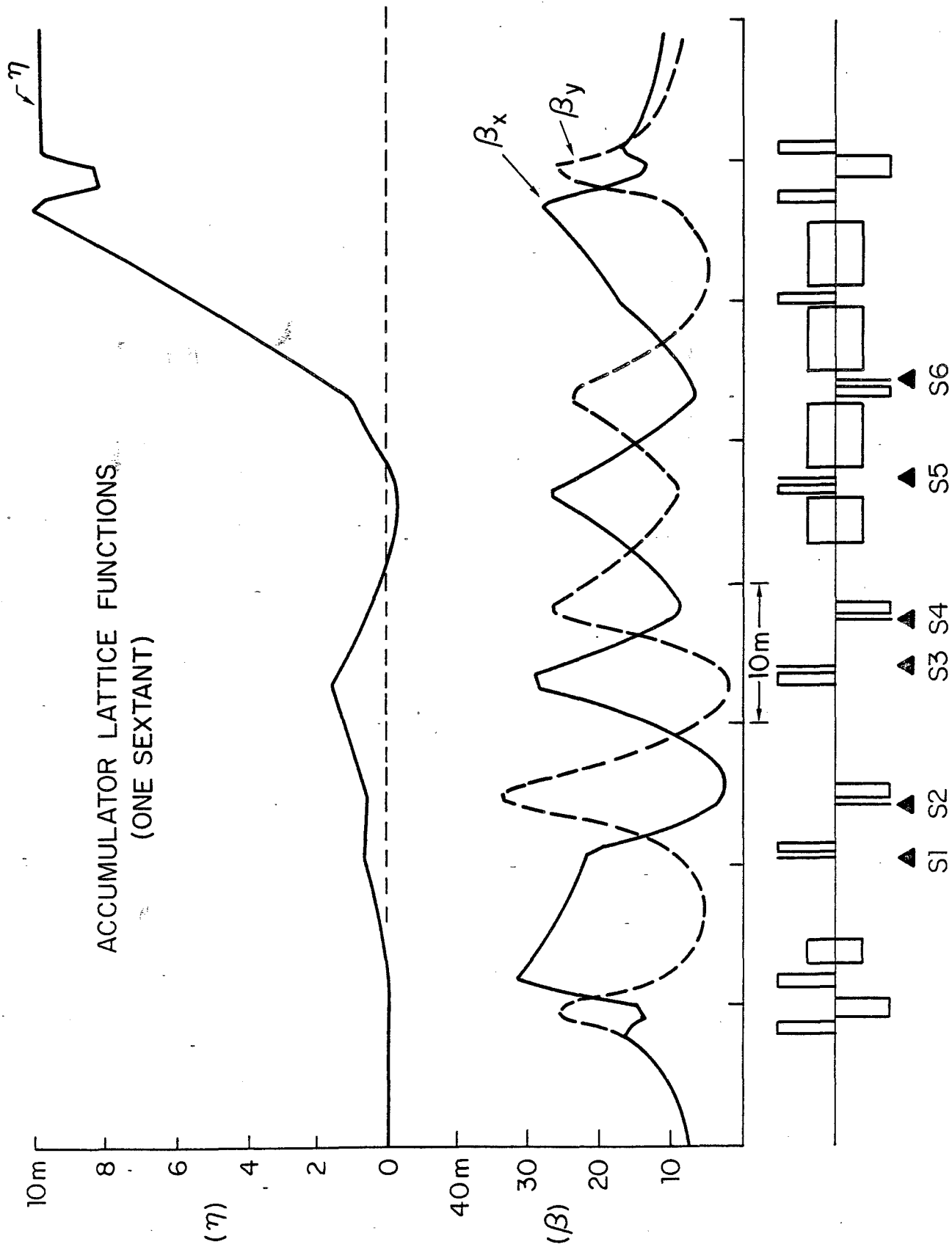


Fig. 5-30

Injection into and extraction from this machine are done in a similar manner. The injection orbit is displaced radially outward by approximately 0.8% in $\Delta p/p$. The shuttered kicker in the high-dispersion straight section is closed just before the p 's are injected. The momentum displacement is enough to allow the injected beam to clear the shutter. Beam is transferred from the Debuncher ring via the 4-m long, 8-kG current septum magnet located at the upstream end of a zero-dispersion straight section. It arrives at the kicker and is kicked onto the injection orbit. The kicker is 2 m long and has a field of 500 G. The shutter is then opened and the beam is rf stacked. A drawing of the injected, stacked and accumulated beams at the position of the shuttered kicker is shown in Fig. 5-31. The injection and extraction positions are shown on Fig. 5-29.

Extraction from the Accumulator is essentially identical to the injection except the beam is extracted vertically with a Lambertson magnet, raising the beam four feet above the ring level to be transported back to the Main Ring. A layout of the extraction straight section is shown in Fig. 5-32.

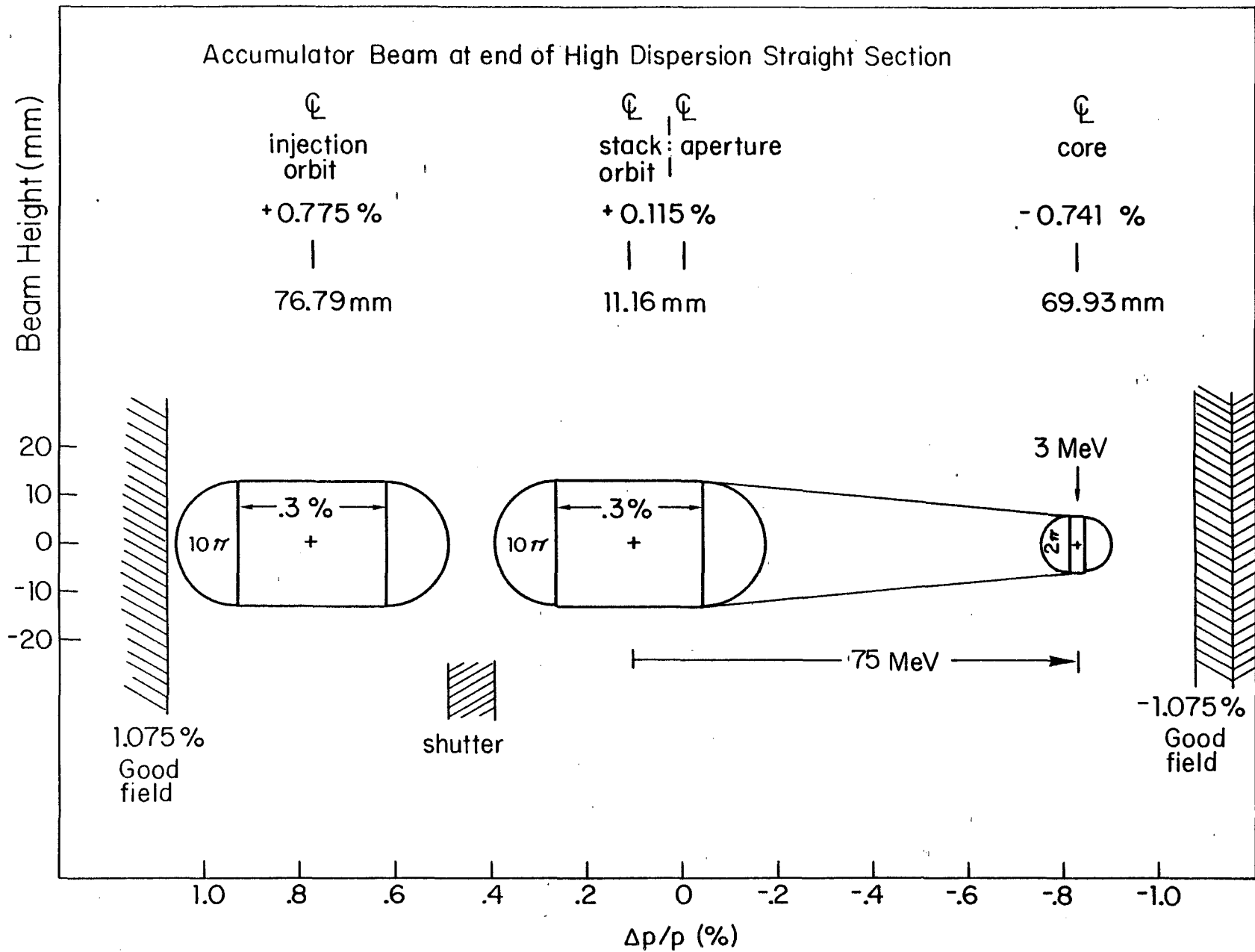
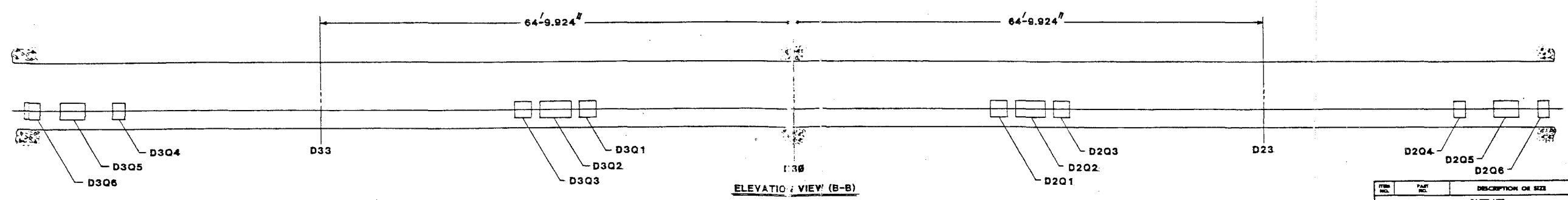
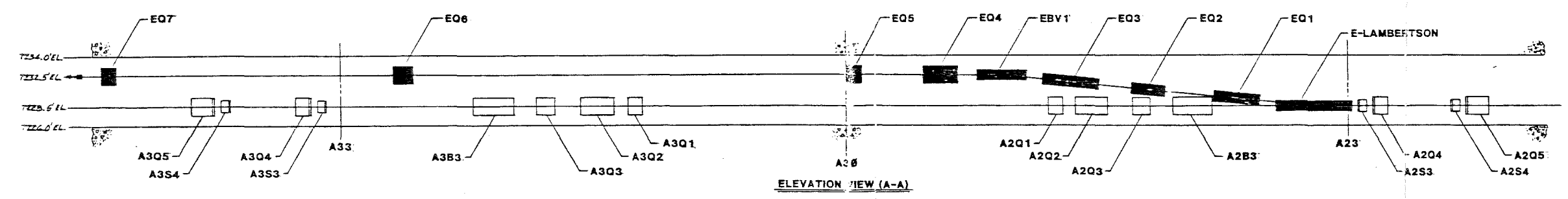
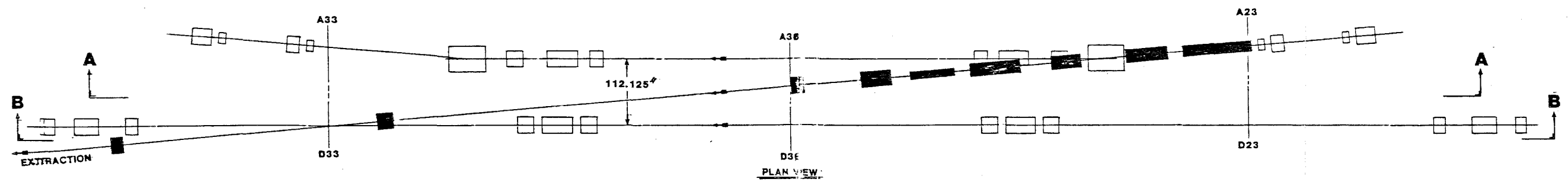


Fig. 5-31



EXTRACTION STRAIGHT SECTION

ITEM NO.	PART NO.	DESCRIPTION OR SIZE	QTY.
PARTS LIST			
UNLESS OTHERWISE SPECIFIED		ORIGINATOR	G. JOHNSON
FRACTIONS (DECIMALS) ANGLES		SCALE	1/4"=1'-0"
1.	2.	3.	4.
1. BREAK ALL SHARP EDGES		APPROVED	
2. NO HOLE SCALE DIMS.		USED ON	
3. DIMENSIONING IN ACCORD WITH ASME Y14.5		MATERIAL	
✓ BALL ALL ROUNDED SURFACES			
PERM NATIONAL ACCELERATOR LABORATORY UNITED STATES DEPARTMENT OF ENERGY			
Figure 5-32			
SCALE	PLANE	DRAWING NUMBER	REV.
1/4"=1'-0"			

Table 5-IV. ACCUMULATOR PARAMETERS

1. General

Kinetic Energy	7.9 GeV
Bend field	16.85 kG
Magnetic bend radius (ρ)	17.46 m
Radius	75.45 m
Revolution time	1.59 μ sec
Superperiodicity	3
Focusing structure	Separated function FODO normal cell
Nominal working point	

ν_x	6.61
ν_y	8.61

Nominal chromaticity

ξ_x	-9.12
ξ_y	-12.71

Chromaticity Corrected Parameters

	Injection Orbit	Stacking Orbit	Core Orbit
Kinetic Energy (GeV)	8.00	7.94	7.87
$\Delta p/p$ (%)	+0.775	+0.115	-0.741
ν_x	6.61	6.61	6.61
ν_y	8.61	8.61	8.61
ξ_x	-0.14	-0.21	-0.14
ξ_y	-2.79	-0.36	3.59
γ_T	5.09	5.33	5.65
$1/\gamma_T^2 - 1/\gamma^2$	0.028	0.024	0.020

2. Magnets

Number of dipoles	30
Number of quadrupoles	78
Number of sextupoles	36

A. Small aperture dipoles

	<u>Length</u>	<u>Field</u>	<u>Number</u>
(B3)	5.0 ft.	16.89 kG	6
(B7)	10.0 ft.	16.89 kG	6
(B8)	15.0 ft	16.89 kG	6

B. Large aperture dipoles

(B9)	15.0 ft.	16.89 kG	6
(B10)	15.0 ft.	16.89 kG	6

C. Small aperture quadrupoles

(Q1)	22.5 in	99.23 kG/m	6
(Q2)	50.7 in	-99.23 kG/m	6
(Q3)	27.6 in	99.23 kG/m	6
(Q4)	20.8 in	99.23 kG/m	6
(Q5)	32.0 in	-99.23 kG/m	6
(Q6)	27.6 in	99.23 kG/m	6
(Q7)	27.6 in	-99.23 kG/m	6
(Q8)	18.0 in	99.23 kG/m	6
(Q9)	18.0 in	99.23 kG/m	6

D. Large aperture quadrupole

(Q10)	18.0 in	30.95 kG/m*	6
(Q11)	33.3 in	88.63	6
(Q12)	58.5	-88.63	6
(Q13)	24.4 in.	88.63	6

*Q10 will be built with missing turns to run in series with the other large aperture quadrupoles.

E. Sextupoles

(S3)	12.0 in.	728.56 kG/m ²
(S4)	12.0 in.	-869.76
(S61)	12.0 in.	437.11
(S62)	12.0 in.	-869.76
(S8)	12.0 in.	-728.53
(S9)	12.0 in.	-217.44

3. Structure

A. Drift Lengths

LS	314.9 in.
01	19.8
02	39.8
03	35.6

04	227.5
05	103.6
06	289.9
07	116.5
08	174.7
010	55.5
011	29.2
012	19.6
LS*	313.1
0S	12.0
0	20.0
00	24.0

B. Sextant Structure (s)

LS (Q1)	01 (Q2)	02 (Q3)	03 (B3)	04 (S3)
0S (Q4)	05 (S4)	0S (Q5)	06 (Q6)	0S (S61)
07 (S62)	0S (Q7)	08 (B7)	0 (Q8)	0S (S8)
00 (B8)	0 (Q9)	0S (S9)	00 (B9)	0 (Q10)
0 (B10)	010 (Q11)	011 (Q12)	012 (Q13)	LS*

C. Ring Structure

S(S)S(S)S(S)

Length of central orbit

474.0702 m
1555.348 ft

4. Aperture and Acceptance

Maximum Lattice functions (central orbit)

	β_x	β_y	α_p
LS (center)	7.78 m	7.60 m	0.00 m
LS* (center)	11.00	8.22	9.67
Small aperture dipole	29.78	21.32	0.83
Large aperture dipole	25.17	7.46	8.74
Small aperture quad	30.23	34.13	1.56
Large aperture quad	27.33	27.43	9.92
Sextupole	26.02	27.55	1.39

Required beam

Emittance

Momentum aperture

$\epsilon_x = \epsilon_y = 10\pi$ mm-mrad
 $\Delta p/p = 2.30\%$

Beam Size

	A_x	A_y
Small aperture dipole	52.4 m	29.2 mm
Large aperture dipole	219.6	17.3
Small aperture quadrupole	68.3	36.9

Large aperture quadrupole	246.3	33.1
Sextupole	62.1	33.2

5.6 RF Stacking System

With the injection shutter closed, antiprotons are injected from the Debuncher ring with a total momentum spread of about 0.2%. The energy spread (18 MeV) and the Accumulator ring revolution period (1.59 μ sec) result in an injected longitudinal emittance of about 29 eV-sec. This beam is bunched adiabatically and decelerated by 0.7% to the end of the tail of the previously stacked antiprotons where it is released by adiabatic debunching. Adiabatic capture can begin immediately following injection and can proceed during the time required for removal of the shutter, about 0.1 seconds.

With a phase-oscillation period of 10 msec and a deceleration time of 30 msec, the entire operation of establishing a moving bucket, deceleration, and adiabatic debunching can be accomplished within 0.1 seconds after the beam is injected.

At frequencies well below the GHz cooling band, the cooled core may be subject to longitudinal instabilities induced by the shunt impedance of the stacking rf cavity or other similar device. The stability criterion resulting from various dispersion analyses can be written in a limiting form

$$\left| \frac{Z}{n} \right| \leq F \frac{(\Delta E/E)^2 E_s \eta}{eI},$$

where the form factor F is about unity for a conservative estimate of the stability of a roughly Gaussian distribution and ΔE is the full width at half maximum.

The cooled core has the parameters

Δp FWHM	4.1 MeV/c
N (antiprotons)	4.3×10^{11}
I	4.32×10^{-2} Amperes
η	0.02

With these parameters the critical value of Z/n is about 1000 ohms. The rf voltage required to establish a given phase-space increases linearly with the harmonic number and, because the power required is $V^2/2R_{sh}$, the

required rf power increases linearly, given the stability limit on the shunt impedance. Consequently, to minimize the cost, size, and complexity, it would appear that rf stacking should be done at the lowest possible harmonic number. On the other hand, very low harmonic numbers and very low voltages result in excessively long synchrotron periods that are not consistent with the rapid production cycling rate. An adequate compromise appears to be $h = 10$, 6.289 MHz. An rf system at this frequency with an effective shunt impedance of $10 \text{ k}\Omega$ meet the requirement that $Z/h \approx 1 \text{ k}\Omega$. The parameters associated with rf stacking at $h = 10$ are listed in Table 5-VI. The shunt impedance of the bunching cavity is in agreement with this stability requirement for harmonics of interest.

Table 5-V. RF STACKING PARAMETERS

Injected Longitudinal Emittance	29 eV sec
Stacking rf Total Bucket Area	30 eV sec
Stationary Bucket RF Voltage	7.8 keV
Stationary Bucket Phase Oscillation Period	9.4 msec
$\Delta p/p$ Required for Stacking	0.7%
Δ (cp)	62.2 MeV
Deceleration Synchronous Phase Angle	10 degrees
$\Gamma = \sin \phi_s$	0.1736
Moving Bucket Factor $\alpha(\Gamma)$	0.6964
RF Voltage During Acceleration	16.1 kV
Time Required for Deceleration	30.2 msec
Number of Cavities	1
Cavity Structure	40 NiZn Ferrite Cores
Cavity Small Signal Shunt Impedance	10 $\text{k}\Omega$
Peak RF Power Requirement	10 kW
Average RF Power Requirement (Cooling, etc)	1 kW
Harmonic Number	10
RF Starting Frequency	6.28695 MHz
$\eta = \gamma_t^{-2} - \gamma^{-2}$	0.019-0.023
β	0.99447
Injection Orbit Circumference	474.202 m
Stacking Efficiency*	98%

*Based on computer simulation

5.7 Accumulator Magnets

The main magnet system consists of 30 dipoles and 78 quadrupoles. In Table 5-IV is shown a list of magnets, lengths, strengths and required apertures. The required apertures were calculated assuming construction tolerances of 2.5×10^{-4} (relative standard deviation) for dipole strengths, dipole level angles (radians), and quadrupole random position

errors (meters). Sufficient space is allowed for at least 4σ , where σ is the standard deviation of the expected orbit position error, or the beam emittance plus momentum spread plus 10 mm whichever is larger. In addition, space is left for 4 mm (thickness plus deflection) vacuum chamber thickness and 5 mm insulation thickness. Several mm must be included also for copper heat transporters to bake the chamber (dipoles) with heaters on the edges.

There are three lengths of dipoles, all with field strengths of 1.689 T. There are 2 different apertures: 3 different lengths in the smaller aperture; one, in the larger. Their properties are described in Table 5-VII. Because of the large sagitta, these magnets will be curved. The coils will be made of four pancakes plus single-layer saddle coils.

There are 13 different quadrupoles, of two different profiles. Q1-Q9 have poletip radii of 43.3 mm and 6 different lengths. Q10-Q13 have poletip radii of 84.1 mm and four different lengths. The properties of these quadrupoles are shown in Table 5-IX. Each quadrupole will have a shunt with capability of about 10% of the quadrupole strength. The coils are fabricated in individual layers and assembled on the quad half cores, which are then assembled as a complete magnet.

There are 30 sextupole magnets of one kind. The maximum strength is 120 T/m, which permits the poles to be parallel-sided. A coil can be made of one flat pancake. These magnets are divided in 4 families which are operated on 4 individual current busses. Their (maximum) specifications are shown in Table 5-VIII.

Table 5-VII. DIPOLES

Lengths	4.572	3.048	1.524	m
Outside dimensions				
gap	60	60	60	m
Good field aperture	100	100	100	mm
Conductor				
Pancake coils	1"x1.25", 0.375" hole dia., 1/16" corner, 1.1362 in. area			
Saddle coils	1.343"x0.787", 0.578" hole dia., 1/16" corner, 0.7911 in.			
Turns				
Pancake coils	56			
Saddle coils	16			
Conductor lengths				
Pancake coils	567.5	400	229.5	m
Saddle coils	182.5	134	85.3	m
Total conductor length	750	534	315	m
Cu Wt	10,769	7,666	4,520	lb
Current	1.181	1.181	1.181	kA
Resistance(43°C)	19.2	13.67	8.06	mΩ
Power	26.8	19.6	11.24	kW

Total dipole power	669			kW
Total Cu Wt	267			klb
Full cross section	0.615			m ²
Fe area				
FeWt,	48	42	20.6	x10 ³ lb
Total Fe wt	1.624			x10 ⁶ lb

Table 5-VIII. ACCUMULATOR QUADS (LARGE BORE)

Lengths	0.178 to 1.274	0.457 to 1.274	m
	total 16.3	total 37.6	m
Poletip radius	84.1	43.27	mm
Conductor	0.82 square	0.4096 square	in.
Total conductor length	24,228	47,083	ft
(all magnets)			
Cu Wt	35,565	27,344	lb
Current	810A	202.5A	A
Resistance	0.442	3.354	Ω
(all magnets)			
Power	290	137.7	kW
(all large quads)			
Full cross section	0.476	0.183	m ²
(Fe area)			
FeWt	134.5	119.4	10 ³ lb

Table 5-IX ACCUMULATOR SEXTUPOLES

Max. B"	120	T/m ²
l eff	0.3	m
poletip radius	50	mm
NI	2000	AT/Pole
Max. I.	200	A
N	10	Turns
Conductor	(3.294") ² with 0.181" hole	
Current density	4.0	A/mm
R	19	m Ω
Max. voltage drop	3.8	volt
Max. ohmic loss	760	watt
Weight, cu	50	lb
Fe	450	lb
No. of magnets	36	
Power supply	1 200A x 50V (12-magnets)	
	2 200A x 50V (12-magnets)	
	3 120A x 15V (6-11)	

4 50A x 6V (6-11)

5.8 Accumulator Vacuum System

5.8.1 Vacuum Requirements. The base pressure is determined by the effects of the residual gas on the accumulated antiproton beam. These effects include particle loss by single Coulomb scattering and nuclear interactions, beam heating by multiple Coulomb scattering, energy loss by ionization, and effects of neutralization by positive ions attracted to the negative beam.

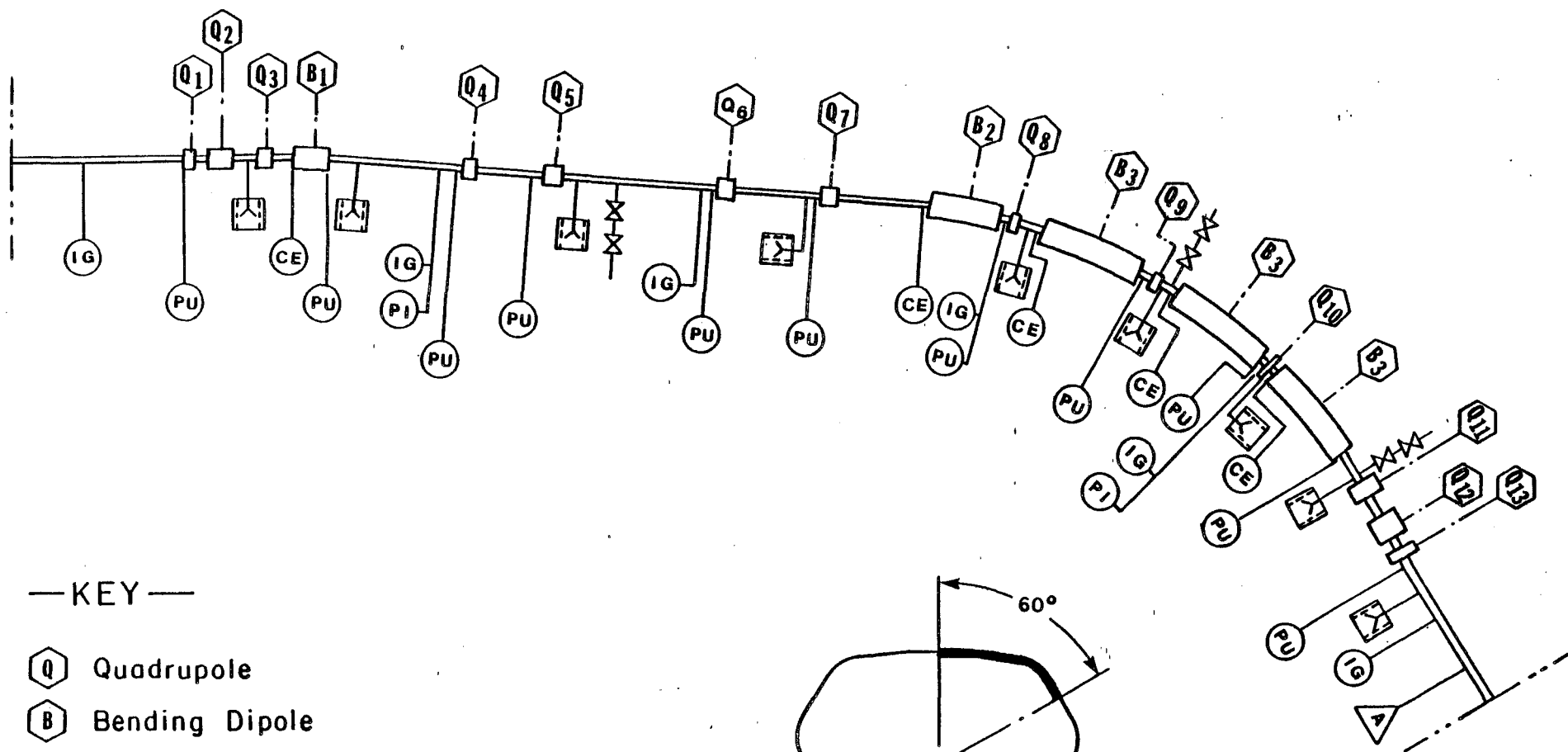
A detailed analysis has been made¹⁰ of these effects. As a result, the system is designed for a nominal pressure of 3×10^{-10} Torr (nitrogen equivalent). At this pressure, the single-scattering lifetime will be 240 hr and the nuclear-interaction lifetime will be 2000 hr. Thus these effects are negligible. The heating rate for the final stack from multiple scattering will be 2×10^{-5} /sec, 10 times less than the cooling rate. (Here a gas composition of 50% H₂, 50% N₂ or CO is assumed). The energy loss per antiproton will be 20 keV/hr. Both the heating and energy loss can be easily compensated by the stochastic-cooling systems. We will keep the nominal design value of the neutralization factor $H < 0.03$. With this value, the scattering by positive ions trapped in the beam will be increased less than 2%. The vertical space-charge tune shift will be reduced by 10^{-3} . Thus these neutralization effects are negligible.

5.8.2 Vacuum system layout and characteristics. The pressure requirement can be met with sputter ion-pumps. Furthermore vacuum-annealed austenitic high-tensile stainless steel will be used for the chambers so that specific degassing rates of better than 1×10^{-12} Torr- $\frac{1}{4}$ /cm²-sec can be attained. The maximum design bakeout temperature is 300 C.









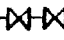
Figure 5-33 shows the vacuum-system layout over one-sixth of the Accumulator ring. The sputter ion pumps should have a speed of 200 $\frac{1}{4}$ /sec. The stochasting cooling P.U. and kickers will be isolated with all metal valves, during the bakeout, to prevent any vacuum contamination. These valves will divide the ring into about 5 irregular vacuum sectors.

The baking equipment (heaters, controls, thermal insulation) will be installed in a permanent fashion to allow bakeout to proceed without major preparations. Exceptions are areas that cannot tolerate the high temperature; e.g., pump magnets, cable feedthroughs and special devices..

Pump-down during bakeout will be carried out using mobile turbopump sets with liquid-nitrogen cold traps. This will allow the use of a large number of pumps in any given section being baked. These carts will be connected to metal valves distributed for that purpose throughout the system. Tests indicate that the pressure during bakeout has little effect on the success of the bake.



—KEY—

-  Quadrupole
-  Bending Dipole
-  Ionisation Pump 200 l/s
-  Gas Analyser
-  Beam Position Pick-Up Electrode
-  Clearing Electrode
-  Ionisation Gauge
-  Pirani Gauge
-  Port for Mobile Pump Station

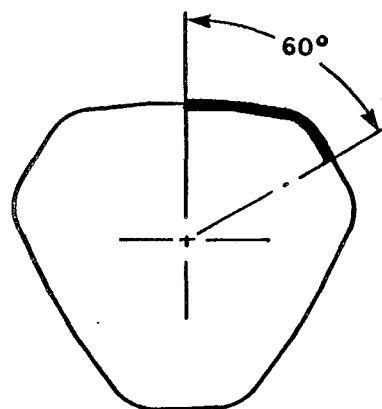


Figure 5-33

Vacuum gauges include 6 Pirani gauges to monitor pumpdown, 36 Bayard-Alpert ionization gauges, and 6 mass-analyzer heads, located near areas of complex equipment to monitor leaks and contamination.

The arrangement has not been completely specified for the straight sections where the stochastic cooling equipment is located. The equipment will be capable of being baked at a maximum temperature of 150°C and materials compatible with the high vacuum requirements will be used. Cryogenic pumping techniques may be used to provide a pumping speed of up to 2000L/sec/m .

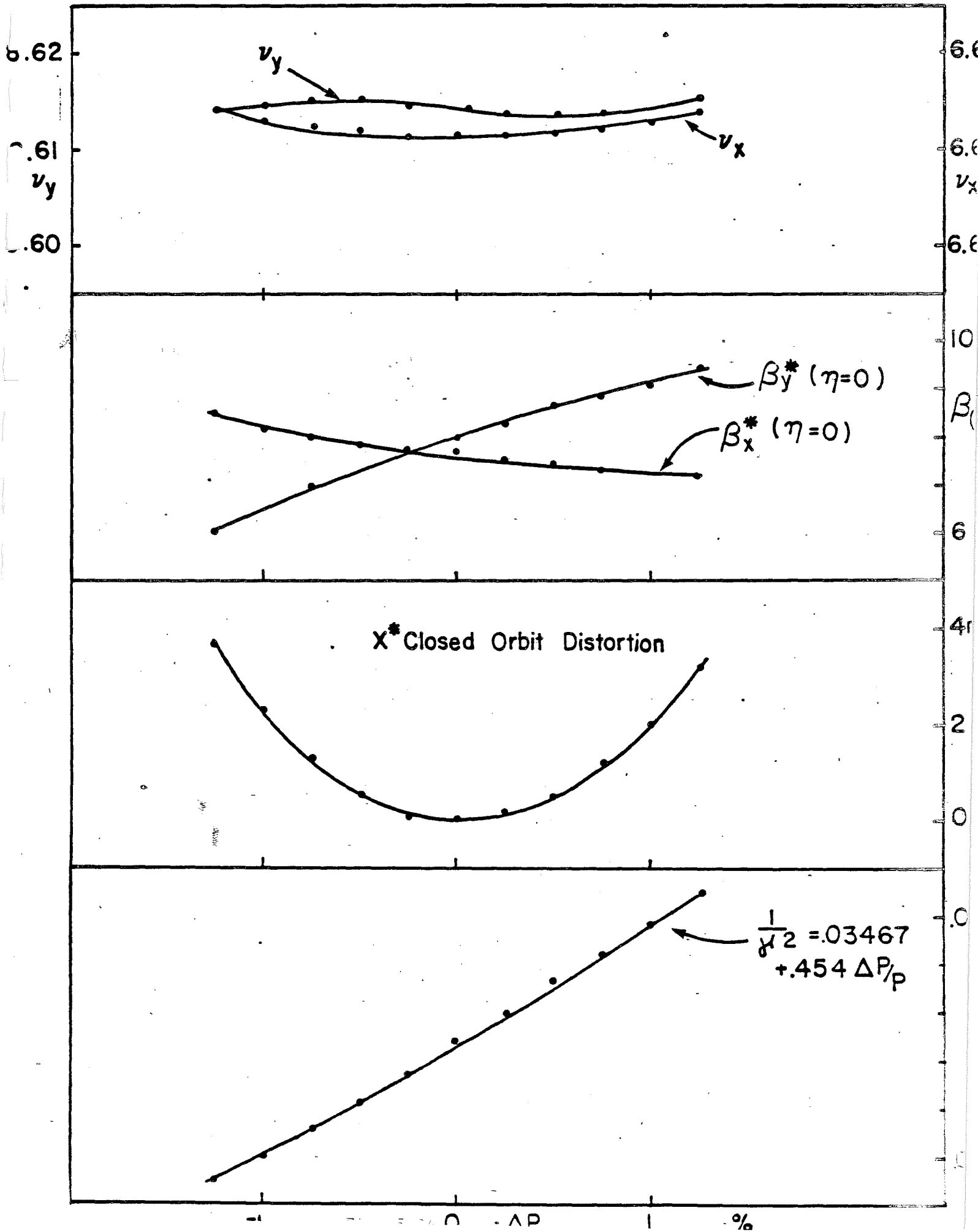
Clearing electrodes will be installed to remove low-energy positive ions and thus keep the neutralization factor $H < 0.03$. There will be a pair of electrodes at the downstream end of each magnet. Ions move longitudinally to the electrodes by $E \times B$ drifting caused by the beam electric field and the ring guide field. This kind of system has been used successfully in the ISR.

The straight sections between magnets will also need clearing electrodes to avoid trapping ions in the cool-beam potential of 5 V. We plan to apply a dc potential of more than 5 V to the clearing electrodes and to the beam-position detector electrodes whenever these are in a suitable location.

All devices and ring sections will undergo a preliminary bake and low-pressure test before being installed. Their design will conform with strict rules of choice of material and will be subject approval by the vacuum coordinator.

The vacuum control system will be constructed along the design evolved for the Tevatron. It is highly modular and economical. Most of the required modules and device controls have already been developed, including ion pump supplies and ion gauge controllers. A card cage containing all control modules interfaces to the host computer through a CAMAC module. Much of the necessary software can be used or adapted.

Accumulator Lattice Function Variations VS. $\Delta P/p$



REFERENCES

1. D. Möhl, G. Petrucci, L. Thorndahl, and S. van der Meer, Physics Reports C, 58 (1980) 73-119.
2. S. van der Meer, "Stochastic Stacking in the Antiproton Accumulator," CERN/PS/AA/78-22 (1978); unpublished.
3. A.G. Ruggiero, "Stochastic Cooling - A Comparison with Bandwidth and Lattice Functions," Fermilab \bar{p} note 171 (1981), unpublished.
4. A.G. Ruggiero, "Pickup Loop Analysis" \bar{p} note 148 (1981), unpublished.
5. S. van der Meer, "A Different Formulation of the Longitudinal and Transverse Beam Response," CERN/PS/AA/80-4 (1980), unpublished.
6. A.G. Ruggiero, "Theory of Signal Suppression for Stochastic Cooling with Multiple Systems," Fermilab \bar{p} note 193 (1982), unpublished.
7. F. Sacherer, "Stochastic Cooling Theory," CERN/ISR/TH/78-11 (1978), unpublished.
8. A.G. Ruggiero, "Revised Intrabeam Scattering Calculation," Fermilab \bar{p} note 192 (1982), unpublished.
9. This discussion follows the discussion of C. Kim, "Design Options for the Fast Betatron Precooling Systems in the Debuncher or in the Injection Orbit," LBL Note BECON-25, unpublished.
10. A.G. Ruggiero, "Vacuum Considerations for the Accumulator Ring," Fermilab \bar{p} Note 194 (1982), unpublished.
11. Unslatter (CERN) unpublished; Neuffer, \bar{p} note 199; Ruggiero, \bar{p} Note 201.
12. F. Voelker (LBL) unpublished; J. Simpson (ANL) unpublished.
13. Avantek model ABG-2015 for example.
14. J. Shanley, Honeywell Inc., private communication (1982).
15. W. Weinreb et al; IEEE Trans. on Microwave Theory and Techniques 30, pg. 849 (1982).

6. EXTRACTION OF ANTIPROTONS FROM THE ACCUMULATOR AND TRANSFER TO THE MAIN RING

6.1 Accumulator Beam Manipulation and Extraction.

Prior to extraction of the first \bar{p} bunch, a nearly Gaussian distribution of \bar{p} 's will exist in the core. The density can be characterized by two numbers, the total number of \bar{p} 's in the core, N_0 , and the rms energy spread, σ . If ϵ represents the energy difference between the particle energy and the most probable energy of the particles in the core, then the density function $\psi(\epsilon)$ can be written as

$$\psi(\epsilon) = \frac{N_0}{(2\pi)^{1/2} \sigma} \exp\left(-\frac{\epsilon^2}{2\sigma^2}\right)$$

The example presented here uses the following values for these parameters; $\sigma = 2.0$ MeV, $N_0 = 4.5 \times 10^{11}$ and $\psi(0) = 10^5 \text{eV}^{-1}$. Because we want to extract an ensemble with the smallest longitudinal emittance, we begin the adiabatic capture with a bucket centered at the peak of the distribution. We plan to extract a single bunch containing 8×10^{10} \bar{p} 's. These \bar{p} 's exist within a range of ± 452.5 keV. The revolution period of the ring is 1.59 μsec , so the longitudinal emittance of the core region selected is 1.44 eV-sec. The Accumulator parameters which are used in this calculation are $R = 75.4716$ m, $\eta = 0.02$, $E_s = 8.938$ GeV, and $\Delta p/p \approx 1.6\%$ ($\Delta p = 142$ MeV/c) from core to extraction orbit. Because η (i.e. $\gamma_t^{-2} - \gamma^{-2}$) varies over the aperture, the rf parameters determining bucket areas must be varied accordingly.

The rf voltage required to develop a single bucket of area 1.44 eV-sec at harmonic h is $V = 2.44 h^3$. At $h = 1$, only 2.44 V is required and it may be difficult to establish such a low voltage with sufficient precision to control accurately the number of \bar{p} 's extracted. We propose to extract using a single $h = 2$ bucket with the remaining bucket suppressed. The required rf voltage is 19.5 V. Following adiabatic capture, a moving bucket will be established for deceleration to the extraction orbit.

The time required for this unstacking process depends upon the choice of rf voltage and synchronous phase angle. In order to minimize both the disturbance of the stacked \bar{p} 's and the particle loss from the moving bucket, the bucket will be moved very slowly with a small phase angle. After the first \bar{p} bunch has been extracted and placed in the Tevatron at 150 GeV, the duration that this bunch is required to reside in the Tevatron at low field depends upon the time required to extract the remaining bunches from the core. If the lifetime at 150 GeV is not long enough, it may be necessary to accelerate the process. Optimization of this time can only be accomplished after the Energy Saver and the Antiproton Source are

operational. The rf voltage required to maintain the specified bucket area, the deceleration rate, and the time required for deceleration to the extraction orbit are shown in Table 6-I for several synchronous phase angles.

Table 6-I. RF PARAMETERS FOR DECELERATION TO THE EXTRACTION ORBIT
(CONSTANT BUCKET AREA 1.44 EV-SEC.)

ϕ_s (deg)	$\Gamma = \sin \phi_s$	$\alpha(\Gamma)$	V_{rf} (volts)	Decel.Rate (MeV/sec)	Decel.Time (sec)
10	0.1736	0.696	36.2	3.33	43
20	0.3420	0.4918	72	12.93	11
30	0.500	0.3334	157	41.1	3.5

Frequency and phase control of the rf system during unstacking may be improved by a phase-lock system that partially locks the system to the coherent component of beam current. Since this component of current is of order 10 mA, detection and phase locking should not be technically difficult. The bunch length during the unstacking process will be about 500 nsec.

When the bunch reaches the extraction orbit, the rf voltage is raised to 100 V, resulting in a total bunch length of 200 nsec or about 60 meters. Since the momentum spread $\Delta p/p$ of this bunch is 5.2×10^{-4} , it can easily be injected into the Main Ring. The $h=2$ suppressed bucket unstacking system is capable of producing a gap voltage of only 100 V, so the remaining 900 V is to be generated by a fixed frequency $h=2$ system at 1.26 MHz. This system will, of course, create two buckets but only one will be populated with antiprotons because of the prebunching of the suppressed-bucket system. The total 1000-V bucket height will be about 12 MeV or $\pm 0.13\%$, so these buckets will not adversely affect antiprotons remaining in the cooled core.

After the 200 nsec bunch is established at the extraction orbit, the extraction kicker shutter is closed, isolating the bunch from the remaining accumulated beam, and the single bunch is extracted and injected into the Main Ring.

Movement of the extraction bucket through part of the stack is a form of displacement acceleration resulting in partial replacement of some of the \bar{p} density in the core. Moreover, the cooling system will very quickly fill the depleted region left by the extracted bunch. During subsequent acceleration of the extracted bunch to 150 GeV and prior to the next extraction, core cooling systems will re-establish a \bar{p} density in the core that is adequate for extraction.

The single-bucket rf wave consists of one complete sinusoidal wave with a period of one-half the rotation period. Because the fundamental frequency is 0.632 MHz, such a wave can easily be generated with Fourier components below 100 MHz. The accelerating structure may consist of an insulating gap in the beam pipe in parallel with a $50\text{-}\Omega$ resistance of sufficient power-dissipating capability. This structure will be contained within a shielded enclosure with sufficiently high shunt inductance (introduced by high-permeability ferrite) so that the load presented to a broad-band amplifier will be essentially real over the operating range. The power requirements will be less than 100 W. The $50\text{-}\Omega$ real impedance presented to the beam by this structure is well within the longitudinal-stability impedance limit.

The additional 900 V at $h=2$ is required only at a single frequency at the extraction momentum. It will be developed by a single ferrite-loaded resonant accelerating cavity with a shunt impedance of 2 k Ω . This shunt impedance meets the beam-stability requirement and the required voltage can be developed with an excitation power of 200 W.

Extraction from the Accumulator occurs using a 2.1336 m long shuttered kicker and a 2.921 m long Lambertson extraction septum. The extraction orbit is rf displaced radially outward to 0.775% in $\Delta p/p$. At point A20 in the high dispersion straight section (see Fig. 5-29) the extraction closed orbit is displaced to 76.7888 mm outward. The orbit parameters are $\beta_x=11.27$ m, $\beta_y=8.91$ m, and $\alpha_x=\alpha_y=0$. The shuttered kicker is centered 6.32 m downstream of point A20; an inward kick of 2.0 mr moves the extraction closed orbit to $x=38.571$ mm and $x'=-2.771$ mrad at the entrance to the Lambertson extraction septum. Figure 6-1 shows the extraction orbit from the kicker center to the Lambertson entrance. At this point the orbit parameters are found to be $\beta_x=20.5$ m, $\beta_y=6.056$ m, $\alpha_x=2.152$, and $\alpha_y=0.692$ relative to the closed orbit. The Lambertson extraction septum then bends the beam up by 100 mrad.

An achromatic translation system restores the extracted beam to target height ($\Delta z=+48$ inches). Then the beam is taken through four modules consisting of: (i) long transport, (ii) left bend, (iii) long transport, and (iv) target bypass. Following this, the beam rejoins the 120 GeV proton line just downstream of quadrupole PQ7B and is reverse-injected into the Main Ring at F17. The orbit parameters are identical for 120-GeV protons and 8-GeV antiprotons at the notch point, the downstream end of PBV2: they are $\beta_x=22.78125$ m, $\beta_y=117.9955$ m, $\alpha_x=1.2588$, and $\alpha_y=6.68625$.

The long transports use quadrupoles in a 90° FODO channel and matching lenses. The periodic structure uses a cell length of 166.73 feet with $\beta_{\text{max}}/\beta_{\text{min}}=86.5716$ m/14.9158 m. The left bend uses three dipoles for a 18.462° bend. The long transport (iii) parallels the long transport carrying the hot \bar{p} to the Debuncher. The target bypass is an achromatic transport using three dipoles and three quadrupoles. Figure 6-2 shows the behavior of the monoenergetic β_y , β_x , η_y , and η_x functions through the extraction system, starting at the Lambertson and ending at the downstream end of PBV2. The sections are explicitly indicated below in Fig. 6-2.

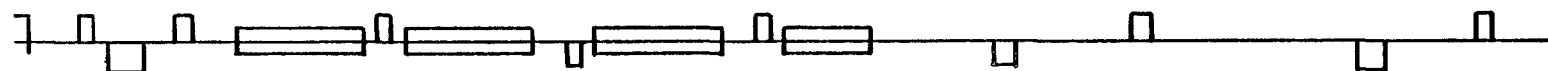
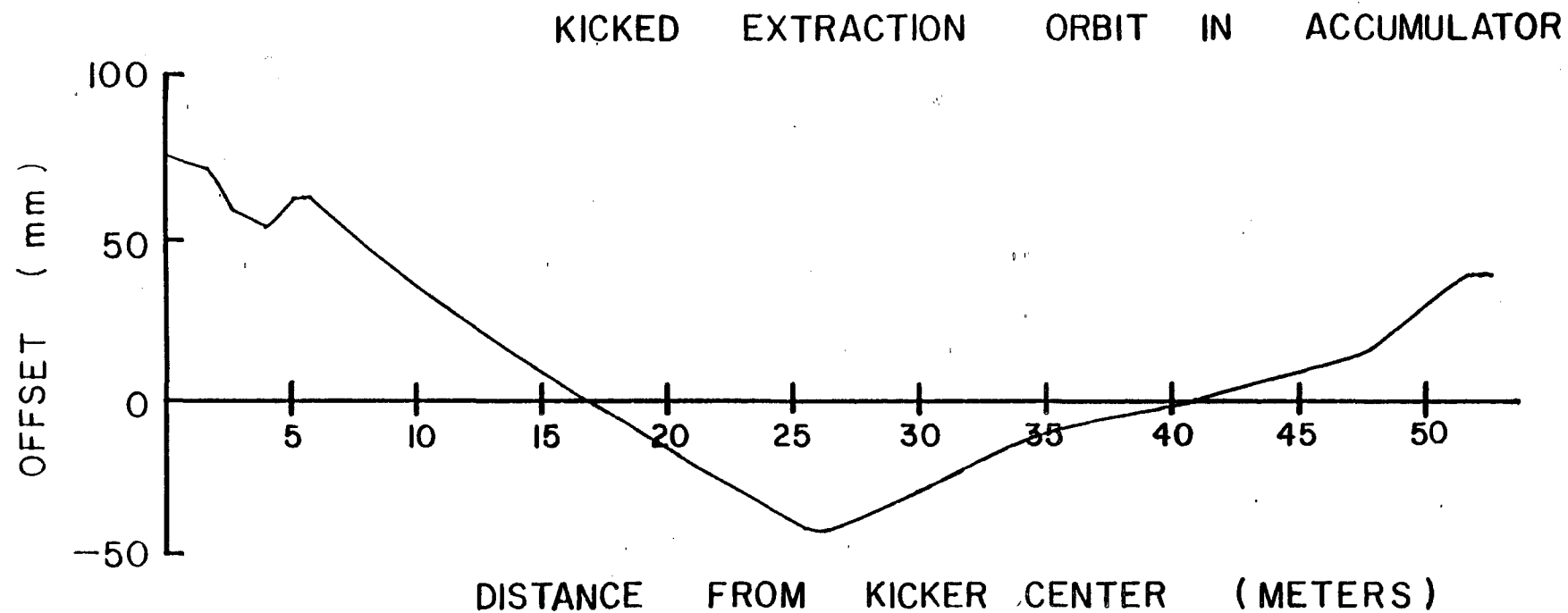


Fig. 6-1

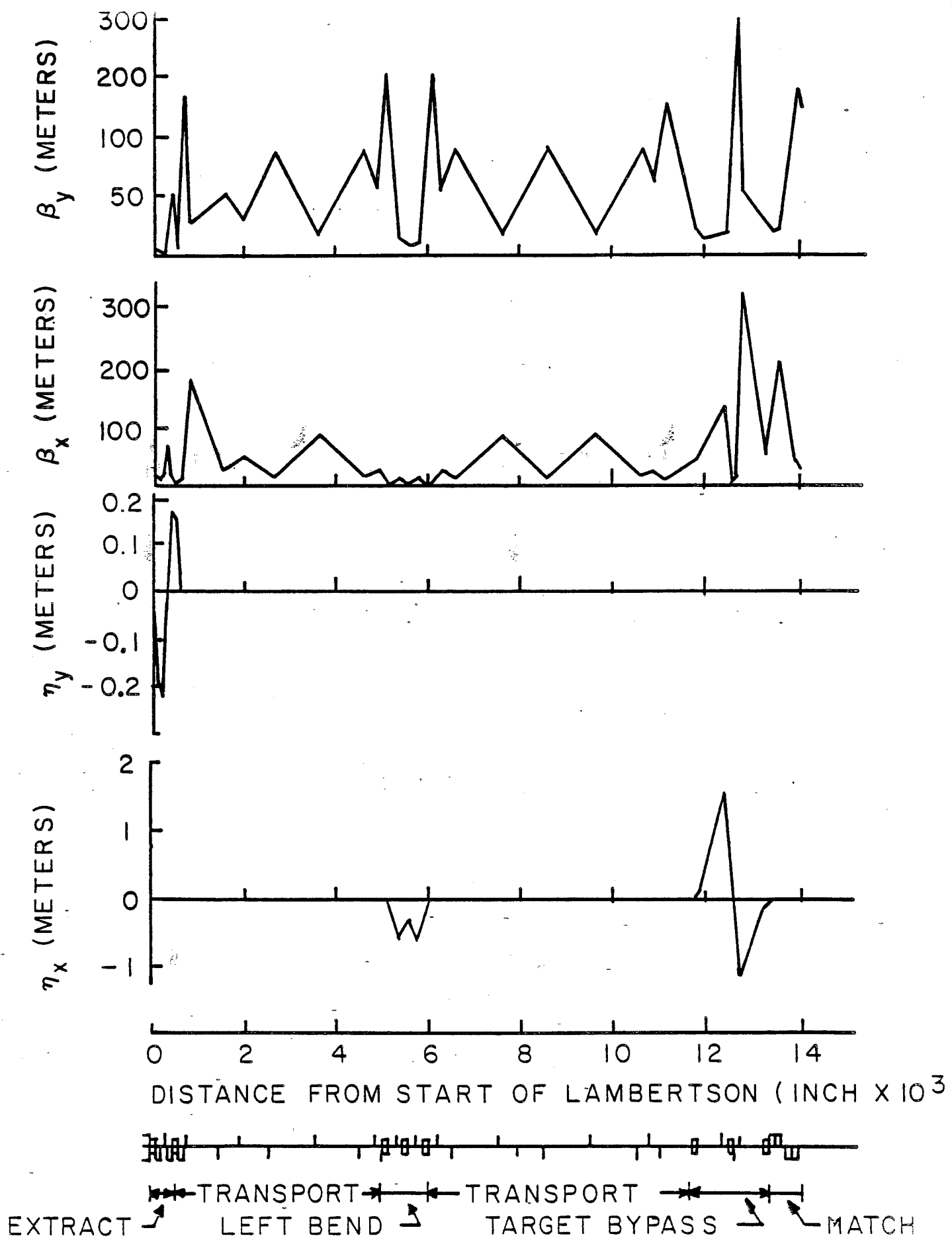


Fig. 6-2. Beam functions β_y , β_x and dispersion functions η_y , η_x for the antiproton beam transport from the Accumulator to the 120 GeV proton transport line.

Table 6-II lists the antiproton transport line elements from the Accumulator to the match point in the proton extraction line (EB6).

Table 6-II BEAM TRANSPORT ACCUMULATOR TO TARGET BYPASS AP-3

X,Y,Z Site Coordinates

Coordinates given at end of element (toward target)

Main Ring Station A0 at X=0.0, Y=0.0

NAME	LENGTH (IN)	FIELD (KG KG/M)	X (FT)	Y (FT)	Z (FT)
ACCUMULATOR RING					728.500
E-LAMBERTSON	115.00	10.15	-117.122	-1350.941	728.979
EQ1	70.00	-127.48	-112.527	-1357.542	729.786
EQ2	50.00	127.48	-106.606	-1366.049	730.826
EQ3	85.90	-127.48	-100.057	-1375.455	731.976
EBV1	75.00	15.56	-95.285	-1382.312	732.500
EQ4	50.70	-131.44	-91.314	-1388.015	732.500
EQ5	22.50	131.44	-85.482	-1396.394	
EQ6	27.60	-51.90	-52.235	-1444.157	
EQ7	20.80	36.31	-30.981	-1474.690	
EQ8	18.00	-36.31	-0.404	-1518.617	
EQ9	18.00	36.31	47.223	-1587.038	
EQ10	18.00	-36.31	94.850	-1655.459	
EQ11	18.00	118.68	110.006	-1677.231	
EQ12	18.00	-121.20	118.763	-1689.812	
EB1	98.42	12.85	124.946	-1697.918	
EQ13	27.60	121.20	134.665	-1709.080	
EB2	98.42	12.85	148.585	-1724.389	
EQ14	27.60	121.20	159.453	-1734.434	
EB3	98.42	12.85	174.946	-1748.148	
EQ15	18.00	-121.20	177.758	-1750.231	
EQ16	18.00	118.68	190.075	-1759.355	
EQ17	18.00	-36.31	211.388	-1775.146	
EQ18	18.00	36.31	278.371	-1824.774	
EQ19	18.00	-36.31	345.353	-1874.403	
EQ20	18.00	36.31	412.335	-1924.032	
EQ21	18.00	-36.31	479.317	-1973.660	
EQ22	22.50	58.46	497.168	-1986.886	
EQ23	18.00	-61.65	511.765	-1997.698	
EB4	98.42	12.42	561.916	-2035.391	
EQ24	22.50	142.71	596.212	-2066.856	
EB5	75.00	12.22	608.552	-2078.510	
EQ25	27.60	-142.61	611.629	-2081.812	
EQ26	32.00	142.26	617.027	-2087.606	
EB6	75.00	12.22	652.141	-2124.948	732.500
EQ27	120.00	11.02	661.097	-2133.163	

EQ27 IS THE SAME MAGNET AS PQ7B IN THE 120 GEV PROTON TRANSPORT LINE

(*) FIELD VALUES ARE FOR POSITIVE BEAMS.

6.2 Main Ring RF Capture and Acceleration

6.2.1 Introduction. We describe here the management of a single 1.5 eV-sec \bar{p} bunch in the Main Ring. The Main Ring is not capable of accelerating such a large emittance in a single bunch without excessive particle loss. For this reason, the bunch is broken up into several (5 or 7) adjacent bunches, accelerated to 150 GeV, and reconstituted into a single bunch at 150 GeV.

6.2.2 Injection and Rebunching. The \bar{p} bunch, about 200 nsec in length, is injected into a matched bucket in the Main Ring at $h=53$. The frequency is 2.5148 MHz and the bucket length, or period, is 397.6 nsec. By locking the phase of the Main Ring rf to that of the Accumulator the \bar{p} bunch can be injected accurately into the Main Ring bucket. The required bucket height is 6.5 MeV, requiring 3300 volts.

After injection, the $h = 53$ rf voltage is raised adiabatically to 15.5 kV so that the bunch length shrinks to 132.5 nsec, which spans exactly 7 'normal' $h = 1113$ rf periods in the Main Ring. With the bunch held at this length by the $h = 53$ rf voltage, the $h = 1113$, 52.813 MHz voltage is raised adiabatically so that the bunch is rebunched into seven bunches. The bunch with the largest area, located at the center of the ensemble of bunches, has a longitudinal emittance of about 0.32 eV-sec. This can be accelerated easily in the Main Ring. This rebunching process is shown in Figs. 6-3 through 6-5 for a uniform initial distribution in the $h = 53$ bucket. After capture in $h = 1113$ buckets, the ensemble of seven adjacent bunches is accelerated to 150 GeV.

The longitudinal phase space area is expected to increase by a factor 1.5 during acceleration. Recent studies in the Main Ring and careful simulation of transition crossing indicate that bunches with initial longitudinal emittance in the range of 0.2 to 0.3 eV-sec are diluted by a factor of about 1.25 between injection and $\gamma=21$, above transition. This dilution is accompanied by a slight bunch-to-bucket mismatch so that further dilution resulting from coherent bunch motion within the bucket results in total dilution during acceleration of about a factor of 1.5.

6.2.3 Bunch Recombination at 150 GeV. At 150 GeV, the Main Ring field is held on flat top while the seven adjacent bunches are coalesced into a single bunch. The $h=1113$ rf voltage is reduced slowly over a period of 0.1 seconds to about 12 kV by counterphasing equal numbers of rf cavities. With this voltage the bucket containing the center bunch is nearly full. Adjacent buckets are not quite full and the total longitudinal emittance of all the bunches is about 2.2 eV-sec. At this time, the $h=53$ rf system is turned on at a voltage level (700 V) such that the $h=53$ bucket is matched to a 2.2 eV-sec distribution extending over the filled $h=1113$ buckets, 132 nsec. At the same time the counterphased Main Ring rf voltage is turned

H=53 BUNCH OF 1.5 EV_S AT 8 GEV IN M R TURN # 0
 HBCKT 1.48E+01 [MV], SBCKT 7.46E+00 [EV-S], ES 8.9383E+03 [MV], NUS 3.62E-04
 DPOT 0. [MEV/S], THS 0. [RAD], THFP 5.927533E-02 [RAD]
 EV1 1.679E-02 [MV], EV2 1.000E-02 [MV], H1 53., H2 1113., ETA -8.17492E-03

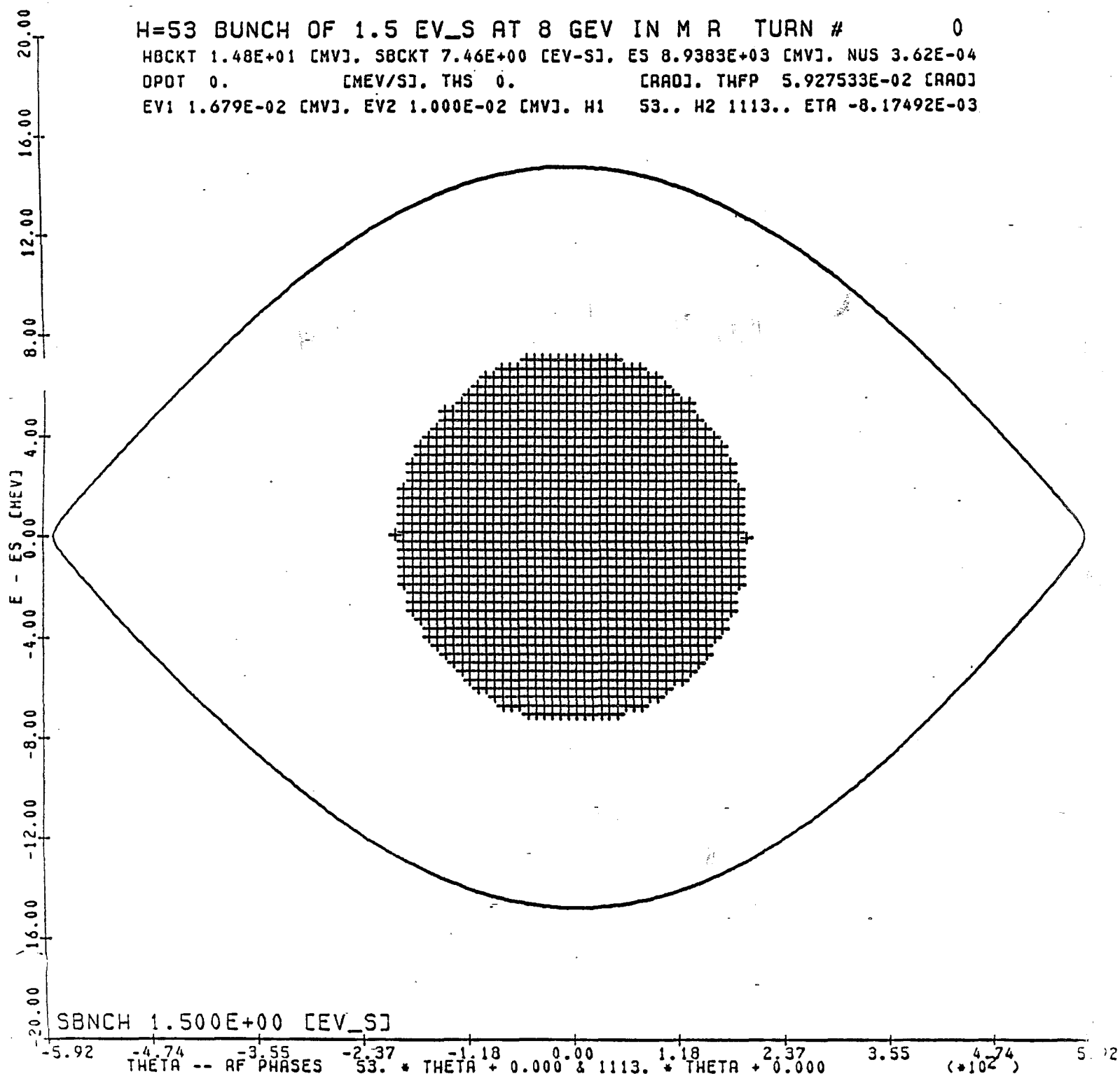


Figure 6-3 Uniform distribution of antiprotons with longitudinal emittance 1.5 eV-sec matched to h=53 bucket in Main Ring. The bunch covers a time span of about 133 nsec, or seven h=1113 stationary bucket lengths.

ADIABATIC CAPTURE AT H=1113 FROM H=53 BUTURN # 1509
 HBCKT 5.15E+00 [MV], SBCKT 1.24E-01 [EV-S], ES 8.9383E+03 [MV], NUS 2.65E-03
 DPOT 0. [MEV/S], THS 0. [RAD], THFP 2.822635E-03 [RAD]
 EV1 1.679E-02 [MV], EV2 4.296E-02 [MV], H1 53., H2 1113., ETA -8.17492E-03

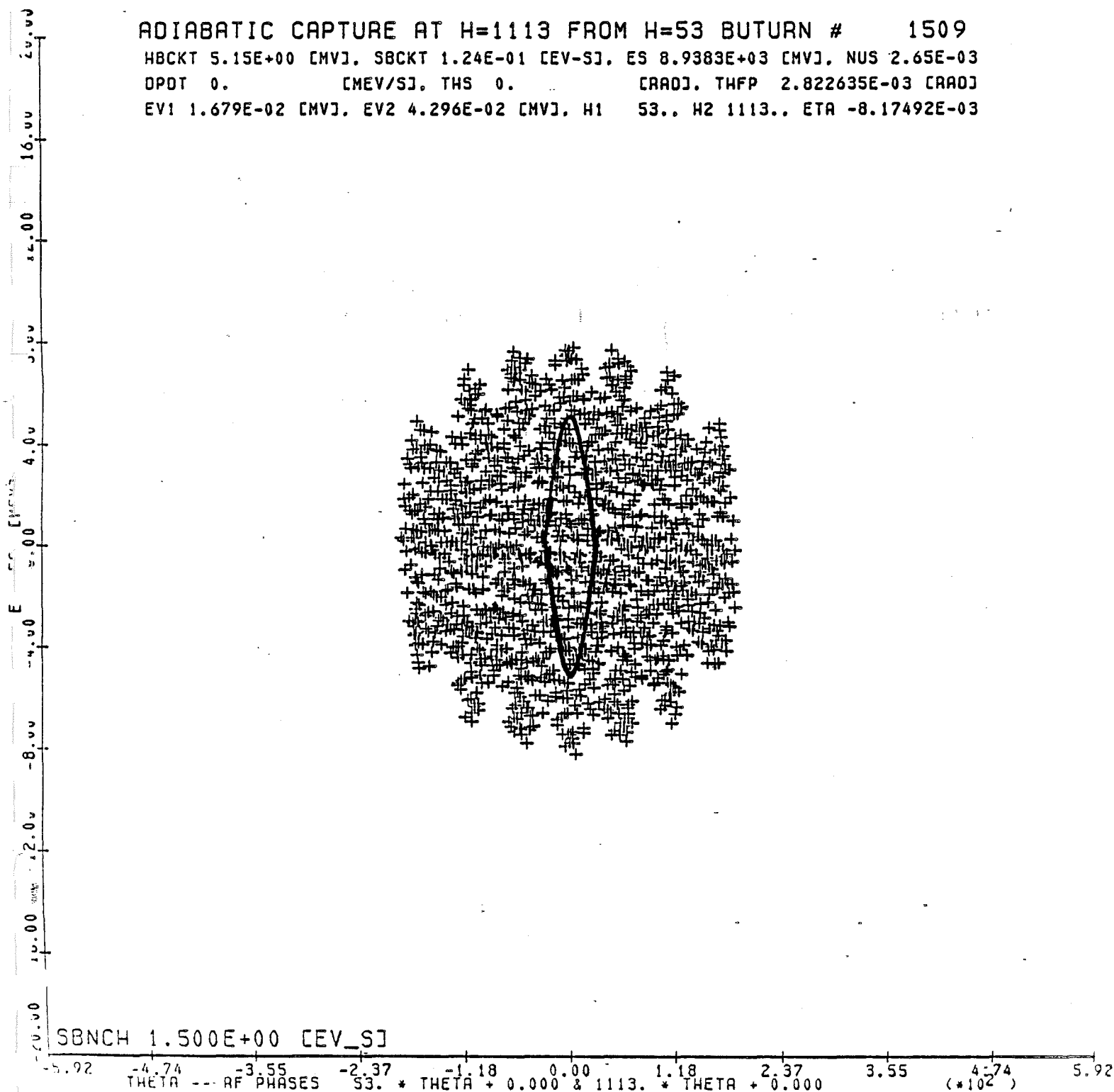


Figure 6-4 Antiproton distribution within an h=53 bucket partially bunched at h=1113 after 1509 turns. The h=1113 bucket size is shown for the center bucket.

FINAL H=1113 BUNCHES

TURN # 2499

H8CKT 1.75E+01 [MV], S8CKT 4.22E-01 [EV-S], ES 8.9383E+03 [MV], NUS 9.03E-03
 DPOT 0. [MEV/S], THS 0. [RAD], THFP 2.822635E-03 [RAD]
 EV1 1.679E-02 [MV], AV2 4.976E-01 [MV], H1 53, H2 1113, ETA -0.17492E-03

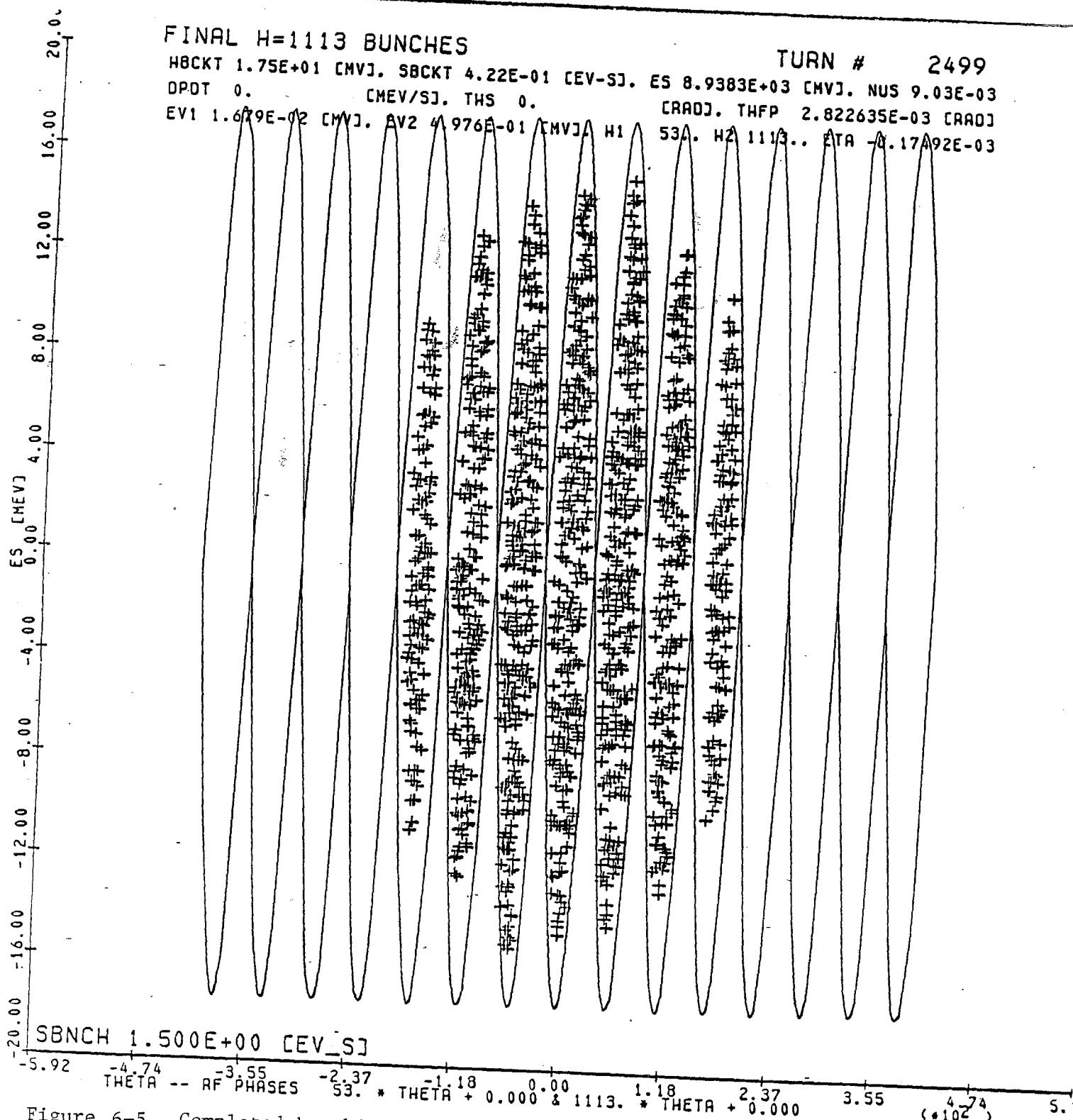


Figure 6-5 Completed bunching of antiprotons within seven adjacent h=1113 buckets. The center bunch has longitudinal emittance of 0.32 eV-sec and the sum of all emittances is 1.6 eV-sec.

to a 2.2 eV-sec distribution extending over the filled $h=1113$ buckets, 132 nsec. At the same time the counterphased Main Ring rf voltage is turned off and replaced by a single small $h=1113$ rf cavity at 12 kV. The voltage of this cavity is then lowered slowly to (nominally) zero so that the seven adjacent bunches are adiabatically debunched into matched orbits in the $h=53$ bucket. A simulation of this process, starting with bunch distributions derived from previously simulated acceleration is shown in Figs. 6-6 through 6-8. The result is a uniform bunch of about 2.4 eV-sec matched to the $h=53$ bucket and spanning a range $\pm\pi/3$.

At this point, the $h = 53$ rf system is suddenly raised to a level of about 65 kV while the $h = 1113$ voltage is removed. The low-momentum \bar{p} bunch, which extends over $7/21$ (or $\pm\pi/3$) of the $h = 53$ bucket, now begins a coherent synchrotron motion into a vertical strip. Since the charge does not extend far into the bucket, this motion is quite linear. After slightly more than one-quarter of a synchrotron-oscillation (about 0.11 sec or 5200 turns), the $h = 53$ voltage is removed and the vertical distribution is recaptured in an $h = 1113$ bucket of a size chosen to match accurately the rotated distribution. The re-applied voltage will create a bucket height of about 125 MeV and the \bar{p} 's (or p 's) are expected to fill this bucket, so the final \bar{p} bunch longitudinal emittance is as large as 3 eV-sec. The $h = 1113$ rf voltage required for this is 500 kV.

In Fig. 6-9, we show the results of a preliminary experiment in bunch coalescing. The experiment is done at $h = 159$ using four adjacent proton bunches. The successive oscilloscope traces starting at the bottom of the pictures show two or four proton bunches merging into a single bunch of larger intensity and emittance, as expected. Since the bucket covered only seven $h = 1113$ bucket lengths, the four bunches extended farther into the bucket than is proposed. This results in a more nonlinear process than will occur in the proposed scheme.

The same sequence could also be done with ensembles containing more bunches or fewer bunches. If nine adjacent bunches were accelerated each bunch would have smaller longitudinal emittance and less dilution would occur during acceleration. Unfortunately the ensemble would extend further into the $h=53$ bucket and the rotation process would be subject to greater nonlinearity. For five bunches the converse would be true. The optimum number of bunches to be accelerated will be determined experimentally when the commissioning begins.

Following recapture, the rf voltage is raised to 1 MV. As a result, the bunch length shrinks to 12 nsec full width, and the bunch height grows to ± 166 MeV, corresponding to a momentum spread $\Delta p/p$ of $\pm 1.1 \times 10^{-3}$. The bunch parameters are ideal for injection into pre-established matching buckets in the Tevatron.

ADIABATIC DEBUNCHING INTO H=53 BUCKET TURN # 1999
 HBCKT 2.41E+01 [MV], SBCKT 1.21E+01 [EV-S], ES 1.5080E+05 [MV], NUS 1.19E-05
 DPDT 0. [MEV/S], THS 3.141593E+00 [RAD], THFP 3.082317E+00 [RAD]
 EV1 9.000E-04 [MV], EV2 1.035E-01 [MV], H1 53.. H2 1113.. ETA 2.80573E-03

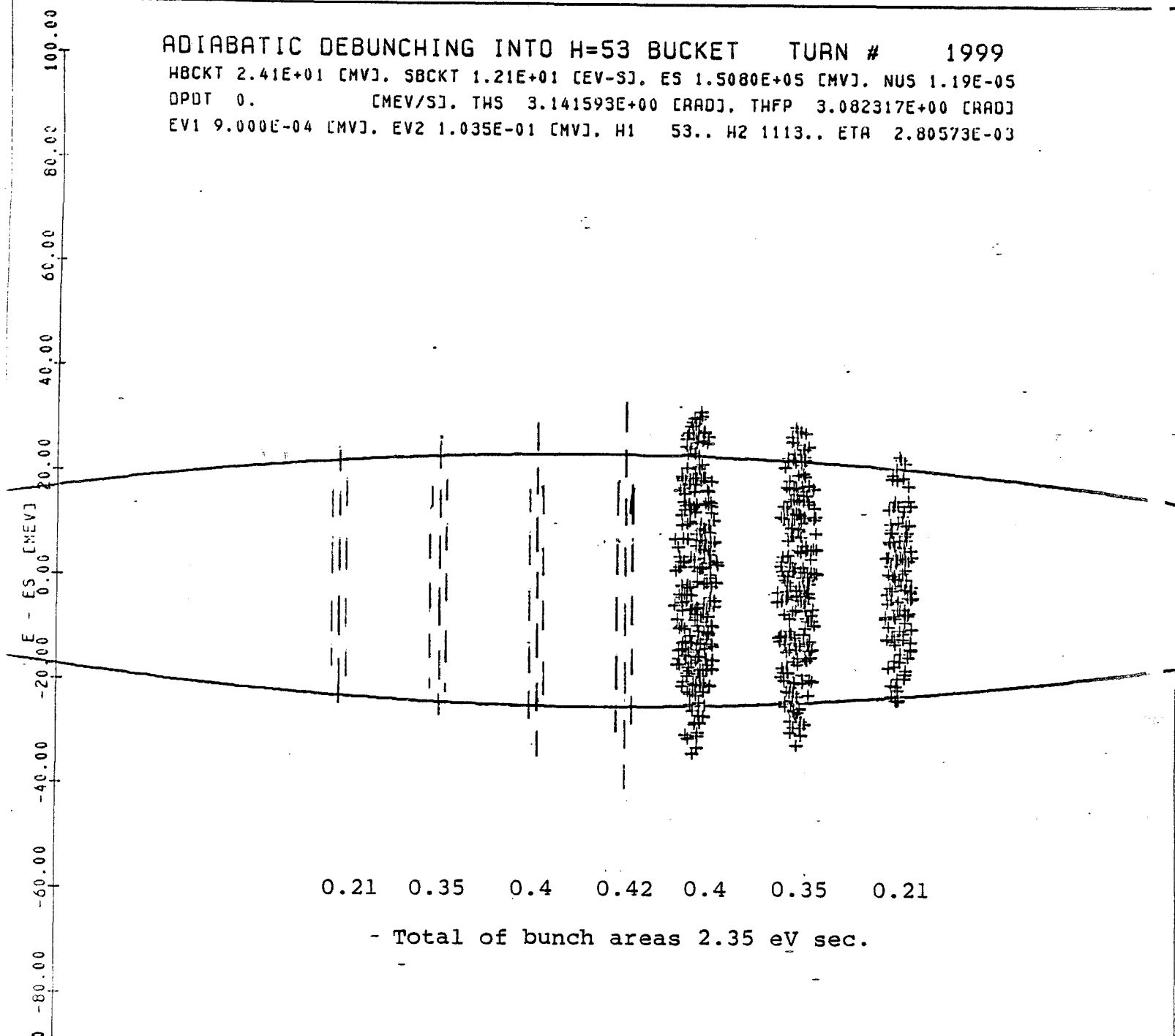


Fig. 6-6 Adjacent antiproton bunches in matched h=53 bucket prior to final h=1113 debunching. Dashed lines indicate location of bunches not tracked in this simulation. The total of the seven bunch longitudinal emittances is 2.35 eV-sec at this point.

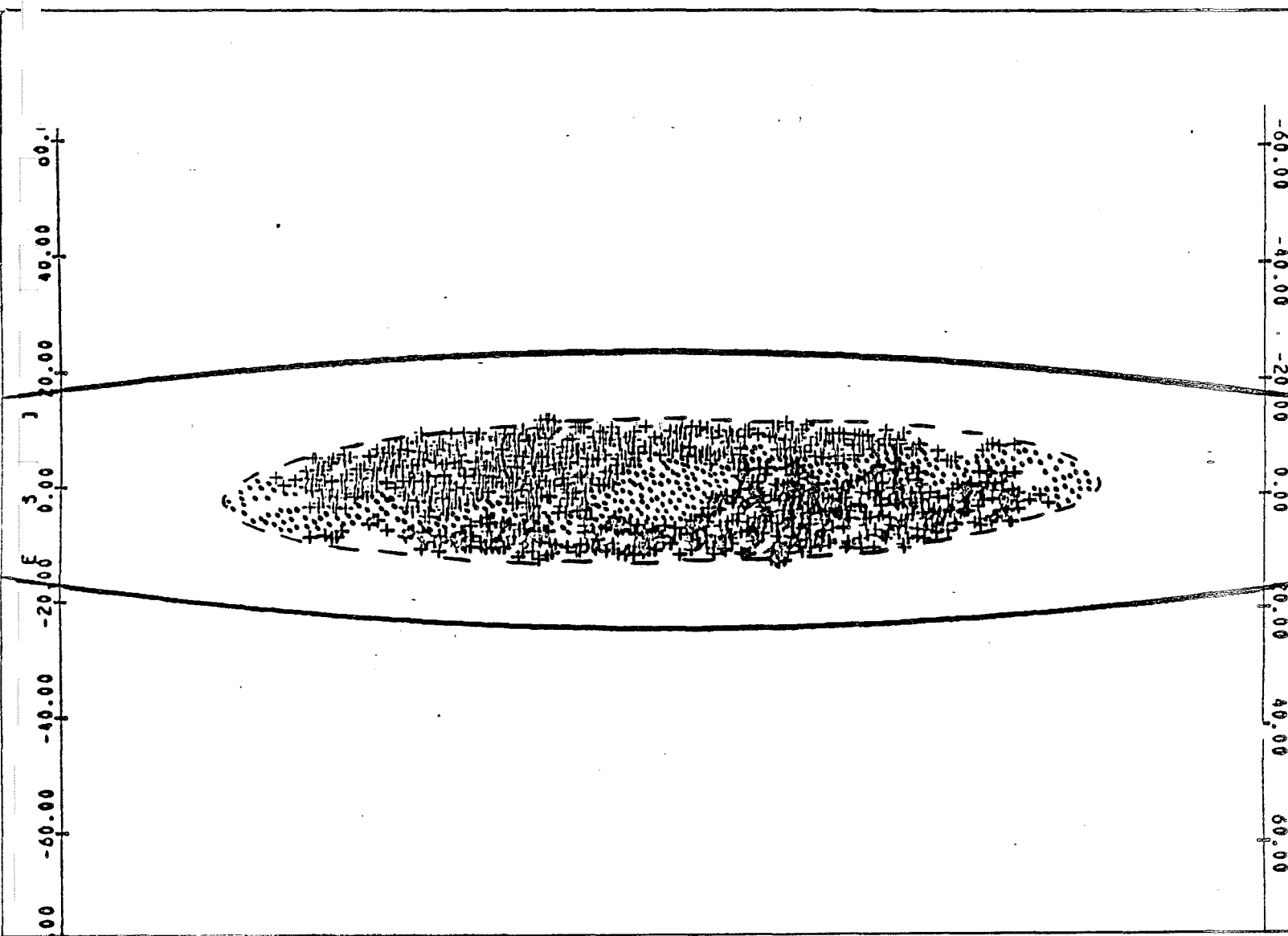


Fig. 6-7 Antiproton distribution within $h=53$ bucket following adiabatic removal of $h=1113$ rf voltage. The bunch extends over a range $\pm\pi/6$ radians within the bucket and the longitudinal emittance (95%) is enclosed by a contour, shown dashed, of area 2.5 eV-sec.

ROTATED PBAR BUNCH AT 150GEV/C

TURN # 26565

HBCKT 2.00E+02 [MV], SBCKT 1.00E+02 [EV-S], ES 1.5080E+05 [MV], NUS 9.86E-05
 OPDT 0. [MEV/S], THS 3.141593E+00 [RAD], THFP 3.082317E+00 [RAD]
 EV1 6.200E-02 [MV], EV2 1.000E-06 [MV], H1 53., H2 1113., ETA 2.80573E-03

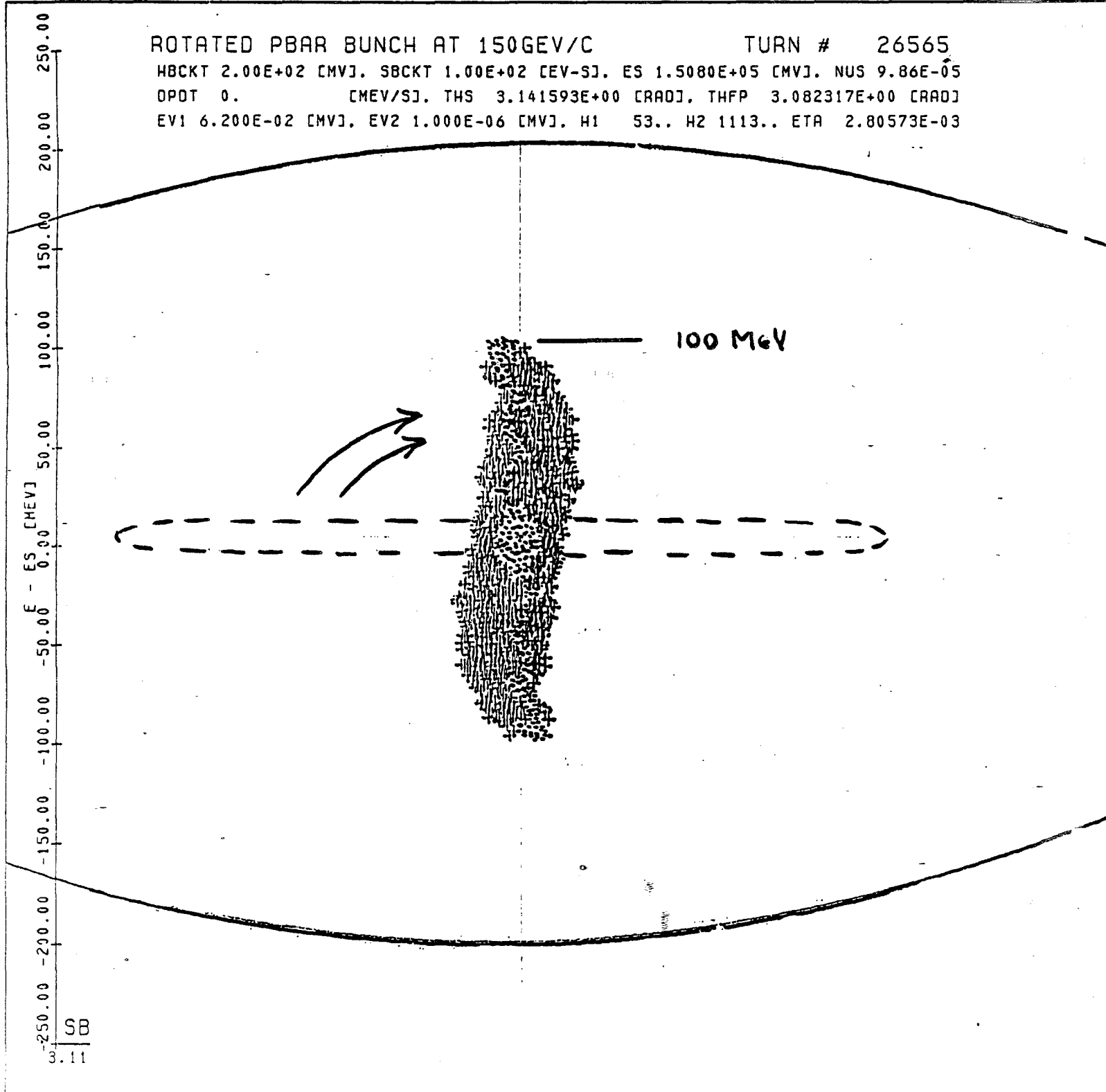


Fig. 6-8 Antiproton distribution following bunch rotation in h=53 bucket.
 The rotated distribution has a full length of about 16 nsec and spans
 an energy range of ± 100 MeV.

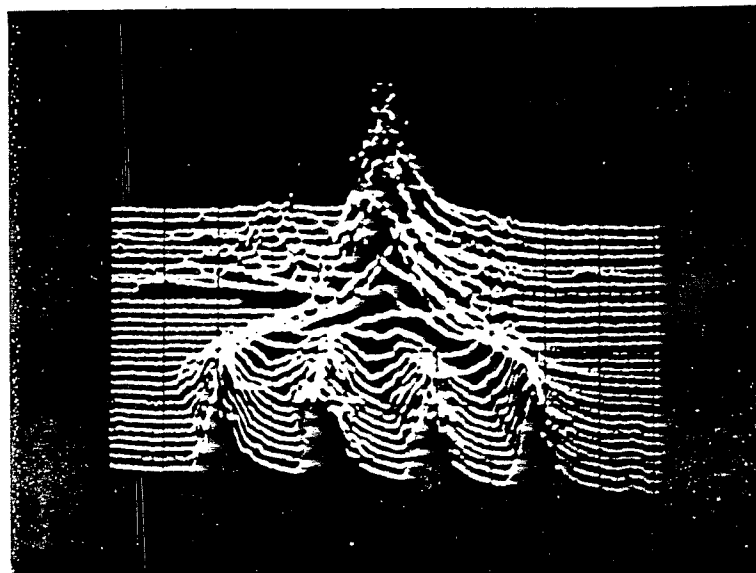
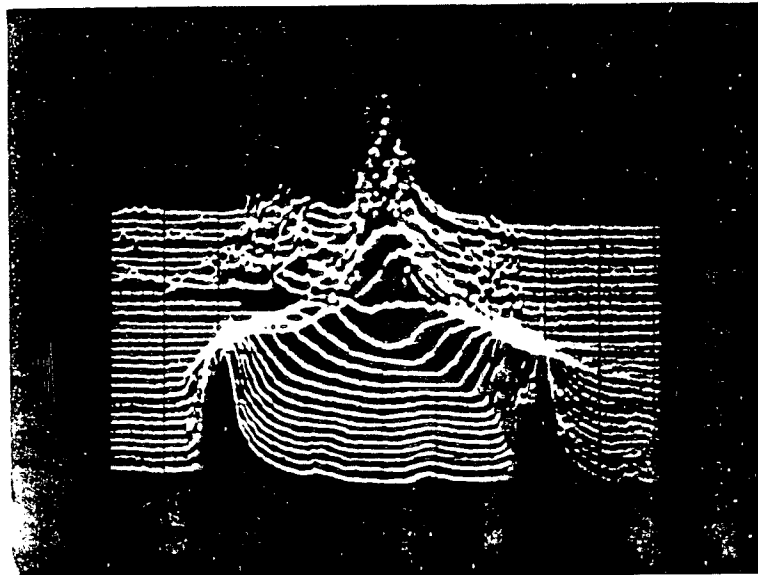


Fig. 6-9 Results of an early experiment in combining adjacent 53 MHz bunches in a lower harmonic bucket. The experiment was done at $h=159$ (7.5 MHz) where the lower harmonic bucket spans seven buckets. In the top picture two bunches, separated by two empty buckets are coalesced. In the bottom picture, four adjacent bunches are coalesced into a single bunch. Time progresses upward in each picture.

7. THE MAIN RING IN TEVATRON I

7.1 Functions of the Main Ring in Tevatron I

The Main Ring is required to perform five separate functions in the Tevatron I mode.

1. Acceleration of protons for antiproton production. During antiproton production and accumulation, the Main Ring will be required to accelerate single batches of protons (approx. 83 bunches) of intensity greater than 2×10^{12} protons per batch to 120 GeV. This will be done routinely on a 2-sec cycle. Each of these acceleration cycles must include the bunch-narrowing technique and extraction at F17 described in Chapter 2.

During this mode of operation, a special low-level rf system must be used. This system will contain provision for transient beam-loading compensation and rf-cavity counterphasing. In addition, the technique for phase-locking the Main Ring to the Booster will be slightly different than that used during fixed-target operation.

2. Injection of \bar{p} 's from the Accumulator into the Main Ring. Bunches of antiprotons containing 10^{11} \bar{p} 's must be transported to the Main Ring and injected.

3. Acceleration of antiprotons to 150 GeV. After a sufficient number and density of antiprotons have been established in the Accumulator, the Main Ring must be used to accelerate groups of antiproton bunches to 150 GeV. This acceleration cycle must include the bunch manipulations at 8 GeV and at 150 GeV described in Sections 6.1 and 6.2. Special additions to the rf systems will be required to accomplish these manipulations. Following these acceleration cycles, the single antiproton bunches must be extracted at EQ for injection into the Tevatron.

4. Acceleration of protons to 150 GeV. The Main Ring will be required to accelerate small ensembles of protons to 150 GeV, where they will be combined to form single proton bunches containing 10^{11} protons. This operation will be similar in many respects to the antiproton acceleration described above and the same special additions to the rf systems will be utilized.

5. Transfer of particles from the Main Ring into the Doubler. Transfers of 150 GeV protons and antiprotons are both described in Chapter 8.

7.2 Antiproton Injection

The antiproton bunches from the Accumulator are matched into the proton extraction line at EB5. They are then transported back down the 120-GeV extraction line and injected into the Main Ring at the F17 Lambertson. Special low-current power supplies are used to power the 120-GeV extraction line to ease regulation problems caused by running large power supplies at 5% levels.

The C48 kicker is also too strong for the reverse injection of the antiprotons at 8 GeV, so that an additional small kicker located at F14 needs to be added. The kicker is a 25 inch long ferrite (tape-wound steel) 380 G magnet with a rise and fall time of 20 μ sec. The gap is 5x3 inches (HXV) and the required current is 2280 A. When fed by 400 feet of 5 parallel RG213's as a simple L-C discharge circuit, the required capacitance is 23 μ F and the required discharge voltage is 1165 V.

7.3 Main Ring Acceleration and Rebunching Hardware

The processes of accelerating small groups of protons and cooled antiprotons to 150 GeV has been described previously in Chapter 6. In those descriptions reference was made to an rf system in the Main Ring operating at $h=53$ (2.515-2.529 MHz) and providing about 65 kV. This requirement will be met by installing two heavily ferrite-loaded rf cavities, each operating at the 20 kW level. These cavities will be refurbished and slightly modified cavities from the Princeton Pennsylvania Accelerator (PPA). Operation of these cavities in the Main Ring will require installation of an anode power supply of about 8 kV, 15 A (120 kW). Small additions to the low-level rf system will also be required to provide appropriate rf driving signals phase-locked to the integrally related $h=1113$ 53 MHz rf.

Small additions to the control system will also be required for remote operation of these systems.

7.4 Main Ring Overpass

The performance of both the Antiproton Source and the Collider Detector can be significantly improved by bypassing the Main Ring beam around the Collider Detector. This bypassing - called here the "Overpass" - has at least two advantages:

- (i) It allows elimination of the asymmetric hole for the Main Ring through the Collider Detector;
- (ii) It allows accumulation of antiprotons to proceed simultaneously with colliding-beam operation. This will increase the average luminosity of the entire system by eliminating the pause of several hours while the antiproton beam is being refreshed.

The design of an overpass for the Main Ring has been worked out in detail by T.L. Collins and is presented here. There are a number of constraints that such a design must satisfy:

- (a) Space must be generated for additional bending elements;
- (b) The new path must close smoothly on to the old path to high precision in both horizontal and vertical dimensions and at all energies with a minimum of programmed external control.
- (c) The path lengths must be the same in old and new paths, or differ by an integral number of rf wavelengths;
- (d) the betatron functions must match, as in any insertion; and
- (e) Any residual dispersion introduced outside the bypass must be negligibly small.

The overpass design limits Main Ring operation to 200 GeV or less. Some magnets are operated at twice the normal field. Consider a set of four bending magnets. The outer two magnets will be unchanged to provide the normal horizontal bend. The inner magnets will be rolled about the beam axis to produce a vertical bend of 32.471 mrad. Such four-magnet sets placed symmetrically around the long straight section (for example, at A41 and B12) will produce a 19-ft vertical separation, enough to miss the entire detector. The new orbit connects smoothly on both ends. A total of four sets (16 magnets) is in the additional circuit. The additional excitation of this circuit will be provided by a separate power supply.

The overpass has approximately 8 in. of extra orbit length. This undesired length is cancelled by combining the vertical bends with a slight inward bend to "cut across" the arc. The inward bend can be accomplished easily by a small inward roll of the vertical-bend magnets.

The betatron functions are easily matched across the insertion. The vertical dispersion introduced in the remainder of the ring must be balanced with some care. It has been reduced by this- balancing to approximately 0.5 m, which is noticeable, but tolerable. Coordinates of the bypass insertion magnets are given in Table 7-I and the effect on the dispersion is shown in Table 7-II.

Table 7-I
Table 7-I. OVERPASS COORDINATES

Numbers in parentheses are for the original main ring ($Z=\theta_v=0$).

Station	x(Feet)	y(Feet)	θ_h (rad)	Z(inches)	θ_v (rad)
A39	962.531 (962.531)	2,285.083 (2,285.083)	.8175454 (.8175454)	0.000	0.00000
A42	1,034.911 (1,034.808)	2,350.493 (2,350.639)	.8535781 (.850017)	19.286	.0322656
A43	1,109.464 (1,109.175)	2,413.368 (2,413.813)	.8860663 (.882488)	57.063	.0322656
A44	1,186.021 (1,185.554)	2,473.789 (2,474.539)	.9185544 (.914959)	94.840	.0322656
A45	1,264.500 (1,263.864)	2,531.691 (2,532.754)	.9510426 (.947430)	132.617	.0322656
A46	1,344.818 (1,344.023)	2,587.013 (2,588.396)	.9835307 (.979902)	170.393	.0322656
A47	1,426.890 (1,425.946)	2,639.697 (2,641.406)	1.0160189 (1.012373)	208.180	.0322656
A48	1,533.772 (1,509.547)	2,703.332 (2,691.728)	1.00448499 (1.044844)	226.656	.0000000
B0	1,686.376 (1,685.357)	2,787.887 (2,789.756)	1.0692033 (1.069198)	226.656	.0000000
B11	1,772.743 (1,771.723)	2,835.248 (2,837.117)	1.0692033 (1.069198)	226.656	.0000000
B12	1,870.616 (1,869.596)	2,887.172 (2,889.042)	1.1016746 (1.101669)	226.656	.0000000
B13	1,958.274 (1,957.352)	2,929.994 (2,931.709)	1.1304914 (1.134140)	207.364	-.0322641
B14	2,047.177 (2,046.446)	2,970.092 (2,971.504)	1.1629795 (1.166611)	169.589	-.0322641
B15	2,137.335 (2,136.786)	3,007.281 (3,008.386)	1.1954677 (1.199083)	131.815	-.0322641
B16	2,228.654 (2,228.275)	3,041.523 (3,042.315)	1.2279558 (1.231554)	94.040	-.0322641

B17	2,321.037 (2,320.818)	3,072.779 (3,073.256)	1.2604440 (1.264025)	56.625	-.0322641
B18	2,414.047 (2,413.981)	3,102.116 (3,102.275)	1.2766880 (1.280261)	18.491	-.0322641
B19	2,507.920 (2,507.920)	3,128.673 (3,128.673)	1.3127319 (1.312732)	.000	.0000000

Table 7-II. MOMENTUM DISPERSION IN THE BEND PLANE WITH AND WITHOUT BYPASS

	with bypass	without bypass		with bypass	without bypass
A39 =	2.86m	2.84m	A42 =	5.77m	5.67m
A43 =	3.45	3.32	A44 =	5.63	5.36
A45 =	2.63	2.50	A46 =	3.36	3.26
A47 =	1.36	1.40	A48 =	1.74	2.00
B12 =	1.07	1.26	B13 =	2.02	2.13
B14 =	1.71	1.68	B15 =	4.04	3.84
B16 =	3.00	2.84	B17 =	5.91	5.65
B18 =	3.02	2.94	B19 =	4.17	4.13

8. THE ENERGY SAVER IN TEVATRON I

8.1 Functions of the Energy Saver in Tevatron I

The Tevatron I project uses the Energy Saver Ring as a 1 TeV storage ring for bunched beam collisions. The construction of this ring which is nearing completion is a separate project which was undertaken for the purpose of operating the Fermilab fixed target program at 500 GeV. It was recognized that the Energy Saver could be used as a 1 TeV storage ring, if proper attention were given to a number of details such as position monitors and beam transfer systems.¹ Since the field quality for slow extraction was at least as dominating as the requirement for colliding beams, the Energy Saver was inherently a useful storage ring. For that reason the Energy Saver was designed so that it could be modified in the future to operate as a 1 TeV collider. These modifications are part of the Tevatron I project.

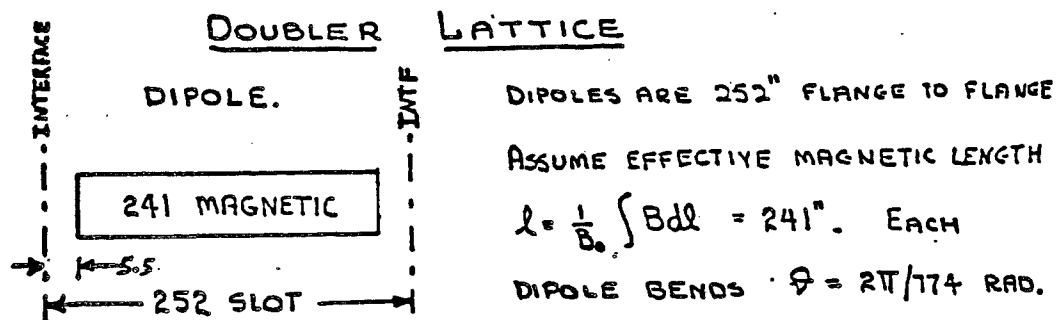
The Energy Saver, after modification, will perform the following functions in the Tevatron I project:

1. Injection. It will sequentially accept bunches of 150-GeV protons and antiprotons from the Main Ring, one bunch at a time.
2. Acceleration. After the appropriate number of bunches have been stored, it will simultaneously accelerate the proton and antiproton bunches to the collision energy.
3. Collision. After acceleration, the beams will be stored and the low-beta sections described in Chapter 9 will be turned on to increase the luminosity.

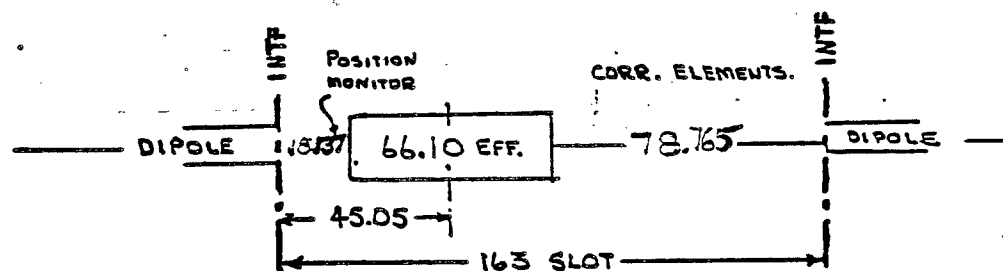
The material presented in sections 8.2 and 8.3 is based on the Superconducting Accelerator Design Report, May, 1979. Since 1979, there have been a number of changes to the design. The changes that are important to the use of the Energy Saver as a collider are described in this chapter. The most notable of these are: the correction coils are separate from the quadrupole windings, the rf system has been expanded to handle the larger longitudinal emittance of the antiprotons, and the beam transfer at E0 has been simplified substantially after it was decided to make the circumference of the Energy Saver exactly the same as the Main Ring.

8.2 Energy Saver Lattice

8.2.1 Ring Location and Normal Lattice. The lattice of the Energy Saver ring is constrained by the requirement that it fit beneath the Main Ring magnets. Therefore, it has the same basic configuration as the Main Ring, which has 6 superperiods with 6 long straight sections and normal cells with 8 dipoles and 2 quadrupoles. Because the Energy Saver dipole ends



QUADS ARE IN SERIES WITH BENDS. AT A CURRENT (NOM. 4527A.)
 WHEN DIPOLE $B_0 l = 45 \text{ kG} \times 241"$, I ASSUME A QUAD GRADIENT
 $G_0 = 19.627 \text{ kG/IN.}$, OR k (AS IN COIL ETC.) $= (G_0 \varphi / B_0 l)^{1/2} = .003833/\text{IN.}$



STANDARD QUAD. SHOWING EFFECTIVE LENGTH $\frac{1}{G_0} \int G dl$ AND ITS
 POSITION IN CRYOSTAT. THERE ARE MANY NON-STANDARD QUADS.

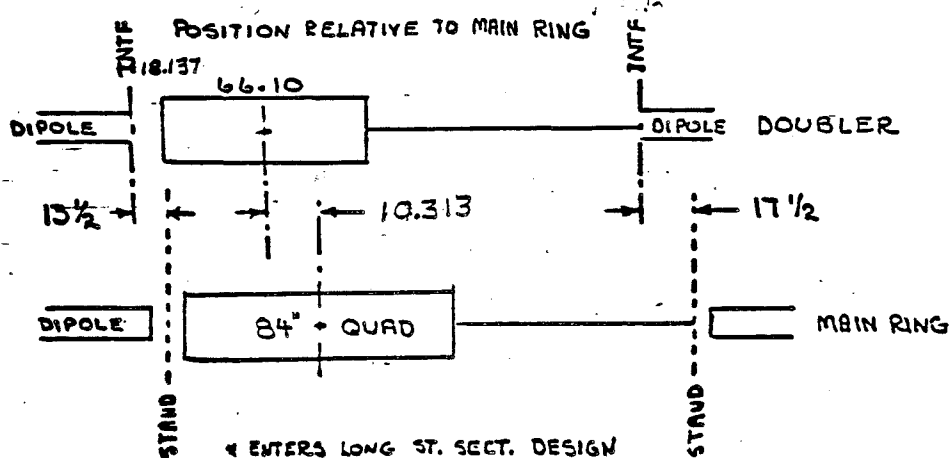


Fig. 8-2 Locations of superconducting magnets relative to main ring.

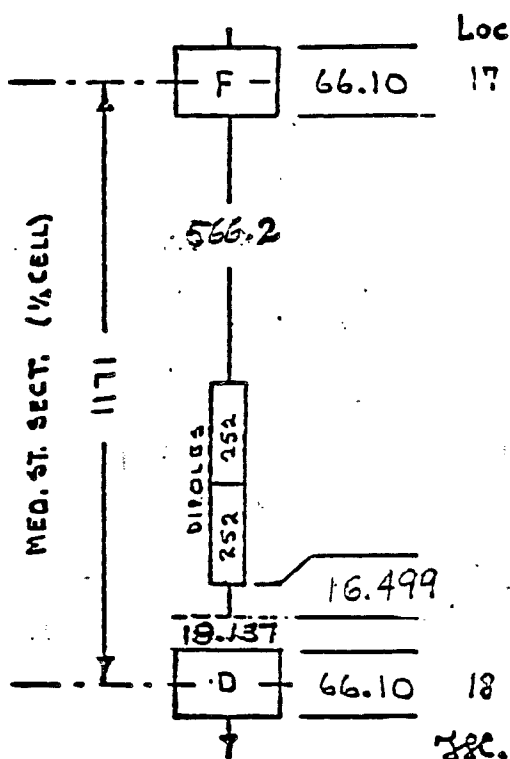


Fig. 8-3. Medium straight section. A standard 1/2-cell with two dipoles omitted. A space of 16-1/2 inches must be inserted at downstream end to close the geometric orbit in the shifted Doubler.

Like the Main Ring, the present lattice has a medium straight section at location 17 formed by omitting two dipoles. Its layout is shown in Fig. 8-3 below. There are long straight sections of "normal" configuration, ones with high beta for extraction, and ones with low beta for colliding-beam interactions. These are discussed separately in subsequent sections. Table 8-I summarizes the warm straight-section lengths available in the lattice. It gives the drift-lengths between "effective" magnetic ends of the elements, the available warm length and the space allotted for the cryogenic bypasses of cold-to-warm transitions and vacuum isolation.

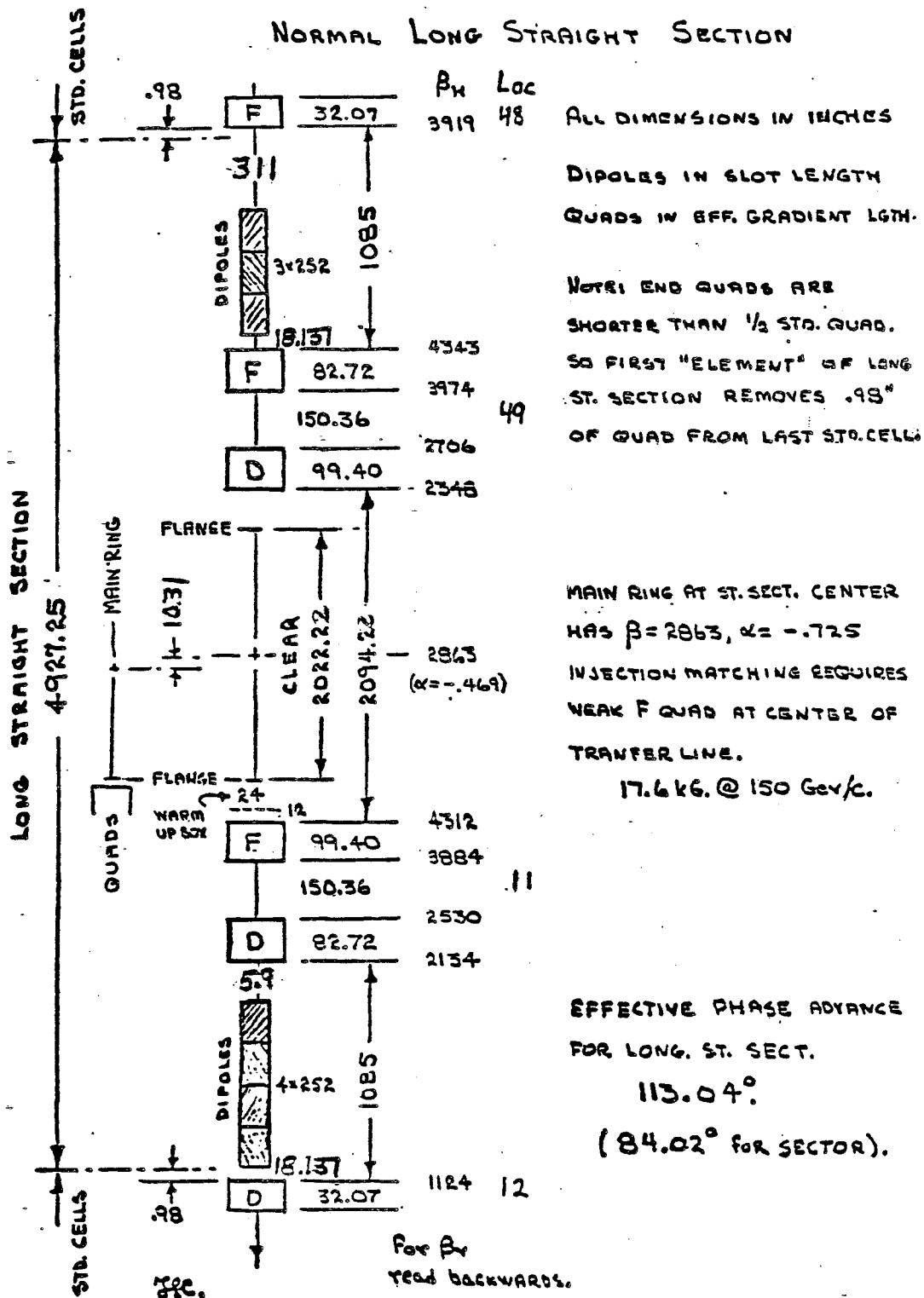


Fig. 8-4. Normal long straight section.

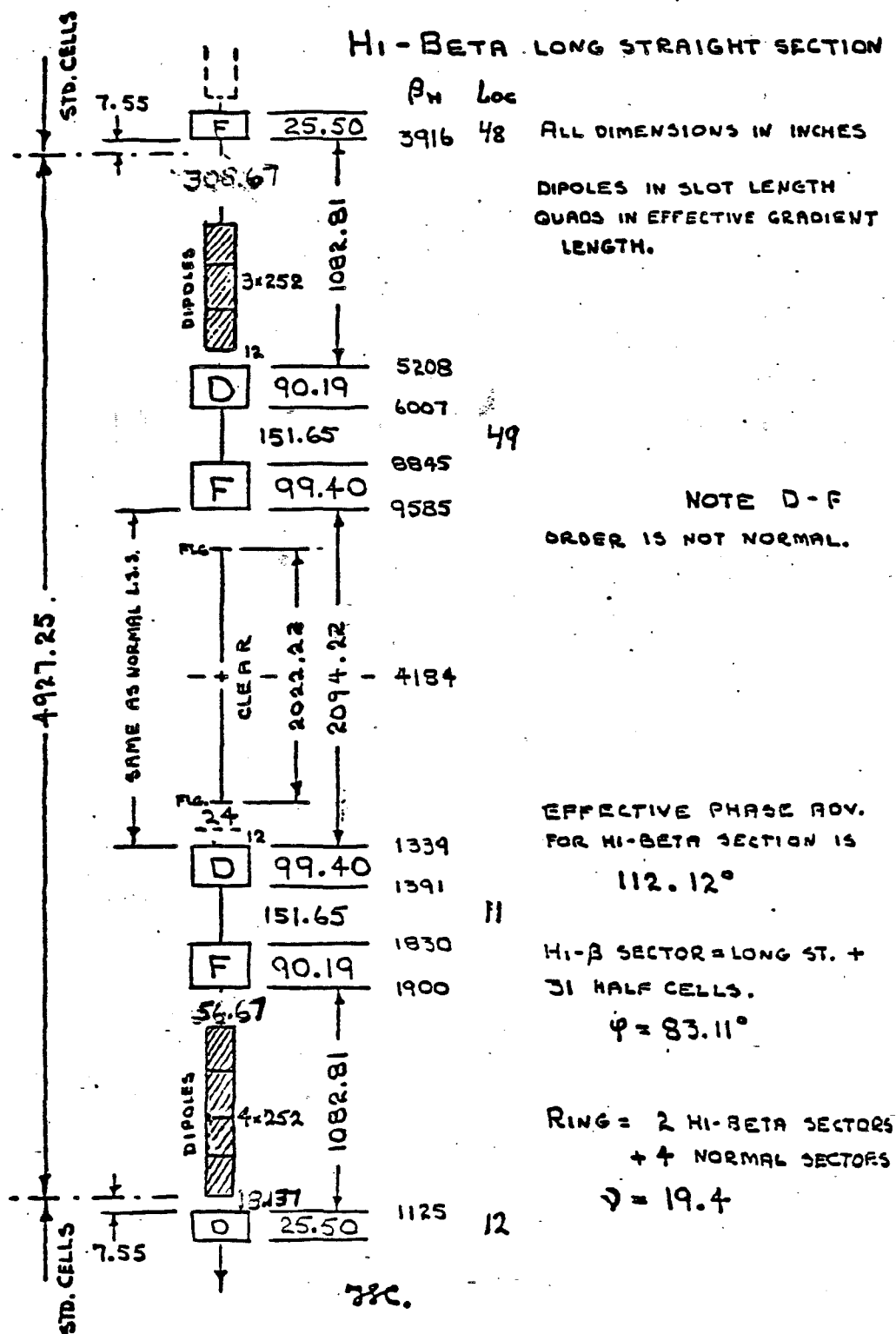


Fig. 8-5 High-beta long straight section.

Table 8-I WARM STRAIGHT-SECTION LENGTHS

Transition (In.)	Drift Length ^a (In.)	Available	
		Warm Length (In.)	Hot-Cold Upstream
<u>Location of Warm Regions</u> <u>Downstream</u>			
Median location 17 (standard quadrupole with corrections)	566.2	493.2	39 34
Normal- β median location 48	310.9	238.9	36 36
High- β median location 48	308.7	236.7	36 36
Normal- β doublet space 49,11	150.36	78.36	36 36
High- β doublet space 49,11	151.65	79.65	36 36
Long straight section	2094.22	2022.22	36 36
Low- β long straight section	600.24	528.24	36 36

^aMagnetic lengths used throughout to define drift lengths.

All medium straight sections at 17 and 48 locations, and all long straight sections are warm. The space between the long straight-section doublets is warm only where necessary.

8.2.2 Normal and High-Beta Long Straight Sections. Figure 8-4 shows the geometry of the normal long straight section together with amplitude functions. The design is very similar to normal Main Ring straight sections with the exception that two, rather than four, quadrupoles are used at either end of the straight section. C0, E0 and F0 are normal long straight sections. With this choice for E0, the lattice functions of the Main Ring and Energy Saver were matched nicely for the purpose of beam transfer.

The high-beta long straight section is illustrated in Fig. 8-5. Here the order of focusing in the doublets is reversed and lengths of all six quadrupoles were changed slightly. A large horizontal beta is produced at the upstream end of the straight section. High-beta straight sections were chosen for A0 and D0 because they facilitated resonant extraction, which places the most severe demands on the size of the good-field aperture. Since the good-field aperture of the superconducting magnets is not large, the use of high-beta at this location of the extraction electrostatic and magnetic septa reduces the aperture required for extraction in the rest of the magnet ring. This choice, which was made for fixed-target operation, will not affect the collider performance.

8.2.3 Lattice Elements. Table 8-II lists the various elements required for a ring incorporating two high-beta long straight sections and four normal long straight sections. The lengths shown are magnetic lengths in inches.

Table 8-II LATTICE ELEMENTS

<u>Element</u>	<u>Magnetic Length (In.)</u>	<u>Number</u>
Dipole	241.0	774
Standard quadrupole	66.1	180
Long straight inner quadrupole	99.4	12
Normal long straight short quadrupole (48,12 location)	32.07	8
Outer quadrupole	82.72	8
High beta long straight short quadrupole (48,12 location)	25.5	4
Outer quadrupole	90.19	4

8.2.4 Low-Beta Long Straight Section. The low-beta straight section at B0 is made by replacing the 32.07 in. quadrupoles at each end of the normal straight section with stronger, separately powered 66.10 in. quadrupoles and adding eight additional quadrupoles within the 2002 in. clear space around B0. During injection these eight quadrupoles are turned off and the two 66.10 in. quadrupoles are excited to a lower current than those in the rest of the ring. After injection and acceleration, the inner eight quadrupoles are turned on, and all ten quadrupoles are slowly adjusted until the final beta-value of one meter is reached. This process is described in detail in Chapter 9. It is noted that these eight quadrupoles will be turned off during fixed target operation. The additional elements required for the low-beta are listed in Table 8-III.

Table 8-III LOW-BETA QUADRUPOLES

<u>Element</u>	<u>Magnetic Length (In.)</u>	<u>Number</u>
Outer quadrupole	66.1	2
(48,12 location)	144.0	6
Inner quadrupole	180.0	2

8.3 CORRECTION SYSTEMS

8.3.1 Types of Correction Elements The correction magnets are built as a cluster of three functionally different superconducting coils which are concentric to one another and the beam tube center line.⁴ Since it was chosen to mount the coils on the beam pipe, or spool piece, between the quadrupole and the adjacent dipole in each cell, the correction magnet package is now called a spool piece. There are two basic types of spool pieces, the regular spool piece which is associated with each regular cell quadrupole, and the others. The distinction arises from the fact that each regular spool piece has two clusters of magnets, while the others have only one cluster of magnets. The upstream cluster of regular spool pieces

contains dipole, sextupole, and quadrupole windings and the downstream cluster contains octupole, sextupole, and quadrupole windings. The orientations of the dipole winding and the downstream sextupole and quadrupole windings provide further differentiation of the types spool piece. The shorter spool pieces also contain three coils. Altogether there are seven types of spool pieces. The types of coils on each spool piece are given in Table 8-IV. The designations for the type of coils are as follows; horizontal dipole (H), vertical dipole (V), sextupole (S), quadrupole (Q), skew quadrupole (SQ), skew sextupole (SS), and octupole (E).

Table 8-IV ENERGY SAVER SPOOL PIECES

Spool piece Type (Code)	Upstream (DSQ coils)	Downstream (OSQ coils)	Length (in.)
"A"	H, S, Q,	None	43
"B"	V, S, Q	None	43
"C"	H, S, Q	E, SS, SQ	72
"D"	V, S, Q	E, SS, SQ	72
"E"	H, S, Q	E, S, Q	72
"F"	V, S, Q	E, S, Q	72
"G"	H, S, Q	E, S, SQ	72
"H"	H, V, SQ	None	50

8.3.2 Correction Magnet Circuits The current leads of each coil are separately brought out of the spool piece cryostat, thereby making it possible to excite every coil independently. As will be discussed later the dipoles are individually excited in order to locally correct orbit dislocations. The sextupoles, quadrupoles, and octupoles are series connected in functional groups in order to adjust global properties such as the tune and chromaticity.

Tables 8-V, 8-VI, and 8-VII show the type of spool piece at each quadrupole location, by pairs of sectors. Superscripts designate the arrangement of the coils into global circuits which will be used when the Energy Saver is commissioned. Coil windings which are not noted in those tables are not connected to power supplies, although this could be done if a need arose.

Table 5-1-1 DC Magnetic Parameters of Correction Element Coil Assemblies

Package	Coil	T(bare)	Iron Factor	T(iron)	Effective length (h)	$\int B dl$ at 50A and 1"	Inductance			
		(a)		(a)			— warm — bare (c)	iron (d)	— cold — iron (e)	
DSQ	Dipole	89.20	1.466	130.8	27.69"	181.1 KG-in	475 μ H	696 μ H	686 μ H	
	Sext.	32.25	1.259	40.60	28.31"	57.16	462	582	556	
	Quad.	31.67	1.662	52.63	28.56"	75.16	293	487	479	
OSQ	Octu.	21.76	1.054	22.94	28.88"	33.12	198	209	198	
	Sext.	24.51	1.281	31.39	28.32"	44.45	300	384	370	
	Quad.	31.67	1.662	52.63	28.56"	75.16	293	487	479	

(a) Gauss at 1"/amp

(b) average of outer and inner coil lengths

(c) based on inductance bridge measurements before installation of Al pipe

(e) allowance for screening effect of superconductor

(d) warm X iron factor.

Table 8-10VL Physical Parameters of Correction Element Coil Assemblies

Package	Coil (a)	Coil inner			θ_{min} (b)		θ_{max} (b)		Coil inner length		Coil outer length (typ)	Iron length	Total # of Turns N	Coil end geometry (c)
		radius	radius	radius	(b)	(b)	(b)	(b)	length	length				
DSQ	Dipole	1.602"	1.814"	2.504"	0°	0°	60°	25 ³ / ₈ "	30"	30"	30"	30"	1170 (2x585)	NEND = Ø
	Sext.	1.854"	2.142"	2.504"	0°	0°	20°	26 ⁵ / ₈ "	30"	30"	30"	30"	1965 (3x655)	2
	Quad.	2.182"	2.335"	2.504"	0°	0°	30°	27 ¹ / ₈ "	30"	30"	30"	30"	1240 (4x310)	Ø
DSQ	Octu.	1.602"	1.870"	2.504"	0°	0°	15°	27 ³ / ₄ "	30"	30"	30"	30"	1500 (4x375)	2
	Sext.	1.910"	2.142"	2.504"	0°	0°	20°	26 ⁵ / ₈ "	30"	30"	30"	30"	1560 (3x520)	2
	Quad.	2.182"	2.335"	2.504"	0°	0°	30°	27 ¹ / ₈ "	30"	30"	30"	30"	1240 (4x310)	Ø

- (a) Packages include either normal or skew coils depending on subclass spec.
- (b) half angles given for normal coil - angles chosen to cancel 3rd harmonic
- (c) using coil end geometry as per Stan Snowden's definition (memo dated 10/24/80)

Table 8-V COIL CIRCUITS IN SPOOL PIECES IN SECTORS A AND D

Quad Loc.	Spool Type	Upstream Coils	Downstream Coils	Quad Loc.	Spool Type	Upstream Coils	Downstream Coils
11	"H"	H, V, SQ ⁴	-----	12	"D"	V	SS ³
13	"G"	H, S ^f , Q	SQ ⁰	14	"D"	V, S ^d , Q	SS ³
15	"A"	H, S ^f , Q	-----	16	"D"	V, S ^d , Q	SS ³
17	"C"	H, S ^f , Q	SQ ⁰	18	"D"	V, S ^d , Q	SS ³
19	"C"	H, S ^f , Q	SQ ¹	21	"B"	V, S ^d , Q	-----
22	"C"	H, S ^f , Q	SS ² , SQ ⁰	23	"D"	V, S ^d , Q	E ⁴ , SS ⁴
24	"C"	H, S ^f , Q	SS ² , SQ ²	25	"B"	V, S ^d , Q	-----
26	"C"	H, S ^f , Q	SS ² , SQ ⁰	27	"D"	V, S ^d , Q	E ⁴ , SS ⁴
28	"C"	H, S ^f , Q	SS ² , SQ ¹	29	"B"	V, S ^d , Q	-----
32	"C"	H, S ^f , Q	SS ¹ , SQ ⁰	33	"D"	V, S ^d , Q	E ⁴
34	"C"	H, S ^f , Q	SS ¹ , SQ ²	35	"B"	V, S ^d , Q	-----
36	"C"	H, S ^f , Q	E ³ , SS ¹ , SQ ⁰	37	"D"	V, S ^d , Q	E ⁴ , SS ⁴
38	"C"	H, S ^f , Q	SS ¹	39	"B"	V, S ^d , Q	-----
42	"C"	H, S ^f , Q	E ³ , SQ ⁰	43	"D"	V, S ^d , Q	SS ⁴
44	"C"	H, S ^f , Q		45	"B"	V, S ^d , Q	-----
46	"C"	H, S ^f , Q	SQ ⁰	47	"D"	V, S ^d , Q	
48	"A"	H	-----	49	"H"	H, S ^d , V, SQ ⁴	

Table 8-VI. COIL CIRCUITS IN SPOOL PIECES IN SECTORS B AND E

Quad Loc.	Spool Type	Upstream Coils	Downstream Coils	Quad Loc.	Spool Type	Upstream Coils	Downstream Coils
11	"H"	H, V, SQ ⁴	-----	12	"D"	V	
13	"C"	H, S _f , Q	SQ ⁰	14	"D"	V, S ^d , Q	
15	"A"	H, S _f , Q	-----	16	"D"	V, S ^d , Q	
17	"C"	H, S _f , Q	E ¹ , SQ ⁰	18	"D"	V, S ^d , Q	
19	"E"	H, S _f , Q	E ¹ , Q ¹	21	"B"	V, S ^d , Q	-----
22	"C"	H, S _f , Q	E ² , SQ ⁰	23	"F"	V, S ^d , Q	E ⁴ , Q ²
24	"E"	H, S _f , Q	E ² , Q ³	25	"B"	V, S ^d , Q	-----
26	"C"	H, S _f , Q	E ¹ , SQ ⁰	27	"F"	V, S ^d , Q,	E ⁴ , Q ⁴
28	"E"	H, S _f , Q	E ¹ , Q ¹	29	"B"	V, S ^d , Q	-----
32	"C"	H, S _f , Q	E ² , SQ ⁰	33	"F"	V, S ^d , Q	E ⁴ , Q ²
34	"E"	H, S _f , Q	E ² , Q ³	35	"B"	V, S ^d , Q	-----
36	"C"	H, S _f , Q	E ³ , SQ ⁰	37	"F"	V, S ^d , Q	E ⁴ , Q ⁴
38	"C"	H, S _f , Q		39	"B"	V, S ^d , Q	-----
42	"C"	H, S _f , Q	E ³ , SQ ⁰	43	(D)	V, S ^d , Q	
44	"C"	H, S _f , Q		45	"B"	V, S ^d , Q	-----
46	"C"	H, S _f , Q	SQ ⁰	47	(D)	V, S ^d , Q	
48	"A"	H	-----	49	"H"	H, V, SQ ⁴	

Table 8-VII. COIL CIRCUITS IN SPOOL PIECES IN SECTORS C AND F

Quad Loc.	Spool Type	Upstream Coils	Downstream Coils	Quad Loc.	Spool Type	Upstream Coils	Downstream Coils
11	"H"	H, V, SQ ⁴		12	F	V	S ³
13	"C"	H, S, Q	SQ ⁰	14	"F"	V, S, Q	S ³
15	"A"	H, S, Q	-----	16	"F"	V, S, Q	S ³
17	"C"	H, S, Q	E ¹ , SQ ⁰	18	"F"	V, S, Q	S ³
19	"E"	H, S, Q	E ¹ , Q ¹	21	"B"	V, S, Q	-----
22	"C"	H, S, Q	E ² , S ² , SQ ⁰	23	"F"	V, S, Q	E ⁴ , S ⁴ , Q ⁴
24	"E"	H, S, Q	E ² , S ² , Q ³	25	"B"	V, S, Q	-----
26	"G"	H, S, Q	E ¹ , S ² , Q ¹ 0	27	"F"	V, S, Q	E ⁴ , S ⁴ , Q ⁴
28	"E"	H, S, Q	E ¹ , S ² , Q ¹	29	"B"	V, S, Q	-----
32	"G"	H, S, Q	E ² , S ¹ , SQ ⁰	33	"F"	V, S, Q	E ⁴ , Q ²
34	"E"	H, S, Q	E ² , S ¹ , Q ³	35	"B"	V, S, Q	-----
36	"G"	H, S, Q	E ³ , S ¹ , SQ ⁰	37	"F"	V, S, Q	E ⁴ , S ⁴ , Q ⁴
38	"E"	H, S, Q	S ¹	39	"B"	V, S, Q	-----
42	"C"	H, S, Q	E ³ , SQ ⁰	43	"F"	V, S, Q	S ⁴
44	"C"	H, S, Q		45	"B"	V, S, Q	-----
46	"C"	SQ ⁰		47	"D"	V, S, Q	
48	"A"	H	-----	49	"H"	H, V, SQ ⁴	

8.3.3 Coil Strength Requirements. The Q^f and Q^d quadrupoles are used to adjust the machine tune. There is a Q^f quadrupole adjacent to every regular horizontally focusing main quadrupole and Q^d quadrupole next to every vertically focussing main quadrupole. The Q^f quadrupoles are connected in one series circuit, and the Q^d quadrupoles are connected in an another. The S^f and S^d sextupoles are also designated in the same way by the adjacent main quadrupole. The S^f and S^ø circuits are used to adjust the chromaticity.

The remaining correction magnets will be used initially for half integer resonant extraction when the Energy Saver commissioning begins. The Q¹ and Q³ circuits will be used for half-integer extraction. The Q² and Q⁴ circuits, which will not be powered initially, can be used in conjunction with the Q¹ and Q³ circuits to correct the $2\nu_x = 39$ and $2\nu_y = 39$ resonances. The 48 skew quadrupoles located in standard cells, SQ³, are connected in series. These will be used to compensate the difference resonance, $\nu_x - \nu_y = 0$. If needed, skew quadrupoles at the ends of the long straight sectors, SQ³, can also be excited to provide additional compensation of the $\nu_x - \nu_y = 0$ resonance.

The circuits SQ¹ and SQ² when powered can be used to manipulate the half integer sum resonance $\nu_x + \nu_y = 39$. The circuits S¹, S², S³, and S⁴, when powered, can affect the driving terms on the $3\nu_x$ and $\nu_x + \nu_y$ resonance should the need arise. Similarly the skew sextupoles SS¹, SS², SS³, and SS⁴ are installed at the locations given in the tables for driving the $2\nu_x + \nu_y$ and $3\nu_y$ resonances.

Octupoles are arranged in four circuits. Circuits E^1 and E^2 provide the two phases of the 39th harmonic for resonant extraction. Circuits E^3 and E^4 produce the zero-harmonic nonlinearity for control of tune versus betatron oscillation amplitude. The strengths of the coils which are appropriate for 1 TeV are expressed as field integrals at 1 in. radius.

Steering Dipoles. The primary function of the steering dipoles is the correction of the closed orbit at all energies. The rigidity of the superconducting-magnet system and the tight tolerance on orbit centering imposed by extraction ruled out the movement of magnets for orbit correction. In order to make efficient use of the available magnet aperture, it was specified that the closed orbit excursions be limited to ± 0.1 in. during extraction. This requirement is met by using the steering dipoles. The steering dipole strength was determined to be 170 kG-in. on the basis of the following analysis:

It is likely that orbit distortions will be large during the initial operation. At points in the normal cells where the amplitude function is a maximum, the rms orbit distortion due to dipole field errors and quadrupole misalignments can be written as

$$\langle x^2 \rangle^{1/2} \approx \frac{1}{4}(a^2 + \frac{5}{9}b^2)^{1/2} \text{ in.},$$

Here a denotes the rms dipole field error in units of 0.1%, and b the rms quadrupole misalignment in units of 0.01 in. In the horizontal plane, a arises from the fluctuation in the field-length product from dipole to dipole. In the vertical plane, a receives contributions from both rotational alignment error and any uncertainty or instability in the dipole field direction. It was assumed that the typical misalignment error introduced into the orientation of the dipole vertical plane during installation was 1 mrad and the stability of that of the vertical plane also had an error of 1 mrad. It was assumed that the quad placement accuracy was 0.02 in. This leads to an rms closed orbit distortion of 0.5 in. The dipole strength required to compensate the deflection generated locally by the quadrupole misalignment and by the eight neighboring main dipoles, is, for uncorrelated dipole errors

$$(\int B dl)_{\text{rms}} = 23(a^2 + 0.31b^2)^{1/2} \text{ kG-in.},$$

a and b have the same significance as in the previous expression. The assumptions made for alignment in the previous paragraph require a 41 kG-in. field integral to correct the rms error. For Gaussian errors, a steering strength of about 130 kG-in. is needed to have 90% probability of successful correction at 100 locations. The steering dipole was designed for a strength of 170 kG-in. This was considered adequate to meet the concerns of the preceding paragraphs.

Trim quadrupoles. Since the main dipoles and quadrupoles are connected in

series, trim quadrupoles assume the burden of tune correction and adjustment. Appropriate quadrupole harmonic terms are needed for half-integer extraction.

One of the main functions of the trim quadrupoles will be compensate for the large incremental increase in tune caused by the low-beta interaction regions used in colliding beams. A typical interaction-region will introduce an added betatron phase advance of close to 180° in both planes of oscillation. The trim quadrupoles must, in effect, lower both tunes - by approximately 0.5 to restore the operating point. The BO design described in Chapter 9 produces a shift in tune of 200° . The required trim-quadrupole strength at 1000 GeV may be inferred from

$$\Delta v_H = 0.0214(B'l)_F - 0.0062(B'l)_D$$

$$\Delta v_V = -0.0062(B'l)_F + 0.0214(B'l)_D$$

The subscripts indicate the focusing character in the horizontal plane of the adjacent quadrupole. A reduction of both tunes by 0.5 requires a contribution to trim quadrupole strength of 33 kG-in.

Tune corrections that must be made to compensate for magnet errors require considerably smaller strengths. A systematic quadrupole term b_1 in the dipoles would produce tune shifts $\pm 1.1 \times 10^3 b_1$ in the two planes of motion. On the basis of the production of 764 dipoles, the average value of b_1 is less than $10^{-5}/\text{inch}$. This b_1 makes an inconsequential demand on the trim quad strengths.

The trim-quadrupole strength was specified at 60 kG-in., safely above the requirement imposed by a single interaction region after allowance for tune correction. In order to operate two interaction regions somewhat greater strength is required. The quad can be excited to higher currents if necessary, although a special supply would be required. Alternatively, the operating point of the collider can be shifted from 19.4 to 19.6 to allow a greater tuning range.

Sextupoles. The principal role of the sextupoles is control of the chromaticity. At the time of the Superconducting Acceleration Design Report, May 1979, high field sextupole moments were cause for concern since b_2 was large. On the basis of the production of 764 magnets, the average value of b_2 is measured to be $10^{-4}/\text{in}^2$. As the following analysis shows b_2 is no longer a cause for concern.

The contributions to the chromaticity from systematic sextupole terms in the dipoles and from chromatic aberration in the quadrupoles can be written as

$$\xi_H = 2.64 \times 10^5 \langle b_2 \rangle - 22$$

$$\xi_V = -2.45 \times 10^5 \langle b_2 \rangle - 22,$$

$$b_2 \text{ in } (\text{in.})^{-2}$$

The constant value of -22 is due to the natural chromaticity of the basic lattice exclusive of enhancements from colliding-beam interaction regions. The magnet-selection criteria impose a bound of $6.0 \times 10^{-4} \text{ in.}^{-2}$ on the magnitude of b_2 . The measured average value of b_2 leads to a chromaticity in one plane or the other of about 50. Compensation of this effect requires sextupole strengths of 4.5 and 1.5 kG-in. at horizontally focusing and defocusing quadrupoles respectively.

A colliding-beam interaction region can be expected to increase the natural chromaticity. For example the design presented in Chapter 9 increased the chromaticity by 9 units to -31. The sextupole associated with the standard cell quadrupole was designed to have a strength of 50 kG-in., value which is conservatively beyond the minimum requirements.

Octupoles. The major purpose of the octupoles is to facilitate resonant extraction. They provide the nonlinearity that divides the phase plane into stable and unstable regions for the case of half-integer extraction. On the basis of the requirements for resonant extraction the individual octupole strength has been specified as 30 kG-in.

Skew quadrupoles. At an early stage of the operation of the Main Accelerator at high energy it was observed that a large horizontal oscillation would couple over into the vertical in a single turn. On the basis of magnet measurements the same thing will occur in the Energy Saver. For that reason skew quadrupoles were incorporated into the spool pieces as noted in Tables 8-V, 8-VI, and 8-VII. The skew quadrupole is similar in all respects to the trim quadrupole except that it is rotated by 45° . It has the same strength of 60 kG-in.

8.3.4 Excitation. In this section, the tolerances on the currents delivered to the correction and adjustment magnets and their arrangement in circuits are discussed. The coils were specified to achieve their nominal design strengths at a current of 50 A. The coils can be separately powered at much higher currents. As noted earlier the circuits for exciting the coils are given in Tables 8-V, 8-VI, and 8-VII.

Current Tolerances. Because of their role in orbit correction, the steering dipoles inherently require independent bipolar power supplies. Stability and ripple suppression at 0.1% of full scale are sufficient to satisfy the demands of injection and extraction. Each of the global circuits, defined in 8.3.2, is powered by a precision supply which provides a current stability in the range of 0.1% to .005%. The most severe requirement which these supplies must satisfy is to provide a relatively unmodulated resonant extraction over 10 seconds.

8.3.5 Power Supplies Two distinct types of power supplies have been built; one with an accuracy of 0.1% in regulation for the steering dipoles and a high precision supply for the other elements. There are 180 steering

dipoles in the standard cells of the lattice, and at least 4 dipoles will be installed at each long straight section. There will therefore be a need for over 200 supplies of the first variety.

The design value is $\pm 50\text{A}$. The supplies will be designed with load compensation and a conventional roll-off characteristic of 20 db/decade.

Steering Dipole Supplies. The current stability and ripple limit for these supplies is $\pm 0.1\%$ of full scale. To complete the specifications, the bandwidth and voltage must be determined. It is reasonable to have a bandwidth that allows the power supply output to follow a constant ramp input within $\pm 0.1\%$ of full scale. The error between programmed input and supply output for a constant ramp is

$$\epsilon = \frac{AB}{2\pi f_0}$$

where ϵ is the lag error (amps),
 A is the power supply DC gain (amps/volt),
 B is the input voltage ramp rate (volts/s), and
 f_0 is the power supply bandwidth or corner frequency (Hz)

For an error of 0.1% (0.05A) and a ramp from 0 to 50 A in 10 s, a power-supply bandwidth of 20 Hz is adequate. With this 20-Hz bandwidth, the equation above then yields a maximum output ramp rate for 0.1% accuracy of 6.3 A/s.

The supplies will be installed in the existing Main-Ring service buildings. The longest lead from the supply to dipole and back will be 1200 feet. At 50A and 35°C, the voltage drop in that length of No. 1 wire is 8.1 V. The load inductance will be approximately 0.7 H; at the maximum ramp rate, for 0.1% accuracy, the drop across the magnet would be 4.4 V. A maximum power supply output of 15 V satisfies these requirements and provides a higher slewing capability for current changes under conditions where the accuracy specification can be relaxed.

A block diagram of such a supply is shown in Fig. 8-6. The control system provides a bipolar analog reference waveform from a generator with 12-bit resolution and 2 bits for commands to operate. The current reading is returned to the control system via a multiplexed A/D along with 8 status and fault bits. Isolation is provided between the control system and the power supply for command, status, and faults by means of optical couplers. Isolation of the analog signals is accomplished through differential drivers and receivers.

High Precision Supplies These supplies are to have a stability and ripple limit in the range 0.005% to 0.01% of full-scale current. They are rated at $\pm 50\text{A}$, $\pm 600\text{V}$. The low ripple current is achieved with a bipolar transistorized output regulator.

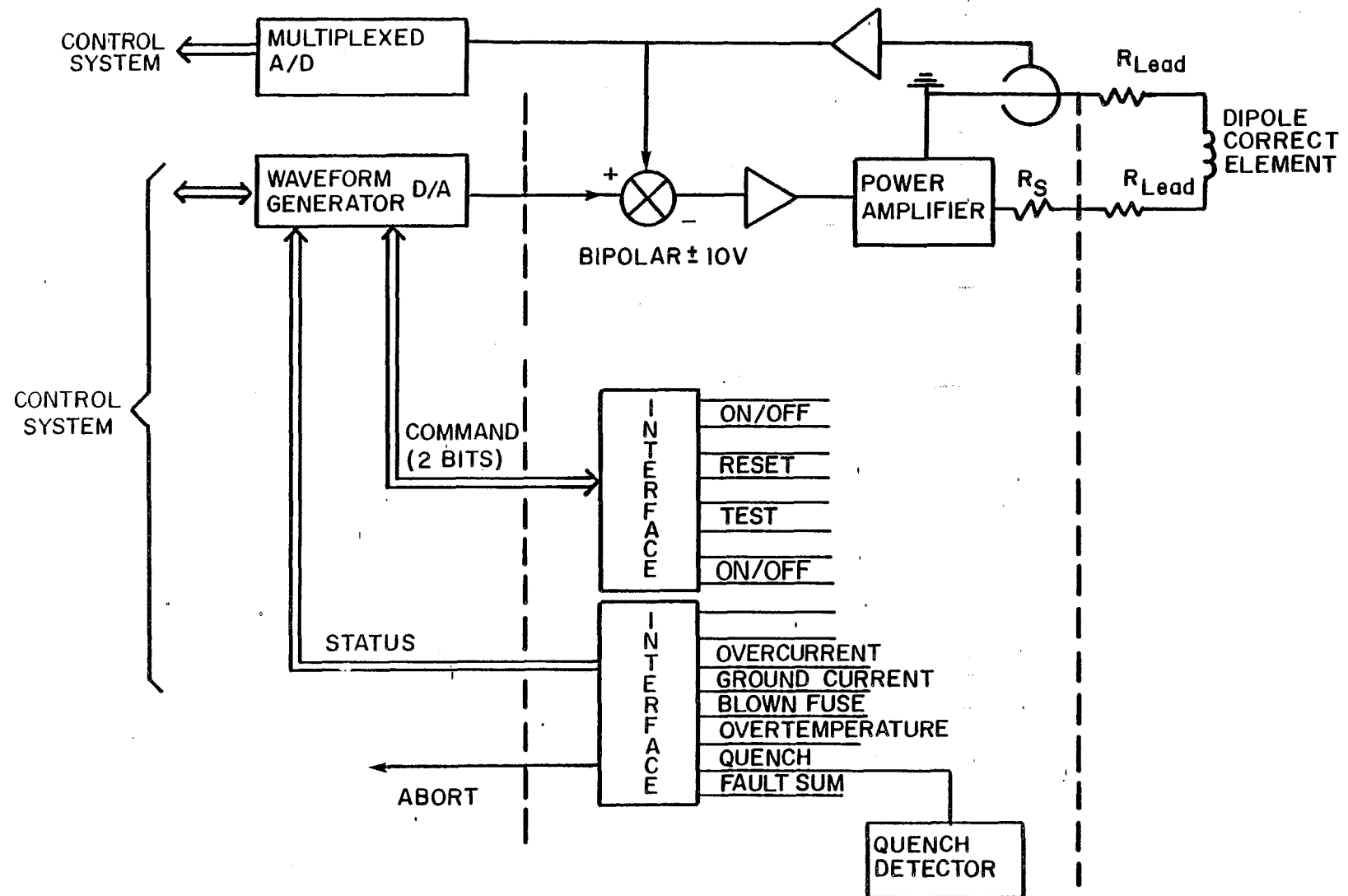


Fig. 8-6

It is noted that certain of these supplies have a relatively high output voltage. To reduce transistor-bank dissipation, these supplies use a bipolar SCR preregulator to provide variable voltage to the output transistor regulator. The preregulators are adjusted to keep a nearly constant voltage across the output transistor banks and thus reduce the transistor-bank requirements. The transistor-bank regulators for the various high-precision supplies are essentially the same. The same is true of the preregulator.

The reference voltage is provided by a high-precision 16-bit D/A and the current sensor is a high quality current transducer with a stability of 1 ppm/°C. The waveform generator is located within the supply to minimize noise pickup. Quench detection is also provided by comparing the voltage across one half the series regulators to the other half.

8.4 Main Ring Extraction and Energy Saver Injection and Abort

The design of the antiproton beam transfer was simplified considerably once the circumference of the Energy Saver was made equal to the Main Ring. Fig. 8-7 is a schematic representation of the EO straight section which shows both the proton and antiproton transfer lines.

The proton injection for colliding beams will proceed with the transfer of a single bunch from the Main Ring to the Tevatron. The bunch will be kicked horizontally across a magnetic septum (Lambertson magnets) in the Main Ring at the upstream end of EO using the existing extraction kicker magnet at C48. This initiates a downward bend (16.6 mrad) towards the superconducting string at E11, 25.5 in. below the Main Ring. The vertical dog-leg is completed by two more Lambertson magnets at the downstream end of the long straight section which brings the beam back on to the horizontal plane. The beam is then placed on the closed orbit by another fast rise time kicker magnet located at the warm E17 medium straight in the Tevatron. Although the basic lattice structures of the Main Ring and the Tevatron are similar, a transverse emittance dilution of approximately ~30% would occur if no attempt were made to match the beam shape. A quadrupole in the injection line will be used to provide both horizontal and vertical matching. Horizontal beam steering is accomplished in the Main Ring and the injection line by a series of bump magnets; the correction dipoles accomplish the corresponding function in the Tevatron.

The antiproton injection uses four additional Lambertsons and two trims as shown in Fig. 8-7. The matching quad is common to both lines. The \bar{p} transfer is accomplished in the same manner as for protons with the Main Ring extraction kicker located at E17 and the saver injection kicker located at D48.

Table 8-VIII lists the kicker requirements for six bunches of protons and six bunches of antiprotons, all equally spaced. This establishes the maximum number of bunches that can be injected. Nevertheless, it is not planned to exceed 3 bunches of protons and 3 bunches of antiprotons at this time. This table is based on injecting the antiprotons first, one bunch at a time and then interspersing the proton bunches among the antiproton

INJECTION LINE SCHEMATIC (VERTICAL)

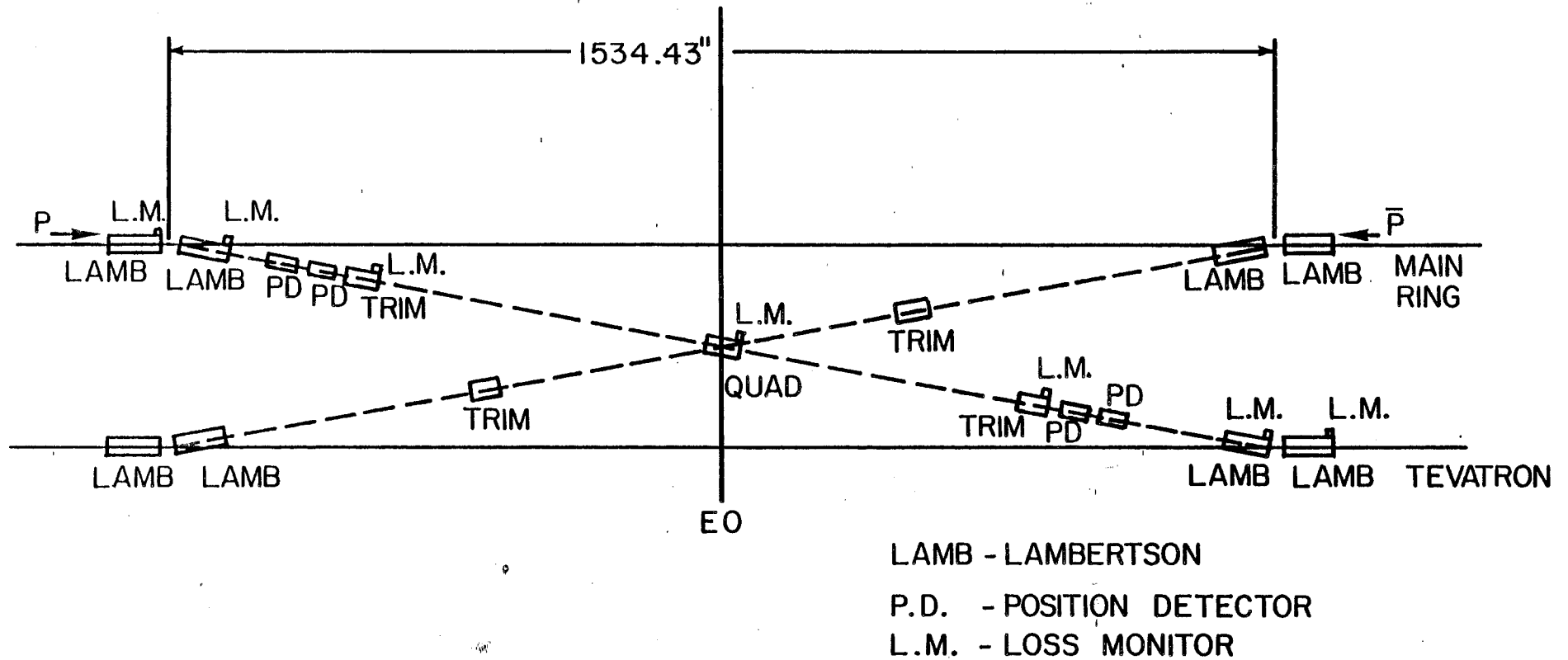


Fig. 8-7

bunches one bunch at a time. The specifications for the proton transfer kickers were set by the requirements for fixed target operations.

Table 8-IX lists the requirements of the proton and antiproton abort kickers. Again the requirements for the proton abort kicker are met in the existing design for fixed target application, and two additional identical units will suffice for the \bar{p} abort kicker.

The abort dump for the protons has been designed for the much more intense proton beam which occurs during fixed target operation. The \bar{p} dump will be a 10-foot long steel block located in the C0 straight section, since the \bar{p} beam intensity is two orders of magnitude smaller. The use of the C48 kicker to inject protons at E0 creates the possibility of introducing uncomfortably large amplitude oscillations through D sector of the Main Ring. In order to reduce the size of these oscillations, where possible, three bump magnets have been installed in the Main Ring at C22, C32 and D38. These three magnets can be excited to produce a closed orbit 180° out of phase with the kicked beam and thus reduce the effective orbit excursions by a factor of 2 throughout most of the sector. Precise control of the beam position in the Main Ring across the long straight section, essential to ensure loss free injection, is provided by another set of bump magnets at D46 and E17. Powered in series these magnets generate an orbit bump similar to that currently used in the Main Ring for extraction. A hypothetical closed orbit suitable for injection is shown in Figure 8-8. The orbit excursions between C22 and D38, D46 and E17 are apparent. Fig. 8-9 shows the same closed orbit modified by firing the kicker which produces the orbit cusp at C48. The orbit amplitude remains approximately constant up to D38 after which the amplitude increases to a maximum offset of 48 mm at D48. The horizontal orbits across the long straight section are shown in more detail in Fig. 8-10a, where the error bars on the Main Ring orbits give the expected beam size (± 4 mm) at the Lambertson septum. With these particular injection parameters, one can see an intrabeam separation of 7 mm with the septum offset at 25 mm. The corresponding Tevatron orbits are shown in Fig. 8-10b. The closed orbit bump between E11 and E17 is generated by the correction coil dipoles at E11, E13, E15, and E17 and serves to reduce orbit excursions within the restricted aperture of the Tevatron as well as decrease the integrated field strength required from the kicker magnet at E17.

The same bump magnets used for the proton extraction in the Main Ring are used to reduce the required kick for the antiproton extraction kicker and an appropriate 3-bump using the D46, D48, and D49 Saver correction dipoles will be used to reduce the maximum orbit distortions at injection and reduce requirements on the \bar{p} injection kicker, in a way analogous to the proton injection 4-bump.

The injection Lambertson magnets are similar in design to the current Main Ring extraction devices. The magnets have 12 turns of water cooled 0.46" square copper giving a useful dipole field aperture of $3.5" \times 0.9"$. The nominal operation current of 1575 A produces a 9 kG field. The maximum useable field is defined by the saturation of the steel (Republic Steel

MAIN RING CLOSED ORBIT
PRIOR TO INJECTION

HORIZONTAL PROJECTION
TUNE : 19.420
MAX. OFFSET : 2.34 cm

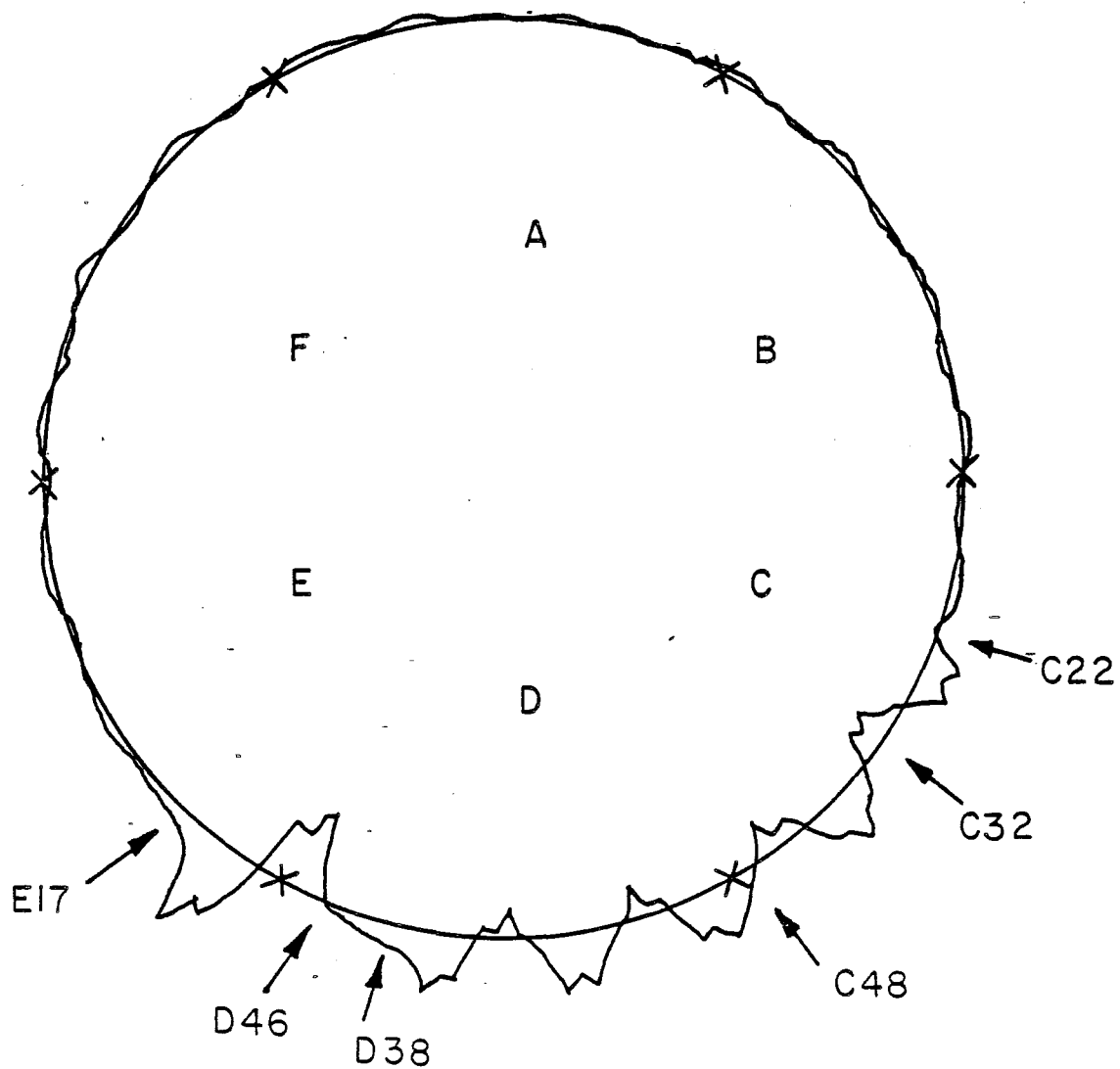


Fig. 8-8

MAIN RING INJECTION ORBIT

HORIZONTAL PROJECTION

TUNE: 19.420

MAX. OFFSET: -4.82 cm

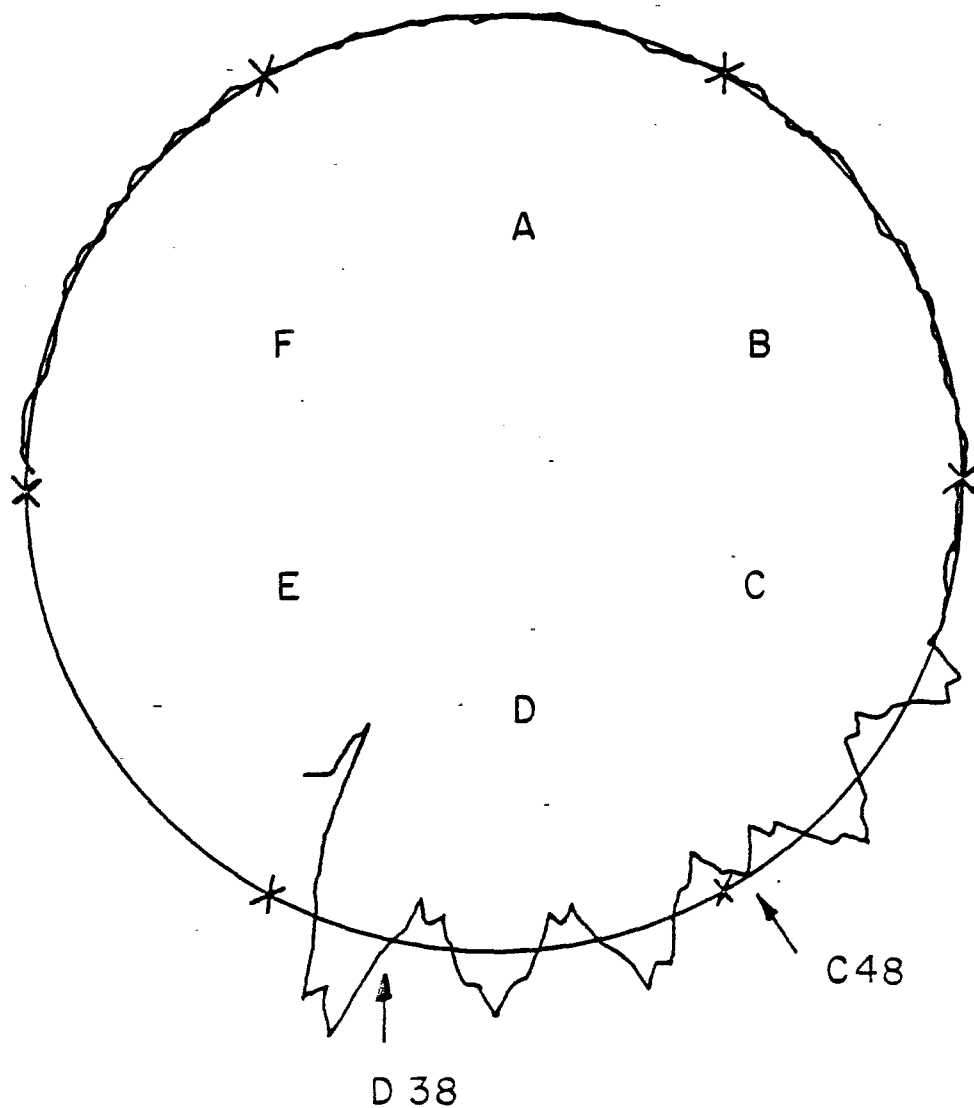


Fig. 8-9

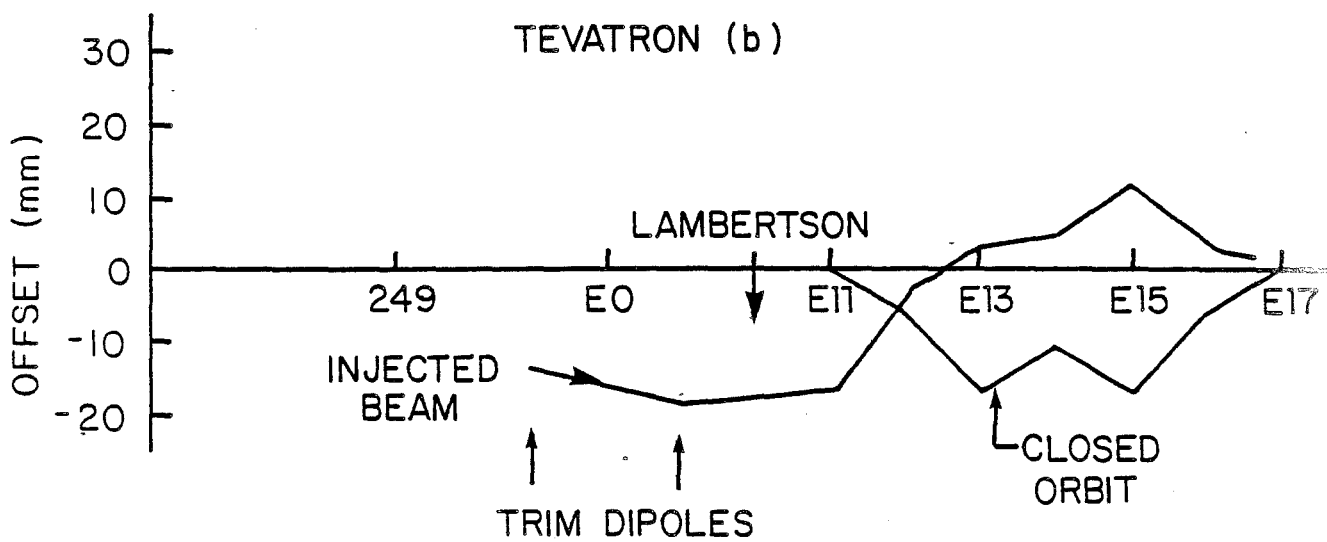
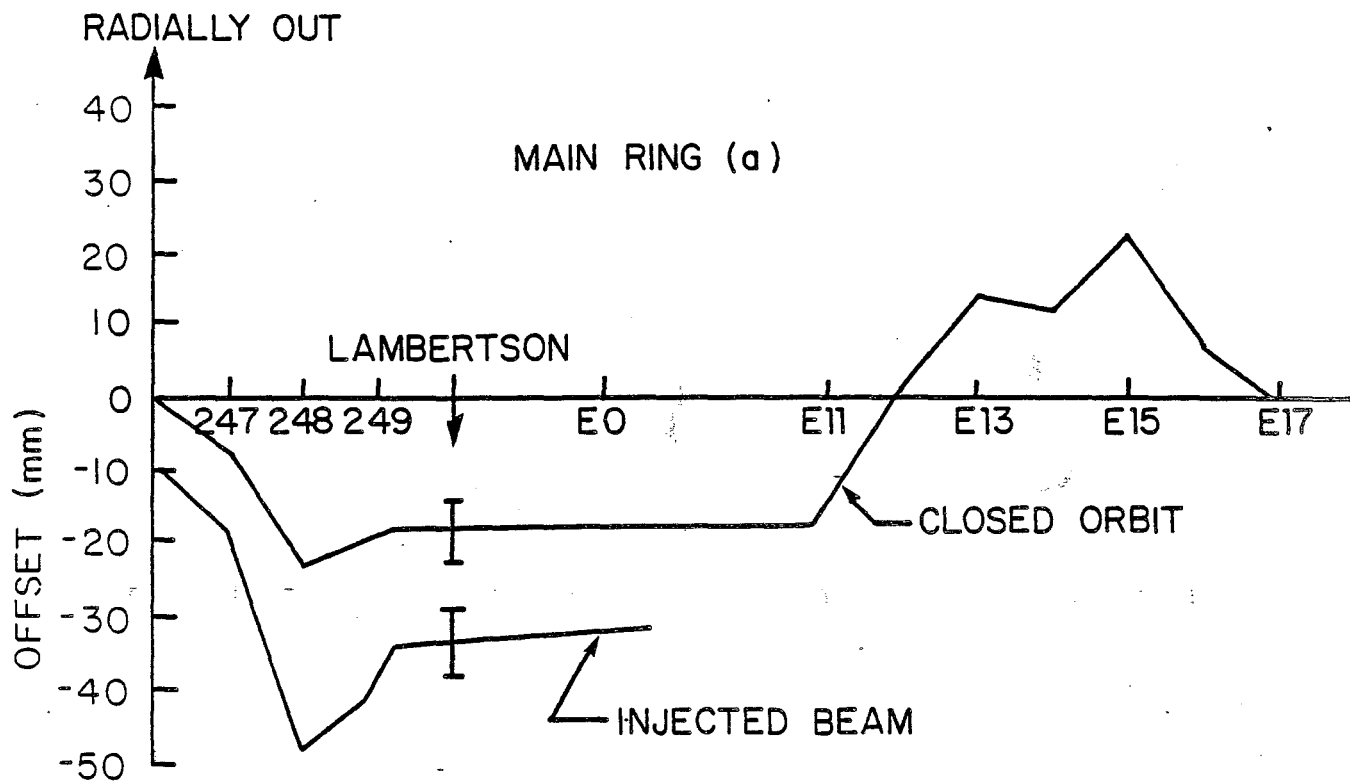


Fig. 8-10

LoCore 'B') and is 12 kG. The septum is 2 in. thick and is formed with a half angle of 45° .

Table 8-VIII. EXTRACTION AND INJECTION MAGNET PARAMETERS

	p	p	\bar{p}	\bar{p}
	Extraction	Injection	Extraction	Injection
B-l	1.97 kG-m	1.33 kG-m	2.5 kG-m	2.5 kG-m
Rise time	20 μ sec	1.39 μ sec	20 μ sec	3.4 μ sec
Fall time	--	2.0 μ sec	--	3.4 μ sec
Magnets	6	4	1	4
Magnet impedance	25 Ω	12.5 Ω	5.5 Ω	10 Ω
Magnet Length (m)	1	1	1	1
PFN's	1	1	1	1
PFN impedance	12.5 Ω	6.25 Ω	1 Ω	10 Ω
Gap (inches)				
HxV	6x2	2x2	6x2	2x2
Voltage	56 kV	43 kV	15 kV	50 kV

Table 8-IX. ABORT MAGNET PARAMETERS

	p	\bar{p}
	Abort	Abort
B-l	24 kG-m	15 kG-m
Rise time	3.2 μ sec	2.0 μ sec.
Location	B-48	C-17
No. module	4	2
Length	2 m	2 m
I_{\max}	19 kA	15 kA

8.5 Acceleration of Protons and Antiprotons

8.5.1 Energy Saver RF Requirements for Colliding Beams When the Energy Saver is used for colliding beams, the rf system must be able to accelerate protons and antiprotons simultaneously from 150 to 1000 GeV. Because the longitudinal emittance of proton and antiproton bunches may be slightly different, it may be necessary to provide different bucket areas for each in order to minimize dilution during acceleration and storage. Dynamic phase adjustment of proton and antiproton buckets will be necessary in order to damp coherent dipole oscillations of the separate bunches. The rf system should also have the capability of moving the azimuthal location of the $\bar{p}p$ collision point. These functions can be satisfied if the rf system allows independent control of the amplitude and phase of the proton and antiproton buckets.

Independent control can be achieved by arranging the cavities in pairs with appropriate spacing and phasing. Consider a pair of cavities separated in space by $3/4\lambda$ ($\lambda=2\pi R/h$, the rf wavelength at $\beta=1$). If the phase of the rf voltage on the downstream cavity is advanced by $\pi/2$ radians the rf fields encountered by a particle moving downstream through the two cavities will be exactly in phase. These same fields are exactly out of phase for a particle moving from the downstream cavity to the upstream cavity.

There will be eight Energy Saver rf accelerating cavities, each of which is capable of sustaining 350 GeV accelerating voltage for colliding beam operations. Five of these cavities will be built as part of Tevatron I. Four cavities will be arranged in two pairs with a spacing of $3/4\lambda$ to accelerate protons and the remaining four will be arranged in two pairs with the same spacing to accelerate antiprotons as shown in Fig. 8-11a. Cavities 1, 2, 3, 4 are phased so that they couple to antiprotons, which move to the left. Cavities 5, 6, 7, 8 couple to protons, which move to the right. The center of cavity number 2 is located at the Tevatron F0 location. Since this location is symmetrically located with respect to the design collision points at D0 and B0, bunches which collide at those points must arrive at the F0 point at the same time (i.e., they collide there also, in the case where there are three bunches each of protons and antiprotons in the collider). The arbitrary angle δ is adjusted to establish the correct collision point. For the spacing shown the required value of δ is $\pi/6$ radians.

These cavities will be adequate for an acceleration rate of 34 GeV/sec at a synchronous phase of 30° . The acceleration time to 1000 GeV will then be 25 sec. The bucket size is ample. The relative phase between the two sets of cavities is adjustable, so that the \bar{p} and p bunches can be rotated relative to each other to move the collision point to any desired azimuth.

8.5.2 Failure Modes. The requirement of orthogonal control of the two sets of cavities establishes uniquely the spacing between pairs of cavities. However, the precise location of the cavities and the selection of which set to assign to protons or antiprotons is arbitrary. The collision point can be adjusted by selection of arbitrary phase angles such as δ as illustrated. The effect of the failure of a single cavity on beam size, luminosity and stability of the collision point is determined by cavity location and deployment. Failure of any rf cavity will always result in some beam deterioration but the damage can be minimized by optimum cavity placement and selection.

The placement of cavities will be partially limited by the location of penetrations and equipment in the rf building and the F0 straight section. The cost of rearranging equipment may not justify the gains that the optimum arrangement provides. The distribution described here is a partial optimization consistent with existing constraints.

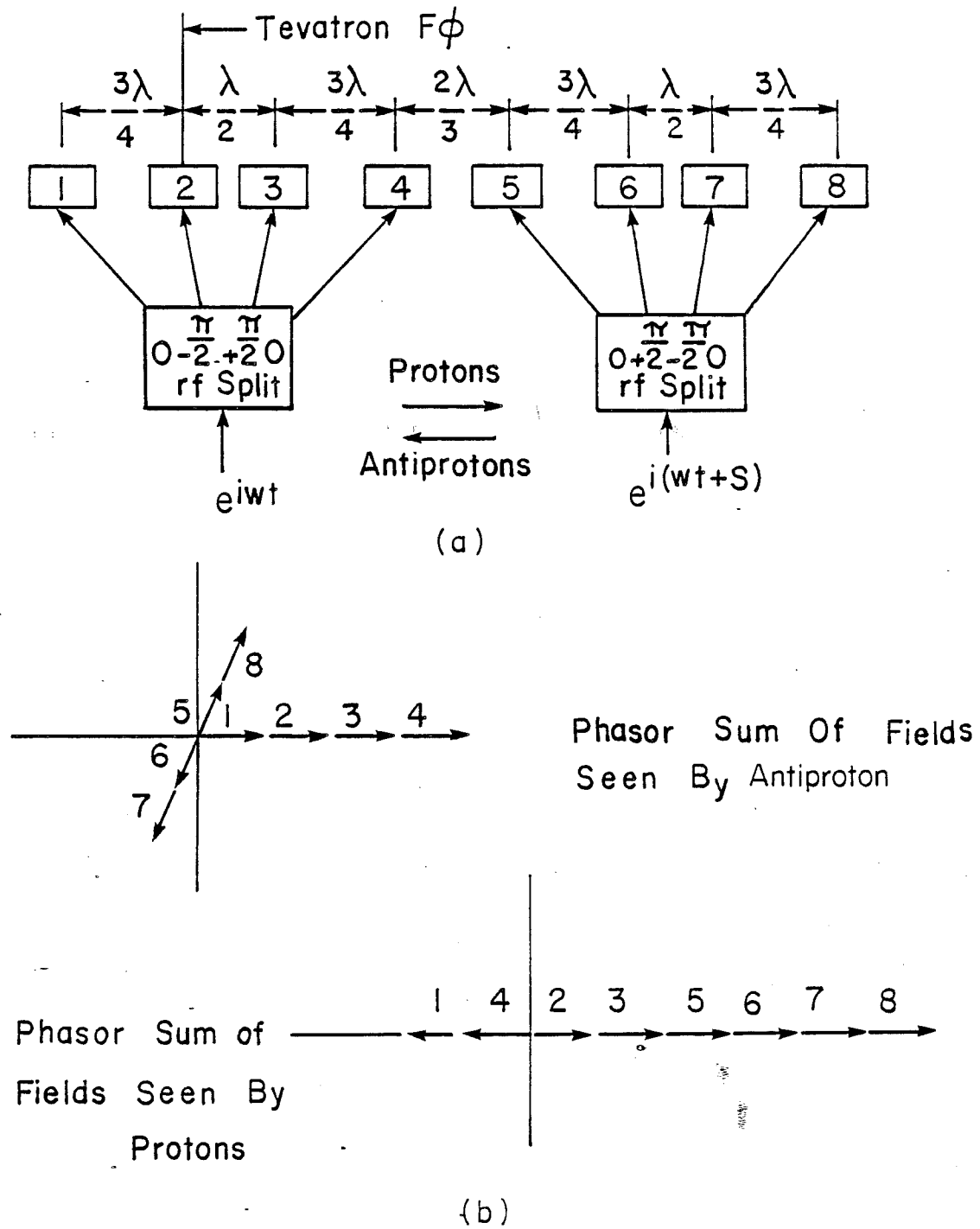


Fig. 8-II

In Fig. 8-11b the instantaneous fields seen by protons and antiprotons are shown. Failure of any one of the proton cavities, 5-8, will result in a sudden change in the phase and amplitude of the rf field seen by antiprotons. The antiproton bunches would immediately start a coherent dipole oscillation about the new phase angle along with higher order oscillations resulting from a change in bucket size. This would appear as an oscillation of the collision point and ultimately a dilution of the antiproton bunch length to cover the entire oscillation range. This dipole motion can be prevented by automatically turning off a second proton cavity so that the balance is restored. Removal of two proton cavities results in a reduction in bucket height by a factor of 0.707. This will cause a bunch quadrupole oscillation with attendant dilution and bunch lengthening but no dipole motion of the bunch or collision point.

On the other hand, failure of one of the antiproton cavities, 1-4, does not cause a phase displacement of the proton field so no additional cavity need be removed from the system. Such a failure results in a decrease in the antiproton bucket height by a factor of 0.866 with a small attendant quadrupole oscillation and bunch lengthening. The effect on the proton bucket height and bunch length is to increase or decrease it by an even smaller factor. In summary, the cavity locations and assignments are such as to minimize the effect of failure of any cavity on the quality of the antiproton bunches at the expense in some cases, of proton bunch quality.

It is conceivable that if many faults occur, resulting in unacceptable dilution of proton bunches, both beams could be decelerated to 150 GeV and the proton bunches replaced with fresh ones while keeping the old antiproton bunches.

8.6 Energy Saver Diagnostics

At the time the Energy Saver components were fabricated, it was recognized that it would be used as a collider. For that reason the beam position detectors were designed so that the proton and antiproton beam could be detected simultaneously. Since the decision to build this type of monitor was made after the preparation of the Superconducting Accelerator Design Report, a description of them is given in Section 8.6.1. The beam-loss monitors of the Energy Saver are described in 8.6.2. Following the first year of operation of the SPS collider the requirements for diagnostics in the Energy Saver were reviewed. The additional diagnostic equipment which should be added to the Energy Saver for colliding beams is given in Section 8.6.3.

8.6.1 Energy Saver Position Detectors. The position detectors in the Tevatron are of the directional-coupler type⁵. There are 216 detectors in all, 108 each for vertical-position measurement (in vertical focusing quadrupoles) and for horizontal-position measurement (in the horizontally focusing quadrupoles). The pickups have about 24 db of directivity (i.e. rejection of signals from beam traveling in the unwanted direction) so that

the pickups can be used to detect \bar{p} 's in the presence of p 's and vice versa.

The fast electronics for extracting the position signal from the pickup signal uses amplitude to phase (AM to PM) conversion to provide a large dynamic range of beam intensity⁶. The electronics was specifically designed to detect single isolated bunches with p 's or \bar{p} 's (collider mode) as well as contiguous filled buckets (batch mode) for fixed-target operation. The lower limit of sensitivity for operation in these modes is about 3×10^9 p 's per bucket (collider mode) or 1×10^8 p 's per bucket (batch mode). The position-signal rise time is about 70 nsec due to the presence of a half-wavelength resonant filter which rings when hit by a signal from isolated p or \bar{p} buckets. The estimated precision of position measurement is about ± 0.5 mm at the lowest intensities. Precision of ± 30 microns has been obtained with high intensities on a detector installed in the Main Ring.

The microprocessor-controlled digitizing electronics allows simultaneously digitizing the position signal from all 216 detectors with about 100 nsec (least significant bit) resolution on the timing for each detector. This "FLASH" picture of a single turn of beam can be used to examine the beam orbit for any complete revolution including injection. Other operating modes include measurements of beam position averaged over many turns to average out the contributions of betatron oscillations. These latter measurements have large RAM memories associated with them to store many measurements without requiring readout by the Host control computer. These data are used to determine closed orbits for correction coil programming and for orbit reconstruction in case of a beam induced quench. The microprocessor circuits can initiate beam aborts if the beam exceeds preset position limits.

The electronics has been designed and built to detect beams in either direction. In order to fully implement these features, coaxial relays must be installed in the tunnel to select the proper pair of ports from the directional coupler pickups. A signal to control them is already provided in the Service Buildings. In addition, a Saver Clock signal (a signal with diphase encoded timing signals on a 10 MHz carrier) must be installed in the \bar{p} direction around the ring. The electronics is already equipped to receive this at the same time it controls the coaxial relays. The control cable for the coaxial relays will also have to be installed.

8.6.2 Beam Loss Monitors. The Tevatron beam-loss monitor system, like the beam-position system has detectors at every quadrupole (a total of 216 around the ring). They are argon-filled chambers designed to have a very large dynamic range and fast response. Their signals are amplified in a fast risetime integrating 4 decade logarithmic readout. Real-time analog output signals are also available for fast time plots. The 60-msec integration time of the electronics corresponds to the response time of the Doubler magnets to beam-induced heating, and therefore is a good monitor of the likelihood of inducing quenches. The beam-loss monitor system, like the beam-position system, can initiate a beam abort if the radiation level exceeds preset limits.

8.6.3 Diagnostics for the Energy Saver Collider Operation. Initial experience from the CERN SPS collider has shown the importance of adequate beam diagnostics. In the Fermilab Collider, much of the tuning of the transfers, acceleration, and storage parameters will necessarily be done with antiprotons, which are relatively rare even if the \bar{p} accumulation works well. Thus, diagnostic devices should work at low beam intensities. Furthermore, since the time to improve transfer and storage efficiency of the Collider will be in competition with other uses of the Tevatron, there must be a complete set of diagnostic devices with well-developed software at the onset of Collider commissioning.

The obvious requirement is to be able to measure the beam intensity, position and emittance as a function of time as the particles make their way to a successful store at 1 TeV.

Beam transfer lines will be equipped with sensitive intensity and profile monitors. The Main Ring and Tevatron will have position and intensity measuring devices which should be well developed by the time collider commissioning begins.

In order to measure the profile of circulating p's and \bar{p} 's in the Tevatron, we are planning to construct several flying wire scanners⁷. These devices flip a thin wire filament through the circulating beam at about 5 m/sec, and the resultant scattered flux is monitored by several scintillator telescopes placed both upstream and downstream of the flying wire. Such a device would be placed near (and in) the B0 Colliding Detector Facility to measure beam position as well as profile. Each flying wire can measure only one coordinate, so several are needed. Such a device has been implemented at the CERN SPS and is recognized as an important diagnostic tool⁸.

Motion of the wire through the beam is about 0.1 mm per turn, which results in about 10 points across a beam 1 mm in diameter. The scattered flux from p's and \bar{p} 's are quite directional, and hence the p and \bar{p} beam profiles are recorded simultaneously in the two sets of scintillators. The emittance blowup per scan is about 6×10^{-6} mm-mrad, hence for the SPS about 200 scans per hour is equivalent to multiple scattering by the residual gas. The heating of the wire (a low-Z material such as beryllium or carbon) is not excessive. The particle flux lost is less than 0.02% per scan.

Longitudinal emittances will be monitored by the devices associated with the Main Ring and Tevatron low-level rf systems.

Schottky scans should be adequate for tune measurements. An active tune measurement is also under consideration.

The intensity and position devices in the Tevatron can give information on individual bunches of protons or antiprotons. In addition, the flying-wire scanner gives bunch-by-bunch information.

References

1. Superconducting Accelerator Design Report, May 1979, Fermilab, Chapter 14.
Fermilab Report UPC 73, F.E. Mills and D.E. Young, November 11, 1978.
Fermilab Report UPC 129, F.T. Cole, April 24, 1980
Fermilab Report UPC 132, S. Ohnuma, June 26, 1980
2. Fermilab Report UPC 96, T.L. Collins, April 1979.
3. Fermilab Report UPC 17, L.C. Teng, December 1, 1978
4. D. Ciazynski and P. Mantsch, "Correction Magnet Packages for the Energy Saver" IEEE Trans. on Nuclear Science, Vol. NS-28 , No. 3, 3275 (1981).
D. Ciazynski and P. Mantsch, "Typical Problems of Correction Magnets for Fermilab", IEEE Trans. on Magnets, Mag-17, 165 (1980).
5. R. Shafer et al., IEEE Trans. Nucl. Sci. 28 , No. 3, page 2290 (1981).
6. Ibid, page 2323.
7. L.R. Evans and R.E. Shafer, Proc. Workshop on Intensity Limitations in Storage Rings, BNL 57236, page 68 (1979).
8. A. Barisy et al., IEEE Trans. on Nucl. Sci. 28 , page 2180 (1981).

9. INTERACTION REGIONS AND EXPERIMENTAL FACILITIES

9.1 EXPERIMENTAL AREAS

9.1.1 B0 Experimental Area. A general purpose detector is being designed and constructed by the Colliding Detector Facility Department, CDF. The desire to measure antiproton-proton collisions and available technology demand a large, massive and complicated apparatus. The B0 Colliding Beam Experimental Area has been designed to handle the assembly, installation, operation and maintenance of such a detector.

The project includes the following:

B0 Collision Hall- an underground structure that will replace approximately 100 feet of the Main Accelerator enclosure, and will contain the experimental physics detectors and both the accelerator and Energy Saver beam components. On the outside wall (away from the accelerator center) will be a large door and movable shield wall that will provide access to the Assembly Hall.

B0 Transition and Equipment By-pass Enclosure- an underground structure that connects the Collision Hall to the existing Main Accelerator enclosures, and provides a passage for personnel, utilities and a magnet-moving vehicle around the B0 Collision Hall.

B0 Assembly Hall- a large pit at the elevation of the Collision Hall and adjoining to the shield-door passage, with a service floor at grade level, all covered by a high-bay building with an overhead crane. The various experimental physics detectors will be assembled, tested and serviced in this hall prior to placement in the B0 Collision Hall.

B0 Site Development- hardstands, access roads, drainage facilities, relocation of utilities, extension of services and temporary earth retaining structures for construction sequencing and adjacent road and building protection.

B0 Primary Power- 13.8 kV feeders, substations and switchgear for extending primary power to the B0 Experimental Area and into the B0 Assembly Hall.

The B0 Collision Hall connects with and becomes a part of the Main Accelerator and Energy Saver enclosures. All systems, services and utilities are designed for compatibility with these systems. Access to the B0 Assembly Hall will be from the adjacent Road D near the Industrial Buildings.

At the time of writing, construction of the B0 area has been in progress for more than three months.

9.1.2 D0 Experimental Area. This experimental area is still in the process of definition and conceptual design. It is expected that a collision hall of approximately 2000 sq. ft. will be built at D0.

9.2 LOW-BETA DESIGN

9.2.1 Lattice Design. As discussed in Chapter 6, the \bar{p} and p bunches are placed at equal spacings around the circumference of the Tevatron, arranged so that one of their crossings occurs in the B0 long straight section, the location of the Collider Detector Facility. There will also be crossings in the D0 long straight section, where space is reserved for a second colliding-beam experimental area, at present in a primordial state of design.

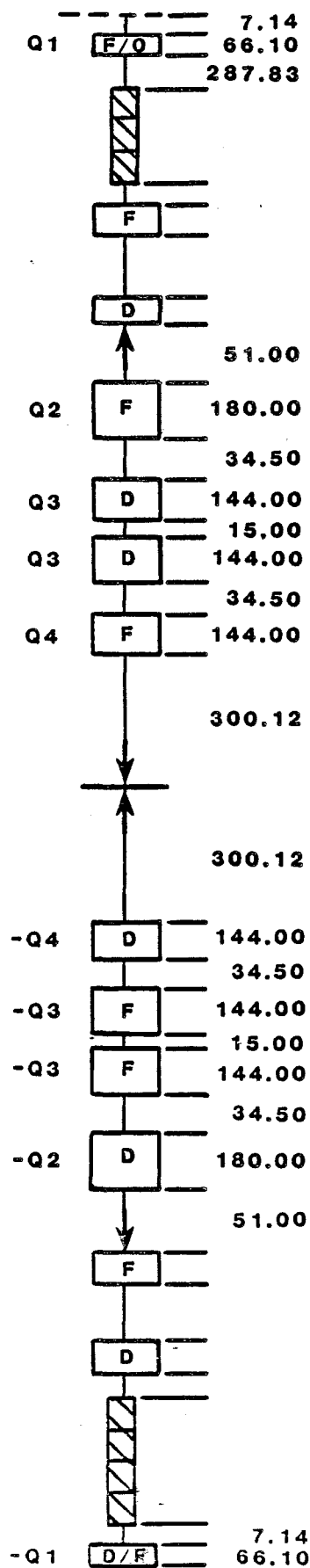
The luminosity can be enhanced for given beam currents by focusing the beams down to narrow waists at the collision point, using extra quadrupoles on either side of the collision point. These quadrupoles give a decrease in the amplitude function β and the low β gives the narrow waist.

It is desirable for our purposes to achieve a minimum β value of 1 meter. Given the Tevatron lattice and dimensions, it is possible to achieve this minimum with a design that utilizes quadrupoles having gradients of 25 kG/in. and requires replacement of a single normal-cell quadrupole on either side of B0, at A48 and B12, by longer quadrupoles. The design uses four separately powered quadrupole buses and either can be adiabatically varied from the normal $\beta^* = 72$ m configuration to $\beta^* = 1$ m, while causing very little betatron mismatch or manipulation outside the interaction region except for correction-quadrupole changes to preserve the overall tunes and sextupole changes to maintain the desired chromaticity.

A layout of the 25 kG/in. low-beta insertion is shown in Fig. 9-1. It requires the replacement of the 32-in. quadrupoles at A48 and B12 with separately powered 66-in. quadrupoles and the addition of two 180-in. quadrupoles and 6 144-in. quadrupoles within the long straight section. These ten quadrupoles are powered anti-symmetrically on four separate circuits and must reach a maximum gradient of 25.5 kG/in. at 1 TeV. In order to keep maximum luminosity point close to the Tevatron B0 location, the quadrupoles at A48 and B12 must be pushed as far upstream as possible. To do this, the normal dipole interface-to-quadrupole magnetic length has been reduced from 18.137 in. to 7.137 in. by changing the upstream bellows and moving the beam detector to the downstream end of the quadrupoles. This motion puts the maximum luminosity point 0.9 in. downstream of the Tevatron B0 for the final low beta of 1 m.

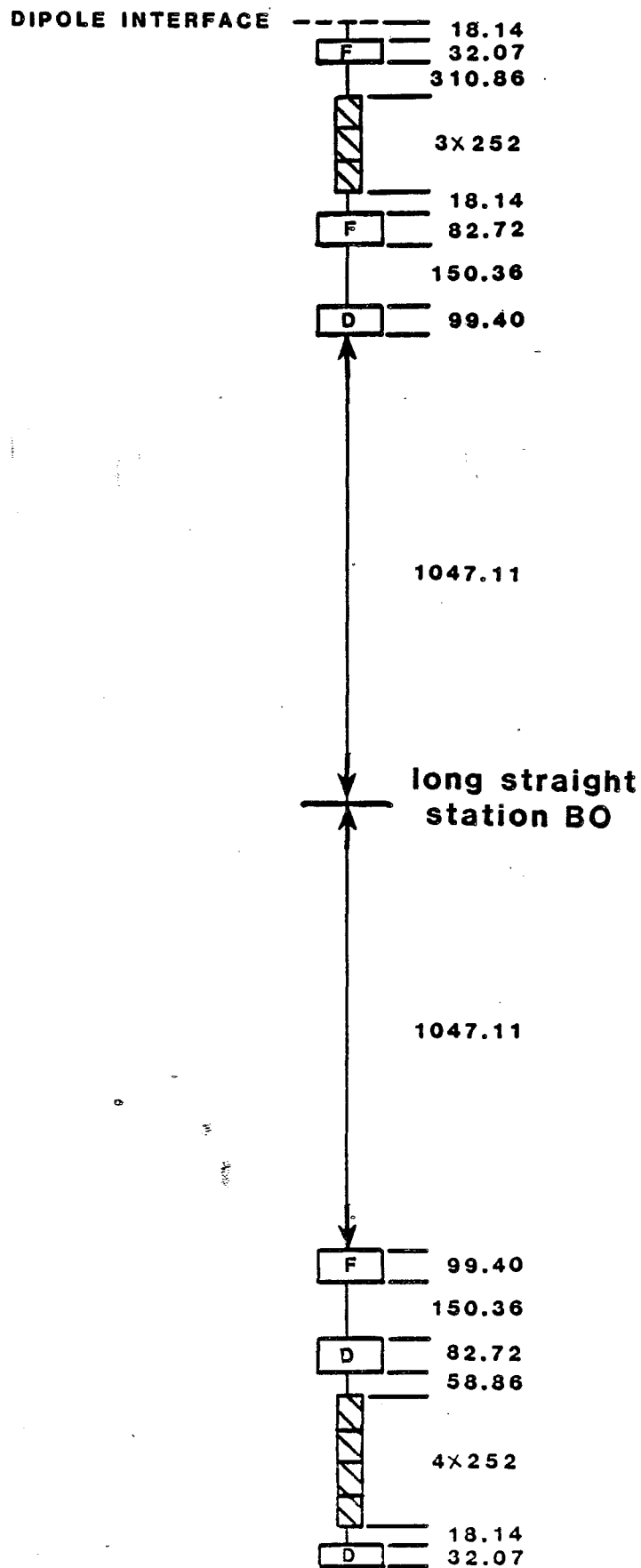
9.2.2. Transition to Low Beta. For normal fixed-target operation, Q1 must run at approximately 10 kG/in. and Q2, Q3, and Q4 must all be off. By contrast, in the low-beta configuration, all the quadrupoles must be on and running quite hard. The problem is to find a method of connecting these two solutions in a stepwise continuous manner while maintaining the overall tune of the Tevatron. This is by no means a simple straightforward

low beta straight section



(a)

normal long straight section



(b)

Fig. 9-1 Low-Beta Geometry. All dimensions in inches

process. The two solutions are in fact quite different and probably cannot be connected without disturbing the normal lattice functions outside the insertion region. A method has been found, however, that does not greatly disturb the rest of the ring. This sequence takes the lattice from a returned fixed mode to a low beta of 1 m.

In all of this sequence, the Tevatron has been retuned to 19.585 in each plane. For particle-antiparticle collisions it is desirable to be above the half integer and the value of 0.585 centers the tune in a region free of all resonances of order lower than 11th. The correction quadrupoles consist of two families, QFC and QDC, located next to the corresponding quadrupoles, QF or QD, at all stations 13 through 47. These corrections have a range of approximately ± 2 kG/in. at 50 amps. QFC has ranges from +0.4 kG/in. to -0.9 kG/in. QDC is given by

$$QDC = 0.0457 - QFC \text{ (kG/in.)}$$

In this turn-on sequence, there is some disturbance to the lattice functions outside the insertion region, for three distinct reasons:

1. The "off" solution and the "low-beta" solution are, in fact, quite different. It is doubtful that they can be connected without allowing some mismatch.
2. The initial sequence, in steps of less than $1/3$ kG/in., was not a very smooth curve. Some amount of mismatch was allowed in order to produce smoother curves.
3. It was found that a higher luminosity can be achieved in the "1 meter low-beta" by introducing some mismatch. This is because the long straight sections are not exactly antisymmetric; one side has more dipole edge focusing than the other, while the low beta quads of necessity are symmetric.

The amount of disturbance to the normal lattice, however, is quite small and should cause no problem since this turn-on will not start until high energy where the beam is very small.

9.3 Hardware Modifications

9.3.1 Magnets. Special - quadrupoles have been designed and are being built for the B0 interaction region. These magnets use special cable with 20 micron filaments and a copper-to-superconductor ratio of 1.3 (as opposed to 8 microns and a ratio of 1.8). This cable has a short sample limit of 5250A at 6.5T. The new quadrupole has added turns to reach higher fields.

There are many new features of the new design. The strength of the coil collars has been carefully considered, as has quench protection. A smaller cross section is being considered to give less interference with the Collider Detector. Because the special quads are powered separately

from the regular Superconducting Ring magnets, the regular excitation currents are bypassed through the quads in a notch at the outside of the coil collar.

The beam monitor and correction magnet at B12 have been redesigned in a special package and relocated downstream of the special quad. Dipole fields will arise from quad misalignment. Even though shimming will be done, misalignments in the high- β regions adjacent to the low- β interaction region can give large orbit distortions and trim dipoles are being designed for correction.

9.3.2 Power Supplies and Bus. Four separate power supplies and associated circuits will be needed for the 1-m β^* design. The supplies will be modified Tevatron holding supplies capable of providing up to 6000 A. The supplies will be located in an annex to the B0 service building and the power will be transported to the magnets via water-cooled copper bus (total length of 4 circuits is 2700 ft). For a current of 6000 A, the power consumed by the bus is 770 kW. Power will enter the magnets through lead boxes constructed especially to fit the 15-in. space provided for them.

9.3.3 Refrigeration. Liquid He refrigeration needs are as follows: quadrupoles (50 W), four pairs of 5 kA leads at 10 W each (40 W + 56 l/hr), two turnaround boxes at 10 W each (20 W), two feed boxes (45 W) and U tubes (5 W), for a total of 160 W plus 60 liters per hour. This refrigeration need can be met initially by the A4(C4) and B1(D1) satellite refrigeration systems. Later, it may be desirable to provide stand-alone refrigeration, and it would certainly be needed if operation at 1.8 K is desired. The 60 liters per hour of liquid He would come from the Central Helium Liquifier through the A4 and B1 refrigerator and magnet systems. The estimated LN₂ requirement is 250 W. Refrigeration estimates for the interaction-region detector magnets are not included here, because it is expected that those needs will be satisfied with but separate refrigeration.

9.3.4 Vacuum. Pressure in the interaction region straight section should not exceed 10^{-9} Torr. This means the warm vacuum pipe through the detector plus a transition piece on either side will require special preparation (possible bakeout). The transition pieces will contain isolation valves and ion pumps, as well as the connections to turbomolecular and roughing pumps.

10. PERFORMANCE AND LUMINOSITY

In this section we describe the colliding-beam performance at 1000 GeV in the Energy Saver. For this purpose, we assume that beams of protons and antiprotons have been accelerated and are circulating in opposite directions so they collide in the center of the low-beta insertion in B0, as well as at other azimuths.

10.1 Beam Geometry

As an example, it is possible to create three bunches of antiprotons each with 6×10^{10} particles and each with a longitudinal phase area of 3 eV-sec, which we define as the area including 95% of the population with a biGaussian distribution. To prepare the necessary number of antiprotons in the Accumulator takes a little more than two hours.

Similarly we can assume that three proton bunches, each with 6×10^{10} particles and a longitudinal area of 3 eV-sec coexist with the antiproton beam. Both beams have equally spaced bunches since the harmonic number 1113 can be divided by 3. In principle there are, therefore, six collision regions equally spaced. We assume here that the two beams are not kept separated by special electrostatic deflectors, the design of which appears to be difficult because of lack of space in the Energy Saver and because of the large rigidity of the particles. An important parameter to determine the bunch dimensions is the peak rf voltage V at 53.1 MHz. We assume here that two sets of four cavities exist and that orthogonal control of the two beams is possible. In this mode of operation, there will be a total of 1.4 MV/turn for each beam.

Using the equations of Chapter 2, which apply to the Tevatron as well as to the Main Ring, we obtain for the rms bunch length $\sigma_z = 40$ cm and for the rms momentum spread $\sigma_p/p = 1.2 \times 10^{-4}$. The area of the stationary bucket is 12.7 eV-sec, four times larger than the bunch area. Finally the phase-oscillation period is $T_s = 27$ msec.

10.2 Beam Cross Section at the Collision Point

As a result of the transverse stochastic cooling in the Debuncher and Accumulator Rings, and because the two beams have roughly the same number of particles, the two beams have the same emittance, which is also the same in both horizontal and vertical planes. The normalized emittance is assumed to be 24π mm-mrad. That is, $\epsilon_v = \epsilon_H = 0.023 \pi$ mm-mrad at 1000 GeV. This includes 95% of the beam with biGaussian distributions.

A low-beta figure of less than 1 m is expected in both planes and therefore

$$\sigma = 0.06 \text{ mm}$$

or

$$\sigma^2 = 3.5 \times 10^{-5} \text{ cm}^2$$

Since the low-beta insertion has very small dispersion, there will be negligible contribution to the beam size from momentum spread.

10.3 Luminosity

Because the low-beta value of 1 m is larger than the rms bunch length (0.4 m), a formula for luminosity valid for constant beam sizes is a good approximation. Thus

$$L = \frac{N_p N_{\bar{p}} B f_0}{4\pi\sigma^2},$$

where $N_p = 6 \times 10^{10}$ is the number of protons per bunch, $N_{\bar{p}} = 6 \times 10^{10}$, the number of antiprotons per bunch, $B = 3$, the number of bunches per beam, and $f_0 = 4.77 \times 10^4$ Hz, and the revolution frequency. This gives

$$L = 1.0 \times 10^{30} \text{ cm}^{-2} \text{ sec}^{-1}.$$

This luminosity figure is definitely within reach with the methods and the techniques described in this report. Several alternative luminosity scenarios can be invented. For instance, it is possible to replenish the collider every hour with one single bunch of protons and antiprotons with 10^{11} particles each, for a luminosity of $10^{30} \text{ cm}^{-2} \text{ sec}^{-1}$.

Higher luminosity figures can also be expected, as high as $6 \times 10^{30} \text{ cm}^{-2} \text{ sec}^{-1}$, by improving either the stochastic cooling (a factor of two), or the beam intensity in the Main Ring and Tevatron (also possibly by a factor of two) or with 6 bunches per beam instead of 3 as assumed here.

10.4 Beam-Beam Tune Shift

Collisions are head on, the emittances of both beams in both planes are all equal, and the lattice functions are approximately the same in both planes. Therefore, the beam-beam tune shift is the same for both dams is independent of the beam energy, and does not depend on the lattice functions. The linear beam-beam tune shift is given by

$$\xi = \frac{3 N r_o}{2 \epsilon_N},$$

where $N = 6 \times 10^{10}$ is the number of particles per bunch, $\epsilon_N = 24\pi$ mm-mrad is the normalized emittance and $r_o = 1.535 \times 10^{-18}$ m is the classical proton radius. We have

$$\xi = 0.0017/\text{crossing}$$

Even with a low-beta insertion, the beam cross-section in the other five collision regions with normal β values is round and the contribution to the beam size from the momentum spread is negligible. Therefore the tune shift per crossing, in case the two beams are not separated, is the same at each crossing as long as the collision is head-on or at least at an angle $\theta \ll \sigma/\sigma_e$. If there are a total of 6 crossings, the total tune-shift per turn

$$\xi_{\text{tot}} = 6 \cdot \xi = 6 \times 0.0017 = 0.01.$$

10.5 Single-Beam and Luminosity Lifetime

We have investigated four possible sources of lifetime deterioration in the Tevatron: residual gas, intrabeam scattering, beam-beam effects and beam-beam cross sections. At the same time an analysis of periodic or random crossings of nonlinear resonances has been initiated. This will help to determine not only possible limits on the amount of nonlinearities in the Energy Saver superconducting magnets, but also on the amount of coherent and incoherent noise amplitude allowable.

10.5.1 Effects of Residual Gas¹. The following effects have been investigated:

- (i) Multiple Coulomb Scattering
- (ii) Single Coulomb Scattering
- (iii) Nuclear Scattering

The first effect causes a constant beam-emittance growth, which leads to both a luminosity decay as well as a single-beam lifetime if an aperture limitation is taken into account. Nevertheless the single-beam decay due to multiple Coulomb scattering is quite negligible. The second and third effects cause an intensity decay, but the last effect is more important than the second one.

The average vacuum pressure expected in the Tevatron is 10^{-8} Torr in the warm regions and 5×10^{-11} Torr in the cold regions with the following gas composition:

warm region: 60% H_2 and 40% CO
cold region: 75% H_2 and 25% He

The intensity decay per beam due to single Coulomb and nuclear scattering is

$$\frac{1}{I} \frac{dI}{dt} = -1.07 \times 10^{-6}/\text{sec}.$$

The emittance growth due to multiple Coulomb scattering is

$$\frac{1}{\epsilon} \frac{d\epsilon}{dt} = 1.3 \times 10^{-6}/\text{sec}.$$

These effects combined lead to a luminosity decay of

$$\frac{1}{L} \frac{dL}{dt} = -3.44 \times 10^{-6}/\text{sec},$$

a loss of 23% of the luminosity in 20 hours.

10.5.2 Intrabeam Scattering². To estimate intrabeam scattering diffusion rates for the colliding-beams mode, we have used the same computer code we used to estimate intrabeam scattering for the Accumulator. For our estimate, we have used the actual Tevatron lattice with the low-beta insertion. From the computer code we have empirically found the following formulas for diffusion rates, which apply to a bunched beam at 1000 GeV. For the momentum spread

$$\frac{1}{\tau_p} = \frac{1}{\sigma_p/p} \frac{d\sigma_p/p}{dt} = \frac{A_p I_p}{(\sigma_p/p)^m \epsilon_p^r} \quad (10-1)$$

and for the horizontal B??Qqatron emittance

$$\frac{1}{\tau_x} = \frac{1}{2\epsilon_x} \frac{d\epsilon_x}{dt} = \frac{A_x I_p}{(\sigma_p/p)^{m_x} \epsilon_x^{r_x}} \quad (10-2)$$

There is actually damping for the vertical betatron emittance.

In these equations σ_p/p is the rms momentum spread, $\epsilon = 2\sigma^2/\beta$ the rms betatron emittance, which we assume to be the same in both planes, and I_p is a measure of the bunch peak current

$$I_p = \frac{N_B e \beta c}{2\sqrt{\pi} \sigma_e},$$

where N_B is the number of particles per bunch, βc the particle velocity, and σ_e is the rms bunch length. Also

$$A_p = 5.7 \times 10^{-23} \text{ Amp}^{-1} \times m^r_p \times \text{hour}^{-1}$$

$$A_x = 12.6 \times 10^{-23} \text{ Amp}^{-1} \times m^r_x \times \text{hour}^{-1}.$$

If $\sigma_p/p = 1.2 \times 10^{-4}$, $\sigma_e = 40 \text{ cm}$, $N_B = 10^{11}$, then $I_p = 3.4 \text{ A}$, and if $\epsilon = 0.0077 \text{ mm-mrad}$, then

$$m_p = 2.2 \quad r_p = 1.4$$

$$m_x = 0.7 \quad r_x = 2.0$$

We obtain as initial diffusion rates

$$\frac{1}{\tau_p} = 5.2 \times 10^{-6} / \text{sec}$$

$$\frac{1}{\tau_x} = 1.1 \times 10^{-6} / \text{sec}.$$

The actual variation of σ_p/p and ϵ_x is obtained by simultaneous integration of Eqs. (10-1) and (10-2). The result is shown in Fig. 10-1.

There is a loss of luminosity caused by intrabeam scattering diffusion in the horizontal betatron oscillation. Assuming vertical and horizontal

**Beam Momentum Spread and Emittance Variation
with Time Due to Intrabeam Scattering**

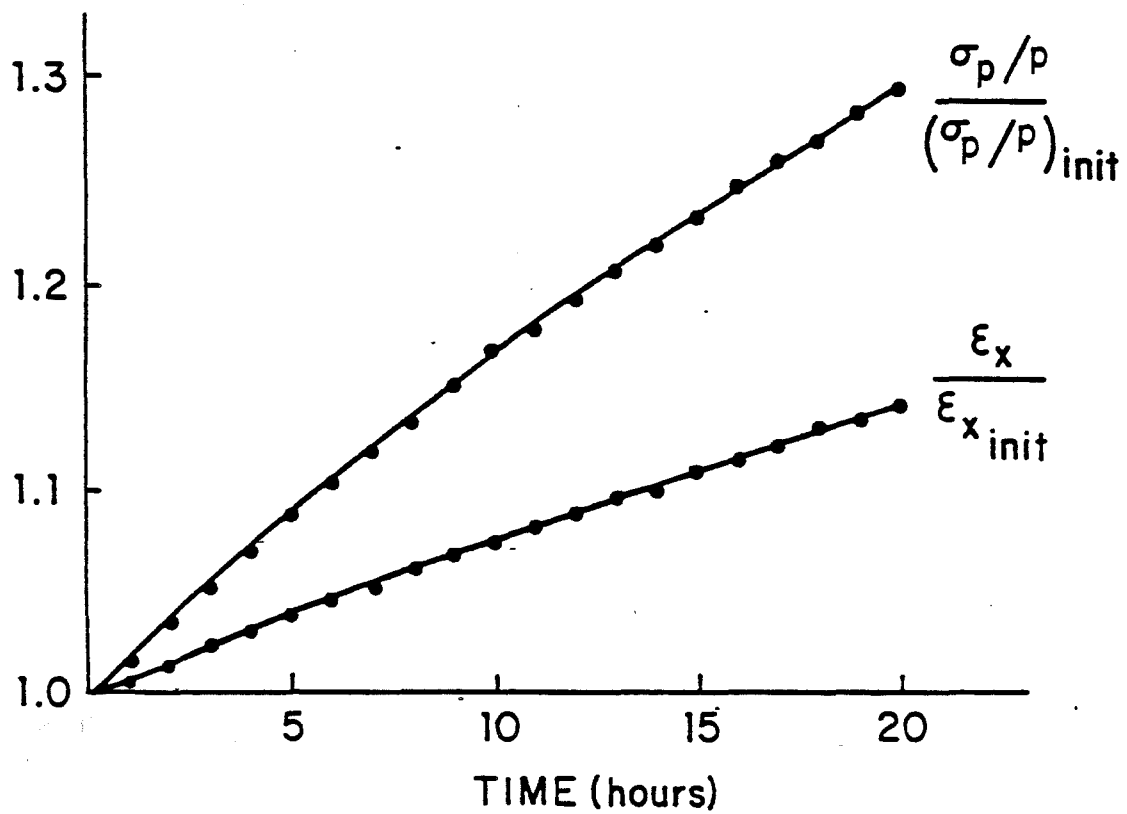


Fig. 10-1

coupling, the loss of luminosity after 10 hours is about 7%. After the same period of time (10 hours), the bunch area has increased by 32%.

10.5.3 Beam - Beam Effects. Beam-beam effects have been extensively simulated on the computer. Several issues have been discussed, studied, and, we hope, resolved.

A systematic search for Arnold's diffusion for the Tevatron parameters has given negative results.^{3,4} We have been able to simulate in some cases up to 20 minutes real time of collisions. From our data, we can extrapolate beam-beam lifetimes of several days. We believe the stability of the system arises from the "roundness" of the beam geometry and of the lattice functions.⁵

We found that the addition of the nonlinear beam-beam interaction to a system already affected by external random noise (such as gas scattering) causes an enhancement of the diffusion rates.⁶ The largest enhancement encountered was a factor 6 for a beam-beam tune shift of 0.06 in proximity to the fourth-order resonance.

We have investigated beam-beam interactions with the beam centers offset or oscillating around each other.⁷ This could be caused by either a dipole oscillation or a finite dispersion in the collision region coupled to the momentum oscillation. We have not noticed any effect of significance.

Of more serious concern are the effects created by betatron tune oscillations. If proper care is not taken, it is possible to cause an emittance growth of a factor two in a few minutes.⁸ Fortunately, we have found a threshold and the growth can be tuned out by either adjusting the betatron tunes or by improving the power-supply regulation to better than 10^{-4} and flattening the lattice chromaticity.

At present, we are investigating multiple crossings per revolution, 2 or 6 instead of 1.

10.6 Beam-Stability Considerations in the Tevatron. As we have seen, each beam is made of three bunches, each with 10^{11} particles and a longitudinal area of 3 eV-sec. The beam intensities, both average and peak, are very modest and dilute. A considerable effort has been made in the recent past to estimate the longitudinal stability of each beam for both individual bunch and bunch-to-bunch modes.^{9,10,11} The beam wall impedance expected in the Tevatron was estimated to be $|Z_n|/n \leq 1$ ohm. Because of the low longitudinal beam density, we believe the beams are quite stable. Moreover, a longitudinal damper operating on each individual bunch is planned.

Fewer calculations have been done for the case of transverse instabilities. But again, we do not foresee major problems. In addition,

a transverse active damper has been proposed¹² that will be fast enough to operate on individual bunches in both radial and vertical modes of oscillation.

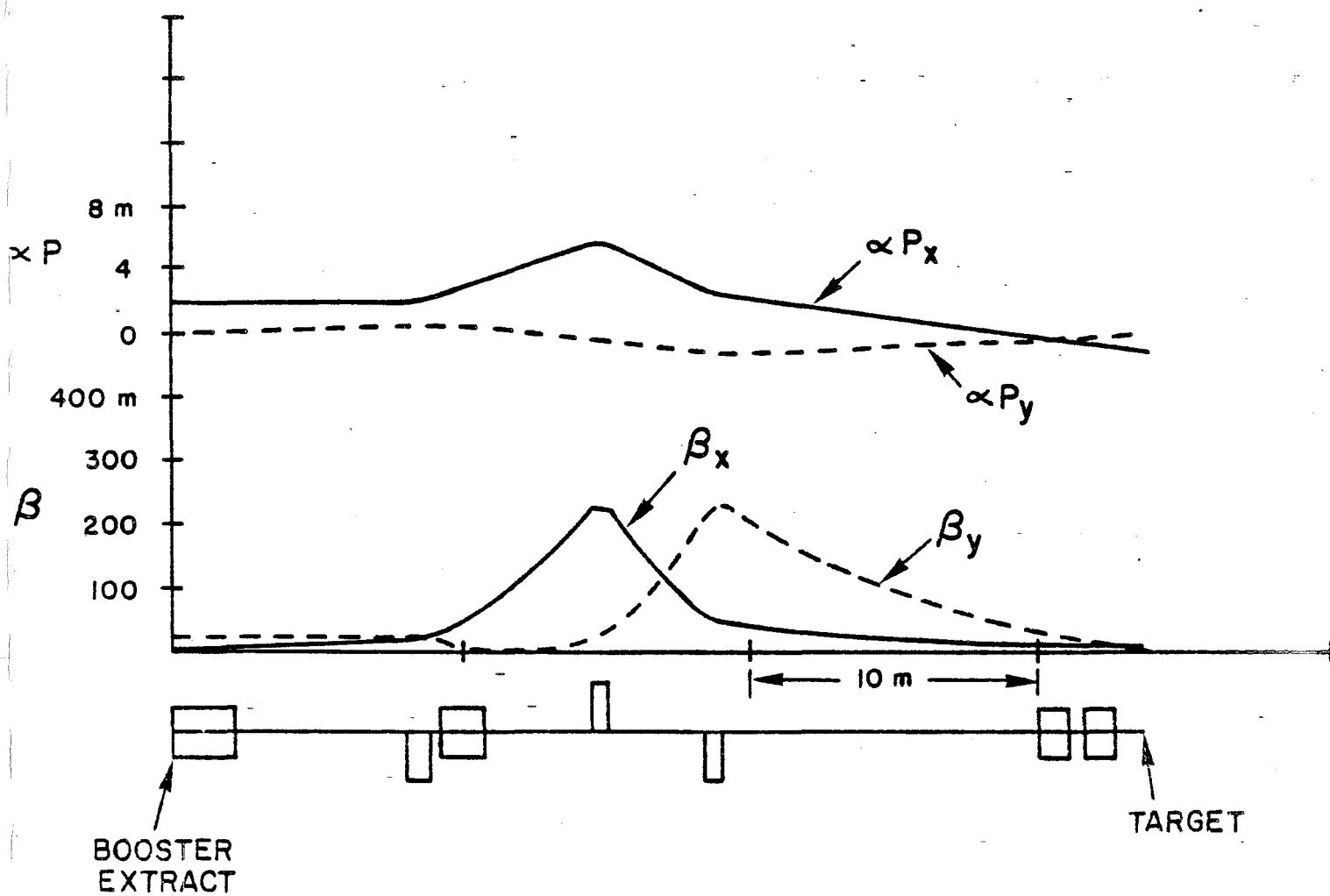
References

1. H. Mizuno, S. Ohnuma, A. G. Ruggiero, "Vacuum and Beam Lifetime in the Doubler," UPC No. 119, Fermilab 21, 1979.
2. A. G. Ruggiero, "Revised Intrabeam Scattering Calculations," Fermilab p-note 192 (1982), unpublished.
3. D. Neuffer, A. Riddiford, A. Ruggiero, "A Search of Arnold's Diffusion in the Beam-Beam Interaction," FN 333, Fermilab, Apr. 1981.
4. D. Neuffer, A. Riddiford, A. Ruggiero, "Long Time Simulation of the Beam-Beam Interaction," FN-343, Fermilab, July 1981.
5. A. G. Ruggiero, to be published in Particle Accelerators, Vol. 12, No. 1.
6. D. Neuffer, A. Riddiford, A. Ruggiero, "Diffusion Enhancement by the Beam-Beam Interaction in 1-D Simulations," FN-357, Fermilab, Oct. 1981.
7. D. Neuffer, A. Riddiford, A. Ruggiero, "Effects of Transient and Modulation of Beam Displacement on Long-time Stability with the Beam-Beam Interaction," FN-358, Fermilab, March 1982.
10. D. Neuffer, A. Riddiford, A. Ruggiero, "Simulations of the Beam-Beam Interaction with Time Modulation at the Tevatron p \bar{p} -Collider," FN-359, Fermilab, Feb. 1982.
9. A. G. Ruggiero, "Individual Bunch Longitudinal Instabilities," Fermilab, UPC-72, Jan. 1979.
10. A. G. Ruggiero, "Bunch-to-Bunch Longitudinal Instabilities," Fermilab, UPC-81, Jan. 1979.
11. King-Yuen Ng, "An Estimate of the Longitudinal Coupling Impedance of the Energy Doubler," Fermilab, UPC-150, May 1981.
12. H.W. Miller, "Transverse Active Dampers for the Tevatron," Fermilab, UPC-36, Jan. 1979.

TABLE 11-II XYZ COORDINATES OF BOOSTER TO DEBUNCHER LINE

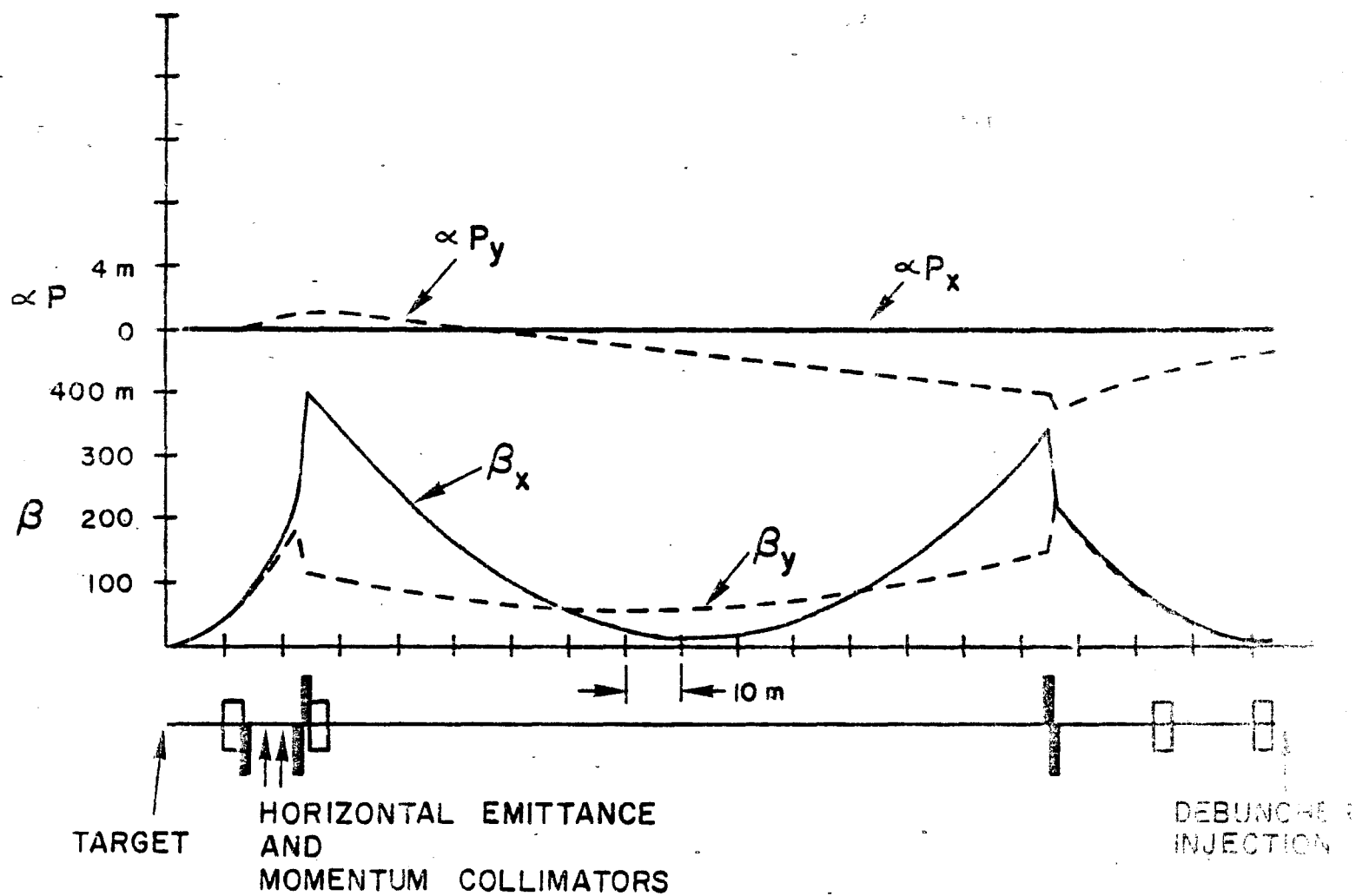
(Coordinates given at end of element (toward Debuncher) Main Ring Station
A0 at X=0.0, Y=0.0)

<u>Name</u>	<u>Length</u> <u>(in)</u>	<u>Field</u> <u>(kG-kG/m)</u>	<u>X</u> <u>(Ft.)</u>	<u>Y</u> <u>(Ft.)</u>	<u>Z</u> <u>(Ft.)</u>
<u>Booster Mid 3</u>			-487.041	-692.928	726.500
<u>B-Septum</u>	84.00	7.28	-483.543	-698.987	726.683
<u>BQ1</u>	32.00	-123.54	-472.558	-718.013	727.8436
<u>BB1</u>	60.00 EPB	-12.14	-469.560	-723.206	728.000
<u>BQ2</u>	22.50	135.75	-462.482	-735.465	727.853
<u>BQ3</u>	22.50	-124.71	-455.995	-746.702	727.723
<u>BB2</u>	40.00	15.00	-435.964	-781.396	727.323
<u>BB3</u>	40.00	-15.00	-433.464	-785.726	727.273
<u>Target</u>	-	-	-431.797	-788.613	727.239
<u>Collimator</u>	-	-			
<u>Dump</u>					
<u>BB4</u>	120.00 EPB	10.49	-410.289	-825.679	727.778
<u>BQ4</u>	22.50	-5.38	-408.855	-828.151	728.087
<u>BQ5</u>	22.50	121.26	-393.758	-854.169	731.345
<u>BQ6</u>	20.80	-128.71	-391.895	-857.379	731.746
<u>BB5</u>	120.00 EPB	-10.49	-385.888	-867.731	732.500
<u>Beam Pipe</u>					
<u>BQ6</u>	22.50	123.32	-176.518	-1228.554	732.500
<u>BQ7</u>	22.50	-123.04	-175.075	-1231.041	732.500
<u>BB6</u>	120.00	-6.89	-141.504	-1288.897	732.146
<u>B-Lambertson</u>	115.00	7.19	-113.324	-1337.461	728.500
<u>Debuncher D23</u>	-	-	-112.863	-1338.255	728.500



BOOSTER LINE TO TARGET

Fig. 11-1



TARGET TO DEBUNCHER LINE

Fig. 11-2